Experimental and chemical kinetic modelling study on the combustion of alternative fuels in fundamental systems and practical engines

By

Edirin Bruno Agbro

B.Eng, M.Eng

Submitted in accordance with the requirements for the degree of Doctor of Philosophy

The University of Leeds

School of Chemical and Process Engineering

August, 2017

The candidate confirms that the work submitted is his own, except where work which has formed part of jointly authored publications has been included. The contribution of the candidate and the other authors to this work has been explicitly indicated below. The candidate confirms that appropriate credit has been given within the thesis where reference has been made to the work of others.

Part of the work in chapter 4 has appeared in the following publications.

A.S. Tomlin, E. Agbro, V. Neverly J. Dlabka, M. Vasinek. Evaluation of combustion mechanisms using global uncertainty and sensitivity analysis: a case study for low temperature DME oxidation, International Journal of Chemical Kinetics 46 (2014) 662-682.

For the above, the candidate carried out the modelling work, computer simulations and analysis of all the data involving the rapid compression machine (RCM). The candidate also wrote the methodology section for modelling of ignition delay times in the RCM. Prof Alison Tomlin wrote the introduction, discussion and conclusions. All other authors contributed to the modelling and computer simulations of the jet stirred reactor (JSR) data.

E. Agbro, M. Materego, M. Lawes, A.S. Tomlin. Low Temperature Ignition Properties of n-butanol: Key Uncertainties and Constraints. Proceedings European Combustion Meeting (2015).

For the above, the candidate carried out the modelling work, computer simulations and analysis of all the data presented in the paper. The candidate also wrote the entire paper.

Prof Alison Tomlin proof read and rewrote part of the discussion. All other authors contributed to the generation of the Leeds RCM data and technical discussions prior to the publication.

E. Agbro, A.S. Tomlin. Low Temperature Oxidation of n-Butanol: Key Uncertainties and Constraints in Kinetics. Fuel 207 (2017) 776-789.

For the above, the candidate wrote the entire paper. Prof Alison Tomlin proof read the paper and reworded part of the discussion.

Part of the work in chapter 5 has appeared in the publication stated below.

E. Agbro, A.S. Tomlin, M. Lawes, S. Park, M. Sarathy. The Influence of n-butanol blending on the ignition delay times of gasoline and its surrogates at high pressures. Fuel 187 (2017) 211-210.

The candidate carried out all the modelling and experimental work and generated all the data presented in the paper. The candidate also wrote the introduction, methodology and part of the result and discussion. Prof Alison Tomlin proof read the draft and wrote part of the discussion. The group from King Abdullah University of Science and Technology, Clean Combustion Research Center, Saudi Arabia, involving S. Park and M. Sarathy developed the *n*-butanol/TRF blended mechanism based on the composition of *n*-butanol/TRF blend supplied by the candidate.

Acknowledgement

First and foremost my sincere appreciation goes to God Almighty for His strength, wisdom and divine provision throughout the course of my study.

I would like to express my gratitude to my supervisor Professor Alison S. Tomlin for her guidance and motivation throughout the period of this research. I thank her for helping to stimulate my interest in chemical kinetics for which I had very little or no background in. I also thank Dr Alexey Burluka for his valuable assistance in the engine work and for the many interesting and insightful discussions in his office.

I would like to thank my sponsor, the Tertiary Education Trust Fund (TETFUND) of Nigeria for providing funding for this research. I also thank the European Cost Actions CM0901 and CM1404 for providing financial support for scientific exchange visits. I thank Professor Fabian Mauss of LOGE Lund combustion Engineering, Germany, for granting me free academic license to use the LOGEengine software. I would like to specially thank Dr Michal Pasternak of LOGE Company for his support with LOGEengine software during my scientific exchange visits to the company.

I also wish to acknowledge the technical staff in the Thermofluid Laboratory in the School of Mechanical Engineering: Paul Banks, Brian Leach and Mark Batchelor, for ensuring that the experimental facilities are always in good condition.

Much appreciation to all my friends and colleagues in the Energy Research Institute: Wankang Zhang, Inna Gorbatenko, Francis Emejeamara, Amal Al-Rahbi, Peace Akubo, Japhet Oladipo, Katrina Adams, Kate Palmer, Julius Gane and others too numerous to mention, for their warm company and support. Your presence made my stay in Leeds worthwhile.

My wife deserve a special thanks for her patience and support during the period of my study. Thanks for being there and for bringing Daniel and Royal into my life.

Finally, much thanks to the greatest mum in the world, Theresa Agbro for her prayers, encouragement and constant calls throughout the period of this research.

Abstract

In this work, experimental data of ignition delay times of *n*-butanol, gasoline, toluene reference fuel (TRF), a gasoline/*n*-butanol blend and a TRF/*n*-butanol blend were obtained using the Leeds University Rapid Compression Machine (RCM) while autoignition (knock) onsets and knock intensities of gasoline, TRF, gasoline/*n*-butanol and TRF/*n*-butanol blends were measured using the Leeds University Optical Engine (LUPOE). The work showed that within the RCM, the 3-component TRF surrogate captures the trend of gasoline data well across the temperature range. However, based on results obtained in the engine, it appears that the chosen TRF may not be an excellent representation of gasoline under engine conditions as the knock boundary of TRF as well as the measured knock onsets are significantly lower than those of gasoline. The ignition delay times measured in the RCM for the blend, lay between those of gasoline and *n*-butanol under stoichiometric conditions across the temperature range studied and at lower temperatures, *n*-butanol acts as an octane enhancer over and above what might be expected from a simple linear blending law. In the engine, the measured knock onsets for the blend were higher than those of gasoline at the more retarded spark timing of 6 CA bTDC but the effect disappears at higher spark advances. Future studies exploring the blending effect of *n*-butanol across a range of blending ratios is required since it is difficult to conclude on the overall effect of *n*-butanol blending on gasoline based on the single blend that has been considered in this study.

The chemical kinetic modelling of the fuels investigated has also been evaluated by comparing results from simulations employing the relevant reaction mechanisms with the experimental data sourced from either the open literature or measured in-house. Local as well as global uncertainty/sensitivity methods accounting for the impact of uncertainties in the input parameters, were also employed within the framework of ignition delay time modelling in an RCM and species concentration prediction in a JSR, for analysis of the chemical kinetic modelling of DME, *n*-butanol, TRF and TRF/*n*-butanol oxidation in order to advance the understanding of the key reactions rates that are crucial for the accurate prediction of the combustion of alternative fuels in internal combustion engines. The results showed that uncertainties in predicting key target quantities for the various fuels studied are currently large but driven by few reactions.

Further studies of the key reaction channels identified in this work at the *P*-*T* conditions of relevance to combustion applications could help to improve current mechanisms.

Moreover, the chemical kinetic modelling of the autoignition and species concentration of TRF, TRF/*n*-butanol and *n*-butanol fuels was carried out using the adopted TRF/*n*-butanol mechanism as input in the engine simulations of a recently developed commercial engine software known as LOGEengine. Similar to the results obtained in the RCM modelling work, the knock onsets predicted for TRF and TRF/*n*-butanol blend under engine conditions were consistently higher than the measured data. Overall, the work demonstrated that accurate representation of the low temperature chemistry in current chemical kinetic models of alternative fuels is very crucial for the accurate description of the chemical processes and autoignition of the end gas in the engine.

Table of Contents

List of Figures

List of Tables

Nomenclature

Symbol		Description
A	-	Pre-exponential factor
A_f	m^2	Flame front area
A_{wall}	m^2	Cylinder wall area
B	m	Engine bore
c_p	J/kg/ K	Specific heat capacity at constant pressure
c_v	J/kg/ K	Specific heat capacity at constant pressure
dt	s	Change in time
E_a	J/mol	Activation energy
f	-	Uncertainty factor
G	-	Uncertainty in rate parameter
h	J/ kg	Specific enthalpy
H^0	J/mol/ K	Standard molar enthalpy
k	-	Rate constant
k_f	-	Rate constant (forward reaction)
k_r	-	Rate constant (reversed reaction)
k_{eq}	-	Equilibrium constant
K	-	Turbulent flame factor
L_r	m	Length of connecting rod
l	m	Integral length scale
M	kg/mol	Molecular weight
$\dot{m}$	kg/s	Mass flow rate
m	kg	Mass
m_b	-	Mass fraction burned
n	-	Temperature exponent
N_r	-	Number of reactions
N_s	-	Number of species
P	bar	Pressure

P_c	bar	End of compression pressure
$\dot{Q}$	J/s	Rate of heat transfer
q	-	Net rate of progress
R	J/kg/ K	Gas constant
$\bar{R}$	J/mol/ K	Universal gas constant
S	m	Stroke/local sensitivity coefficients
S^0	J/mol/ K	Standard molar entropy
S_L	m/s	Laminar flame speed
S_T	m/s	Turbulent flame speed
s	m	Piston position
t	s	Time
T	K	Temperature
T_c	K	End of compression temperature
U	J/kg	Specific internal energy
U	J	Total internal energy
u	m/s	Root mean square velocity
V	m^3	Volume
V_c	m^3	Clearance volume
V_d	m^3	Displacement volume
v	-	Stoichiometric coefficient
$\dot{w}$	-	Rate of molar production of specie
W	J	work
X	-	Species symbol
x	-	Mole fraction of component *i or j*
Y	-	Mass fraction of specie

Greek symbols

θ	degree	Crank angle
τ	s	Ignition delay time
τ_c	s	Critical value of ignition delay time
τ_t	s	Turbulent mixing time
γ	-	Ratio of specific heats
ρ	kg/m^3	Density
ε	m^2/s^3	Turbulent kinetic energy dissipation rate
ϕ	-	Equivalence ratio

Abbreviations

ABE	Acetone butanol ethanol
AFR	Air fuel ratio
BDC	Bottom dead centre
bTDC	Before top dead centre
C	Carbon
CAI	Controlled autoignition
CFD	Computational fluid dynamic
CFR	Comparative fuel research
CI	Compression ignition
CSP	Computational singular perturbation
DI	Direct injection
DME	Dimethyl ether
EGR	Exhaust gas recirculation
FFT	Fast Fourier transform
FTIR	Fourier transform infrared
GIFT	Gevo integrated fermentation technology
GM	Genetically modified

GUI	Graphical interface
H	Hydrogen
HCCI	Homogenous charge compression ignition
HDMR	High dimensional model representations
KLSA	Knock limited spark advance
KAUST	King abdullah university of science and technology
LLNL	Lawrence livermore national laboratory
LTC	Low temperature combustion
LUPOE	Leeds university ported optical engine
MAPO	Maximum amplitude of pressure oscillations
MBT	Maximum brake torque
MBMS	Molecular beam mass spectrometry
MFB	Mass fraction burn
MC	Monte Carlo
MON	Motor octane number
NI	National instrument
NTC	Negative temperature coefficient
O	Oxygen
ODE	Ordinary differential equation
ON	Octane number
PID	Proportional integral derivative
PC	Personal computer
PCI	Peripheral component interconnect
PON	Pump octane number
PRF	Primary reference fuels
PSR	Perfectly stirred reactors
RCM	Rapid compression machine
RPM	Revolution per minute
RON	Research octane number
RTSI	Real-time system integration

S	Sensitivity of fuel
SI	Spark ignition
SRM	Surface response model/ stochastic reactor model
TKE	Turbulent kinetic energy
TDC	Top dead centre
TRF	Toluene reference fuel
JSR	Jet stirred reactor
NTC	Negative temperature coefficient
QRS	Quasi-random sampling
VI	Virtual instrument
VPR	Variable-pressure flow reactor

Subscripts and superscripts

accel	Acceleration
b	burned
comp	Compression
const	Constant
decel	Deceleration
in	Inlet flow
min	Minimum
max	Maximum
out	Outlet flow
0	Initial or original value
∞	Infinity
u	Unburned zone
r	Reactions
s	Species

Chapter 1

Introduction to topic and scope of thesis

1.1 Background

Combustion of petroleum-based fuels presently represents over 85% of the world's energy demand and world energy demand is predicted to increase by around 30% by year 2030 [1]. The use of traditional fossil fuels have been blamed for environmental issues like climate change, acid deposition, and tropospheric ozone increases [2]. The foreseeable increase in energy demand in addition to other issues like increasing world population growth rate and environmental pollution makes it obvious that it is time to start looking at alternative sources of energy. This becomes even more apparent for the transportation sector which is hugely dependent on oil [3]. The development of new and efficient engine technologies and the use of alternative fuels are two major options being currently explored or targeted for achievement of a lower carbon footprint. While new engine technologies like the homogenous charge compression ignition (HCCI) engine, low temperature combustion (LTC) engine etc., have been shown to offer significant reductions in emissions and specific fuel consumption as well as improved thermal efficiencies, they are still currently under intensive research and are yet to be fully commercialised. In order to be able to meet the increasing energy needs and emissions requirement of future generations, it is crucial that research into the use of alternative fuels be vigorously pursued alongside research into the use of new engine technologies. The application of biofuels in the transportation sector could go a long way in helping to reduce the level of greenhouse gas emissions currently impacting negatively on the environment and the health of people living in metropolitan areas of the world [4]. Biofuels can be produced from a vast reservoir of biomass resources which are believed to generate lower net carbon dioxide emissions and which could be produced locally and sustainably in a way that could even lead to the economic development of the rural community and in general the agricultural sector.

Alcohols such as methanol, ethanol and butanol are being projected as satisfactory fuels that could be produced from renewable sources, and used successfully within internal

combustion engines. Alcohols, along with other oxygenated fuels, have been shown to have the potential to improve engine performance and emissions because of some of their unique physical and chemical properties [5-8]. Because methanol and ethanol have much higher octane number (ON) and latent heat of vaporisation compared to gasoline, engines running on them can be operated at higher compression ratios resulting in higher thermal efficiency. On the other hand, ethanol possesses an energy density that is about 30 % lower than that of gasoline meaning that far more ethanol would be required to cover the same unit of distance as gasoline because of the lower energy it delivers per litre of fuel [9, 10]. Although ethanol has been used extensively as a blend with gasoline (gasoline-ethanol blend with 10 % ethanol, also known as E10, is the normal blend in the US while E05 is usually employed in Europe), its low energy density currently limits its use to low blending ratios as major modification of current engine technology would be required before higher blending levels can be applied. In addition, ethanol has a tendency for attracting water (water absorption) and can thus easily corrode normal fuel supply pipelines [11].

There is presently a strong support for biobutanol (*n*-butanol or 1-butanol) as a potential replacement for ethanol in spark ignition (SI) and compression ignition (CI) engines due to its numerous similarities with gasoline and advantages over ethanol. Due to its higher energy density (see Table 1.1), butanol offers better fuel economy when blended with gasoline compared to ethanol. With many properties (i.e. lower heating value and stoichiometric air-fuel ratio) that are more similar to gasoline than ethanol, butanol can be blended with gasoline at higher concentrations without the need for engine retrofitting or modification [11]. In one of the studies reported in the literature [12], up to 80 % of butanol by volume was blended with gasoline. Other advantages of butanol over ethanol include its tolerance for water contamination in gasoline and less tendency to corrosion allowing it to be transported with existing distribution fuel pipelines. The properties of butanol such as its higher cetane number and lower vapour pressure compared to ethanol, similar viscosity with diesel and better miscibility in diesel fuel makes it a more attractive fuel for use in compression ignition engines [13]. Although biofuels are a potential alternative to fossil fuels, current available production routes are surrounded with a few challenges. The application of food crops like sugar cane, corn, cassava, sorghum, oil palm etc. as biomass feedstock for the production of first

generation biofuels like ethanol, biobutanol and biodiesel is seen as potentially detrimental to the food chain as this could lead to serious food scarcity and consequently drive the price of food beyond the reach of the average people [14, 15]. In addition, the destruction of large expanses of forest land for cultivation of energy crops could have serious implications for our environment and ecosystems and could lead to loss of biodiversity. These concerns are currently being addressed by the use of lignocellulosic biomass materials as opposed to food crops for the production of second-generation biofuels. Recent advances in biofuel feedstock and production technologies can also go a long way to help reduce the negative impacts of biofuels [11, 16].

Table 1.1: Properties of gasoline, *n*-butanol, ethanol and methanol [11]

Fuel	Gasoline regular (PON 87)	*n*-Butanol	Ethanol	Methanol
Chemical formula	$CH_{1.87}$	C_4H_9OH	C_2H_5OH	CH_3OH
Specific gravity	0.7430	0.8097	0.7894	0.7913
Lower Heating Value (MJ/kg)	42.9	32.01	26.83	20.08
Stoichiometric air-fuel ratio (kg_{air}/kg_{fuel})	14.51	11.12	8.94	6.43
Energy density (MJ/l)	31.9	25.9	21.2	15.9
Latent heat of vaporisation (at boiling point) (kJ/kg)	349	584	838	1098
Octane number (RON+MON)/2	87	86	100	99

One of the major challenges in the production of biobutanol is the low productivity of the fermentation process and high energy cost of the separation process. To take advantage of the various potential benefits of biobutanol, a number of players across the globe are now involved in the research and development of novel alternatives to the economically unfavourable Acetone Butanol Ethanol (ABE) fermentation process, which would make the commercial scale production of biobutanol feasible. Gevo, one of the major companies at the fore front of second generation biofuel production, with headquarter in Englewood, Colorado, is known to have invented an optimal process called the Gevo Integrated Fermentation Technology (GIFT) for the production of iso-butanol from sustainable biomass feedstock. Gevo currently produces iso-butanol at their first fermentation plant in Luverne Minnesota. The plant is regarded as the first

commercial-scale biobutanol plant in the world [17]. Green Biologics Limited, a renewable chemical and biofuel company in the UK, has also come up with improvements on the traditional fermentation process and employs a newly developed genetically modified (GM) microbial strain in the production process of *n*-butanol. The advanced genetic optimisation process significantly reduces both the production cost and the capital cost of implementation. In January 2015, Green Biologics revealed plans to commercially produce *n*-butanol from a 21 million gallon-per-year retrofitted ethanol plant in 2016 [18]. Butamax Advanced Biofuels, a joint venture between BP and DuPont formed in 2009, has also made significant investment in the research and development (R&D) of the technology required for commercial scale production of *n*-butanol for use as a blending component in the transport sector [19, 20]. Under the BP-Dupont partnership, a fleet of the official cars used in the 2012 Olympic Games were successfully fuelled with a blend of 24 % by volume of biobutanol in gasoline confirming again its compatibility with the current engine infrastructure. Other companies in the forefront of biobutanol development and commercialisation include: Cobalt Biofuels, Tetravitae Bioscience and METabolic Explorer, France [21].

Apart from alcohols, another alternative fuel that has drawn the attention of many researchers in recent times is dimethyl ether (DME). DME as an oxygenated fuel has been proposed as a potential alternative to diesel and biodiesel fuels due to its high cetane number, high oxygen content and low boiling point. DME (the simplest ether with no carbon to carbon bond in molecular structure) is currently being promoted as a fuel additive for use in compression ignition engines because of its low sooting and polluting potential. It is claimed that the use of DME could lead to reduction in the level of particulate emissions due to its oxygen content and reduction in NOx emissions due to its shorter ignition delay compared to diesel [22, 23]. DME can be produced from natural gas, coal or biomass but the most cost effective feedstock for DME is natural gas at remote locations [24]. DME is particularly attractive in countries with vast reserves of coal and natural gas because it offers a promising window for reducing incessant fuel crises as well as meeting emission standards [23].

1.2 Motivation

It is clear from the foregoing that alternative fuels such as biobutanol and DME are increasingly gaining attention for commercialisation because of their significant role in the goal towards achieving lower carbon emissions as well as energy security in the near future. However the suitability of a liquid fuel as an alternative transportation fuel depends not only on their physical and chemical properties but largely on their combustion and emissions characteristics [13]. These properties to a huge extent will determine whether or not the alternative fuel is compatible with existing or new engine technologies and with the conventional fuel that it partly or fully replaces. A wider penetration and sensible use of biofuels and biofuel mixtures in internal combustion engines thus require first and foremost, a thorough understanding of their properties and the effect of their use in terms of engine efficiency and pollutant formation.

Despite the promising results that have already being obtained from experiments, a detailed investigation and understanding of the behaviour of these new fuels in real engines under a wide range of conditions is needed and this can only be fully realised through computer modelling and analysis. Computer modelling and simulation provides the ability to relatively solve the complex problems related to these new and completely different fuels cheaply and quickly without having to go into the rigors of very expensive and time consuming experimental testing [25]. Where experimental measurements are difficult or impossible, the wide range of data provided through computer modelling can also be effectively utilised for the design, testing and control of new and conventional combustion technologies required to use alternative fuels optimally. While the application of a predictive engine numerical code valid for these fuels could help to unlock their full potential, the employed models must however account for the effect of the fuel reaction mechanism on the combustion process [3]. Therefore, accurate prediction of the combustion and emissions behaviour (ignition properties, heat release rates, amount of emissions) of alternative fuels in practical engines strongly depends on the development of detailed and accurate reaction mechanisms which describes at a molecular level how the reactants (i.e. fuel and air) are converted into products through a series of intermediate elementary steps.

Various numerical models raging from simple zero-dimensional, empirical and quasi-dimensional thermodynamic models to more complex multidimensional fluid dynamic models have been employed for predicting the combustion and emission properties of reacting flows [26-28] while incorporating some level of chemistry ranging from single step reaction to detailed chemistry. Current efforts are strongly geared towards being able to accurately predict the details of combustion in a complex flow field, where both fluid dynamics and chemistry interact and influence predictive combustion targets such as peak pressures, autoignition, knock, pollutant species formation and heat release rates. In general, fluid mechanical problems still tax the largest computer, and the addition of chemistry makes the solution impossible. The computational cost of such endeavours has given rise to the need for the use of reduced and simplified mechanisms in reacting flow problems. In order to develop reduced models, one must first start with the detailed chemical kinetic schemes and set of experimental data. Reduction methods including sensitivity analysis and uncertainty analysis are quite useful in the context of developing skeletal and reduced mechanisms [29].

In the past, attempts have been made to predict autoignition in engines using various simple empirical models. Two of such correlations are the popular Douaud and Eyzat (D&E) model derived from the Arrhenius function and the Livengood-Wu integral both of which are fully described in section 2.2.4.1 of this thesis. In terms of chemical kinetic modelling, the prediction of autoignition in the engine has been limited to the use of very basic global chemical reaction mechanisms developed for a limited number of fuels, i.e. the 'Shell model' comprised of 5 species and 8 generalised reactions representing chain/degenerate branching and termination steps and the skeletal Keck model. However these global kinetic models, just like the empirical models, have been proven to be grossly inaccurate in terms of agreement with measured data [30]. The use of detailed or reduced reaction mechanisms that are coupled to main engine combustion models offers a far greater capability to predict autoignition in an engine to a higher level of accuracy and therefore forms the basis for this study.

However current kinetic models of alternative fuels are still subject to considerable inaccuracies introduced through the inherent uncertainties in their input data (i.e. rate parameterisation and thermochemical data). Methods exploring the sensitivities of chosen predictive targets (e.g. ignition delays, flame temperatures, species

concentration) to these inherent uncertainties, such as local and global sensitivity/uncertainty analysis can help to identify the most important parameters that largely dictate the predictive accuracy of these models. Information provided via sensitivity and uncertainty analysis could help to focus effort on the parameters (e.g. rate constants) with the largest influence on predictions through more detailed experimental and theoretical studies in order to improve model parameterisation, thus helping to improve the overall predictive accuracy and robustness of the schemes.

It is important to mention at this point that chemical kinetic models of fuel combustion are generally developed and validated within a range of well-controlled experimental configurations where operating conditions resemble those obtainable in practical combustion devices such as the HCCI and SI engine. Such configurations include shock tubes and rapid compression machines for ignition delay measurements, combustion bombs and opposed-flow (laminar) diffusion flames for laminar flame speed determinations, and jet-stirred and flow reactors as well as premixed flames for species measurements. However, in most of the above fundamental setups, the impact of fluid dynamics and transport processes are suppressed and the prevailing *P*-*T* conditions are much more representative of the *P*-*T* conditions occurring before autoignition in HCCI and or controlled autoignition (CAI) engines rather than in SI engines. This could pose a challenge to the application of these models in simulating practical engine configurations where the influence of flow is normally significant and where for example as in an SI engine, higher *P*-*T* conditions prevail in the end gas due to the high compression induced on it by the propagating flame. Therefore it crucial to test the applicability of these models under practical engine conditions in order to establish their capacity and robustness in reproducing observed target engine combustion properties. Although a very few number of detailed and reduced chemical kinetic models of alternative fuels like DME, *n*-butanol and their blends with conventional fuels have been developed by the kinetic community for use within the context of engine simulations, these models have been hardly applied or investigated under real engine conditions where the effect of fluid dynamics, high variable pressures and temperatures as well as variable volume combustion and flame propagation (as in SI engine) are accounted for; so this research attempts to fill the void. Moreover, there is currently a huge need to link

our current fundamental kinetic understanding of alternative fuels with their performance in real engines conditions-this is the main driving force of this research.

The broad questions that this research seeks to answer are:

- Are current computer models of alternative fuels sufficiently well quantified to assist our understanding of the processes that occur in real engines where they are needed for optimisation and design?
- How does alternative fuels performance in real engines differ from their performance in fundamental systems?
- How does the combustion of alternative fuels in real engines differ from the combustion of fossil fuels in real engines?
- How do the performance of surrogate fuels in fundamental combustion systems and practical engines differ from the performance of the real fuels they mimic?

1.3 Research objectives

The overall aim of this research was to investigate and assess the fundamental chemical kinetic modelling of alternative fuels developed under idealised (engine-like) conditions, in both fundamental and practical engine setups. The research is looking to bridge the gap between the fundamental chemical kinetic modelling of alternative fuel combustion and their behaviour in real engine applications where they are needed for engine optimisation and design. Therefore a modelling and experimental approach cutting across both fundamental set ups such as rapid compression machine (RCM), jet stirred reactor (JSR) as well as flow reactors and practical engine set ups such as the spark ignition (SI) engine has been adopted in this study with the main focus being on *n*-butanol when blended with gasoline.

The specific objectives of this research are:

1. To carry out the chemical kinetic modelling of the ignition delay times of DME in an RCM and species concentrations of key pollutants in a flow reactor in comparison with available experimental data from open literature.

2. To carry out the chemical kinetic modelling of the ignition delay times of *n*-butanol in an RCM and species concentrations of key pollutant in a JSR in comparison with available experimental data from open literature.

4. To provide new experimental data of the ignition delay times of *n*-butanol, gasoline, toluene reference fuel (TRF), gasoline/*n*-butanol blend and TRF/*n*-butanol blends measured in in an RCM which could be used for the validation of chemical kinetic modelling of the same fuels.

5. To develop and investigate the performance of a gasoline surrogate based on a TRF in capturing the main trend of gasoline and gasoline/*n*-butanol blending behaviour in both the RCM and engine.

6. To carry out chemical kinetic modelling of the ignition delay times of *n*-butanol, TRF and TRF, *n*-butanol blend in the RCM in comparison with the measured data from the Leeds RCM.

7. To evaluate detailed and reduced chemical kinetic schemes of DME, *n*-butanol, TRF and TRF/*n*-butanol blend using both local and global uncertainty/sensitivity analysis in the context of simulating homogenous zero-dimensional reactor models like the RCM and JSR.

8. To investigate the influence of *n*-butanol blending on the combustion and knock properties of gasoline using the Leeds University Optical Engine and to also use the measured data for validation of the modelling work.

9. To investigate the performance of a gasoline surrogate based on a TRF in capturing the main trend of gasoline/*n*-butanol blending combustion behaviour in the Leeds University Optical Engine.

10. To implement a reduced version of the chemical kinetic mechanism of TRF/*n*-butanol blend in the LOGEengine software.

11. To carry out the chemical kinetic modelling of the combustion, autoignition and knock properties of *n*-butanol, TRF and TRF/*n*-butanol blend under real engine conditions using the LOGEengine software in comparison with measured data.

12. Comparison of measured and predicted data of autoignition obtained within the RCM and that obtained within the engine setup.

1.4 Thesis outline

The thesis is divided into seven chapters as outlined briefly below.

Chapter 2: Provides background knowledge of the combustion process, autoignition and knock in SI engines, combustion chemistry and methods of modelling combustion in practical engines.

Chapter 3: Describes the methods employed for acquiring all experimental data presented in this study as well as the numerical approaches used in the modelling programme.

Chapter 4: Presents the results and discussion of the chemical kinetic modelling study of DME and *n*-butanol oxidation carried out within both the RCM and constant volume reactors (JSR and flow reactor) with ignition delay times in the RCM and species concentrations in reactors as the predictive output.

Chapter 5: Presents the results and discussion of the chemical kinetic modelling study of the influence of *n*-butanol blending on the ignition delay times of gasoline and its surrogates in the RCM. The experimental data obtained for *n*-butanol, gasoline, TRF, gasoline/*n*-butanol blend and TRF/*n*-butanol blend using the Leeds RCM for validation of the modelling work are also presented alongside the predicted results.

Chapter 6: Presents the results and discussion of the chemical kinetic modelling study of the influence of *n*-butanol blending on the combustion, auto-ignition and knock properties of gasoline and its surrogates in the spark ignition engine. The measured data obtained for gasoline, TRF, gasoline/*n*-butanol blend and TRF/*n*-butanol blend using the Leeds University Optical engine (LUPOE) for validation of the modelling work are also presented alongside the predicted results.

Chapter 2

Background information/literature review

2.1 Reciprocating internal combustion engines

The internal combustion engine plays a very significant role in the field of power, energy and propulsion. Although the term internal combustion engine is mostly used to refer to reciprocating internal combustion engines, gas turbines are also regarded as internal combustion engines. The earliest appearance of successful internal combustion engines were the spark-ignition engine invented by Nicolaus A. Otto in 1876 and the compression ignition engine invented by Rudolf Diesel in 1892. Following that initial success these engines have overtime undergone various modifications in order to take advantage of available new engine technologies as well as meet the stringent regulations on engine exhaust gas emissions [31]. The primary function of the internal combustion engine is the conversion of chemical energy stored in fuel molecules into mechanical energy through burning (combustion) of fuel and oxidiser inside the engine cylinder. Chemical energy of the fuel is first converted to thermal energy by means of combustion or oxidation with air inside the engine, raising the temperature and pressure of the gases within the combustion chamber. The high-pressure gas then expands and by mechanical mechanisms rotates the crankshaft, which is the output of the engine. The crankshaft is connected to a transmission/power-train to transmit the rotating mechanical energy to drive a vehicle.

The reciprocating internal combustion engine is one of the most widely used forms of engine in the automobile field [26]. The spark ignition engine (SI), also known as the gasoline engine and the compression ignition engine (CI), also known as the diesel engine, are the two major classes of reciprocating internal combustion engines. In the SI engine the fuel-air mixture is ignited by a spark while in CI engines air is compressed to a high temperature and pressure sufficient enough to auto ignite the fuel charge.

In the reciprocating internal combustion engine (Figure 2.1), a piston travels up and down in a cylinder and with the aid of a connecting rod and crankshaft mechanism, power is transmitted from the engine piston to the drive shaft. The linear motion of the

piston is converted to a rotary motion of the drive shaft in the process. The piston comes to rest at top dead centre (TDC) and bottom dead centre (BDC) when the cylinder volume is minimum and maximum respectively. The minimum cylinder volume is called the clearance volume V_c, while the volume swept by the piston is called the displaced (or swept) volume V_d. The swept volume is the difference between the maximum cylinder volume and the clearance volume. The compression ratio r_c is the ratio of maximum volume to minimum volume. For spark ignition engines compression ratios are usually in the range of 8 to 12 while for compression ignition engines, they are within the range of 12 to 24 [31].

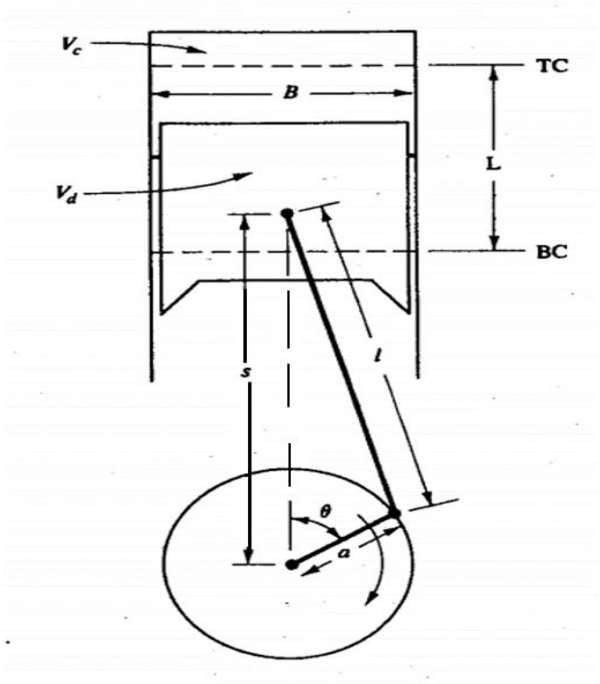

Figure 2.1: Piston and cylinder geometry of a reciprocating engine. B = bore; L = stroke; l = connecting rod length; a = crank offset; s = piston position; θ = crank angle. Adapted from [31].

To complete the sequence of events that yields one power stroke in a four-stroke cycle, two revolutions of the crankshaft are required. Both types of engine can be designed to operate in either four strokes or two strokes of the piston. The four-stroke cycle is made up of the following:

1. Induction stroke: At the start of the induction stroke, the inlet valve is open and the piston is at TDC. The piston then travels down the cylinder, drawing in a

fresh charge of air. For a SI engine, the charge is a premixed mixture of air and fuel.

2. Compression stroke: At the start of the stroke, the inlet valve is closed and the piston is at BDC. The piston travels back to TDC with all valves closed, compressing the mixture to a small percentage of its volume and raising the temperature and pressure in the cylinder. As the piston approaches TDC, ignition occurs and combustion is initiated. For a CI engine the fuel is only injected close to the end of the compression stroke.
3. Power stroke or expansion stroke. At the start of the stroke, both valves are closed and piston is at TDC. Combustion which was initiated close to the end of the compression stroke, propagates through the charge and the resulting high-temperature, high-pressure gases push the piston down, forcing the crank to rotate. As the piston approaches BDC, close to the end of the power stroke, the exhaust valve opens and exhaust blowdown occurs.
4. Exhaust stroke: When the piston reaches BDC, exhaust blowdown is complete, but the cylinder is still full of exhaust gases at approximately atmospheric pressure. With the exhaust valve still open, the piston now travels up the cylinder from BDC in the exhaust stroke and some of the remaining exhaust gases are expelled from the cylinder. As the piston approaches TDC, the inlet valve starts to open such that it is fully open at TDC. Near TDC, the exhaust valve on the other hand, starts to close and it is fully closed just after TDC to begin the next cycle. The time when both the intake and exhaust valve are open is known as "valve overlap".

The four-stroke cycle delivers one power stroke in two revolutions of the crankshaft. The two-stroke cycle was developed to obtain higher power output from a given engine design and a simpler valve design [32] . In the two-stroke cycle, the separate induction and exhaust stroke is built into the compression and power stroke respectively. The two strokes are explained as follow:

1. Compression stroke: At the start of this stroke the inlet and exhaust valves are closed. The piston then travels up the cylinder, compressing the cylinder content and simultaneously drawing fresh charge into the crankcase. For cases of a non-

premixed mixture, the fuel is injected as the piston approaches TDC and combustion is initiated.

2. Power or expansion stroke: The piston is forced down by the high-pressure, high-temperature combustion gases and in that process compresses the charge in the crankcase. As the piston approaches BDC, first the exhaust port is uncovered and most of the combustion gases are expelled from the cylinder in a blow down process. When the piston arrives BDC, the intake port is uncovered and the fresh charge which has been compressed in the crankcase flows into the cylinder and at the same time displaces the remaining combustion gases by a process known as scavenging.

2.2 Combustion in spark ignition engines

In SI engines the fuel and air mixture is premixed in the intake system before entering into the engine cylinder. For combustion (spark ignition and flame propagation) to occur satisfactorily, the air-fuel ratio is usually held at close to stoichiometric conditions. The equivalence ratio of the mixture of air and fuel influences pollutant emissions, the tendency for autoignition (and consequently knock), efficiency and power output [26]. In SI engines, premixing is usually achieved with a carburettor or fuel-injection system. In a carburettor air flows through a venturi, and the pressure drop generated causes fuel to flow through an orifice, the jet. Early fuel injection systems were controlled mechanically, but the usual form of control is now electronic. Fuel is not normally injected into the cylinder during the compression stroke as this will require high-pressure injection equipment, and it would reduce the time for preparation of a homogenous mixture. A popular method used instead of carburettors is fuel injection into the intake manifold or inlet port of the engine [31]. When port injection is applied, the fuel is simply injected across separate set of injectors from a low-pressure fuel supply system into each intake port, just beside the inlet valve of each cylinder. Another way it is done is by using a single injector to inject the fuel close to the mouth of the inlet manifold [26]. Direct injection stratified charge engines, which operate with high injection pressures, have also been developed recently and these provide opportunity for fuel economy gains.

At the start of one engine cycle of a four stroke SI engine, the intake valve is open and the piston is at the top of the cylinder (TDC). As the piston descends down the cylinder, fuel and air mixture is induced into the cylinder. On the return stroke of the piston, just after BDC, both the intake and exhaust valves are closed and the cylinder content (which is a mix of fresh charge and residual burned gases remaining from previous cycle) is compressed to a pressure and temperature that are above atmospheric conditions as the piston travels across the cylinder volume. Compression ratios obtainable in spark ignition engines are in the range of 8 to 12 and relative to compression ignition engines this would usually lead to lower power output per engine stroke [31]. Lower compression ratios are applied in SI engines in order to reduce tendency for engine knock due to autoignition of the air-fuel mixture during the compression process [16]. Just before the end of the compression stroke, (i.e. between 10 and 40 crank angle degrees before TDC), the premixed fuel and air charge is ignited by a spark plug and the resulting flame travels through the mixture of fuel, air and residual gases in the clearance volume to finally get quenched at the cold wall of combustion chamber. The time it takes to complete combustion is usually around 40 to 60 crank angle degrees, depending on the design of the engine and its operating conditions. As combustion evolves within the combustion chamber, a rapid rise in pressure and temperature results and drives the piston down across the power or expansion stroke. The spark timing for which maximum torque can be obtained for a certain air-fuel ratio is called the maximum brake-torque timing (MBT) [31]. More advanced (earlier) timing or retarded (later) timing than optimum gives lower output and efficiency. If ignition occurs too late, both the piston work during the compression stroke as well as the output work during the expansion stoke are reduced due to decreased cylinder pressures obtained across the entire cycle. In addition combustion will most likely not be complete before the exhaust valve opens at the end of the expansion stroke and this can lead to overheating of the exhaust valves. On the other hand if ignition happens too early, excessive pressure rise may develop before the end of the compression stroke (i.e. before TDC) leading to reduction in power as well. Moreover the peak pressures and temperatures that develop due to early ignition may be large enough to cause engine knock [26]. In the expansion stroke, as the piston approaches BDC, the exhaust valve opens and a blow down process occurs due to the difference in pressure between the cylinder and exhaust manifold. Finally, after BDC, the piston begins to move up the

cylinder in the exhaust stroke, forcing out the remaining burned gases in the cylinder and the entire cycle is repeated.

2.2.1 Stages of combustion in SI engines

Pressure rises obtained during combustion in an ideal engine occur exclusively under constant volume conditions (i.e. within the clearance volume) but in an actual engine this is completely different. Combustion in an actual SI engine can be divided into the following three stages as shown in Figure 2.2 [32, 33].

1. Ignition lag stage (or early flame development stage)
2. Flame propagation stage
3. After burning stage (or flame termination stage)

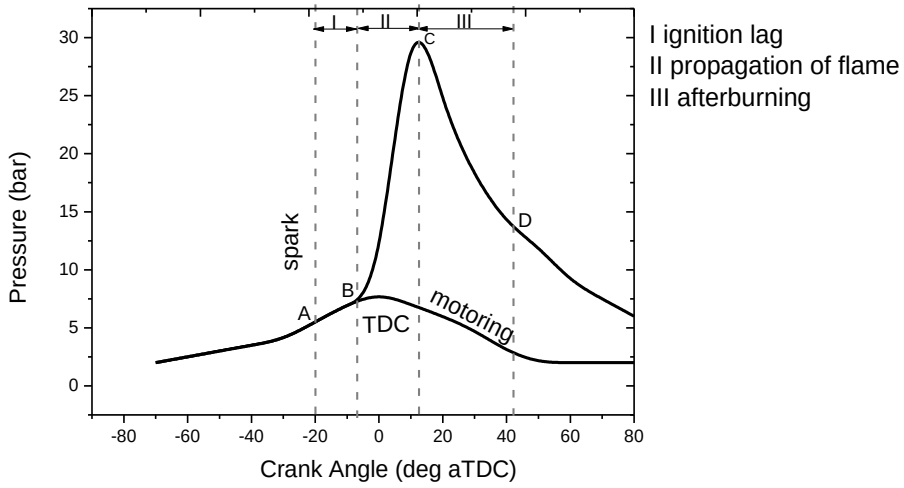

Figure 2.2: Stages of combustion in an SI engine. The line labelled 'motoring' represents the non-firing pressure cycle. Adapted from [32].

In Figure 2.2, A is the point of spark discharge (say 20^0 bTDC). B is the point at which the energy produced from the propagating flame is big enough for the start of the pressure rise to be clearly visible (say 8^0 bTDC) and C is the point of peak pressure [32]. Therefore AB, BC and CD represent the ignition lag stage, flame propagation stage and flame termination stage respectively.

2.2.1.1 Ignition lag phase

The ignition lag period, represented by path AB in Figure 2.2, marks the beginning of a self-propagating flame nucleus. During flame development, there is little or no work done as no substantial combustion has yet occurred. Ignition lag refers to the time interval between the instant of spark and the instant where there is a noticeable rise in pressure due to combustion. Ignition lag is the time interval in the process of chemical reaction during which molecules get heated up to self-ignition temperature, get ignited and produce a self-propagating nucleus of flame. This process is driven by chemical kinetics and it is a function of the type of fuel, temperature and pressure, amount of exhaust gas in combustion chamber and the oxidation rate. The ignition lag is generally expressed in terms of crank angle (θ).

2.2.1.2 Flame propagation phase

This phase represented by BC in Figure 2.2, is driven by the physical processes and it is responsible for increasing the radius of the flame across the combustion chamber. During this phase there is significant pressure rise, which provides the force that produces the work in the expansion stroke and the flame propagates practically at constant velocity [34]. The turbulence intensity and the reaction rate are the major factors that determine the heat-release rate and the two parameters are significantly influenced by the composition of the mixture.

2.2.1.3 After burning

This is the third and final phase of the combustion process which leads to flame termination. The after burning phase represents the phase of slow evolution of combustion after the attainment of peak pressure at point ‘C’ in Figure 2.2. The beginning of this phase is the point of maximum pressure as shown on the indicator diagram. The lower flame speeds encountered during this phase leads to a drastic fall in the rate of combustion and the in-cylinder pressures will continue to fall until the end of the expansion stroke [31].

2.2.2 Autoignition and knock in SI engine

In an SI engine combustion is initiated towards the end of the compression stroke with the aid of spark discharge from a spark plug. Once the fuel air mixture around the spark plug is ignited by spark energy, a flame kernel is formed and the kernel gradually evolves until it becomes a fully developed self-sustaining flame front which now propagates steadily across the entire combustion chamber volume [35-38] compressing the unburned mixture ahead of it to higher temperatures and pressures. Under abnormal (knocking) combustion, the advancing flame front together with the moving piston, compresses the end gas to high *P*-*T* conditions sufficient enough to accelerate the chemical reactions in the end gas at locations remote from the spark plug and a spontaneous ignition (autoignition) of the end gas occurs [39]. Following the autoignition and rapid consumption of the end gas, sonic pressure waves are generated from the autoignition spot which further interacts with the flame front to produce very high frequency pressure oscillations within the engine cylinder. The resulting high pressure oscillations impinge on the engine cylinder walls causing vibration and a sharp audible (pinging) sound generally referred to as knock [35]. Engine knock is a highly undesirable combustion phenomena because apart from the discomfort it brings to vehicle drivers and passengers, it can lead to serious damage of the engine hardware. Under normal non-knocking combustion, the unburned mixture (end gas) is completely consumed by the advancing flame front before the chemical reactions in the end gas are able to develop to the point where autoignition occurs. Figure 2.3 shows a schematic diagram of the combustion process in an SI engine under normal and knocking conditions while Figure 2.4 shows typical pressure traces obtained under normal and abnormal combustion in an SI engine. The sensitisation or induction period of the end gas generally referred to as ignition delay time and the occurrence of autoignition itself are a function of the composition and type of fuel alongside the temperature and pressure of the end gas [38]. Therefore, fuels that are less reactive (e.g. exhibit longer ignition delay times) are more capable of withstanding the additional compression and heating imposed on the end gas by the expanding flame front without auto-igniting compared to very reactive fuel with shorter ignition delays.

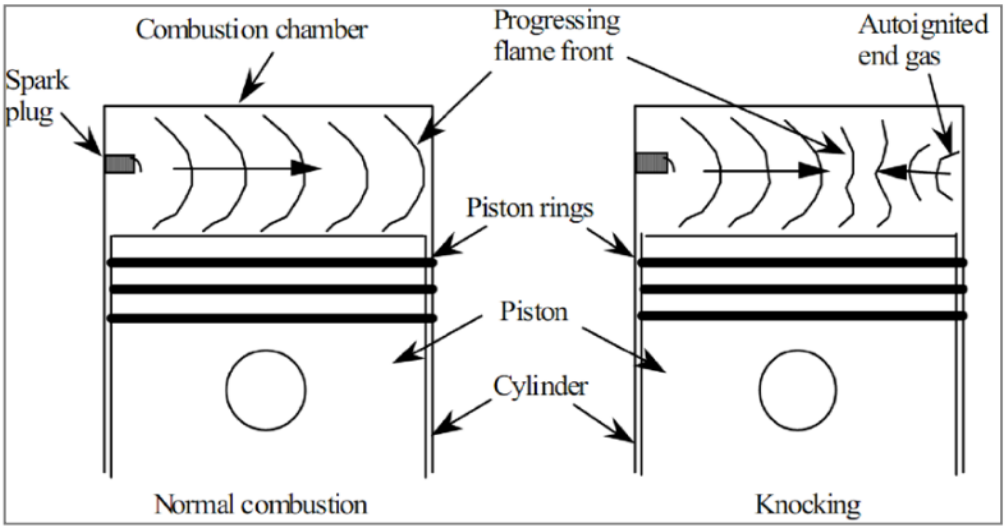

Figure 2.3: Schematic diagram illustrating the normal and knocking combustion in an SI engine. Taken from [37].

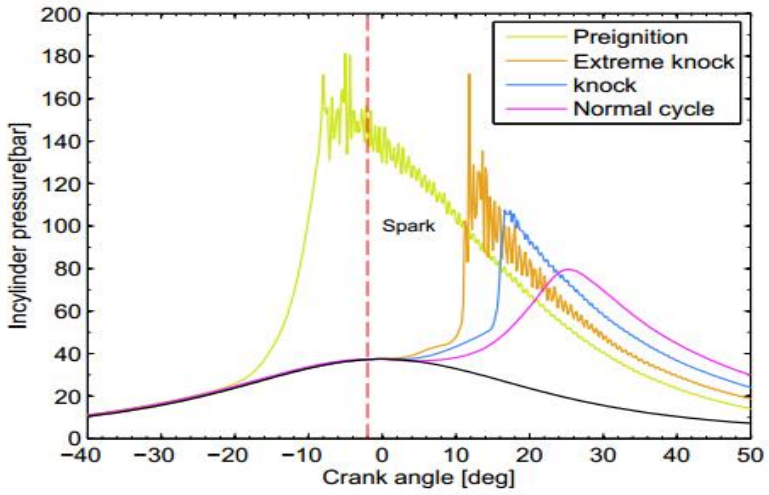

Figure 2.4: Typical pressure traces illustrating pre-ignition, light knock, extreme knock and normal combustion obtained in a boosted SI engine. Taken from [40].

Another form of abnormal combustion which may also lead to knock is self-ignition. Self-ignition occurs when the end gas is ignited by other sources apart from the electrical discharge from the spark plug such as overheated surfaces and glowing deposits in the combustion chamber. The overheated surfaces include spark plugs and valves while the glowing deposits may include carbon deposits and hot engine oil droplets [31, 41]. Self-

ignition occurring before the normal spark ignition is referred to as pre-ignition while that occurring after the mixture is spark ignited is called post ignition. Self-ignition can be generally avoided in engine operation through sufficient cooling of spark plugs and valves and the use of deposit prevention additives [30].

Apart from autoignition theory, the theory of detonation has also been advanced as being responsible for the phenomena of knock. The detonation wave theory proposes that knock occurs as a result of the rapid consumption of the end gas ahead of the propagating flame due to the impact of a shock or detonation wave. Filey [42] proposed that detonation waves are generated by the slow oxidation reactions in the end gas. Bradley and Kalghatgi [43] believe that in addition to the pressure waves arising from the autoignition of the end gas, pressure waves (detonation waves) arising from sudden acceleration of the flame front due to flame instabilities also contributes to the occurrence of engine knock. Detonation theory is however unpopular because of lack of sufficient data to support its proposition.

2.2.3 Factors affecting autoignition

2.2.3.1 Engine operating variables

As the rate of the reactions leading to autoignition of the end gas are a function of temperature and pressure, factors including engine operating parameters and fuel properties affecting the *P-T* conditions of the end gas would therefore impact on the autoignition behaviour of the end gas. For a given fuel of specific size and chemical structure, engine operating parameters that lead to higher pressures and temperatures of the end gas would normally result in earlier onset of knock. Some of the key factors affecting autoignition and knock in a spark ignition engine are described below.

Spark timing: At a more advanced spark timing, ignition occurs earlier in the compression stroke allowing the temperatures and pressures to develop to higher peak values. Therefore, the tendency for knock occurrence as well as its intensity increases as the spark timing is advanced due to higher pressure and temperature conditions. In engine calibration, there is an optimum spark timing that gives a maximum brake torque (MBT) and highest efficiency. The knock limited spark advance (KLSA) of a specific engine and fuel type is the spark timing at which knock becomes significant. For an

engine with a KLSA retarded relative to the optimum spark timing, the engine is forced to operate at a spark timing retarded away from the optimum spark timing and consequently lower efficiency in order to avoid the impact of knock [35].

Compression ratio: The compression ratio of an engine can be increased by reducing the clearance volume. Increasing the compression ratio leads to higher temperatures and pressures due to higher compression of the end gas. Although the use of higher compression ratio increases the thermal efficiency of an engine, the propensity for the occurrence of knock is also increased for such engines.

Intake pressures and temperatures: Autoignition is driven by underlying chemical reactions. Based on the Arrhenius law (Equation 2.16), the rate of a chemical reaction is a function of temperature and pressure, and as a result, higher pressure and temperature conditions of the end gas would accelerate the autoignition chemistry as well as the tendency for knock. The tendency for knock is increased in boosted (turbocharged) engines compared to naturally aspirated engines due to their higher intake pressures.

Engine speed: The speed of propagation of the flame increases with increase in engine speed. This is because an increase in engine speed would lead to an increase in turbulence as well as swirl and consequently the turbulent intensity in the engine cylinder [44]. Moreover, at higher speeds the autoignition reactions in the end gas are deprived of sufficient time to develop and advance and as a result, the faster propagating flame is able to consume the end gas before the autoignition condition is attained. Therefore, the knock tendency of the end gas is reduced as engine speed is increased.

Exhaust gas recirculation (EGR): EGR is mainly employed in modern automobiles for the reduction of nitrogen oxide emissions. EGR works by diluting the air - fuel mixture with non-combustible gases, thereby reducing the maximum in-cylinder temperature and burning rate and as a result lower concentrations of NO_X are produced during combustion [33]. With lower burning rates, the peak pressures are reduced and in combination with the lower maximum temperatures produced, the tendency for knock is also reduced with the use of EGR.

Equivalence ratio: The equivalence ratio of the air-fuel mixture affects the flame speeds and consequently the cylinder temperature and pressure as well as the time available for induction of autoignition reactions before the end gas mixture is consumed by the propagating flame. Lower induction time increases the propensity for knock occurrence. An end gas mixture that is slightly rich in fuel is more susceptible to knock compared to rich mixtures [45].

2.2.3.2 Fuel factors

The octane number (ON) is an indication of a fuels ability to resist self-ignition (pre-ignition or autoignition) which is normally the source of engine knock. The test for the octane number of a fuel is performed in a single cylinder, overhead valve and variable compression ratio engine known as the Comparative Fuel Research (CFR) engine. Two standard versions of the test are carried out in the CFR engine leading to two different types of rating namely the research octane number (RON) and the motor octane number (MON) [33, 35]. In determining the octane number of a fuel in a standard CRF test, the anti-knock performance of the fuel in the CFR engine is compared to that of a mixture of iso-octane (assigned a reference rating of 100 for very good performance) and *n*-heptane (assigned a reference rating of 0 for very poor performance) which produces similar knocking behaviour as the fuel been tested. For example a gasoline fuel that exhibits a similar knocking behaviour as that of a blend of 85 % iso-octane and 15 % n-heptane would have an ON of 85. The operating conditions under which MON test is performed are more severe compared to that of the RON test and as a result the RON of some fuels is higher than the MON [35]. Some of the disadvantages of pre-ignition or autoignition in the end gas include reduction in engine efficiency and excessive wear and damage of engine parts through knock. Fuels with higher octane number, are able to withstand higher compression ratios before autoignition of the end gas occurs [46]. In SI engines ignition is initiated by a spark and it is important for the fuel-air mixture to avoid autoignition during the compression process, thus a high octane number is desired [16, 33].

In terms of how the fuel structure affects autoignition, hydrocarbon fuels with longer chain length have lower octane number. The octane rating of branched chain hydrocarbon fuels are generally higher compared to those of straight chain hydrocarbons

with similar number of carbon atoms. The octane rating of a hydrocarbon fuel can be improved by blending them with oxygenated fuels (e.g. ethanol and biobutanol) with higher anti-knock properties [16].

Table 2.1: Test conditions for measurement of octane numbers Adapted from [33].

	RON	**MON**
Engine speed	600 RPM	900 RPM
Compression ratio	Adjusted to get standard	knock
Air-fuel ratio	Adjusted for maximum	knock
Inlet temperature	52 ^{0}C (125 ^{0}F)	149 ^{0}C (300 ^{0}F)
Inlet pressure	Atmospheric	atmospheric
Ignition timing	13 ^{0} bTDC	19 ^{0} - 26 ^{0} bTDC
Coolant temperature	100 ^{0}C (212 ^{0}F)	100
Oil temperature	57 ^{0}C (135 ^{0}F)	57

2.2.4 Modelling autoignition in SI engine

The models employed to date for predicting autoignition delay time in engines fall into two major categories, namely empirical models based on the Arrhenius function, and chemical kinetic models of either detailed, reduced or skeletal form.

2.2.4.1 Empirical correlations

The rate of a chemical reaction is a function of the concentrations of the reactants and the system temperature (and therefore the rate coefficient). The Arrhenius law (see Equation 2.16) expresses the relationship between the rate coefficient and temperature. Based on the Arrhenius law, an empirical correlation can be formulated for the global reaction rate that defines the relationship between the ignition delay time τ and the global activation energy as well as the system temperature and pressures.

$$\tau = A\, P^{-n} exp^{(B/T)} \tag{2.1}$$

where *A, n* and *B* are constants determined by fitting model to measured datasets of ignition delay times using regression analysis.

Over the years, several modifications have been made to the model shown in Equation 2.1 based on model fit to different sets of experimental data of ignition delay times from

different engines. One of the most widely tested and accepted form of the correlation is that proposed by Douaud and Eyzat (D&E) [47] expressed as:

$$\tau = 17.68 \left(\frac{ON}{100}\right)^{3.402} P^{-1.7} \, exp^{(3800/T)} \tag{2.2}$$

Interestingly, the D&E model also accounts for fuel effects through the inclusion of the ON number. The ON in equation 2.2 represents the average of the RON and MON of the given fuel [48]. However, the model was originally developed for primary reference fuels (PRF). The ability of PRF fuels in reproducing the autoignition behaviour of gasoline depreciates considerably at *P-T* conditions different from those of the standard RON and MON test, therefore the D&E model is expected to give inaccurate results of autoignition predictions when used in the context of practical engines where *P-T* conditions are more severe compared to those prevalent in the RON and MON test. Significant disparity between measured autoignition delay times and autoignition delay times predicted using the correlation of D&E have been reported in previous works [48-50] carried out at the university of Leeds.

Equation 2.2 estimates the ignition delay times of a fuel mixture under constant pressure and temperature before the point of autoignition. Equation 2.2 is most appropriate for predicting ignition delay times for instance, in the RCM where compressed temperatures and pressures are fairly constant during the induction period. In the spark ignition engine for example, the temperature and pressure conditions of the end gas during the induction (delay) period are constantly changing with crank angle advanced and as a result the overall ignition delay time response is determined by the cumulative effect of the underlying reactivity across the temperature range. In order to account for the effect of changing *P-T* conditions in practical engines, Livengood and Wu [51] proposed that the degree of reactivity required for thermal ignition of the end gas at a specific temperature and pressure is cumulative and inversely proportional to the corresponding autoignition delay time. In their model autoignition is said to have occurred at a critical value t_c when the solution of the integral in Equation 2.3, becomes unity.

$$1 = \int_0^{t_c} \frac{1}{\tau(P,T)} \, dt = \int_0^{t_c} \frac{dt}{A \, P^{-n} exp^{(B/T)}} \tag{2.3}$$

where τ is the autoignition time at a specific temperature and pressure. Incorporating the Douaud and Eyzat correlation into the Livengood-Wu integral yields the form,

$$1 = \int_0^{t_c} \frac{dt}{17.68 \left(\frac{ON}{100}\right)^{3.402} P^{-1.7} \, exp^{(3800/T)}} \tag{2.4}$$

The Livengood-Wu model was however shown in [30] to be incapable of predicting the autoignition delay times at low *P*-*T* conditions. While the D&E and the Livengood-Wu integral are widely applied in the automotive industry for autoignition and knock prediction due to their computational advantage, results based on both models are significantly unreliable due to their inherent shortcomings. Chemical kinetic modelling which employs a more fundamental approach through modelling of the underlying chemistry, is expected to produce more accurate predictions of the combustion behaviour of fuels compared to the D&E and Livengood-Wu models and is therefore explored in this study.

2.2.4.2 Chemical Kinetic models

There is a consensus that autoignition of the end gas in an SI engine is mainly driven by the fuel chemistry (chemical kinetics) [52] which also is influenced by the engine operating parameters (e.g. temperature and pressure) and factors affecting the fluid dynamics of the reactive system (e.g. combustion chamber, intake valve and exhaust valve design). The awareness of the role of chemical kinetics in the numerical prediction of knock in practical engines has in the past few years equally sparked a great interest in the research and development of chemical kinetic models of fuel oxidation. The chemical kinetic process leading up to autoignition of the end gas may involve thousands of intermediate elementary reaction steps of varying reaction rates (rate of production or destruction of the involved species) and with the size of the detailed reaction mechanism generally determined by the size and complexity of the parent fuel molecule. Chemical kinetic modelling attempts to generate the reaction mechanism and to also provide the rate parameterisation of these reactions alongside the thermo-physical properties of the involved species. The process of validation of these models also requires the development of a computer or numerical model (see section 2.7 for description of types of models) describing the geometry and operating conditions of the combustion device in which the reaction mechanism would be applied or studied. The

chemical kinetic model when coupled to the computer model of the specific combustion application, a system of differential equations representing the conservation of mass, energy, momentum and species concentration results. This set of differential equations when solved for the unburned zone via integration, allows the evolution of the various properties of the system such as pressure, temperature, heat release, species concentrations etc. to be determined and analysed. Autoignition or knock onset may be predicted at the point of significant heat release rate [53].

The simplest and most basic form of chemical kinetic models that have been used for modelling of the end gas autoignition in engines are the global chemical kinetic models also known as single step models. At the University of Leeds, various skeletal mechanisms including the foremost and popular 'Shell model' developed by Halstead [54], have been used for predicting autoignition of hydrocarbons in the engine with limited success - the 'Shell model' is comprised of five species and eight generalised reactions representing chain/degenerate branching and termination steps. The 'Shell model' was updated and further extended by Cox and Cole [55] to include 10 species and 15 reactions based on the fundamental kinetic understanding available as at that time. Following the work by Cox and Cole, a larger size reaction mechanism made up of 13 species and 18 reactions and covering both the low and high temperature oxidation of simple branched chain alkanes (e.g. iso-octane) was later developed by Hu and Keck [56] based on the work of Cox and Cole [55] and Benson [57], for autoignition simulations. At the University of Leeds, a number of the extended version of the Hu and Keck mechanisms [58-60], generally referred to as the Skeletal Keck mechanisms have been employed for modelling autoignition in the engine. The Skeletal Keck mechanisms were shown in Khan [30] to display significant discrepancies in terms of their autoignition predictions. Compared to the detailed Lawrence Livermore National Laboratory (LLNL) mechanisms for PRF proposed in Curran et al. [61] and three reduced versions of the LLNL PRF scheme reported in [62-64], the performance of the Skeletal Keck mechanisms was less good. The three reduced versions of the PRF mechanism were however reported in Khan [30] to perform equally well as the detailed LLNL PRF mechanism.

An up to date review of the reaction mechanisms developed so far for DME and *n*-butanol oxidation for use in the context of engine simulations as at the time of the study,

is provided in section 2.5. While a very few number of detailed and reduced mechanisms of gasoline oxidation exist currently in the open literature, no combined mechanism of oxidation of TRF/*n*-butanol was available in open literature as at the time of this study. For the purpose of this study a detailed and reduced TRF/*n*-butanol blended mechanism was therefore developed in collaboration with the King Abdullah University of Science and Technology (KAUST) group for use in the framework of autoignition simulation of TRF/*n*-butanol blends in both RCM and SI engines. The detailed mechanism provided by the KAUST group is made up of 1944 species and 8231 elementary reactions while the reduced version of the same mechanism is comprised of 527 species and 2644 reaction steps. More information on the detailed TRF/*n*-butanol blended mechanism can be found in [65]. Also, a more detailed treatment of the subject of chemical kinetics and some of the common methods for evaluating chemical kinetic models are presented in section 2.3-2.6.

2.3 Combustion chemistry: chemical kinetics

Chemical kinetics refers to the branch of science that studies the rate at which a chemical reaction occurs [66]. Apart from telling the speed of a reaction, chemical kinetics also sheds light on exactly how the reaction occurs, i.e. the reaction mechanism. For a gas phase chemically reacting flow process occurring in an internal combustion engine, sub processes such as heat release, flame stabilisation, ignition delays, and pollutant emission formation are to a large extent controlled by the rate of each individual chemical reaction which in turn is a function of the temperature and concentrations of the reactants [16].

The rate of a reaction is the rate at which the reactants are transformed into the products. It is the change in the concentration of the reactant and product that occurs during a given period of time. For a general elementary reaction:

$$aA + bB = cC + dD \tag{2.5}$$

the reaction rate in terms of the concentrations of the species can be written as:

$$rate = -\frac{1}{a}\frac{d[A]}{dt} = -\frac{1}{b}\frac{d[B]}{dt} = \frac{1}{c}\frac{d[C]}{dt} = \frac{1}{d}\frac{d[D]}{dt} \tag{2.6}$$

Where [A] and [B] stand for the molar concentrations of the reactants A and B respectively, while [C] and [D] are the molar concentrations of the products C and D respectively and a, b c and d are the stoichiometric coefficients [67].

2.3.1 The rate law

The rate law is a mathematical equation that describes the progress of a chemical reaction. The reaction rate law expression shows how the rate of a reaction depends on the concentrations of the reactants. Each concentration is expressed with an exponent which tells the order of the reaction with respect to each reactant while the rate constant converts the concentration expression into the correct unit of rate (Ms^{-1}). The exponent on the rate law indicates how the rate is affected by the concentration of each reactant.

For the general reaction given in Equation 2.5, the rate of the reaction is proportional to the concentrations of the reactants and the rate law has the form:

$$rate \propto [A]^a[B]^b \tag{2.7}$$

where *a* and *b* are the reaction order determined from experiments. The overall reaction order can be found by adding the exponents on the reactants in the rate law. By introducing a temperature dependent constant known as the rate constant k_f in the Equation 2.7, the reaction rate equation becomes:

$$rate = -\frac{1}{a}\frac{d[A]}{dt} = k_f[A]^a[B]^b \tag{2.8}$$

In theory, elementary reactions can occur in both the forward and reversed direction. . The rate law for the reversed form of equation 2.8 can be expressed as:

$$\frac{1}{a}\frac{d[A]}{dt} = k_r[C]^c[C]^d$$

where k_r is the reversed rate constant and *c* and *d* are the reaction order.

When chemical equilibrium is attained both the forward and reversed rates are the same and at that point, we have that:

$$k_f[A]^a[B]^b = k_r[C]^c[C]^d \tag{2.9}$$

$$\frac{[C]^c[C]^d}{[A]^a[B]^b} = \frac{k_f}{k_r} \tag{2.10}$$

$$\frac{k_f}{k_r} = k_{eq} \tag{2.11}$$

The equilibrium constant k_{eq} relates the forward rate to the reversed rate and can be calculated from standard thermodynamic properties using the relationship:

$$k_{eq} = \exp\left(\Delta S^0/_R\right) * \exp\left(-\Delta H^0/_{RT}\right) \tag{2.12}$$

where ΔS^0 and ΔH^0 are respectively the standard molar entropy and enthalpy changes of the reaction computed from the respective standard molar entropies S^0 and enthalpies $H^0$of the species taking part in the reaction and *R* is the gas constant.

The standard molar entropies and enthalpies of the species taking part in the reaction can be estimated using the NASA polynomials in the thermodynamic data of the chemical kinetic model for the involved species. The NASA polynomials are polynomials fitted to the thermodynamic data of the different species using the least square approach. Most of the thermodynamic data were calculated based on various theoretical methods including electronic structure calculations and bond additivity rules [30]. In the thermodynamic data seven polynomial coefficients are specified for the low temperature range typically from 300 K to 1000 K and another seven for the high temperature range usually from above 1000 K up to 5000 K. The NASA polynomials for standard molar heat capacity at constant pressure ${C_p}^\theta$, enthalpy H^θ, and entropy S^θ, take the form:

$$\frac{{C_p}^\theta}{\bar{R}} = a_1 + a_2T + a_3T^2 + a_4T^3 + a_5T^4 \tag{2.13}$$

$$\frac{H^\theta}{\bar{R}T} = a_1 + \frac{a_2}{2}T + \frac{a_3}{3}T^2 + \frac{a_4}{4}T^3 + \frac{a_5}{5}T^4 + \frac{a_6}{T} \tag{2.14}$$

$$\frac{S^\theta}{\bar{R}} = a_1 \ln T + a_2T + \frac{a_3}{2}T^2 + \frac{a_4}{3}T^3 + \frac{a_5}{4}T^4 + a_1 \tag{2.15}$$

Where T is temperature in Kelvin, $\bar{R}$ is the universal gas constant in kJ/kmol and the a_n parameters are the NASA polynomial coefficients.

2.3.2 Temperature dependence of rate coefficients

Based on the results from studies involving the measurement of the rate coefficients at different temperatures, it is known that in most cases, they increase non-linearly with temperature. Such behaviour is often described by the Arrhenius equation which is given by:

$$k = A\ exp\left(\frac{-E_a}{RT}\right) \tag{2.16}$$

where A is the pre-exponential factor and E_a is the activation energy. A relates to the frequency factor and represents the probability that collision will occur with the proper orientation for reaction. The units of A are s^{-1}, $cm^3mol^{-1}s^{-1}$, $cm^6mol^{-2}s^{-1}$ for unimolecular, bimolecular and termolecular reactions respectively. These units corresponds to first, second and third order reactions respectively. Generally, the pre-exponential factor is not a constant but a function of temperature. This effect may be accounted for by introducing a modified pre-exponential factor $A.T^n$, which includes the effect of collision and the steric factor associated with the orientation of the colliding molecules. For example, the modified Arrhenius equation therefore becomes,

$$k = A.T^n\ exp\left(\frac{-E_a}{RT}\right) \tag{2.17}$$

where A is a constant and n is known as the temperature exponent. From the Arrhenius equation, the plot of $log\ k$ versus $1/T$ (also known as Arrhenius plot) will result in a linear graph with slope $= E_a/RT$ and intercept $log_e A$. For some reactions, the Arrhenius plot is not linear. The nonlinear characteristics can be however explained theoretically [68].

2.3.3 Rate of production and consumption of species

The general form of an elementary reaction step can be described by:

$$\sum_{j=1}^{N_s} v'_{ij} X_j \rightarrow \sum_{j=1}^{N_s} v''_{ij} X_j \tag{2.18}$$

where v' and v'' are the stoichiometric coefficients on the left hand side (reactant) and right hand side (product) of the reaction step and N_s is the number of species and X_j are species symbols.

The net rate of progress q_i, of the ith reaction given by the difference between the forward and reversed rates takes the form:

$$q_i = k_{fi} \prod_{j=1}^{Ns} [X_j]^{v'_{ij}} - k_{ri} \prod_{j=1}^{Ns} [X_j]^{v''_{ij}} \quad (2.19)$$

Where k_{fi} and k_{ri} are the forward and reversed rate constants of the *i*th reaction respectively, and $[X_j]$ is the molar concentration of the *j*th species.

The summation of the net rate of progress variable for all the reactions involving the *j*th species gives the rate of molar production $\dot{w}_j$ of the *j*th species (chemical source term) and is given by:

$$\dot{w}_j = \frac{d[X]_j}{dt} = \sum_{i=1}^{N_R} v_{ij} q_i \qquad (j = 1, 2 \ldots, N_s) \quad (2.20)$$

where $v_{ij} = v''_{ij} - v'_{ij}$, and N_R is the number of reactions.

The number of equations in the systems of ODEs given by Equation 2.20 is equal to the number of species in the chemical kinetic scheme and because the equations are coupled, they must be integrated simultaneously at every time step in order to determine the state of the system. The above systems of ODEs for rate of change of species concentrations must also be coupled to the energy and mass conservation equations given in the next section and solved to determine the temperature history of the system. Common software with the set of chemical kinetic libraries capable of solving (integrating) these sets of equations depending on the reactor type, include commercial software such as CHEMKIN [69] and COSILAB [70] and the open source CANTERA software [71].

2.3.4 Governing equations

Two types of homogenous reactors namely constant volume reactors (e.g. shock tubes and JSR) and variable volume reactors (e.g. RCMs) were simulated in the course of this work using the CANTERA [71] set of chemical kinetic libraries. A brief description of

the coupled general governing equations for conservation of mass, species and energy are presented below.

2.3.4.1 Mass conservation

The change in the total mass of the reactors content is due to the flow of mass across the reactors inlets $\dot{m}_{in}$ and outlets $\dot{m}_{out}$, and the rate of production of species on the reactors surface $\dot{m}_{wall}$:

$$\frac{dm}{dt} = \sum_{in} \dot{m}_{in} \quad - \sum_{out} \dot{m}_{out} + \dot{m}_{wall} \tag{2.21}$$

Surface reactions were not considered, so Equation 2.21 becomes:

$$\frac{dm}{dt} = \sum_{in} \dot{m}_{in} \quad - \sum_{out} \dot{m}_{out} \tag{2.22}$$

2.3.4.2 Species conservation

The rate at which specie *j* is produced in a homogeneous phase reactions is $V\dot{w}_j M_j$. The rate of change in the mass of each species is therefore given by:

$$\frac{d(mY_j)}{dt} = \sum_{in} \dot{m}_{in} Y_{j,in} - \sum_{out} \dot{m}_{out} Y_{j,out} + V\dot{w}_j M_j \tag{2.23}$$

where *m* is the mass of the reactors content, Y_j is the mass fraction of each species, *V* is the volume of the reactor, $Y_{j,in}$ is the mass fraction of the *j*th species entering the reactor, $Y_{j,out}$ is the mass fraction of the *j*th species leaving the reactor, and M_j is the molecular weight of the *j*th species.

Since the mass fraction of gas leaving the reactor is the same as that in the reactor volume, $Y_{j,out} = Y_j$. By expanding the derivative on the left hand side of Equation 2.23 and substituting $\frac{dm}{dt}$ from Equation 2.22 the equation becomes,

$$\frac{d(mY_j)}{dt} = m\frac{dY_j}{dt} + Y_j \frac{dm}{dt} \tag{2.24}$$

$$m\frac{dY_j}{dt} + Y_j\left(\sum_{in} \dot{m}_{in} - \sum_{out} \dot{m}_{out}\right) = \sum_{in} \dot{m}_{in} Y_{j,in} - \sum_{out} \dot{m}_{out} Y_j + V\dot{w}_j M_j \tag{2.25}$$

$$m\frac{dY_j}{dt} = \sum_{in} \dot{m}_{in} \left(Y_{j,in} - Y_j\right) + V\dot{w}_j M_j \quad (2.26)$$

2.3.4.3 Energy conservation

Based on the First Law of Thermodynamics the general equation for total energy change across the system is given by:

$$\frac{dE}{dt} = \dot{Q} + \dot{W} + \sum_{in} m_{in} (h + e_k + e_P)_{in} - \sum_{out} \dot{m}_{out}(h + e_k + e_P)_{out} \quad (2.27)$$

where E is the total energy of the system, $\dot{Q}$ and $\dot{W}$ are the rate of heat and work transfer across the system control volume, h, e_k and e_p are the specific enthalpy, kinetic energy and potential energy of the mass flows leaving and entering the control volume respectively.

The total energy given by the left hand side of equation 2.27 is equal to the sum of internal, kinetic energy and potential energy. Assuming the kinetic and potential energy changes are negligible,

$$\frac{dE}{dt} \cong \frac{dU}{dt}$$

The rate of work supplied into the system due to volume change is given by,

$$\dot{W} = -P\frac{dV}{dt}$$

Since kinetic and potential energy changes are negligible, the term $(h + e_k + e_P) \cong$ h and the last two terms on the right hand side of equation 2.2.7 becomes,

$$\sum_{in} m_{in} h_{in} - \sum_{out} m_{out} h_{out} = \sum_{in} \dot{m}_{in} \sum_j^{Ns} Y_{j,in} \; h_{j,in} - \sum_{out} \dot{m}_{out} \sum_j^{Ns} Y_{j,out} \; h_{j,out}$$

where $h = \sum_j^{Ns} Y_j \; h_j$

Therefore equation 2.27 becomes,

$$\frac{dU}{dt} = \dot{Q} - P\frac{dV}{dt} + \sum_{in} \dot{m}_{in} \sum_j^{Ns} Y_{j,in} \; h_{j,in} - \sum_{out} \dot{m}_{out} \sum_j^{Ns} Y_{j,out} \; h_{j,out} \quad (2.28)$$

The energy conservation equations can be derived from equation 2.28 in terms of the specific enthalpy (at constant pressure) and specific internal energy (at constant volume). The energy balance equation that is applied to a specific system or setup would depend on whether constant volume or constant pressure is assumed within the system. The energy conservation equation in terms of the specific enthalpy is given by,

$$mc_p \frac{dT}{dt} + \sum_j^{Ns} h_j \sum_{in} \dot{m}_{in} Y_{j,in} + \frac{m}{\rho} \sum_j^{N_s} w_j H_j - V \frac{dP}{dt} = \dot{Q} + \sum_{in} \dot{m}_{in} \sum_j^{Ns} Y_{j,in} \; h_{j,in} \tag{2.29}$$

If equation 2.29 is simplified further by dividing by volume and considering pressure to be constant, the equation becomes,

$$\rho c_p \frac{dT}{dt} = \sum_{in} \frac{\dot{m}_{in}}{V} \sum_j^{Ns} Y_{j,in} \, (h_{j,in} - h_j) - \sum_j^{N_s} w_j H_j + \frac{\dot{Q}}{V} \tag{2.30}$$

The energy conservation equation in terms of internal energy is given by,

$$mc_v \frac{dT}{dt} + \sum_j^{Ns} u_j \sum_{in} \dot{m}_{in} Y_{j,in} + \frac{m}{\rho} \sum_j^{N_s} w_j U_j = \dot{Q} - P \frac{dV}{dt} + \sum_{in} \dot{m}_{in} \sum_j^{Ns} Y_{j,in} \; u_{j,in} + \sum_{in} \dot{m}_{in} \sum_j^{Ns} Y_{j,in} Pv - \sum_{out} \dot{m}_{out,} Pv \tag{2.31}$$

Again, if equation 2.31 is simplified further by dividing by volume and considering volume to be constant, the equation becomes,

$$\rho c_v \frac{dT}{dt} = \sum_{in} \frac{\dot{m}_{in}}{V} \sum_j^{Ns} Y_{j,in} \, (u_{j,in} - u_j) - \sum_j^{N_s} w_j U_j + \sum_{in} \frac{\dot{m}_{in}}{V} \frac{R_0 T_{in}}{\overline{M_{in}}} - \dot{\sum}_{out} \frac{\dot{m}_{out}}{V} \frac{R_0 T}{\bar{M}} + \frac{\dot{Q}}{V} \tag{2.32}$$

The details of the derivation of equation 2.29 and 2.31 can be found in the LOGESOFT manual.

2.3.4.4 Constant volume reactor

The constant volume reactor is a form of a closed system and there is no flow of mass across a constant volume reactor. The energy balance for mass therefore becomes,

$$\frac{dm}{dt} = 0 \tag{2.33}$$

Also, $Y_{j,in} = Y_j$ and the conservation equation for species becomes

$$m\frac{dY_j}{dt} = V\dot{w}_j M_j$$

which alternatively can be written as,

$$\frac{dY_j}{dt} = \frac{\dot{w}_j M_j}{\rho} \tag{2.34}$$

Since volume is constant, the form of the energy conservation equation given by equation 2.32 should be applied and since $u_{j,in} = u_j$, equation 2.32 becomes,

$$\rho c_v \frac{dT}{dt} = \frac{\dot{Q}}{V} - \sum_j^{N_s} w_j U_j \tag{2.35}$$

2.3.4.5 Perfectly stirred reactor (PSR)

The PSR is a constant pressure vessel that has an inlet and outlet streams which allows a mixture of a particular composition and temperature to flow across it. In the PSR, steady state solution of the conservation equations can be assumed due to the high level of mixing attainable in the reactor.

The change in the total mass in the PSR is given by equation 2.22 as,

$$\frac{dm}{dt} = \sum_{in} \dot{m}_{in} - \sum_{out} \dot{m}_{out} \tag{2.36}$$

Based on the high level of homogeneity in the reactor due to strong mixing, the composition of the gas leaving the reactor is the same as the one inside the reactor. Thus, $Y_{j,in} = Y_j$ and the conservation equation for species is given by equation 2.26 as,

$$m\frac{dY_j}{dt} = \sum_{in} \dot{m}_{in} \left(Y_{j,in} - Y_j\right) + V\dot{w}_j M_j$$

which alternatively can be written as,

$$\frac{dY_j}{dt} = \sum_{in} \frac{1}{\tau_j}\left(Y_{j,in} - Y_j\right) + \frac{\dot{w}_j M_j}{\rho} \tag{2.37}$$

where $\tau_j = \frac{m}{m_j}$ is the residence time. The residence time is an indication of the level of mixing in the reactor.

Based on equation 2.37, the rate of change of mass fraction of any specie Y_j is dependent on the production rate by chemical reactions (source term) and the influx to the PSR.

Since pressure in the PSR is constant, the energy equation of the form given by equation 2.30 can be applied which is given by,

$$\rho c_p \frac{dT}{dt} = \sum_{in} \frac{m_{in}}{V} \frac{1}{\tau_j} \sum_j^{Ns} Y_{j,in} \left(h_{j,in} - h_j \right) - \sum_j^{N_s} w_j H_j + \frac{\dot{Q}}{V} \quad (2.38)$$

2.3.5 Reaction order

The rate of a reaction can depend on how much reactant is present in more than one way.

Zero order: For a zero order reaction, the change in concentration of reactant has no effect on the rate. The general form of the rate equation for a zero order reaction is given by:

$$rate = k[A]^0 \quad (2.39)$$

First order: For a first order reaction, rate is directly proportional to the reactants concentration. In this case, doubling the concentration of the reactants doubles the rate. The general form of the equation is:

$$rate = k[A] \quad (2.40)$$

Second order: For a second order reaction, doubling the concentration of reactant quadruples the rate and when the concentration of reactants is tripled, the rate increases by a factor of 9. The general form of the equation is:

$$rate = k[A]^2 \quad or \; rate = k[A]^1[B]^1 \quad (2.41)$$

which has an overall order of 2.

In a chemical process, reactions may be represented by a single step known as an overall reaction or through a series of steps known as reaction step or elementary reaction. A set of several reaction steps is what makes up a reaction mechanism. The reaction mechanism is thus the sequence of events that describes the actual process by which reactants become products. One of the aims of chemical kinetics at the molecular (microscopic) level is to predict reliable reaction mechanisms from experimental rate laws. Finding the reaction mechanism (a collection of elementary steps) of a particular fuel could involve great efforts, and information available from experimental investigations and detailed theory are quite useful in understanding the process [72]. Elementary reactions take place as a result of a collision process and occur on a molecular level in a single step, without involving any intermediates. The reaction order in the rate law of an elementary reaction is directly based on its molecularity and they are always integers and valid for all experimental conditions [68]. The molecularity of a reaction gives the number of molecules that are involved in the reaction process. The reaction of hydroxyl radicals (OH) with molecular hydrogen to form water and hydrogen atoms is an example of an elementary reaction.

$$OH + H_2 \rightarrow H_2O + H \tag{2.42}$$

Based on the number of reactants involved, elementary reactions can be classified into three categories namely: unimolecular, bimolecular and trimolecular reactions. Unimolecular reactions describes reactions in which one reactant molecule rearranges (isomerisation or dissociation) to form products according to the reaction Equation 2.43 [72]:

$$A \rightarrow \text{Products} \tag{2.43}$$

An example of a unimolecular reaction is the isomerisation reaction $CH_3OCH_2O_2 \leftrightarrow CH_2OCH_2O_2H$, which can be found in the DME reaction mechanism where methoxymethyl-peroxy radical ($CH_3OCH_2O_2$) isomerises to form methoxymethyl-peroxy radical ($CH_2OCH_2O_2H$). The reaction rate law for unimolecular reactions is first-order at high pressures but at low pressures, their rate coefficient is also a function of the total concentration [M] resulting in a second order rate law. Thus the rate coefficient of a unimolecular reaction could be written as $k\,(T)$ or $k\,(T, [M])$ [72].

Bimolecular reactions on the other hand, involve a collision between two reactants molecules (or atoms, radicals) of the same or different chemical species, according to the reaction equations:

$$A + B \rightarrow \text{Products or } \quad A + A \rightarrow \text{Products} \tag{2.44}$$

An example from the DME reaction mechanism is the reaction of hydrogen peroxide with the hydrogen atom to form water and the hydroxyl radical, $H_2O_2 + H \rightarrow H_2O + OH$

Bimolecular reactions are the most commonly encountered reaction types and they follow a second-order rate law.

Termolecular reactions are those where three reactant molecules collide together at the same time. The probability of occurrence of termolecular collision is by far lower compared to bimolecular collision but are more fertile because the probability for the redistribution of momentum and energy is higher [73]. They are generally recombination reactions of the type.

$$A + B + C \rightarrow \text{Products} \quad \text{or } A + A + B \rightarrow \text{Products or } A + A + A \rightarrow \text{Products} \tag{2.45}$$

An example of termolecular reactions in the combustion of hydrogen is:

$$H + CO + H_2O \rightarrow HCO + H_2O \tag{2.46}$$

Termolecular reactions obey a third-order rate law and are very important in combustion processes. It is important to note that the above radical recombination reactions, will only occur if the third body, M, is involved in the collision. Recombination reactions are exothermic, hence the need for a third body that must take away some of the energy [68].

Overall or global reactions are a result of several elementary reactions. An example of a global reaction is:

$$CH_4 + 2O_2 \rightarrow CO_2 + 2H_2O \tag{2.47}$$

The rate laws of global reactions are complex and the reaction order which is a function of time and reaction is not generally an integer [73]. In equation 2.47, the reaction is

depicted to occur all at once in a single step known as global or overall reaction but in reality, in a chemical process, reactions occur through a series of intermediate elementary reaction steps as mentioned previously. A global reaction cannot be used to sufficiently understand the details of a chemical process or system but a reaction mechanism provides such platform.

2.3.6 Experimental determination of rate law

The reaction order is determined from experimental evidence. If the initial rate of a reaction measured for several starting concentrations of reactants is known from experimental data, the rate law for the reaction and the rate constant can be determined by using simple table logic (inspection) or simple algebra. Once the reaction order and rate constant is known, the rate of reaction for any given concentration of reactant can also be calculated. The order of the reaction can also be deduced from the graph of the plot of initial rate versus concentration [74]. For zero order, a straight line horizontal to the abscissa axis is produced and the rate is independent of concentration. In the case of first order, a straight line with a constant slope is produced and in this case, rate is proportional to concentration. An upward sloping curve is produced for a second order reaction when rate is plotted against concentration. Alternatively, for a second order reaction, a straight line is produced when rate is plotted against the square of the concentration and this is usually necessary in order to determine the rate constant which is given by the slope of the straight line graph of rate = k [concentration]^2. Rate laws determined through the above approach are referred to as differential rate laws [74].

Sometimes, based on the type of experimental data that is available, the reaction order is complex and is not obvious using the linear graphical method described above. In such instances, a more systematic log-log graphical procedure is required in order to avoid the difficulty of finding the possible reaction order. With this approach, the value of the order and rate constant can be read directly from the graph. For example:

$$rate = k\,[reactant]^n \tag{2.48}$$

Taking logarithm of both sides

$$log\ rate = log\ k + n log\ [reactant] \tag{2.49}$$

Log rate when plotted against log [reactant] will give a linear graph with a gradient equal to *n* and an intercept equal *log k*.

It is important to state that the differential method using initial rates described above is only reliable when the reactions progress very slowly. In cases where the reaction progresses too quickly, the level of uncertainty in the measured rate becomes very large [68]. The Integrated rate law method on the other hand is determined from experimental concentration and time data and is based on calculus [75]. By merely plotting concentrations of reactants against time, it is usually not obvious if the experimental data represents a zero, first or second order reaction. However by integrating the differential form of the rate law, an equation relating reactant concentration with time will always result and from linear plots made, the rate constant and reaction order can then be determined directly [74]. An example of this is illustrated for a zero order reaction below.

For a general reaction a A → products

where *a* is the stoichiometric coefficient and *A* is the species symbol.

$$\text{rate of reaction} = -\frac{1}{a}\frac{d[A]}{dt} = k[A]^n \tag{2.50}$$

where *n* is the order of the reaction.

For a zero order reaction: *n* = 0. Therefore,

$$\text{rate of reaction} = -\frac{1}{a}\frac{d[A]}{dt} = k[A]^0 \tag{2.51}$$

$$d[A] = -akdt \tag{2.52}$$

Integrating Equation 2.52 gives the integrated rate law expression for a zero order reaction,

$$[A] = [A]_0 - akt \tag{2.53}$$

2.3.7 Pressure dependence of rate coefficients

Unimolecular reactions require collision to proceed to product in most cases (there are also photon induced unimolecular reactions) and as a result the rate constant of unimolecular reactions is sometimes dependent on pressure or total concentration. The underlying elementary processes behind the reaction mechanism of such unimolecular reactions can be explained by the Lindemann model.

In the Lindemann mechanism, a unimolecular dissociation reaction is comprised of three separate steps:

$$A + M \rightarrow A^* + M \quad (2.54f)$$

$$A^* + M \rightarrow A + M \quad (2.54b)$$

$$A^* \rightarrow \text{products} \quad (2.55)$$

where M represents any gas molecule and A* is the excited reactant capable of overcoming the potential energy barrier to form products.

The first step of the Lindmann mechanism represents collisional activation to form energised molecules of A* while the second step describes the collisional deactivation process through the loss of excess energy as a result of the collision of A* with surrounding molecules. The last steps describe a unimolecular fragmentation of energised molecule A* to form products [72].

Taking the rate of reaction 2.54f (forward reaction), 2.54b (backward reaction) and 2.55 as k_{24f}, k_{24b} and k_{25} respectively,

the rate at which product is formed is given by

$$\frac{d[products]}{dt} = k_{25}[A^*] \quad (2.56)$$

The net production of A* can be written as:

$$\frac{d[A^*]}{dt} = k_{24f}[A][M] - k_{24b}[A^*][M] - k_{25}[A^*] \quad (2.57)$$

By considering steady state conditions for A*, then we can solve for A*

$$\frac{d[A^*]_{ss}}{dt} = k_{24f}[A][M] - k_{24b}[A^*][M] - k_{25}[A^*]_{ss} = 0 \quad (2.58)$$

Or

$$[A^*]_{ss} = \frac{k_{24f}[M]}{k_{24b}[M]+k_{25}}[A] \quad (2.59)$$

Thus for the overall unimolecular reaction A → products, the net rate of reaction is given by:

$$\frac{-d[A]}{dt} = \frac{d[products]}{dt} = k[A] \quad (2.60)$$

Therefore we can also write:

$$-\frac{d[A]}{dt} = \frac{d[products]}{dt} = k_{25}[A^*]_{ss} = \frac{k_{25}k_{24f}[M]}{k_{24b}[M]+k_{25}}[A] = \left[\frac{1}{k_{25}k_{24f}/k_{24b}} + \frac{1}{k_{24f}[M]}\right]^{-1}[A] \quad (2.61)$$

The effective rate constant for a unimolecular reaction A → products is defined by the above equation and it is given as:

$$k = \left[\frac{1}{k_{25}k_{24f}/k_{24b}} + \frac{1}{k_{24f}[M]}\right]^{-1} \quad (2.62)$$

For reactions carried out at very low pressures $\left(i.e.P \rightarrow 0 \; and \; [M] = \frac{P}{RT} \rightarrow 0\right) \; and$

$$k_0 = k_{24f}[M] \quad (2.63)$$

Thus, at the above low- pressure limit, the rate constant of a unimolecular reaction is proportional to pressure. On the other hand, at the high-pressure limit, [M] → ∞ and the rate constant becomes,

$$k_\infty = k_{25}k_{24f}/k_{24b} \quad (2.64)$$

Thus, at the high-pressure limit, the rate constant is independent of pressure and is constant for a fixed temperature.

For the overall unimolecular reaction, the pressure dependence of the rate constant can also be written as:

$$\frac{1}{k} = \frac{1}{k_0} + \frac{1}{k_\infty} \tag{2.65}$$

Figure 2.5 illustrates the plot of the pressure dependence of the rate constant of a unimolecular reaction. The figure shows the special case where the high pressure limit is independent of temperature.

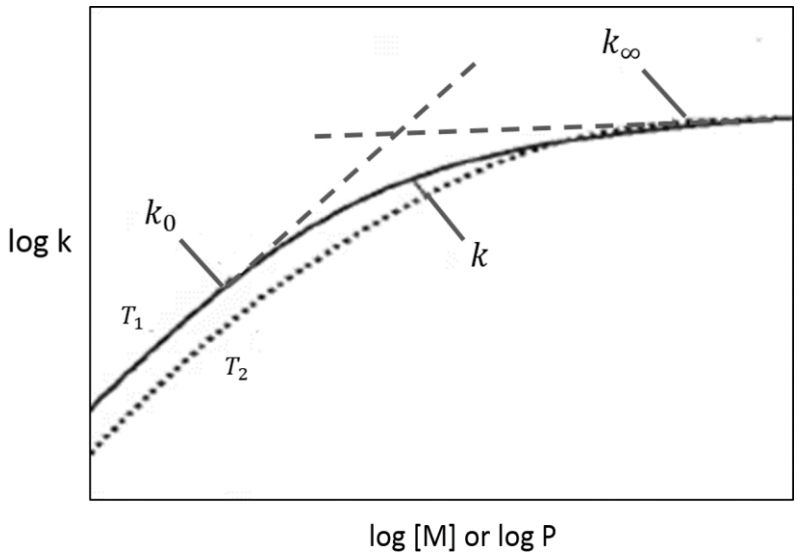

Figure 2.5: Illustration of fall-off curves for a thermal unimolecular dissociation or recombination reaction for different temperatures, T_1 and T_2. Adapted from [72].

For bimolecular reactions, the rate constants are in almost all cases dependent on only temperature but there are few cases in which the reverse is the case. More details on pressure dependence of elementary reactions can be found in [76-79].

2.3.7.1 Falloff reactions

A reaction is termed as a falloff if its rate exhibits first order in [M] at low pressures but exhibits zero-order in [M] as [M] takes on higher values (i.e. as pressure increases). The Lindmann expression derived in section 2.3.7 (Equation 2.65) is the simplest form of the rate coefficient for a falloff reaction.

The Lindemann expression for the rate coefficient of a falloff reaction can also be written in a more general form as:

$$k_f(T,[M]) = \frac{k_0[M]}{1+\frac{k_0[M]}{k_\infty}} \tag{2.66}$$

If the non-dimensional reduced pressure term in equation 2.66 is defined as:

$P_r = \frac{}{k_\infty}$, then equation 2.66 may be written as:

$$k_f(T,P_r) = k_\infty \left(\frac{P_r}{1+P_r}\right) \tag{2.67}$$

Accurate models for unimolecular reactions that exhibit the falloff behaviour are actually more complicated than the Lindmaan formulation given by equation 2.67. To account for this effect, the expression of equation 2.67 is multiplied by a function $F(T,P_r)$, known as the falloff function and equation 2.67 becomes:

$$k_f(T,P_r) = k_\infty \left(\frac{P_r}{1+P_r}\right) F(T,P_r) \tag{2.68}$$

A popular falloff function is the Troe falloff function given by [80] as:

$$log_{10}F(T,P_r) = \frac{log_{10}F_{cent}(T)}{1+f_1^2} \tag{2.69}$$

where $F_{cent}(T) = (1-A)\exp(-T/T_3) + Aexp(-T/T_1) + (-T_2/T)$,

$f_1 = (log_{10}P_r + C)/N - 0.14(log_{10}P_r + C)$, $C = -0.4 - 0.67 - log_{10}F_{cent}$ and

$N = 0.75 - 1.27\ log_{10}F_{cent}$.

2.4 Combustion chemistry: reaction mechanisms of fuel oxidation

The oxidation of fuels in combustion reactions is driven by the formation of highly reactive radicals such as O, OH and H. Chain-reaction mechanisms associated with combustion processes are initiated by these free-radical species. In radical-chain reactions, an intermediate product produced in one step generates a reactive

intermediate species in a subsequent step and then that intermediate generates another reactive intermediate, and so on [68].

A chain reaction mechanism is usually made up of four steps, namely:

1. Chain initiation
2. Chain propagation
3. Chain branching
4. Chain termination

In the chain initiation steps, radical species are produced by dissociation of the reactants. The chain propagation and branching step involve the creation of additional radicals as previously generated radicals react with stable compounds in the system. The chain termination step brings the chain to a stop as radicals combine and forms stable species [16].

Some of the features of a chain reaction can be illustrated by some of the reactions in the hydrogen oxidation mechanism.

$$H_2 + O_2 \rightarrow 2OH. \quad (2.70)$$

During the initiation step, the reactive species (represented by the dot), is produced from the stable species. The rapid chain propagation step is given in this case by equation 2.71 and it involves the reaction of the reactive intermediate species with stable species to form other reactive species.

$$H_2 + OH. \rightarrow H. + H_2O \quad (2.71)$$

The chain branching step given by equations 2.72 and 2.73 involves the reaction of one reactive species with a stable species to form two reactive species

$$H. + O_2 \rightarrow OH. + O. \quad (2.72)$$

$$O. + H_2 \rightarrow OH. + H. \quad (2.73)$$

Reaction 2.74 is a highly endothermic reaction and will thus progress at a very slow rate at low temperatures and other reactions which destroy the H atoms (termination

reactions) become competitive. This is the reason for the steady reaction witnessed in some H_2-O_2 systems where H radicals are introduced. Explosion of the mixture may however occur but only at higher temperatures as more and more reactive species (i.e. H, OH, O) are produced as a result of reactions 2.71-2.73 in the chain system with reaction 2.72 progressing more rapidly. A good example of this is the production of a flame in combustion as a result of branching reactions predominating over chain termination reactions and the fuel mixture is consumed very quickly as large quantities of radicals are formed [68].

In the chain termination step (i.e. reaction 2.74 in the gas phase), the reactive species react to form stable species. The HO_2 radical shown on the left hand side of equation 2.74 is stable at only low temperatures.

$$H\bullet + O_2 + M \rightarrow HO_2 + M. \qquad (2.74)$$

In reaction 2.74, M stands for any gas which is a third body that is required to carry away the excess energy contained by the newly formed HO_2 radical. This is necessary to prevent the HO_2 radical from disintegrating immediately.

2.4.1 Low temperature chemistry and autoignition of hydrocarbon fuels

There is currently a huge interest in understanding the low-temperature oxidation chemistry due to its significant role in the autoignition process of the end gas in an SI engine and most importantly, all current advanced low temperature combustion concepts that work by compression ignition. Homogenous charge compression ignition (HCCI) engines that operate on the principle of combining gasoline and diesel engine represent one such concept. The major advantage of HCCI technology is its ability to give very low NOx emissions due to lower combustion temperatures, and the absence of soot in the exhaust [27]. The HCCI concept is however yet to be implemented due to the difficulties in controlling the ignition and combustion rate. In the HCCI engine technology, a premixed charge of fuel and air is compressed and auto-ignites when a favourable temperature is attained; however, the ignition timing might not always agree with that desired for optimal efficiency and controlled emissions [72]. Because ignition and combustion in the HCCI engine is determined mainly by the autoignition chemistry

of the fuel, understanding the chemical kinetics which controls the autoignition of alternative fuels is crucial for implementing this technology [81].

The general mechanism for the low-temperature oxidation of hydrocarbon fuels is shown in Figure 2.6. The reaction mechanisms for combustion at low temperatures are quite complex compared to those that occur during high-temperature hydrocarbon oxidation. While the production of reactive radical species and kinetics are highly dependent on the fuel or parent hydrocarbon for the low-temperature oxidation mechanism, the dependence of kinetics on the fuel structure tends to become less significant when considering high-temperature hydrocarbon oxidation.

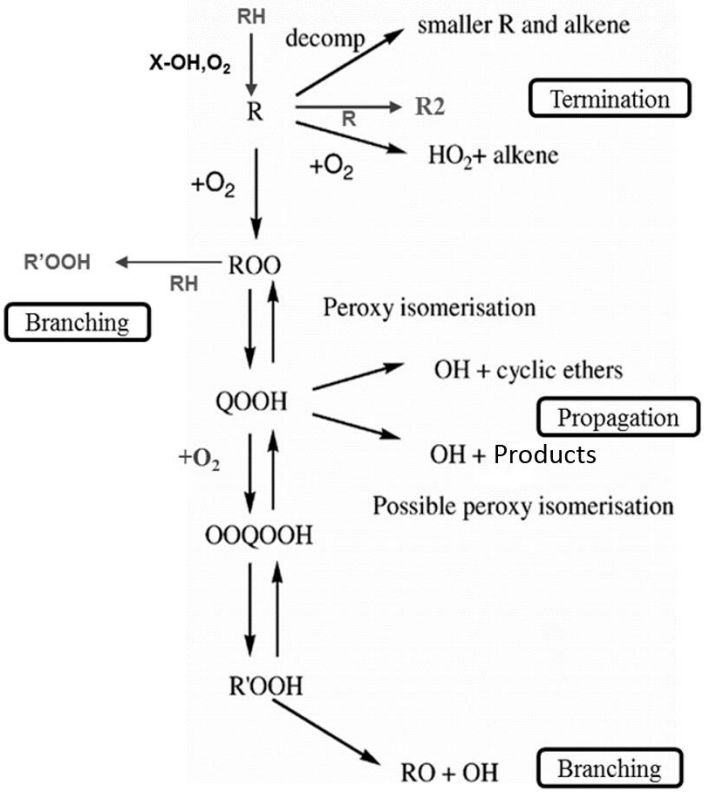

Figure 2.6: Low temperature oxidation chemistry of Hydrocarbon. Adapted from [82].

In the low-temperature scheme shown in Figure 2.6, the parent alkane (RH) undergoes hydrogen abstraction (H-atom loss) during a short initiation reaction with O_2 and then mainly by reaction with OH radicals to form an alkyl radical (R). Under low temperature conditions, the alkyl radical adds to O_2 to form a peroxy radical (RO_2). Other ways the

alkyl radical can react include its decomposition resulting in either the production of smaller radicals (R) and an alkene or its self-reaction to form stable products (R2) or a reaction that leads to the formation of HO_2 and a conjugate alkene, having the same number of carbon atoms as the parent alkane. The reaction leading to HO_2 formation is regarded as a termination step because HO_2 is a relatively inert species. The peroxy radical formed from the reaction R + O_2, isomerises through an internal hydrogen abstraction, going through a cyclic transition state to give alkylhydroperoxide (QOOH) with a new radical centre [82, 83]. The isomerisation reaction of RO_2 to QOOH has an enormous influence on the low-temperature oxidation chemistry. Depending on the size of the cyclic ring present in the transition state at low temperature, the formation of alkenes and HO_2 radicals can compete with the isomerisation reaction by direct elimination from RO_2.

The QOOH formed may decompose into cyclic ethers having ring sizes of three to six atoms or form oxygenated products such as aldehydes, or ketones and OH or by β-scission into HO_2 radicals or conjugated alkenes or smaller species. The highly reactive hydroxyl radical, OH may then further propagate the chain [72]. At low temperature, QOOH radicals may further add to O_2 and yield an unstable intermediate known as peroalkylhydroperoxide (O_2QOOH) which reacts further by a second internal isomerisation to produce a nonradicalic R'OOH and an OH radical.

The very fast unimolecular decomposition of R'OOH at low temperature leads to the production of two radicals (RO and OH) and with the rapid multiplication in the number of radicals, chain branching and rapid oxidation of the fuel is significantly enhanced at low temperature. Another route that promotes chain branching is the formation of R'OOH via H-abstraction by RO_2 from the alkane RH [72, 84].

2.4.2 High temperature chemistry of hydrocarbon fuels

At relatively higher temperatures, the equilibrium of reaction, $R+O_2 \rightarrow RO_2$ begins to shift towards the left (back to the reactants) and the termination reactions through formation of the HO_2 radical and the conjugated alkene is favoured over the branching reaction of RO_2 radicals. In addition the unimolecular decomposition of QOOH previously mentioned becomes competitive with O_2 addition to QOOH leading to a decrease in the production of hydroperoxides (O2QOOH). This decrease leads to a

decrease in reactivity within the 700 - 800 K temperature range thus resulting in a region of negative temperature coefficient (NTC) where the rate of reaction decreases with an increase in temperature. In the NTC region ignition delay times exhibit an 'abnormal' behaviour as the ignition delay times begin to increase with increasing temperature. In the intermediate temperature regime where HO_2 reaction is favoured, H_2O_2 is formed through the reactions (HO_2 + H and HO_2 + HO_2) which at higher temperatures dissociates to form reactive OH radicals [72].

At higher temperatures, reactivity is increased through the new branching step involving the decomposition of H_2O_2 (H_2O_2 (+M) = 2OH (+M)).

At temperatures above 900 K, small alkyl radicals produced via decomposition of initial alkyl radicals, further break down to form alkenes and H atoms. The H atoms react with oxygen to form OH and O atoms, and O atoms by H-abstraction from fuel, further causes the regeneration of OH radicals. By this branching step, ignition is fully developed and combustion goes to completion [83].

2.4.3 Mechanism of pollutant formation in combustion

In practical combustion systems like the internal combustion engine, the major pollutant by-products generated are NOx (NO and NO_2), carbon dioxide (CO_2), carbon monoxide (CO), unburnt hydrocarbons (UHC) and soot [72]. Computer models used for simulating various combustion properties in internal combustion engines should to a large extent be able to accurately predict pollutant emissions from these engines. When detailed chemical kinetic models of fuel oxidation are implemented in engine codes, the chemistry of carbon monoxide (CO) and hydrocarbon are normally included. The formation and oxidation of NOx in combustion engines (especially in diesel engines), is commonly modelled with the generally accepted extended Zel'dovich mechanism which is comprised of a series of elementary steps given by:

$$O + N_2 \leftrightarrow NO + N \tag{2.75}$$

$$N + O_2 \leftrightarrow NO + O \tag{2.76}$$

$$N + OH \leftrightarrow NO + H \tag{2.77}$$

NO in turn can, can further react by various routes to form NO_2, including the following

$$NO + H_2O \leftrightarrow NO_2 + H_2 \quad (2.78)$$

$$NO + O_2 \leftrightarrow NO_2 + O \quad (2.79)$$

In the event that a more comprehensive NOx model involving more elementary step is required, then one could append the nitrogen reactions from the GRI mechanism (methane or natural gas mechanism), or a more up to date mechanism of methane to the mechanism of the fuel oxidation [85]. Conversely, the chemistry or chemical processes of particulate matter and soot formation and oxidation is a quite complex process involving nucleation, surface growth and oxidation and coagulation processes [85, 86]. Factors that influence the formation of soot in practical combustion devices include: temperature, fuel composition, flame configuration, fuel-oxygen ratio etc. [16]. Because it is relatively more expensive to model the various processes involved during the formation of soot compared to fuel oxidation, it is a usual practice for modellers to resort to the use of empirical models which are commonly employed in computational fluid dynamic (CFD) simulations. Simulating pollutant formation is not the focus of this work. However, a detailed description of the dominant route for the formation of soot can be found in [86].

2.4.4 Surrogates for complex fuels

Practical fuels such as gasoline used in real combustion systems are complex mixtures of different types of hydrocarbon species. The various species that make up these fuels also contain different numbers of carbon atoms and generally, the size of a detailed reaction mechanism increases with the numbers of carbon atoms [87]. It is almost impracticable to generate detailed mechanisms describing the entire chemistry of the species in a real fuel and use the same in engine combustion codes to predict desired combustion properties because of the size and complex nature of a detailed kinetic model [83]. It is generally accepted that the behaviour and properties of complex practical fuels can be effectively reproduced by simpler fuel models known as surrogates. A surrogate fuel can be defined as a fuel that is made up of limited numbers of small species and whose behaviour mimics some particular characteristics of a target

fuel that is made up of a very large number of species [88, 89]. In addition to its computational advantage, surrogate fuels are also needed for experimental purposes.

For a surrogate fuel to accurately reproduce the combustion characteristics of a target fuel, either the chemical (autoignition, flame speed, formation of pollutants) or/and physical characteristics (e.g. evaporation) of the target fuel must be considered in its development, depending on the target property or application [89]. Primary reference fuel (PRF) is a commonly used surrogate for gasoline and is a mixture of iso-octane and *n*-heptane [88]. The IDEA surrogate, made up of 70 % *n*-decane and 30 % 1-methylnepthalene by volume is a typical surrogate for diesel fuel [83]. Surrogate mechanisms that are highly detailed may contain more than 1000 species and 4000-10000 reactions [87, 88, 90].

While PRFs may be sufficient to predict certain combustion properties (e.g. flame propagation) in SI engines, knock prediction in SI engines and the HCCI mode of combustion would however require that certain target properties of gasoline such as H/C ratio, octane rating and octane sensitivity be appropriately matched by the intended surrogate. By definition, PRFs basically have the same RON and MON values but gasoline and non-PRFs would have different RON and MON values as different PRF compositions are required to match the autoignition properties of gasoline under the two different engine conditions in which the RON and MON test is carried out. This implies that whereas the sensitivity of PRFs (the difference between the RON and MON) is zero, gasoline and most practical fuels would have sensitivity greater than zero [91, 92]. Sensitivity is a measure of the deterioration in the octane quality (anti-knock property) of a fuel as the end gas temperature increases above the standard MON test condition. Therefore PRFs cannot provide a realistic representation of the octane sensitivity exhibited by gasolines and other practical fuels under real engine conditions where the temperatures and pressures are higher than those in the RON and MON test [92]. This makes PRFs unsuitable surrogates for gasoline in terms of simulating combustion, autoignition and knock in real engine applications. The addition of non-paraffinic compounds such as alkenes and aromatics to PRF provides the opportunity to formulate gasoline surrogates with non-zero sensitivities. One such commonly used surrogate is toluene reference fuel (TRF) comprising toluene, iso-octane and *n*-heptane.

The effectiveness and suitability of TRF as a surrogate for autoignition application has been validated through various experimental studies using shock tube, flow reactor and rapid compression machines. In the work of Gautier [93], ignition delay time measurements for two TRF surrogates in a shock tube were found to closely match the ignition delay times data for reference gasoline (RD397) across the temperature range of 850 - 1250 K and pressure range of 15 - 60 atm. Kukkadapu [81] later provided validation data for the low temperature region for the same reference gasoline RD387 through new ignition delay time measurements carried out in a rapid compression machine. Predicted ignition delays based on the mechanism of Mehl [88] were also compared with gasoline data with good agreement. Chaos et al. [94] also formulated a TRF gasoline surrogate and investigated its performance relative to reference gasoline via measured species profiles in a variable pressure flow reactor. Pitz et al. [95] recommended the use of such a 3-component surrogate mixture to meet immediate developmental needs. However, 4-component surrogates involving TRF/1-pentene and TRF/2-pentene have also been formulated and investigated by e.g. [96-98], as well as complex multicomponent surrogates for various non-oxygenated gasolines [99, 100].

2.4.5 Methodology for formulating the composition of gasoline surrogates

Although different compositions of surrogates have been used so far to represent gasoline in various studies as mentioned section 2.4.4, only a few of them [101-103] have reported a clear methodology for formulating an appropriate surrogate for gasoline. In Morgan et al., [101] a surface response model (SRM) that maps various TRF mixtures from a MON/RON/sensitivity space to a composition space was developed based on ten new experimentally determined RON/MON data of ternary mixtures of toluene, n-heptane and iso-octane mixtures. The model was validated for a high-octane gasoline with RON 98.5 and MON 88 by comparing HCCI simulations that employed a ternary surrogate composition (obtained via the inverse of the model) with experimental data obtained for the reference gasoline. However, the composition of the two TRF surrogate blends generated by Morgan based on their derived equations, contain a very high percentage of toluene which is not very representative of a gasoline surrogate.

Mehl [103] developed two sets of empirical models which could be used alongside the known composition of a particular gasoline to determine an appropriate surrogate for

that gasoline. One of the models correlates the sensitivity of the surrogate to the slope of the logarithm of the ignition delay time in its NTC region while the other model correlates the anti-knock index (AKI) of the surrogate to the logarithm of the ignition delay in the NTC region at 825 K. The composition of aromatics and olefins controls the gradient of the NTC region and the appropriate composition required to match the sensitivity of the surrogate with that of gasoline is determined using the hydrogen carbon ratio (H/C) of the gasoline as constraint. The final PRF content (ratio of iso-octane/*n*-heptane) in the surrogate is determined by adjusting the ratio of isooctane to n-heptane until a match is found between the AKI of the surrogate (determined using the appropriate correlation) and that of gasoline. However, the sensitivity of the surrogate proposed by Gautier et al [93] was over estimated by Kukkadapu [104] using Mehl's correlations to be 6 as the sensitivity of the same surrogate was later determined by Knop [105] as 2.4 based on their measured RON and MON data.

Pera and Knop [102] proposed a methodology for calculating the composition of a gasoline surrogate targeted for autoignition and knock predictions within internal combustion engine configurations. In this approach, appropriate constraints such as RON, MON, molar mass, H/C and oxygen carbon ratio (O/C), were chosen in order to directly match the autoignition response of gasoline as well as indirectly match its physical properties such as lower heating value, stoichiometric air-fuel ratio, boiling point or distillation and density. Based on the target application of the study, the RON of gasoline which is a primary measure of its autoignition quality, was considered the most significant constraint. The H/C was considered the next most important before the MON given that properties such as lower heating values, density and boiling point are all a function of the atomic content (carbon, hydrogen and oxygen content) of gasoline fuel. A major constraint that must also be satisfied by the surrogate mixture is that the sum of the mole fractions of each component in the mixture must be unity. In defining a TRF surrogate the RON and H/C constraints were deemed sufficient to recover all the properties of gasoline when the sensitivity of the surrogate is close to that of gasoline. A quaternary mixture targeted to match oxygenated gasoline, would include an oxygenate compound and would require an additional constraint of O/C in order to match the oxygen content of the gasoline. For a multicomponent surrogate, up to five or six compounds from the entire chemical family could be employed giving us the

opportunity to also constraint the model with the MON of gasoline and thereby reproducing the sensitivity of gasoline in the model. Table 2.2 presents a list of the various surrogates developed so far for gasoline in open literature

Table 2.2: List of various gasoline surrogates in literature [104]

Reference	Molar percentage
Gauthier et al. (2004)	*iso*-C_8H_{18}/*n*-C_7H_{16}/$C_6H_5CH_3$ = 56/17/28
Naik et al. (2005)	*iso*-C_8H_{18}/*n*-C_7H_{16}/C_7H_8/C_5H_{10}-1/MCH = 60/8/20/4/8
Vanhove et al. (2006)	*iso*-C_8H_{18}/C_6H_{12}-1/$C_6H_5CH_3$ = 47/18/35
Chaos et al. (2007)	*iso*-C_8H_{18}/*n*-C_7H_{16}/$C_6H_5CH_3$ = 68.7/10.3/21
Lenhert et al. (2009)	*iso*-C_8H_{18}/*n*-C_7H_{16}/$C_6H_5CH_3$/C_5H_{10}-1 = 40.6/13/40.7/5.7
Mehl et al. (2011)	*iso*-C_8H_{18}/*n*-C_7H_{16}/$C_6H_5CH_3$/C_5H_{10}-2 = 48.8/15.3/30.6/5.3

2.4.6 Gasoline surrogate mechanisms

Several kinetic surrogate models of gasoline combustion have appeared in the open literature. While a good number of mechanisms have been developed for PRF (iso-octane and n-heptane blend) [106-108], current efforts are geared towards development of kinetic schemes of TRF [109] and more complex blends [88, 110, 111]. Mehl [88] developed a mechanism based on a four component surrogate model for autoignition modelling in an engine and validated it against ignition delay data covering a wide range of conditions of pressure (20 bar and 40 bar), temperature (640 - 950 K) and equivalence ratio (lean to stoichiometric). A reduced version of the same mechanism was later produced in [103] with the focus of using the mechanism in CFD engine simulations. While a few chemical kinetic modelling studies have been reported on TRF and more complex surrogates, much is still needed to be done to unravel the most important reaction steps underlying the low temperature autoignition behaviour of TRFs as gasoline surrogates. This work aims to partly contribute towards that goal.

2.5 Review of DME and *n*-butanol chemical kinetic studies

2.5.1 DME chemical kinetic studies

One of the foremost chemical kinetic studies on DME oxidation at high temperatures is the one reported by Dagaut et al. [112] where the concentration profiles of reactants,

products and intermediate species were measured in a jet-stirred reactor under experimental conditions of P = 1 - 10 atm, T = 800 - 1300 K and equivalence ratio 0.2-2.0. Based on results from their study, a detailed chemical kinetic model was proposed and predictions of model were compared with their measured data with reasonable agreement. The JSR data of Dagaut et al. [112] and shock tube data of Pfahl et al. [113] were modelled in Curran et al. [114] using a chemical kinetic mechanism they developed based on the hierarchical nature of reacting systems. Results of their shock tube modelling work showed the need to include a suitable low-temperature sub-mechanism in the kinetic scheme. In addition, the work showed that the rate parameters for unimolecular fuel decomposition and methoxy-methyl radical β-scission would require some tuning in order to obtain better agreement with experimental data. Dagaut et al. [115] developed an improved version of the reaction mechanism developed in their previous study, reported in [114] by including the low-temperature sub-mechanism in the scheme and validated the same against ignition delay measurements of DME oxidation in a shock tube at conditions of P = 10 atm, ϕ = 0.2 - 1, T = 550 - 1100 K and measurements of concentration profiles of reactants, intermediates and products of DME oxidation in a JSR at P = 3.5 atm, ϕ = 0.2 - 1 and T = 1200 - 1600 K. The mechanism was also tested with reasonable agreement against the shock tube data reported in [113] and species data obtained previously in [112] in a jet-stirred reactor. At around 750 K, the model however over predicted the reactivity of DME's oxidation. Fischer et al. [116] studied the high temperature kinetics of dilute mixtures of DME in a variable-pressure flow reactor (VPR) at P = 2.5 atm and T = 1118 K and in an atmospheric-pressure flow reactor at T = 1085 K for equivalence ratios ranging from 0.32 to 3.4. In their work, they tested a high-temperature DME kinetic scheme published previously in [114], against species data from their reactor and then attempted to improve the mechanism by effecting some changes on it. The changes did not however improve on the level of model's agreement with their experimental data. The low-temperature chemistry of the oxidation of dilute DME was investigated by Curran et al. [117] using the variable-pressure flow reactor previously reported in [116], under initial reactor temperature condition of 550 - 850 K, pressure and equivalence ratio ranges of 12-18 atm and 0.7-4.2 respectively. Results of modelling of species evolution in their VPR using a detailed kinetic scheme published in a previous work [114], show that the mechanism is unable to predict the formation of formic acid specie measured in the

reactor. A high level of agreement was however obtained after adding the chemistry for the formation and oxidation of formic acid to the scheme. The mechanism was also validated with high accuracy against the low-temperature kinetic data of Dagaut et al. [115] obtained in a JSR and that of Pfhal et al. [113] obtained in shock tube. A good number of DME flame studies exploring the high temperature oxidation chemistry of DME have also been reported in [118-122].

Zheng et al. [123] obtained ignition temperature data of nitrogen-diluted DME and heated air in non-premixed counter flow configuration. The results of the comparison made between the measured data and predicted data using the mechanism of Curran [114], showed huge over-prediction of the measured data. Zhao et al. [124] carried out pyrolysis experiments in a Princeton variable-pressure flow reactor (VPFR) at a temperature of 980 K and pressure of 10 atm. A high-temperature kinetic model, incorporating theoretically calculated decomposition rates was constructed and was combined with the low-temperature scheme of Curran et al. [117] with some adjustment to the key reaction rates. The revised model was tested with good agreement against their new high temperature pyrolysis data and a wide range of high and low temperature experimental data. The model was also shown to perform better than the previous DME mechanisms reported in [115, 117].

Metcalfe et al. [125] developed a detailed hierarchical chemical kinetic scheme describing the oxidation of small hydrocarbons (i.e. methane, ethane, ethylene and acetylene) and oxygenated species (i.e. formaldehyde, methanol, acetaldehyde and ethanol). The rate parameters for the most dominant reactions that drive the oxidation of individual stable species were carefully chosen based on measured or calculated values found across the open literature. The mechanism was validated across a large spectrum of initial conditions and experimental configurations such as shock tubes, flow reactors, jet-stirred reactors and flame setups. Liu et al. [126] demonstrated good prediction of measured key species of low-pressure DME flames (diluted with or without CO_2) using three kinetic models reported in [118, 124, 125] and an updated kinetic scheme developed in their study based on the mechanism of Zhao et al. [124]. H_2O_2 is a key intermediate species influencing the chemistry leading to hot ignition. At low temperature, H_2O_2 can be used as an indication of the level of H abstraction from fuel by HO_2 and it's therefore a good measure of the extent of low-temperature reactivity

[127]. Guo et al. [128] quantitatively measured the formation of H_2O_2 and other intermediate species (O_2, CO, CO_2, H_2, CH_2O, CH_3OCHO) in a helium-diluted DME atmospheric flow reactor using Molecular Beam Mass Spectrometry (MBMS) and micro gas chromatography (μGC) methods at low temperatures ranging from T = 490 - 750 K. A comparative study of experimental data and predictions of two kinetic schemes reported in Zhao et al. and Yasunaga et al. [124, 129] revealed that large quantities of H_2O_2 are produced from the low-temperature and intermediate temperature oxidation of DME. The model of Zhao displayed better agreement with experimental data compared to the model of Yanasuga in terms of the predicted concentrations of H_2O_2 and most other species.

Some recent work on ignition delay time measurements in shock tubes have also been reported in open literature. Ignition delay times and OH-time histories were obtained by Cook et al. [130] behind a reflected shock tube and mechanisms developed in Fischer et al. [116] and Zhao et al. [124], tested against measured data, showed that ignition delay times are well predicted while OH-time histories are poorly predicted by both schemes. An update was made to the rate constant of the reaction ($CH_3OCH_3 \rightarrow CH_3O + CH_3$) that majorly drives OH production, using a value estimated based on their measured data and other values from previous experiments. The update was found to significantly improve agreement between the calculated and measured values of OH.

Hu et al. [131] measured ignition delay times of stoichiometric DME/*n*-butane blends behind a reflected shock tube for different blending ratios of DME at temperatures of 1200 - 1600 K and pressures of 1.2 - 5.3 atm. Correlations of their data using regression analysis show that ignition delay times decreases with increasing pressure and DME blending ratio and increases with 1000/T. Predictions of ignition delay times using the mechanism developed by Donato et al. [132] showed good agreement with experimental data for temperatures above 1400 K but over-predicts data for temperatures below 1400 K. More recent studies involving the measurement and chemical kinetic modelling of DME in shock tubes can be found in [133-135].

The only chemical kinetic modelling study reported on DME autoignition using a rapid compression machine as at the time of this study is that of Mittal et al.[136]. In the study, ignition delay times were measured at compressed conditions of T = 800 - 1300 K, P =

10 - 20 bar and equivalence ratios of 0.43 - 1.5. The results of the chemical kinetic modelling of ignition delay times of DME/O_2/N_2 mixtures using the reaction mechanism of Zhao [124] show that DME exhibits the well-known two stage ignition and NTC behaviour. The work also sheds light on the impact of the slow reactions occurring during the compression phase on the predicted overall ignition delay indicating the need to model both the compression and post compression events occurring in the RCM.

2.5.2 Butanol chemical kinetic studies

Combustion studies involving the four isomers of butanol are on-going but *n*-butanol is probably the most widely studied among the four isomers. The following provides an up to date review of the experimental and chemical kinetic modelling studies of biobutanol oxidation and combustion in fundamental setups.

The study of Barnard et al. [137] is one of the earliest experimental studies carried out on *n*-butanol pyrolysis. Based on the analysis of the various products formed during tests carried out in a static reactor, formaldehyde, carbon monoxide, methane and hydrogen were identified as the major species produced. A mechanism of butanol oxidation was proposed in line with observed characteristics. His mechanism suggests a unimolecular decomposition pathway for *n*-butanol following the fission of the $CH_3CH_2CH_2$-CH_2OH bond to form *n*-propyl radical and hydroxymethyl radical. *n*-propyl radical then undergoes b-scission reactions to form ethene and methyl radical while hydroxymethyl radical decomposes through b-scission reactions to form formaldehyde and the hydrogen radical. Smith et al. [138] looked at diffusion flames of the four biobutanol isomers and also proposed a reaction mechanism for *n*-butanol oxidation. In their mechanism, the chain initiation steps involve hydrogen abstraction reactions and then a series of b-scission reactions to produce species like propene, ethane and 1-butene. Robert et al. [139] in another work, reported the results of their experiments in which the laminar burning velocities of 1-butanol-air mixtures, at equivalence ratios of ϕ = 0.7 - 1.1 were measured using shadow images of a Bunsen flame cone. A maximum burning velocity of 46 cm^{-1} was recorded in their experiment.

Moss et al. [140] measured ignition delay times in a shock tube for the four isomers of butanol for temperatures and pressures ranging from 1200 – 1800 K and 1 - 4 bar respectively. Results of their work indicate that *n*-butanol decomposition is dominated

by hydrogen abstraction reactions which yield radicals that greatly favour the chain branching steps. A reaction mechanism representing the oxidation pathway of the four isomers of *n*-butanol oxidation, containing 161 species and 1256 reactions was also proposed and validated against their experimental data.

Dagaut et al. [20] also reported results of their work using *n*-butanol in a jet-stirred reactor. In their work in which they investigated the oxidation of pure 1-butanol in a jet-stirred reactor at conditions of P = 10 atm, T = 800 - 1150 K and ϕ = 0.5 - 2.0, it was reported in agreement with Moss et al. [140] that the 1-butanol consumption pathway is dominated by hydrogen abstraction reactions from the alpha, beta and gamma carbons of *n*-butanol. They also developed a reaction mechanism for 1-butanol oxidation and comparison of model predictions with their JSR data was in reasonable agreement.

Sarathy et al. [141] in a recent work presented an improved version of the reaction mechanism proposed by Dagaut et al. [20] and validated it against species data obtained in an atmospheric JSR, species and temperature profiles of *n*-butanol in an opposed-flow diffusion flame and burning velocity data from an *n*-butanol premixed laminar flame.

Several studies involving butanol flames have also been reported in open literature. One of such work is that carried out by McEnally and Pfefferle [142] in which pollutant emissions of non-premixed co-flowing flames of methane/air mixtures doped with butanol isomers were investigated for oxygenated fuel effects. Unimolecular dissociation through four-centred eliminations or C-C bond fissions were identified as the major pathway through which all four butanol isomers were consumed in the co-flowing flame. Yang et al. [143] studied laminar premixed flames of the four isomers of butanol at low pressure. The method of photoionisation mass spectrometry was employed to detect stable and transient combustion intermediates without providing concentration profiles. Grana et al. [144] obtained new experimental data of *n*-butanol and iso-butanol from a non-premixed counter flow flames configuration. Gas samples taken from the flames were analysed for various species using gas chromatography and coated thermocouples were employed to measure the flame temperature profiles. A reaction mechanism was also developed using a hierarchical approach and validated with new experimental data as well as various data in open literature obtained from flow

reactors, batch reactors, JSRs and high temperature shock tube setups. Black et al. [145] developed and tested a chemical kinetic model against ignition delay time measurements of *n*-butanol obtained in a shock tube and data of *n*-butanol oxidation obtained in a 10 atm JSR by Dagaut et al. [20], with good success. Their shock tube experiment was conducted under conditions of reflected pressures of 1, 2.6 and 8 atm and temperatures ranging from 1100 - 1800 K for equivalence ratios of 0.5, 1 and 2.

Harper et al. [146] constructed a detailed reaction mechanism using the Reaction Mechanism Generator (RMG) software developed originally by Song [147] and tested the model with good result against new *n*-butanol pyrolysis data obtained from a bench-scale reactor setup and recently published data of *n*-butanol mole fraction profiles as well as ignition delay times obtained across various configurations.

Based on the forgoing, it is clear that only a small amount of fundamental chemical kinetic studies have been carried out on butanol oxidation, particularly ignition delay times measurements at elevated pressures and low to intermediate temperatures. It should be noted that most of the aforementioned mechanisms only contain the high temperature reaction classes and cannot predict ignition delay. However, very recently, Sarathy et al. [148] proposed a detailed reaction mechanism that includes both the high-temperature and low-temperature reaction pathways for the four isomers of butanol with the reaction rate parameters determined from rate rules. The kinetic model was constructed by adding primary reactions of tert-butanol, 2-butanol, and iso-butanol and related radical reactions to the 1-butanol reaction mechanism proposed by Black et al. New reaction classes for all the butanol isomers were also added to better predict high and low-temperature combustion behaviour. The mechanism which contains 426 species and 2335 reactions was validated with reasonable agreement against a wide range of recently published experimental data which includes: speciation data from low pressure laminar premixed flames, premixed laminar flame velocities under atmospheric pressures, species data from a high pressure JSR, ignition delay times from a high pressure RCM and ignition delay times from atmospheric and high pressure shock tubes.

2.6 Combustion chemistry: methods for model evaluation and improvement

After a reaction mechanism which includes the relevant reactions has been compiled for a particular fuel or a family of similar fuels, simulation results from computer codes implementing the chemistry of the fuel are subsequently compared with experimental data from configurations such as JSRs, flow reactors, RCMs, shock tubes and laboratory flames in different configurations and any facility that is able to model the kind of combustion environment that is relevant to conditions obtainable in practical combustion systems [22]. A very important aspect of model validation and evaluation is comparing results obtained from simulations using a chemical kinetic model with experimental data obtained under similar conditions. Uncertainties in the input model significantly affect the results of predicted targets and must therefore be accounted for in the process [149]. Moreover, it is important to know which of the model parameters contributes most to the predictive uncertainty of important targets. When one is armed with such knowledge, model improvement methods such as theoretical, experimental or optimisation techniques can then be properly focused on those specific model parameters in order to improve the accuracy of the model predictions [149]. The wide range of analysis methods for investigating and improving mechanisms include local and global sensitivity analysis, and uncertainty analysis. Optimisation techniques involving fitting are performed to improve a mechanism and fit to experimental indirect results [150].

2.6.1 Methods for obtaining reliable experimental data to validate models under wide ranges of experimental conditions

The chemical kinetics of a fuel greatly influences combustion properties such as ignition delays, pollutant formation and heat release rates and all of these occur in an environment that is surrounded by a complex flow field. Although the combustion process in a motored engine more accurately mimics what happens in a real engine, the influence of fluid flow on the combustion process makes it very difficult to accurately determine the effects of chemical kinetics. Rather than validate a fuel's chemistry model in complex combustion flow field configurations involving both chemistry and fluid dynamics, such as in a SI engine, a more realistic alternative is to perform the study

based on predominantly chemical kinetics, assuming an idealised flow fields [151]. Experimental data derived from tests carried out using idealised combustion systems helps in validating chemical kinetic schemes and in development of more accurate chemical kinetic models which can then be applied for modelling and understanding combustion in practical engines [152].

For a chemical kinetic model to be successfully used to make predictions of combustion properties in practical engines, it should be validated against experimental data that cuts across the entire spectrum of conditions (i.e. temperatures, pressures and equivalence ratios) obtainable in practical engines [2, 16, 152, 153]. Some of the common homogenous combustion devices from which experimental validation data could be obtained include shock tubes, flow reactors, perfectly stirred reactors (PSRs), motored engines and RCMs [151]. The shock tube and RCM are commonly used for studying low-temperature oxidation processes such as ignition delay times which is a global measure of reactivity. While the use of flow reactors and JSRs for speciation studies is well reported in open literature, the application of the RCM and shock tube for such is however uncommon but developing. A summary of the RCM employed in various chemical kinetic studies can be found in [154] while a review of the application of shock tubes for chemical kinetic studies can be found in [155].

2.6.1.1 Flow reactors and perfectly stirred reactors (PSRs) for chemical kinetic studies

As mentioned in the previous section, flow reactors and PSRs are commonly used for performing speciation studies. With flow reactors, the temperatures and species concentrations can be measured directly. The temperature evolution within a flow reactor can be easily obtained through measurements with thermocouples. In speciation studies involving flow reactors, samples of the reacted mixture can be conveniently taken and then subjected to analysis using various detection techniques including Fourier Transform Infrared (FTIR) spectroscopy, gas chromatography or mass spectrometry [2]. Quartz is usually employed for designing flow reactors so as to significantly reduce the probability of wall reactions. However the range of pressures that can be realised in flow reactors are generally low. Higher temperatures and pressures can be realised with PSRs but at these conditions, the reaction time scales and

mixing time scales are quite close thus making it extremely difficult to achieve fast and uniform mixing of the reactants. PSRs can be employed to investigate the influence of the residence time on the rate of chemical reaction by simply adjusting the rate of mass flow. A detailed description of the features of the flow reactor and JSR including their operating principles can be found in [2].

2.6.1.2 Shock tubes for chemical kinetic studies

With shock tubes, higher pressures and temperatures can be achieved while avoiding a complex flow field but the uniform conditions can only be sustained for a time scale lower than 10 ms [152]. The shock tube is commonly employed for temperature regimes above 1000 K. Within the low-temperature range, the residence time present in the shock tube (< 10 ms) is not enough for the temperature of the reactive mixture to be well resolved (i.e. attain equilibrium) [156].

The shock tube is basically a long tube which is divided into two sections, namely the driver section (Figure 2.7) which contains a high pressure gas, and a driven section which contains the low pressure fuel mixture. In the shock tube a plane wave is generated by allowing a high pressure gas to expand into the low pressure reactive fuel vapour mixture across a separating diaphragm which gets ruptured in the process. The temperature and pressure of the mixture is raised quickly as the generated shock wave travels through the reactive mixture occupying the long driven section of the tube. In many of the shock tubes, the shock wave is reflected at the tube end wall and while it travels back cross the driven section of the tube, it further heats up the reactive mixture to higher temperatures and pressures [2]. Pressure transducers placed on the tube side wall and uniformly spaced along the driven section of the tube are used for measurement of the shock velocity across the mixture. The temperatures are determined from the shock velocity measurements. A pressure transducer placed at the end wall is used for measurement of pressure at the end wall while the shock velocity and consequently temperatures at the end wall are determined by extrapolation of axial shock velocity profile to the end wall [131]. The time scale within which measurements can be made in the shock tube is usually lower than 10 ms and temperature measurements can fall within the range of 700 – 3000 K [2]. Apart from the conventional shock tube which is used basically for carrying out time dependent speciation studies, the single pulse shock

tube is one popular class of shock tube that can be used to generate speciation data from a thermally reacting flow mixture through instantaneous heating and then rapid quenching of the gas mixture. The gas mixture is heated to a high temperature known as the reflected shock temperature for a constant period of time referred to as the residence time and then suddenly quenched to room temperature in order to retain the high temperature composition. The upper limit of such temperature (usually less than 2500 K) is determined by the reaction rate and the residence time (usually between 1 to 3 ms) [2]. The residence time on the other hand is dependent on the geometric parameters of the shock tube. Gas chromatography is one of the common gas sampling methods used for analysing the different product species formed by the reacting mixture in a pulse shock tube.

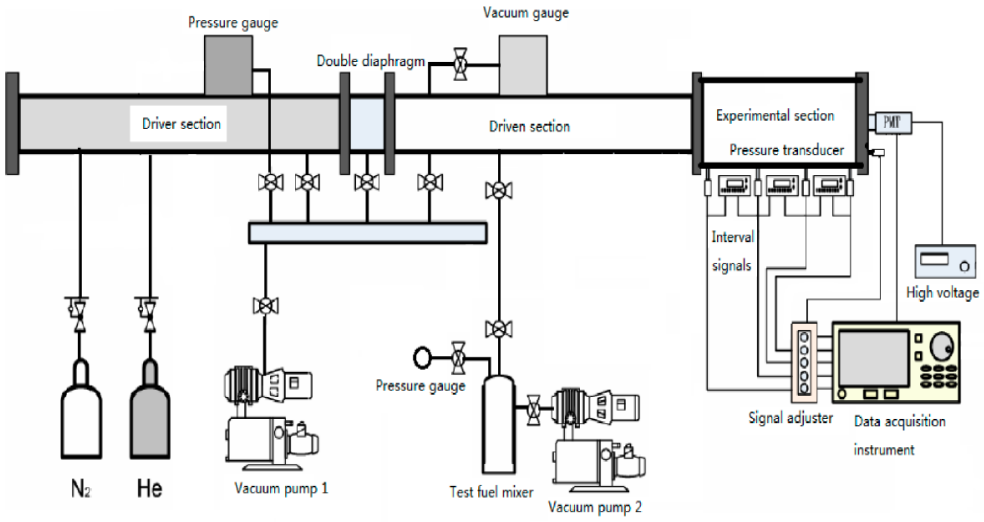

Figure 2.7: Schematic diagram of the shock tube. Taken from [131].

2.6.1.3 The rapid compression machine (RCM) for chemical kinetic studies

The RCM unlike the shock tube can be operated to attain high temperatures and pressures for time scales in excess of 10 ms and the ignition delay times can be directly measured. However the heat loss and fluid dynamics effects peculiar to the RCM makes it very challenging to exclusively investigate the effect of chemistry or molecular structure on the combustion process. The development of the RCM has evolved in recent times and while heat loss is being accounted for through various approaches, the fluid dynamics and mixing effect is targeted for elimination by designing a crevice on the piston. The inclusion of the crevice on the piston head helps to create a homogenous

core reaction zone in the RCM as fluid dynamic processes and undesired mixing of cold gases near the combustion chamber wall are suppressed [152]. This added feature makes it easy to accurately determine the pressures and temperature in the RCM which is highly desired as far as chemical kinetic modelling studies are concerned.

The RCM is basically an ideal single cylinder internal combustion engine than can be used for chemical kinetic studies at conditions that are relevant to internal combustion engine studies. The RCM is reported to be able to operate at engine related compressed temperature and pressure conditions of 600 – 1100 K and 1 - 70 bar respectively [154]. A basic feature of the RCM is a piston that compresses a gas fuel mixture of given composition to temperatures and pressures high enough to initiate the combustion of the reacting mixture. The RCM can be designed to operate as a single piston or twin piston machine. By using the adiabatic core hypothesis, the temperature attained at the end of compression can be determined from the initial pressure and temperature of the mixture, the initial composition of the reactive mixture and the experimentally measured pressure at the end of compression [157]. For a given compression ratio, the temperature of the compressed gas mixture at the end of the compression stroke can be changed by varying the mixture composition (i.e. by varying the composition of the inert gas). While the autoignition process and the evolution of the combustion process is usually studied as a function of pressure, temperature and mixture composition, species production and evolution can be monitored and analysed based on rapid sampling techniques using gas chromatography methods. The time lapse for the compression process is usually allowed to be very small (i.e. between 10 – 70 ms) so that the assumption of an adiabatic compression process can be considered to be reasonably valid [154]. After compression, the combustion of the reactive mixture is assumed to occur under a constant volume chamber and typical time scales for the study of the combustion process are in the range of 1 to 200 ms [2]. When the RCM is being used for autoignition studies, the progress of the combustion process is monitored in terms of the pressure history. From the pressure history data, the ignition delay time which by definition is the time lapse from the point of end of compression to the point of ignition (i.e. point of commencement of combustion) is determined (Figure 2.8). In the design of the RCM some major considerations are always kept in mind and implemented. Firstly the RCM must be able to complete the compression of a reactive mixture within the shortest possible time and

this is usually taken care of by the driver mechanism of the machine. Secondly the RCM must be designed in such a way that at the end of compression, the combustion process is allowed to go on under constant volume with thermodynamic properties held constant during the process. This is usually achieved with the aid of an effective braking system. Lastly the RCM must be designed in such a way that during operation it is able to deliver the desired range of thermodynamic properties (i.e. temperature and pressure) at the end of compression [154]. The temperature and pressure at the end of compression T_c and P_c respectively are a function of the initial temperature and pressure T_i and P_c respectively, the volumetric compression ratio (which is a function of the RCM geometric parameters) and the heat capacities of the reacting mixture. For example,

$$P_c = P_i r^{\gamma} \; and \tag{2.80}$$

$$T_c = T_i r^{\gamma - 1} \tag{2.81}$$

r is volumetric compression ratio which is also given by:

$$r = \left(\frac{v_i}{v_c}\right) \tag{2.82}$$

γ is the ratio of the specific heats at constant pressure, c_p to the specific heat at constant volume, c_v,

$$\gamma = c_p / c_v \tag{2.83}$$

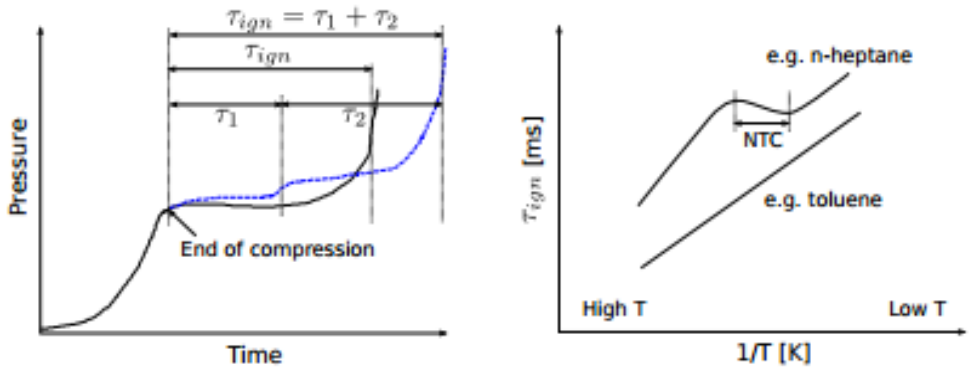

(a) (b)

Figure 2.8: (a) Typical pressure traces illustrating a single stage and two stage ignition in the RCM alongside the definition of ignition delay. τ_1, τ_2, and τ_{ign} are the first-stage, second-stage and overall ignition delay respectively. (b) Plot of ignition delay times measured in the RCM as a function of temperature. Taken from [30].

2.6.2 Sensitivity analysis and uncertainty analysis

Sensitivity analysis helps us to determine the relative parameter importance (i.e. parameters with largest influence on model predictions) by exploring the relationship between input values of a mathematical or numerical model and its prediction [150, 158]. With sensitivity analysis, one can then decide on which parameters should be prioritised for model improvement. Within the field of combustion, one may decide to investigate how changes in rate parameters or thermodynamic data affect predictions of key target parameters like ignition delay times, flame speeds or species concentration profiles [29]. Sensitivity analysis can be applied over wide range of temperatures, pressures and equivalence ratios including conditions where practical combustion devices such as internal combustion engines operate and not just only for conditions for which experimental data are available. Uncertainty analysis helps us to evaluate the predictive uncertainty that filters into key model output due to our lack of knowledge of model input parameters. Uncertainty analysis enables the modeller to estimate error bars for model predictions, and consequently, one can easily see the degree or extent to which a model's prediction can be relied upon [150].

When a full sensitivity analysis is required, then it is important to specify the uncertainty range of each input parameter in order to calculate the sensitivity coefficients. The sensitivity coefficients estimated through this approach are a measure of the contribution of the uncertainty of each input parameter to the overall predictive uncertainty of the model [159]. In a more general approach of sensitivity analysis one can simply investigate the model response to fixed perturbations made on the input parameters. This is usually necessary when the knowledge of the input uncertainties is highly limited or application of more advanced methods may be computationally expensive. Although this approach alone doesn't calculate the contribution of input uncertainty to model output uncertainty, it could however be used as a screening tool to remove unimportant parameters before applying more expensive methods [29].

2.6.2.1 Local sensitivity analysis

The change in the output (e.g concentrations) with time of a given spatially homogenous reactor system can be represented by a system of ordinary differential equation given by:

$$\frac{dY}{dt} = f(Y, x), \quad Y(t_0) = Y_0 \tag{2.84}$$

The species concentration Y is the dependent variable while time t is the independent variable. Y_0 is the initial concentration vector and x is the parameter vector of the system containing m elements which may include rate parameters, thermodynamic data, pressure dependence parameters etc. With the aid of a Taylor series expansion the concentration at any time t due to changes in the input parameter x can be modelled in details as.

$$Y_i(t, x + \Delta x) = Y_i(t, x) + \sum_{j=1}^{m} \frac{\partial Y_i}{\partial x_j} \Delta x_j + \frac{1}{2} \sum_{k=1}^{m} \sum_{j=1}^{m} \frac{\partial^2 Y_i}{\partial x_k \, \partial x_j} \Delta x_k \Delta x_j + \cdots \tag{2.85}$$

The term $\frac{\partial Y_i}{\partial x_j}$ represents the first-order local sensitivity coefficient while $\frac{\partial^2 Y_i}{\partial x_k \, \partial x_j}$ represent the second-order local sensitivity coefficient. The local sensitivity coefficient represents the change in the model output Y_i due to small changes in the value of the input parameter$s$ x_i relative to their nominal values while keeping all other parameters fixed at the same time [150]. The elements contained in the local sensitivity matrix $S = \frac{\partial Y_i}{\partial x_j}$ give the local sensitivity coefficients. The units between input parameters and/or target output may differ. Therefore for a proper comparison to be made between sensitivity coefficients, a dimensionless normalised sensitivity coefficient given by $\left(\frac{x_j}{Y_j}\right)\left(\frac{\partial Y_i}{\partial x_j}\right)$ is normally used [160]. Some of the methods that have been developed for the solution of S include the Brute-force method [160], Greens Function method [161] and the decoupled-direct method [162]. In the Brute-force method, each input parameter is perturbed one after the other by a small percentage away from the nominal value and the percentage change in the model output is simulated and results ranked. In order to calculate sensitivity indices for a system of m input parameters using the Brute-force method, then a total number of $m+1$ simulation runs must be performed. The decoupled-

direct method solves the following equation using the Jacobian from the original kinetic equations.

$$\frac{d}{dt}\frac{\partial \boldsymbol{Y}}{\partial x_j} = J\frac{\partial \boldsymbol{Y}}{\partial x_j} + \frac{\partial \boldsymbol{f}}{\partial x_j}, \qquad \frac{\partial \boldsymbol{Y}}{\partial x_j}(t_0) = 0, \qquad (j = 1, 2, \dots, m) \tag{2.86}$$

Or in matrix form

$$\dot{\mathrm{S}} = JS + F, \qquad S(0) = 0, \tag{2.87}$$

where $J = {\partial f}/{\partial Y}$ represents the Jacobian and $F = {\partial f}/{\partial x}$, $S_i = {\partial Y_i}/{\partial x}$ represent the *i*-th column vector of the sensitivity matrix S.

2.6.2.2 Local uncertainty analysis

An input parameter having a very low sensitivity coefficient could at the same time contribute greatly to model output uncertainty due to its high uncertainty factor and vice versa. In order to be able to know the most important input parameters that require further improvement, the information about the input uncertainties should be integrated into sensitivity analysis. This can be done by quantifying the contribution of each input parameter to the overall predictive uncertainty [29].

If the variance of a group of uncorrelated parameters $\sigma^2(x_j)$ is known, then the variance of the output Y is given by:

$$\sigma^2(Y) = \sum_j (S)^2 \sigma^2 (x_j) \tag{2.88}$$

where $S_i = \frac{\partial Y_i}{\partial x_j}$ are the local sensitivity coefficients of the input parameters. The fractional uncertainty of each input parameter in Equation 2.88 weighted by its sensitivity coefficient provides an estimate of the relative importance of the input parameter as well as its contribution to the overall uncertainty. Such approach is expected to give a better measure of parameter importance than $\frac{\partial Y_i}{\partial x_j}$ alone since the uncertainty of each parameter has been incorporated. The use of local uncertainty analysis is based on the assumption that the model response is linear across the entire input parameter range but this is usually not the case. However, when used in the context

of just identifying important input parameters for improvement rather than for estimation of error bars, they could be very useful and may offer better computational savings compared to the global methods described in the following section.

The combustion and chemical kinetic community have over the years made various recommendations for uncertainties in rate parameters across a set of temperature ranges based on data evaluations. The uncertainty factor is defined as:

$$f = log_{10}\left(\frac{k^0}{k^{min}}\right) = log_{10}\left(\frac{k^{max}}{k^0}\right) \tag{2.89}$$

where k^0 is the recommended value of rate coefficient based on assessment of available experimental and theoretical studies. k^{min} and k^{max} are the possible extreme values of the rate coefficient which are positioned symmetrically around k^0.

Therefore, $\frac{k^0}{k^{min}} = \frac{k^{max}}{k^0} = G_i$ gives the value of the uncertainty in the rate parameter. By writing the input uncertainty in terms of the uncertainty factor, the Equation becomes,

$$f = log_{10}G_i \quad or\ G_i = 10^f \tag{2.90}$$

The knowledge of the uncertainties G_i, enables us to estimate the uncertainty ranges or $\sigma^2(x_i)$ for the input parameters which can then be used in the context of local and global uncertainty methods.

2.6.2.3 Global sensitivity and uncertainty analysis

Global sensitivity analysis provides information about the sensitivity of the target to changes in each parameter within the entire range of the input parameter space. This approach allows one to be able to investigate the impact of model input parameters (e.g reaction rates) across their entire range while also accounting for the effect of parameter interactions as well as non-linearity in the models response. Global uncertainty and sensitivity methods give a better ranking of the contribution of each parameter uncertainty to the output variance especially in cases where the non-linearity and uncertainties in models are quite high [29].

The global techniques are usually built around a sampling approach in which many simulations are carried out with samples covering the entire domain of input space. The standard Monte Carlo (MC) analysis employs a random sampling approach. The drawback of this method lies in its inability in generating a uniform sample as the randomly selected samples can be close in some region of the parameter space and wide apart in some other regions (Figure 2.9a). In an attempt to improve on the MC approach, methods incorporating some form of control on parameter sampling, such as the Latin hypercube sampling or quasi-random sampling approach have also been explored. While the Latin hypercube sampling approach performs reasonably well in terms of its relatively good coverage of the entire input space, it requires large computer time when dealing with models with large input parameters. A low-discrepancy sequence, which measures the uniformity of a sequence, has been suggested as a better option compared to the Latin hypercube method. The most commonly employed low-discrepancy sequences are those of Faure, Halton and Sobol. The Sobol's quasi-random sequence is usually employed because of its faster convergence capability compared to other low-discrepancy sequences and the standard Monte Carlo random sampling approach [149]. Figure 2.8 shows a comparison of the different sampling techniques for a 2 parameter sample. As shown on Figure 2.9, Sobol's sequence provides a higher degree of uniformity of samples across the parameter space compared to the other methods shown in Figure 2.9.

Following the sampling and performance of model runs, there is a need to estimate now the global sensitivity index- a factor that gives an indication of the input parameters that contribute most to the variance in the predicted output. MC simulations and surface response methods (SRMs) are among the most common methods usually employed for investigating the relationship between the input and output distributions [149, 150]. MC approaches use scatter plots for each parameter to see the overall effects. Calculations of full sensitivity coefficients using the standard Sobol's MC based approach is quite computationally expensive and results are difficult to interpret for large numbers of parameters. In the SRM, the sensitivity indices are calculated using a functional meta-model fitted to sample input-output distributions that are based on the full model runs. The accuracy of the calculated sensitivities is dependent on the accuracy of the constructed meta-model which in turn is a function of the sample size, the fitting

approach used in constructing the meta-model and the complexity of the response surface [150]. Therefore, the SRM is by far a more optimal approach when considering a system that is highly computationally expensive due to the large size of parameters involved. Some of the global sensitivity analysis methods that are based on SRM and functionally built around meta-models include orthonormal polynomials, polynomial chaos expansions, Gaussian process models, neural networks and High Dimensional Model Representations (HDMR) [29].

In the HDMR, the output is expressed as a finite hierarchical function expansion given by:

$$Y(\mathbf{X}) = f(\mathbf{X}) = f_0 + \sum_{i=1}^{n} f_i(x_i) + \sum_{1 \le i < j \le n} f_{ij}(x_i, x_j) + \cdots + f_{12\ldots n}(x_1, x_2, \ldots, x_n) \quad (2.91)$$

where the zeroth-order term f_0 represents the mean effect, the first-order term $f_i(x_i)$ represent the effect of variable x_i acting alone upon the output $Y(\mathbf{X})$ and the second-order term $f_{ij}(x_i, x_j)$ stands for the combined effect of the variables x_i and x_j on the output $Y(\mathbf{X})$.

The random sampling HDMR (RS-HMDR) technique is a direct method that could be used to analyse the input-output relationship of a model without the need for a large number of model runs [163].

In the HMDR approach, the input-output response surface (mapping) to which the meta-model is fitted is developed using a quasi-random sample of inputs and the component functions of meta-model are approximated using orthogonal polynomials. The first- and second-order sensitivity indices can be calculated simply from the polynomial coefficients. Examples of the application of the HDMR approach employing a Sobol's quasi-random sequence for global sensitivity analysis of combustion mechanisms can be found in [164-166].

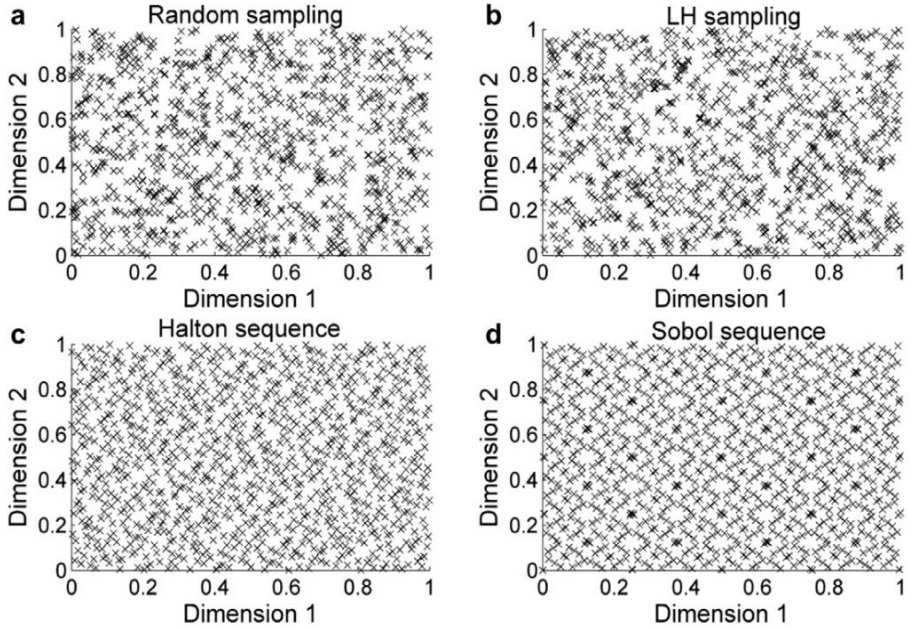

Figure 2.9: Comparison of samples generated based on different sampling approaches for a 2-parameter model with N = 1024 (a) Random samples (b) Latin hypercube sequence (c) Halton sequence (d) Sobol quasi-random sequence. Taken from [167].

2.7 Modelling combustion in internal combustion engines

2.7.1 Introduction

The combustion model plays a very important role when it comes to using computers in simulating the engine operating cycles of internal combustion engines. The combustion process in itself is also directly influenced by every component of the other aspects of the operating cycle ranging from the intake, compression, expansion and down to the exhaust strokes. The combustion process in a real engine is a quite complex phenomenon given the fact that it occurs in a three-dimensional, time dependent, turbulent flow in a space which is bounded by a combustion chamber wall whose shape varies with time, and whose heat transfer is difficult to predict. In addition, combustion involves the burning of fuels that practically contain blends of hundreds of organic compounds whose chemistry are yet to be fully understood [26, 168]. The quality of any model to a large extent, depends on how exactly it represents the actual physical process, how well it has been tested and validated, it's computational cost as well as the time and effort required to interpret the results of computations made with the model .

Three approaches are usually employed when it comes to modelling combustion in engines. The different classes of combustion model in order of increasing complexity are as follows:

i. Zero-dimensional models
ii. Quasi-dimensional or phenomenological models
iii. Multi-dimensional models

These can be further classified broadly as thermodynamic or fluid dynamic models, depending on whether the governing equations which form the major part of the model are built around energy conservation or on a detailed analysis of the fluid dynamics [31]. The Zero-dimensional and quasi-dimensional models are based on a thermodynamic analysis of the contents of the engine cylinder during the engine operating cycle while the multi-dimensional models require a detailed description of the fluid flow geometry [168].

2.7.2 Zero-dimensional models (single zone models)

The zero-dimensional models, sometimes referred to as thermodynamic models, are based on the First Law of Thermodynamics and mass balance only [169]. In the zero-dimensional model, the entire combustion chamber is taken to be a single, homogenously mixed zone. Energy conservation is applied to the single zone while accounting for the work absorbed and produced by the piston work as well as the heat release due to combustion of fuel. The heat transfer across the walls of the combustion chamber may be considered but mass loss through blow-by is often considered negligible. Also, conservation of momentum is not considered and spatial variations of composition and thermodynamic (pressure, temperature, composition, etc.) and transport (viscosity, thermal conductivity, diffusion coefficients) properties are considered negligible. The assumption of an ideally mixed combustion chamber means that the heat released during the combustion phase of the engine cycle can only be accurately modelled by empirical sub-models and pollutant formation rates that are highly dependent on local temperatures and mixture compositions cannot be accurately determined. These models make use of an empirical ‘heat release model’ with time as the only independent variable [26]. Empirical models try to reproduce the characteristic heat release rates obtained from experiments by simple mathematical equations with as

few parameters as possible [169]. The Wiebe function is usually used for this purpose with rate of mass burning or heat release rate specified as a function of the crank angle [168]. By ignoring the inhomogeneity in the engine cylinder and the effect of the cooler thermal boundary layer and considering flow into crevices to be negligible, the single zone model tends to over predict the overall heat release rate and as a result, the rate of pressure rise and the maximum in-cylinder pressure due to combustion are also overestimated. However, single zone models can be used to estimate ignition timing and the formation of NOx emissions to a very good degree of accuracy since both processes are basically a function of the highest temperature in the combustion chamber, which is close to the average temperature of the gas the mixture [27, 170].

2.7.3 Quasi-dimensional models

The main common feature of quasi-dimensional models is the inclusion of some aspects of the physical and chemical processes in the basic thermodynamic model. In the zero dimensional model, the combustion rate (burn rate) is defined by a simple burning law (e.g. Wiebe correlation) whereas in the quasi-dimensional model the combustion rate is predicted from more fundamental physical quantities such as laminar flame speeds, turbulent flame velocity, turbulent intensity, turbulent integral length scales, the jet characteristics in any jet-mixing process, and the kinetics of the fuel-oxidation process [31, 171]. The idea behind this is to predict the ignition delay and combustion rate as a function of engine design and operating parameters. By this approach, quasi-dimensional models, attempt to account for the interaction or link that exists between engine design as well as operating condition and the combustion process without the need for prior measurement and the details and complexity that are characteristic of multi-dimensional models [168, 169].

Quasi-dimensional models can be used within the framework of multi-zone modelling of HCCI and diesel engines or within the two-zone/three zone model of the SI engine where both zones are separated by a thin propagating flame front.

2.7.3.1 Multi-zone models

Multi-zone models were developed in an attempt to overcome some of the limitations encountered with the use of the single-zone models. When applied in the context of the

HCCI engine, the entire combustion chamber is divided into a number of computational zones representing the various physical regions present in the combustion chamber. With this approach, geometrical and physio-chemical phenomena which significantly affect combustion can then be included in the model without having to deal with the high computational demand involved with the use of CFD methods [170]. In the multi-zone model, the temperature, composition, volume and all thermodynamic properties are allowed to vary from one zone to another, but within the confine of each zone they are regarded as uniform. With the effect of temperature or species gradients within the combustion chamber reasonably accounted for, combustion properties such as emissions formations, combustion duration, heat release, in-cylinder peak pressure and pressure rise rates are therefore better predicted compared to single zone models [27].

When a large number of zones are used, due to the spatial resolution, the heat release rate no longer has to be described by solely empirical correlations like the Wiebe function. Instead, it can be pre-estimated based on physical and chemical sub models for local processes like spray formation, air-fuel mixing, droplet evaporation, ignition and combustion including pollutant formation [169]. For CI (diesel) engines, the mixing of the air and the fuel jet is all important, and a turbulent jet-entrainment model is necessary. Phenomenological (quasi-dimensional) models are used widely in diesel engines because of their potential to properly describe the injection process which has a great influence on mixture formation and the resulting combustion process [169]. Since the time histories of different fuel elements will not be the same, a multi-zone combustion model is usually needed to trace the individual fuel elements. The prediction of NOx emissions will provide a powerful check on any such model, since NOx production will be very sensitive to the wide variations in both temperature and air/fuel ratio that occur in compression ignition engines.

Despite the above advantages of multi-zone models, the assumption of homogeneity within each zone, and the computation of the chemical source term using the average temperature and composition of the air fuel mixture, generally represents an oversimplification of the actual physical problem.

2.7.3.2 Two-zone SI engine models

In SI engines, a popular approach employed is by modelling the burning process as a flame front of area A_f (usually assumed to be sections of the surface of a sphere) separating the combustion chamber into two zones (burned and unburned zone) and propagating through the unburned mixture at the turbulent flame speed S_T. Thus the rate of burning is

$$\frac{dm_b}{dt} = \rho_u A_f S_T \tag{2.92}$$

S_T is then related to the laminar flame speed e.g., by $S_T = KS_L$, where K is a constant representing the turbulent flame factor.

2.7.4 Multi-dimensional models

Despite the advantages of multi-zone models, they are still unable to produce a high spatial resolution of engine cylinder. The ability to describe the motion of the charge within the combustion chamber and the effects of turbulence is also completely lacking [169]. Multi-dimensional CFD models on the other hand are able to fully predict the geometry dependent turbulent flow and flame propagation within the engine cylinder by simply solving numerically the equation for mass, momentum, energy and species conservation in three dimensions. With multi-dimensional models, it is possible to determine the spatial distribution of gas velocity, temperature and composition within the combustion chamber of the engine during the combustion process [168]. Multi-dimensional models rely on sub-models to describe the turbulence, chemical kinetics and boundary layer effects and as such, they are limited by the inadequacy of such sub-models. Presently, from the perspective of computational demand, only one dimensional and two dimensional problems can be successfully handled even with very simple sub-models for turbulence and chemistry due to the complexity introduced by the various physical and chemical processes.

Multi-dimensional models are more useful compared to thermodynamic models where the effect of changes in combustion chamber geometry and flow are significant. Therefore, due to their high computational cost, they are usually employed for modelling just the combustion chamber as against modelling of the full engine cycle

[168]. Thermodynamic models (zero dimensional and quasi dimensional) due to their simplicity and relatively lower computational cost, offer better advantages compared to multi-dimensional models when used in the context of parametric studies of the influence of engine design and operating conditions as well as fuel effects on the engine efficiency and emissions [171].

The KIVA code is one of the most widely used computational fluid dynamic codes in the automotive industry and it is capable of solving the conservation equations of mass, momentum and energy of a chemically reacting flow for the prediction of autoignition, heat release and pollutant emissions in practical engines. Because of the computational cost involved in such simulations, simplified models for fluid dynamics, spray dynamics and reaction mechanism are highly needed [45]. However, over simplification of the chemical kinetic models significantly reduces the reliability of these models as well as limititing our full understanding of the underlying chemistry driving the various combustion processes. An attempt has been made in this study to bridge the gap by investigating various combustion phenomena by using both detailed and reduced chemical kinetic models of alternative fuels within a less computationally expensive SI engine thermodynamic combustion model.

Chapter 3

Experimental and modelling procedures

3.1 Introduction

The first part of this chapter presents the methods employed for acquiring all experimental data presented in chapter 5 and chapter 6 of this work. Ignition delay times were measured using the Leeds RCM while all engine data including pressure, knock onset and knock intensity data were measured using the LUPOE-2D engine test bed. The procedure employed for developing the gasoline surrogate (TRF) used in both the experimental and modelling work involving the Leeds RCM and LUPOE-2D is also described in the first section of this chapter. Also presented in this chapter are the numerical approaches used for modelling of ignition delay times in the RCM and species concentrations in the JSR as well as the methods (local and global sensitivity/uncertainty analysis) used in evaluating the various chemical kinetic mechanisms studied in this work. The last section of this chapter presents a brief description of the LOGEengine software and its two-zone SI engine thermodynamic model employed for simulating end gas autoignition in this work as well as a detailed description of the approach used for chemical kinetic modelling of autoignition and knock in the engine using the LOGEengine code.

3.2 Experimental work

3.2.1 Measurement of ignition delay times of gasoline, gasoline/*n*-butanol blend and their surrogates in Leeds RCM

3.2.1.1 Gasoline surrogate

As mentioned in section 2.4.4, a toluene reference fuel (TRF) surrogate is currently the most viable trade-off between accurate representation of gasoline and accurate and sufficient quantification of chemistry models. The reasonable extent of agreement between TRF and gasoline, in addition to the availability of well validated chemical mechanisms of its oxidation pathways, makes it currently a more feasible surrogate for

gasoline in terms of ignition delay modelling compared to more complex surrogates [102] and blending effects, and hence it is used in this work.

3.2.1.2 Reference gasoline

The reference gasoline, PR5801 that was modelled in this work satisfies European standards and was supplied by Shell Global Solutions. The ON or AKI of the reference gasoline given by (RON+MON)/2 is 91 while the H/C ratio is 1.934. The components and properties of the reference gasoline are presented in Table 3.1.

3.2.1.3 Gasoline surrogate formulation

Gasoline anti-knock performance under realistic engine conditions depends on the temperature and pressure conditions but historically has been classified as a function of the RON and MON of the fuel, or alternatively of the RON and sensitivity of the fuel. According to the model of Kalghatgi [172], the effective octane number, known as octane index (OI), is given by $\mathrm{OI} = (1 - \mathrm{K})\ \mathrm{RON} + \mathrm{K\ x\ MON} = \mathrm{RON} - \mathrm{K\ x\ S})$ where K is an empirical factor accounting for the influence of the engine operating conditions and $\mathrm{S} = \mathrm{RON} - \mathrm{MON}$ is the sensitivity of the fuel. As mentioned in [102], the Kalghatgi correlation suggests that a correct representation of the Research Octane Number (RON) and a proper estimation of the gasoline sensitivity are enough to formulate the composition of a surrogate that can well reproduce the autoignition properties of gasoline. Other important properties include the hydrogen to carbon atom ratio and the aromatic content of the fuel which affect key combustion properties such as lower heating value, density and boiling point.

The method of Pera and Knop [102, 105] was employed for formulating the TRF surrogate used in this work based on the following constraints:

$$\sum_{i=1}^{n} x_i = 1 \tag{3.1}$$

$$\frac{\sum_{i=1}^{n} x_i H_i}{\sum_{i=1}^{n} x_i C_i} = \frac{H}{C} \tag{3.2}$$

$$\frac{\sum_{i=1}^{n} x_i O_i}{\sum_{i=1}^{n} x_i C_i} = \frac{O}{C} \tag{3.3}$$

$$\sum_{i=1}^{n} ON_i \, x_i = ON \tag{3.4}$$

where *n* represents the number of components in the surrogate, x_i is the mole fraction of component *i* and H, C represent the number of hydrogen and carbon atoms in each of the respective fuel components. The implication of Equation 3.1 is that for an *n*-component surrogate, only *n*-1 properties of the target fuel can be used to constrain the surrogate model. In this study, the RON and the hydrogen to carbon atom ratio of the fuel have been selected and matched and hence other quantities such as the MON and the O/C ratio may not be matched exactly. The components and composition of the surrogate formulated in this work, referred to as TRF95, are presented in Table 3.1 alongside those for the reference gasoline. Table 3.1 shows that the TRF formulation gives quite a close match to the aromatic content of the gasoline with a reasonable representation of the MON and sensitivity based on calculations using a linear blending law and MONs for the surrogate components as listed in Table 3.4. The use of a linear blending rule based on a simple average of compound values weighted by the volume fractions for determination of ON of fuel mixtures, has been shown in various studies [101, 173-176] to be inadequate for formulating surrogate mixtures for gasoline. The linear-by-mole blending rule for determination of ONs of TRF mixtures was demonstrated in [102, 105] to produce results that are as accurate as the complex formulations found in the literature and was therefore employed for formulating the TRF surrogate mixture in this study The composition of the TRF/*n*-butanol blend surrogate (80% TRF / 20% butanol by volume), referred to in this work as TRFB20 is presented in Table 3.2 while the properties of the reference gasoline in comparison with the two surrogates investigated are presented in Table 3.3. Table 3.4 gives the properties of the single compounds used in the computation for each surrogate.

Table 3.1: Comparison of the composition of reference gasoline and formulated three-component surrogate

Gasoline component	**PRF801[a] % volume**	**TRF95 Surrogate Component**	**TRF95 % mole**	**TRF95 % volume**
Paraffins	47.1	Iso-octane	57.50	65.64
		n-heptane	11.25	11.40
Olefins	7.9	-	-	-
Naphthenes	8.2	-	-	-
Aromatics	26.0	Toluene	31.25	22.97
Oxygenated (ethanol)	4.7	-		

[a] Values are taken from analysis supplied by Shell Global Solutions

Table 3.2 - Calculated % composition for blended surrogate.

Gasoline-butanol component	**TRFB20 % mole**	**TRFB20 % volume**
iso-octane	41.21	52.51
n-heptane	8.07	9.12
toluene	22.41	18.38
n-butanol	28.32	20.00

Table 3.3: Properties of reference gasoline and surrogates

PARAMETER	PRF801	TRF95	TRFB20
RON	95	95	95.3 [b]
MON	86.6	89.8 [b]	86.5 [b]
H/C	1.934	1.934	2.032
O/C	0.011	0.000	0.043
S= RON-MON	8.8	5.2	8.8
AKI =(RON+MON)/2	90.8	92.4	90.9
AFR	14.2	14.5	13.6

[b] Calculated based on a linear blending law and component properties list in Table 3.4.

Table 3.4: Compound properties used for computations in this work. Properties are taken from [102, 177]

Compound	RON	MON	Molar weight (g/mol)	Density At 298K (kg/m^3)	Lower heating value (kJ/kg)
n-heptane	0.0	0.0	100.2	684	44566
Isooctane	100.0	100.0	114.2	692	44310
Toluene	120.0	103.5	92.1	867	40589
n-butanol	96[c]	78[c]	74.12	810	33100

[c]Values are taken from [177]

3.2.1.4 Description of the Leeds RCM

The Leeds RCM (Figure 3.1) was used for acquiring all of the experimental data presented in this study. The RCM is a heated single piston machine that is driven by compressed air and stopped by a hydraulic system. The three major sections of the RCM are the driving air reservoir, the hydraulic oil chamber and the combustion cylinder/chamber, which are all linked together by a piston assembly. Compressed air from the air reservoir is used for firing the piston which then compresses the premixed mixture of fuel and oxidant/diluents in the combustion cylinder/chamber to a pre-

calculated temperature and pressure and combustion is made to occur under constant volume. Driving pressures of up to 20 bar can be used on the piston but a realistic value of 13.2 bar was maintained in the experiments in order to avoid the piston from firing due to excessive pressure beyond its holding capacity. Some of the major geometric and operating parameters of the RCM are given in Table 3.5.

The initial pressure in the combustion chamber is measured using a static pressure gauge COMARK C9557 while pressures during compression and after compression are measured using a piezoelectric dynamic pressure transducer Kistler 6045A. The combustion chamber cylinder is heated with four band heaters, each supplied with a power of 375 kW while the cylinder head is heated by 6 cartridge heaters fitted into end plugs positioned around the circumference of the cylinder head.

A 4 mm diameter stainless steel mixture feed pipe used for conveying the mixture from the mixing chamber, where the mixture is prepared, to the combustion chamber, is wrapped round with a heating cable to prevent condensation of the mixture along the pipe. Four Proportional Integral Derivative (PID) temperature control units wired to four K type thermocouples positioned on the mixing chamber, feed pipe work, cylinder and combustion chamber, which display real time temperature in ^{0}C allow one to be able to regulate the initial temperatures needed to obtain a pre-vaporised and homogenous mixture. A data acquisition system owned by National Instrument (NI) was used for collection and recording of the dynamic pressure and piston displacement data while a LabVIEW virtual instrument (VI) was used to display and save the acquired data.

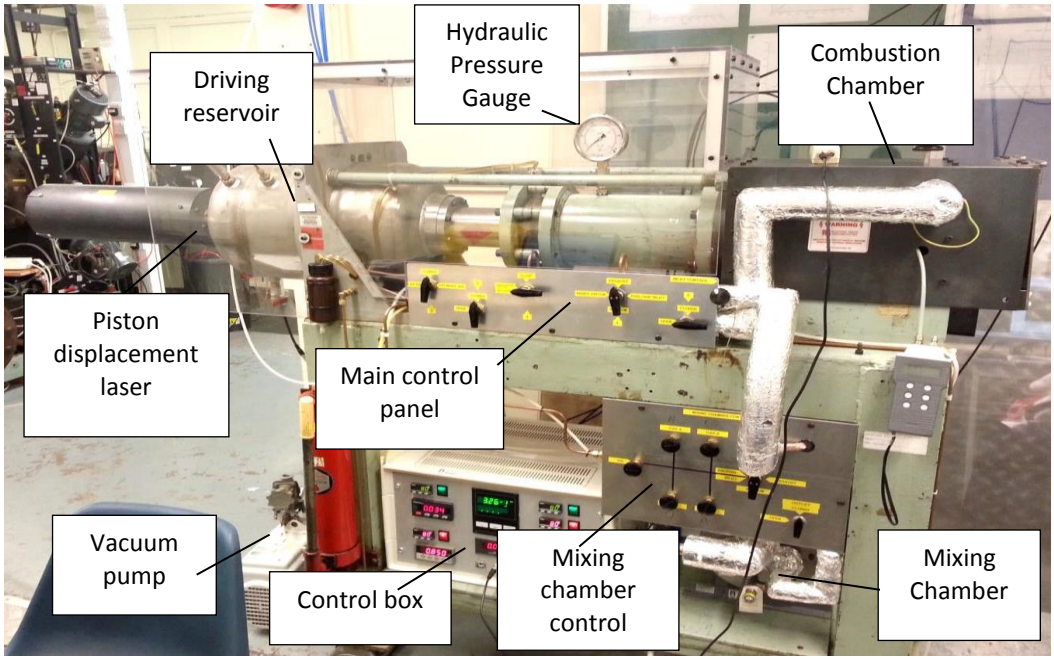

Figure 3.1: University of Leeds Rapid Compression Machine (RCM).

Table 3.5: Key parameters of the Leeds University rapid compression machine

Parameter	Value
Maximum pneumatic driving pressure	20 bar
Maximum hydraulic locking pressure	40 bar
Maximum post compression pressure with good damping	30 bar
Maximum initial combustion chamber temperature	100^{o}C
Maximum initial combustion chamber pressure	1.5 bar
Compression ratio range	8.9-24
Compression time	20 ms
Laser measurement range	30 mm
Cylinder volume	412.3 mm^{3}
Piston radius	23 mm
stroke	230 mm

3.2.1.5 Mixture preparation and test procedure

The fuels used in this study are: reference gasoline PR5801, iso-octane (UN1262), *n*-heptane (UN1206) and toluene (UN1294), all supplied by Shell Global Solutions, and high purity (99.5+ %) *n*-butanol supplied by Fischer Scientific. Oxygen was used as the oxidant while diluents including oxygen, nitrogen, carbon dioxide and argon were used depending on the desired compressed temperature and pressure conditions. Preparation of the fuel-air mixtures was carried out in a separate mixing chamber, initially purged with high pressure air to remove all residuals and heated to the pre-set temperature for 2 hours. The liquid fuels were then administered into the combustion chamber via a syringe while gases were added based on their calculated partial pressures. The prepared mixture was left for over 30 minutes to obtain homogeneous mixtures for the test. The temperature and pressure of the mixture, which determines the volume of liquid fuel injected, is chosen such that the partial pressure of each fuel component is less than the vapour pressure of the fuel to ensure full vaporisation.

Experiments were performed for gasoline, TRF for T = 678 - 858 K, at P = 20 bar and ϕ = 1. Gasoline/*n*-butanol blends and TRF/*n*-butanol blends were then studied at the same conditions by mixing 20% *n*-butanol by volume to the gasoline and the surrogate mixture as defined in Table 3.1. Non-reactive tests were also carried out for all conditions with the oxygen in each mixture replaced by nitrogen. The pressure data from the non-reactive tests were used for generating the volume profiles used in the variable volume ignition delay simulations.

Ignition delay measurements are usually referred to the temperature and pressure conditions at the end of compression. These conditions were pre-calculated using the adiabatic core hypothesis in which compression is taken to be quick enough to assume an adiabatic core gas with heat loss occurring only at the boundary layer. The temperature of the adiabatic core gas at the end of compression T_c, is given by:

$$\frac{T_c}{T_i} = \left(\frac{P_c}{P_i}\right)^{\frac{\gamma-1}{\gamma}} \tag{3.5}$$

where T_i and P_i are the initial temperature and pressure, T_c and P_c are the temperature and pressure conditions at the end of compression, and γ is the temperature-dependent

specific heat ratio. A range of end of compression temperatures were obtained by varying T_i, P_i and γ. The specific heat ratio γ is varied by varying the type of diluents used and/or the respective concentrations of the diluents in the mixture. The thermodynamic data employed in the adiabatic compression calculations were obtained from [178]. The experimental temperature and pressures at TDC are usually slightly lower that the values predicted using the isentropic core relation due to heat loss across the core gas. In order to minimise the error in the use of the adiabatic core relations, the actual temperatures at the end of compression were computed using Equation 3.5 where P_c is now the measured pressure at the end of compression, while T_i, P_i and γ are the same as in Equation (3.5). The ignition delays reported in this work are based on the compressed temperature conditions computed from the measured pressures. The other main factors contributing to the error or uncertainty in the calculated actual compressed temperature are the error in the measured initial pressure and temperature as well as the measured compressed pressure. The computed ignition delay time is defined as the time from the end of compression (at TDC) to the point of maximum rate of pressure rise $\left(max\left({}^{dP}/_{dt}\right)\right)$. The time at the end of compression is determined experimentally from the point where the piston displacement becomes zero. The ignition delay times reported in this work represent an average of 3-5 runs made for each test condition with errors between runs <10% based on one standard deviation.

3.2.2 Measurement of the autoignition and knock properties of gasoline, gasoline/*n*-butanol blend and their surrogates in the Leeds University Ported Optical Engine (LUPOE)

3.2.2.1 Introduction to LUPOE-2D research engine

The Leeds University Ported Optical Engine, Version 2 and Disc-shape Combustion Chamber (LUPOE-2D boosted) was used for acquiring all engine data presented in this work. The name 'LUPOE-2D boosted' was given based on recent modification made by Ling [40] on 'LUPOE-2D ' to transform the engine from a naturally aspirated engine to one that can be used for investigating combustion in the high pressure regime. The modifications which are detailed in [40] include; a decrease of the number of rings of circular exhaust holes on liner from four to two in order to increase the effective

compression ratio and the installation of an independently-controlled solenoid valves on the exhaust line to increase the charging time. The engine was originally, a commercial single cylinder Lister Petter PH1 diesel engine and was modified considerably in the Thermofluid workshop in the School of Mechanical Engineering in order to adapt it to the requirement of a research setup. The engine cylinder head, liner and piston went through different phases of modification to bring it to its present state. The original cylinder head was removed and replaced with a disc-shaped head to help in achieving a uniform in-cylinder flow field in the combustion chamber and to also allow for variation of the compression ratios. Major modifications were made to the breathing system (intake and exhaust system) in order to reduce large-scale flows and its attendant effects to the minimum. The overhead valve system were replaced with two diametrically opposed ports to allow for full-bore optical access which is made possible via one top and two opposite side windows for flame structure analysis and visualisation of gas molecules. The dimension of the ports and angle of inclination (20 ^{o}C below the horizontal axis) is chosen so as to minimise the influence of turbulence (swirl and tumble motion) in the cylinder that is common with the valve arrangement and to also allow for the attainment of a more uniform thermodynamic state at the commencement of compression. The exhaust gases are removed from the cylinder through two rings of circular exhaust holes or perforations drilled around the liner (see Figure 3.3). In addition, the engine is operated on a skip-firing mode in order to enhance the scavenging process for adequate removal of residual gases from the cylinder. In the skip firing mode, the engine is programmed to run on multiple motoring cycles in between two firing cycles. This helps to ensure that most of the burnt gases are properly expelled and mixture composition at the beginning of each firing cycle is relatively homogenous and similar to that at the intake ducts. The breathing system is controlled basically by the piston motion/location and operates in such a way that the exhaust ports are cut off by the piston at the time the intake ports are still open. LUPOE-2D can be operated either with a metallic cylinder head or a full-bore optical head (fitted quartz window) for high speed filming but the metallic head was used for all of the experiments in this study since the focus was on investigating engine knock which can potentially damage the optical head. A spark plug located in the center of the cylinder head is employed for igniting the fuel mixture. The main design specifications of LUPOE-2D are given in Table 3.6 while a 3-D view of the engine is shown in Figure 3.2.

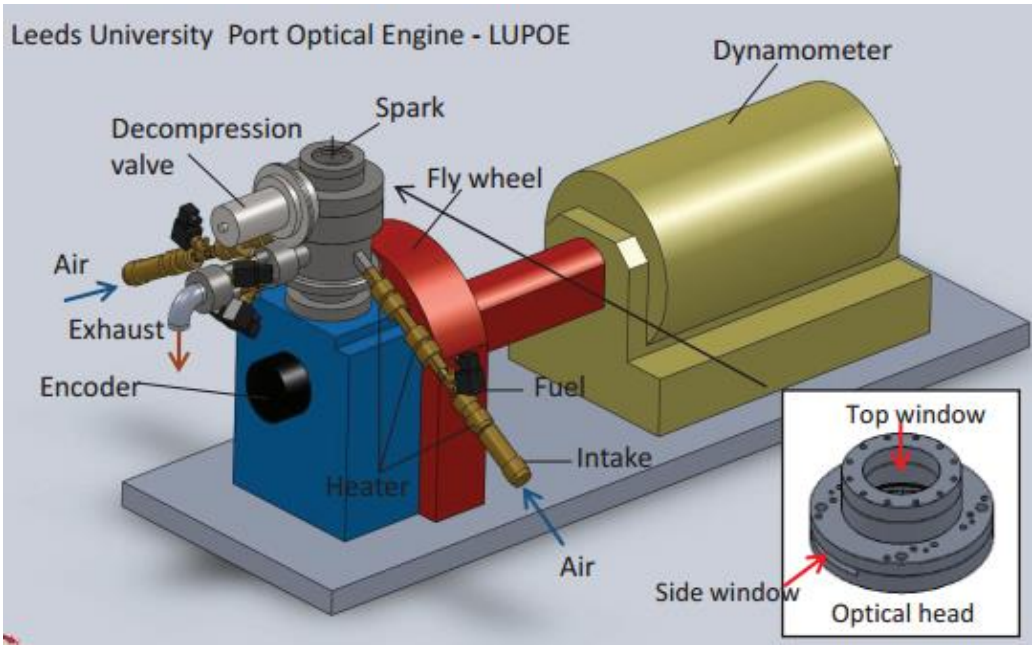

Figure 3.2: CAD drawing of LUPOE-2D with the details of optical head shown in the insert [40].

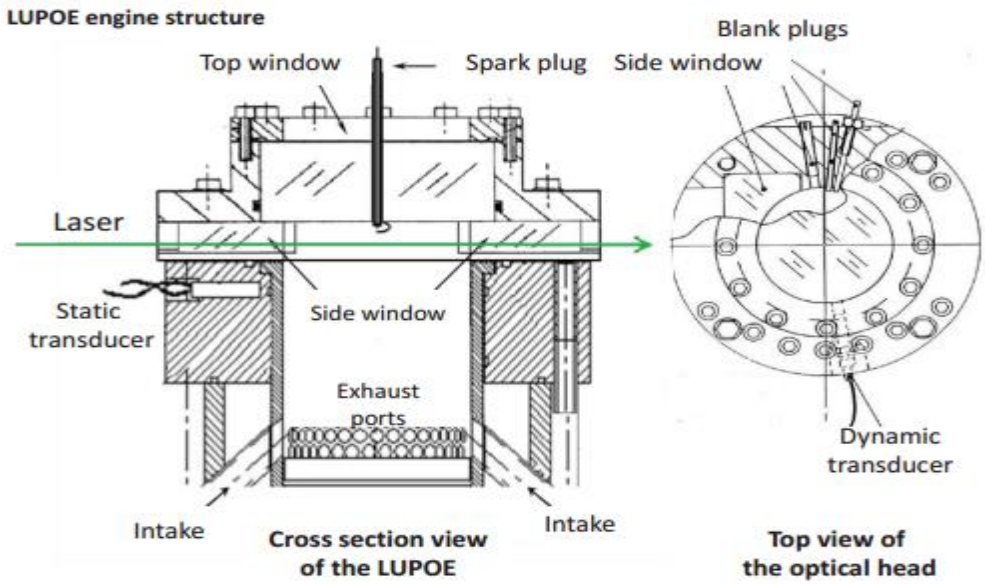

Figure 3.3: A cross sectional view of LUPOE-2D and a top view of the optical head [40].

Table 3.6: LUPOE-2D design specifications. Adapted from [40]

Bore (mm)	80
Stroke (mm)	110
Clearance height (mm)	8
Connecting rod length (mm)	232
Compression ratio	11.5
Intake ports opening/closure (^{0} CA aTDC)	108
Exhaust ports opening/closure (^{0} CA aTDC)	121

3.2.2.2 Fuel and air supply

Combustion air, regulated to about 4 bar, is supplied to the intake ports via a high pressure compressed air line within the laboratory. The fuel was supplied from a two-litre tank and mixed together with the air through a bespoke fuel injector located at the middle of a venturi meter which is positioned about 350 mm upstream of each intake port. The required mass flow rates of both fuel and air were set at the beginning of the experiment and were maintained constant with the aid of mass flow controllers to ensure a uniform composition at the beginning of each cycle. The air mass flow rate was controlled using two thermal mass flow meters designed to adapt to changes in mass flow rate due to pressure fluctuations while the mass flow rate of fuel was controlled with the aid of an accurate Series M53 Bronkhorst Coriolis mass flow controller. The fuel was pumped from the fuel tank across the Bronkhorst digital mass flow controller with the aid of an electrical pump after first of all going through a filter and a pressure regulator while a Bosch regulator was employed to maintain the fuel pressure at 0.3 MPa. Ahead of the pressure regulator, the fuel line is split into two lines which feed into the two separate intake ports. Before using a different fuel mixture for the experiment, the mass flow controllers and fuel lines were thoroughly purged with pressurised air for about half an hour to remove every trace of the previous fuel in order to avoid cross contamination of fuel. After that, the new fuel is allowed to flow from the fuel tank across the fuel lines for about a minute to remove any leftover of fuel residues. A series of five 175 W band heaters and one 200 W band heater positioned along the length of the intake were employed to raise and maintain the temperature of the intake air. The heat supplied to the air enable the air-fuel mixture to completely vaporise before being

supplied to the engine. Heating of the cylinder barrel and head was accomplished with the help of 50 W cartridge heaters equally spaced around the barrel. The temperatures were monitored and controlled by thermocouples positioned in the cylinder barrel just upstream of the intake port with readings processed by a Digitron 4801 control unit. In this work, all experiments were performed with the temperature of the control unit set to 50^0 C. Figure 3.4 shows a schematic diagram of the air/fuel flow system of LUPOE-2D.

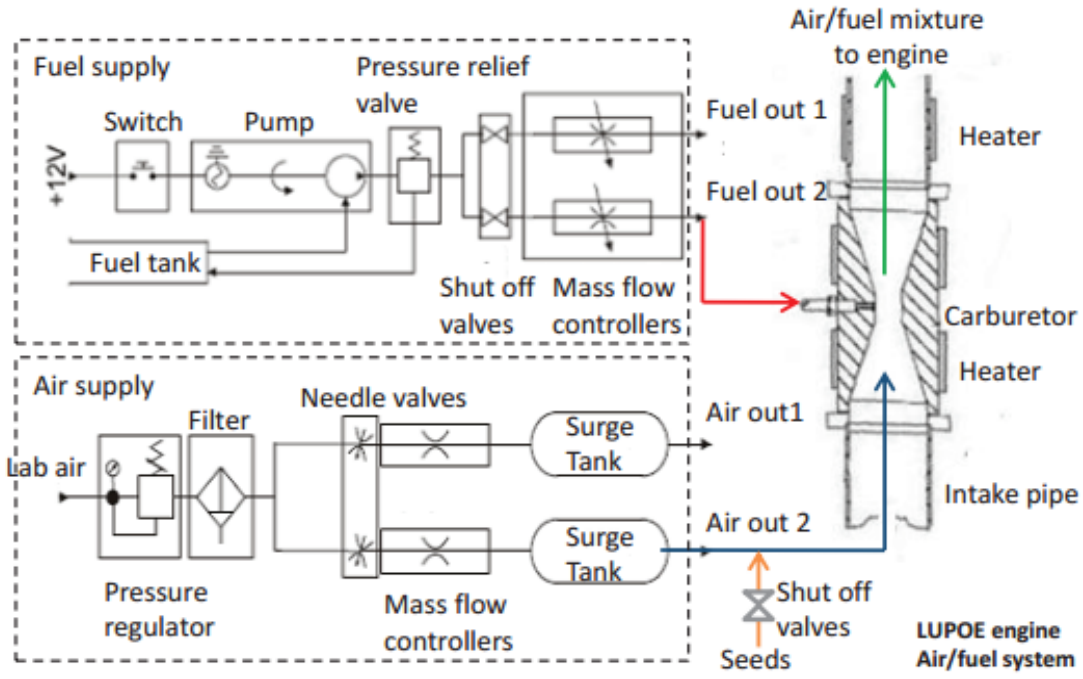

Figure 3.4: Schematic diagram of the air/fuel flow system of LUPOE-2D [40].

3.2.2.3 Engine control and data acquisition system

The control system (Figure 3.5) employed in LUPOE as at the time of this study, is a bespoke control system designed and implemented by Ling [40]. The control system is comprised of a micro controller Dspic6014A which represents the core of the control system and a microchip MPLAB ICD 3 in-circuit debugger system used for debugging and programming the microcontroller. The coding and debugging of the microcontroller is made possible with the help of the MPLAB integrated development environment (IDE) software tools. The microcontroller operates in synchronisation with the TDC signal and shaft encoder clock signals to send out electrical signals required to trigger ignition, valve operation timing, laser and data acquisition start timing. The

microcontroller also controls how long each of the above devices run and the input parameters for the devices can also be changed easily by assigning new values within the microcontroller.

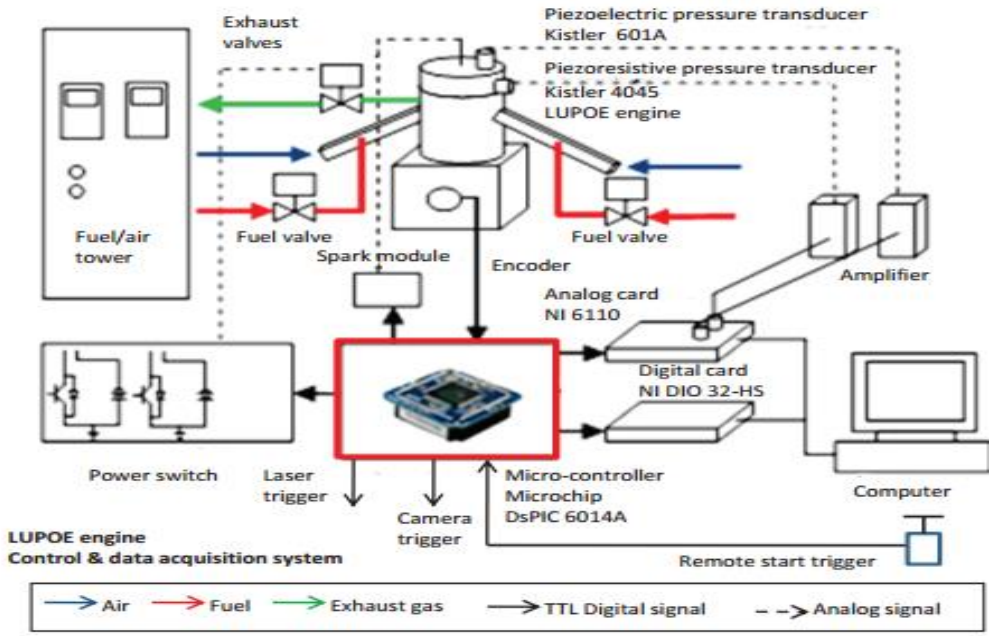

Figure 3.5: Schematic diagram of the control and data acquisition system of LUPOE-2D [40].

The in-cylinder pressure was measured using two types of pressure transducers. One is a Kistler piezoelectric pressure transducer Type 601A which is a dynamic pressure transducer used for measuring rapidly changing pressure in the engine cylinder due to its high response rate. The dynamic pressure transducer which measures the in-cylinder gauge pressure, was mounted flush to the cylinder wall with only the diaphragm exposed to the chamber surface. A Kistler charge amplifier Type 5007 set to 10 mechanical units per volt (0 - 10 V range) was employed to amplify the output charge of the dynamic pressure transducer. A reference pressure was provided for the dynamic pressure through a Kistler absolute pressure transducer (Type 4045A20) which was located at the lower end of the piston barrel where it measured the pressure during the initial phase of compression. The location of the absolute pressure transducer (60 bTDC where the pressure is normally between 0.25 - 0.3 MPa.) is chosen such that the absolute pressure transducer is protected from the high temperatures and pressures experienced during the later part of the compression phase and also the combustion phase. The signal from the

absolute pressure transducer is amplified using a Kistler Series 4601A piezoresistive amplifier set to 0.5 mechanical units per volt (0 - 10 V range). In-cylinder pressure data were sampled at 0.2 crank angle resolution (interval) based on a total of 1800 output pulses produced by the shaft encoder per revolution.

The pressure measured by the dynamic transducer P_{dyn} is gauge while that of the absolute pressure transducer P_{abs} is absolute. The gauge pressure read by the dynamic pressure transducer was converted to an absolute pressure which is equivalent to the cylinder pressure P_{cyl} (see Fig 3.6) using the following relation,

$$P_{cyl} = P_{dyn} + (P_{abs}(\theta_{EPC}) - (P_{dyn}(\theta_{EPC})) \quad (3.6)$$

where θ_{EPC} is the crank angle at the point of exhaust port closure which is given by the reference crank angle of 60 ^{0} bTDC.

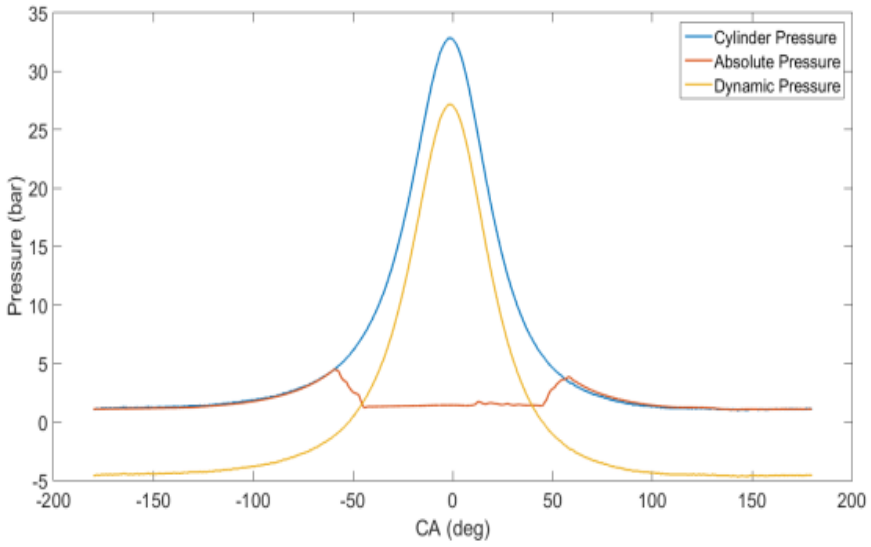

Figure 3.6: Diagram showing dynamic pressure re-alignment using the reference pressure.

3.2.2.4 Dynamic pressure and static pressure calibration

Before the experiments were carried out, the absolute and dynamic pressure transducers were calibrated using a Budenberg dead weight tester as they are prone to decrease in efficiency due to continual exposure to high temperatures and pressures. In calibrating

the 4045A20 absolute pressure transducer, dead weights of different capacity (sizes) were loaded on the machine and the resulting static fluid pressure was applied on the pressure transducer. A simple LabVIEW VI was developed to record the voltage produced by the transducer in response to each applied load to check for linearity and hysteresis. The same experimental setup was used to calibrate the dynamic pressure transducer but in this case, the applied load was changed quickly and the pressure transducer response to the release in applied load was recorded using a LabVIEW program. Figure 3.7 and Figure 3.8 show the calibration curve for the absolute and dynamic pressure transducers respectively.

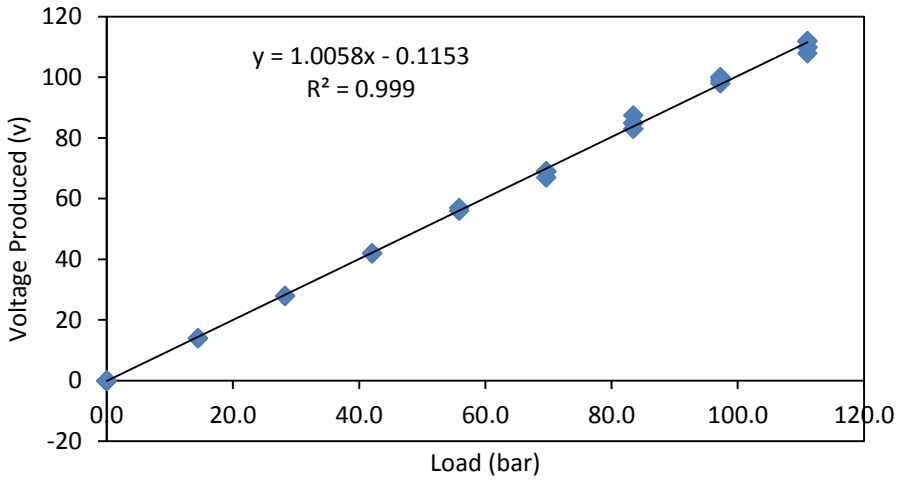

Figure 3.7: Calibration curve of absolute pressure transducer.

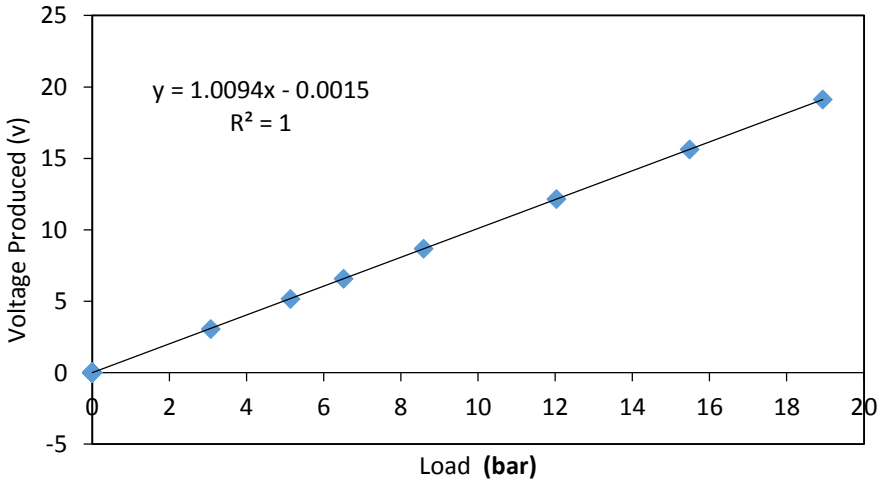

Figure 3.8: Calibration curve of dynamic pressure transducer.

All experimental data were recorded using a data acquisition system comprising of a personal computer (PC), a LabVIEW programme and two National Instrument Peripheral Component Interconnect (PCI) cards. Dynamic and absolute pressure analogue signals were connected to two different channels of National Instruments 6110 analogue PCI card (accurate to 12 bits) to convert the signals to digital forms while digital signals (TDC, BDC etc.) were recorded by a National Instruments DIO-32HS digital PCI card. Both the analogue and digital PCI cards were linked together through a Real-Time System Integration (RTSI) cable which enabled the internal sample clocks of both the analogue and digital systems to be synchronised in a master/slave type orientation, making it possible to record both signals at the same time. Visualisation of the synchronous signal recording was made possible through a LabVIEW operation panel. All signals were sampled at 200 kHz (22.2 samples per CA at 750 RPM) and sampling of both digital and analogue signals commenced at BDC pulse to ensure that every recorded data begins with a complete firing cycle. The engine was operated on a Skip firing ratio of 20 during the experimental test in order to prevent the residual gases of the firing cycle from diluting the fresh charge. In the skip firing mode, the engine is allowed to go through several motoring cycles after each firing cycle and this comes with the additional cost of large storage memory required for recording of unimportant motoring cycles. This challenge is avoided through a multi-trigger data recording approach in which only two motoring cycles before a firing cycle and one motoring cycle after the firing cycle are recorded (Figure 3.9).

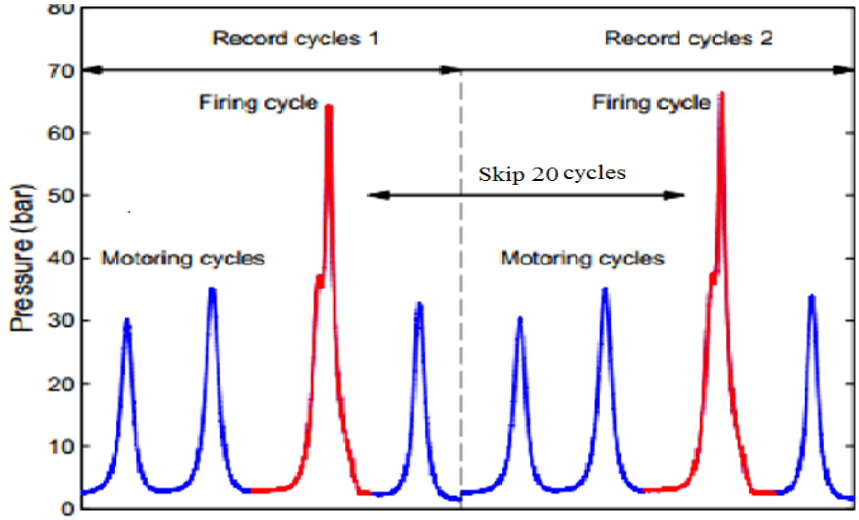

Figure 3.9: Schematic diagram of engine skip firing and multi-trigger sequence.

3.2.2.5 Fuels and test procedure

A total of four fuel mixtures, tested previously in the Leeds RCM were also tested in the experiments carried out using LUPOE-2D. These included a reference commercial gasoline of RON 95, toluene reference fuel (TRF), a blend of 20 % by volume of *n*-butanol with 80 % by volume of gasoline and a blend of 20 % by volume of *n*-butanol with 80 % by volume of TRF. Similar set of fuels were tested across both the RCM and engine in order to allow for a reasonable comparison of the behaviour of the fuels across both set ups in line with the objective of the study. The components and composition of the reference gasoline which was supplied by SHELL, is given in Table 3.1. The TRF mixture was formulated to represent complex gasoline for use in the context of the chemical kinetic modelling of the autoignition behavior of gasoline and its blend with *n*-butanol under practical engine conditions. The methodology used in formulating the TRF surrogate is described in detail in section 3.2.1.3 while the composition of the formulated TRF surrogate is presented in Table 3.1. Table 3.2 gives the volumetric composition of the formulated *n*-butanol/TRF blend. The various properties of the reference gasoline and the formulated surrogates such as the RON, MON, Air-fuel ratios etc., are given in Table 3.3.

Throughout the experiments, LUPOE-2D was operated on a speed of 750 RPM at an initial charge temperature of 323 K, boosted pressure of 1.6 bar and equivalence ratio of 1. Table 3.7 shows the range of operating parameters employed in the experimental test carried out in LOPOE-2D. A combination of a skip firing ratio of 20 and fueling cycles of 14 were found to produce autoignition free operation during the compression phase while also allowing cylinder volume to be properly purged of exhaust gas residues from the firing cycle. The spark timing was gradually advanced by 1^{o} beginning from 2^{o} bTDC until the knock limited spark advance (knock boundary) was identified. The knock boundary is equivalent to the spark timing in which knock occurred in over 90 % of the total firing cycles [40]. The spark timing was further advanced above the knock boundary until the maximum peak pressure recorded in the cylinder was within the maximum allowable pressure limit of 120 bar which the cylinder head is able to withstand. The spark timing was advanced to a limit of 10 CA bTDC for gasoline, gasoline/*n*-butanol blend and TRF/*n*-butanol blend but up to a limit of 8 CA bTDC for TRF since the peak in-cylinder pressures reached the maximum allowable value at these

conditions. At a spark advance of 8 CA bTDC, a large proportion of the cycles were knocking across the four sets of fuels.

Across the range of spark timing investigated for each fuel mixtures and set of tests, knocking cycles were identified by listening to the audible pinging sound caused by impact of the pressure waves on the piston (audible detection by the ear alone) and from the recorded pressure traces. For each condition of spark timing tested, a maximum of 13 firing cycles were recorded from every test. Overall, a total of 13 to 39 firing cycles were captured for each set of condition and for firing cycles in which knock occurred, three knocking regimes namely mild knock, average knock and super knock were identified.

Table 3.7: Experimental test conditions

Parameter	Value
Equivalence ratio	1
Intake temperature	323 K
Intake pressure	1.6 bar
EGR	0 %
Mass flow rate of air	10.17 g/sec
Engine speed	750 RPM

3.2.2.6 In-cylinder pressure data processing and analysis

The various output signals from the engine including the analogue pressure signals of the dynamic and absolute pressure transducers as well digital signals of TDC, BDC, shaft encoder and ignition were all recorded originally with respect to time. Re-sampling of the original data with respect to crank angle was accomplished with the help of MATLAB codes originally developed in [40] and slightly modified in this study. Additional variables required to run the code include sampling rate, skip-firing ratio, reference crank angle and scaling factors of pressure transducers (bar/volt) while geometric parameters such as engine bore, stroke and clearance height were held fixed in the code. The raw pressure data was cut into individual cycles using the BDC signal location as the reference point allowing both the firing cycles and motoring cycles to be

identified. The effect of noise in the analogue pressure signals of each firing cycle was eliminated using a low pass 2nd order Butterworth filter with a cut-off frequency of 2 KHz while the built in-MATLAB function 'filfilt' was subsequently applied to ensure a zero phase shift. The peak pressure of each firing cycle is given by the maximum value of the pressure cycle filtered by a low-pass filter. When the low pass filter was not applied, it was therefore possible to identify the condition under which knock was present.

3.2.2.7 Determination of autoignition and knock in LUPOE-2D

The knock properties of a fuel mixture undergoing combustion in an engine can be characterised using two key properties namely, the knock onset and knock intensity [31]. Two different methods of determining the knock onset location and knock intensity from measured in-cylinder data outlined in [40] and [179] were explored in this study. In the first method, the knock-related pressure oscillations are decoupled from the main in-cylinder pressure by applying a wide bandwidth FFT filter of 2.5-12 kHz to the measured in-cylinder pressure data of each firing cycle. This method eliminates the noise signals in the low and extremely high frequency range, leaving only the knock pressure oscillations. In the method of Worret outlined in [40], the knock onset is determined by simply scanning across the filtered band pass pressure oscillations until a specific threshold value is exceeded. In general, the selected threshold should be below the maximum amplitude of the band pass filtered knock oscillation but above the noise signal caused by engine vibrations. The knock intensity (degree of knock) in this case is given by the maximum amplitude of pressure oscillations (MAPO) (i.e. the band bass filtered pressure oscillations).

In the method of Liu [179] illustrated in Figure 3.11, the knock onset position is given by the first prominent point of inflection on the measured pressure trace which leads further into a series of pressure fluctuations. The point of inflection is determined by computing the rate of change of the pressure gradient with crank angle travelled over any three points on the pressure data using the equation,

$$KN = \frac{(P_n - P_{n-1})/\Delta\theta - (P_{n+1} - P_n)/\Delta\theta}{\Delta\theta} \quad (3.7)$$

Similar to the method of Worret, the knock onset was finally identified by scanning through the values of KN until a preset threshold was exceeded. The knock intensity in this method is given by the maximum amplitude of the pressure rise rate.

For both methods, selecting a single threshold value for all engine conditions could potentially lead to large errors in identifying the correct knock onset location due to the inherent problem of cyclic variability in engine pressure data. In using the method of Worret, after an initial visual inspection of the knock pressure oscillations for all knocking conditions, a varying threshold value of 0.2 - 0.5 bar of the amplitude of knock oscillations was chosen in order to identify the knock onset location. In the case of Liu's method, a threshold value of 20 – 30 bar/CA^2 was chosen for the same purpose. In both methods, the data (pressure oscillations or KN) before top dead center (TDC) were cut off in the analysis in order to eliminate the error due to the influence of spark.

Figure 3.10 illustrates the method of Worret for two typical band pass filtered pressures plotted on top of their respective knocking pressure cycles that were measured in LUPOE-2D at a spark timing of 8 CA bTDC. The knock onsets estimated for each cycle based on the method of Worret are given by the crank angle location of the vertical line on the horizontal axis. Figure 3.11 illustrates the Liu's method for the same knocking cycles shown in Figure 3.10 with the computed second and first derivatives of pressure superimposed upon the unfiltered in-cylinder pressure. Here, the knock onsets are also given by the location of the vertical line shown on the x axis. As shown in Figure 3.10 and 3.11, for all cases considered, Liu's method gave a better estimation of the knock onsets compared to the method of Worret and was therefore adopted in this study.

According to Ling [40] knock happens later than the point of the onset of autoignition. In his work, combustion imaging from a camera was used to distinguish between both by superimposing and comparing both the autoignition onset detected by imaging with the knocking pressure trace recorded at similar conditions. Ling also noted that the crank angle difference between the two parameters is about 0.2 CA which is relatively negligible. Since the study of combustion using imaging is beyond the scope of this work and since autoignition onset is the key parameter been predicted in the knock modelling programme, the autoignition onset calculated from the experimental data was considered to be appropriate for comparison with the predicted data.

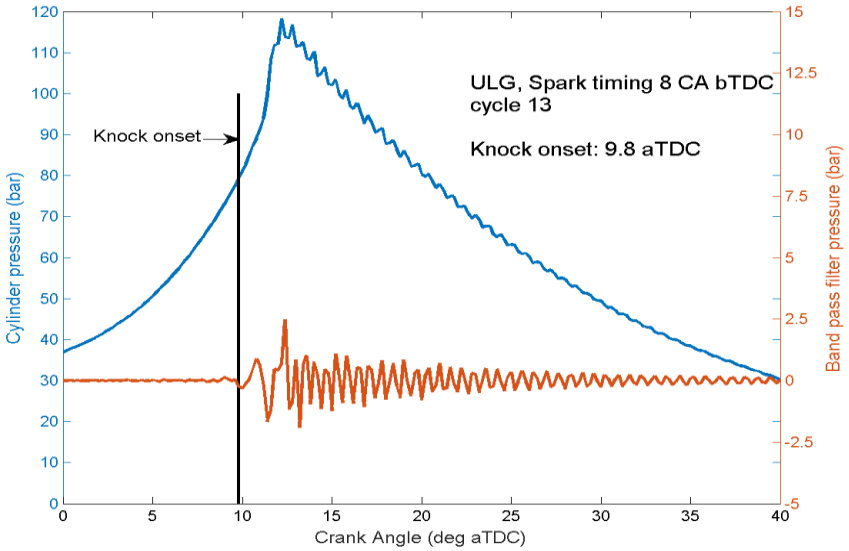

(a)

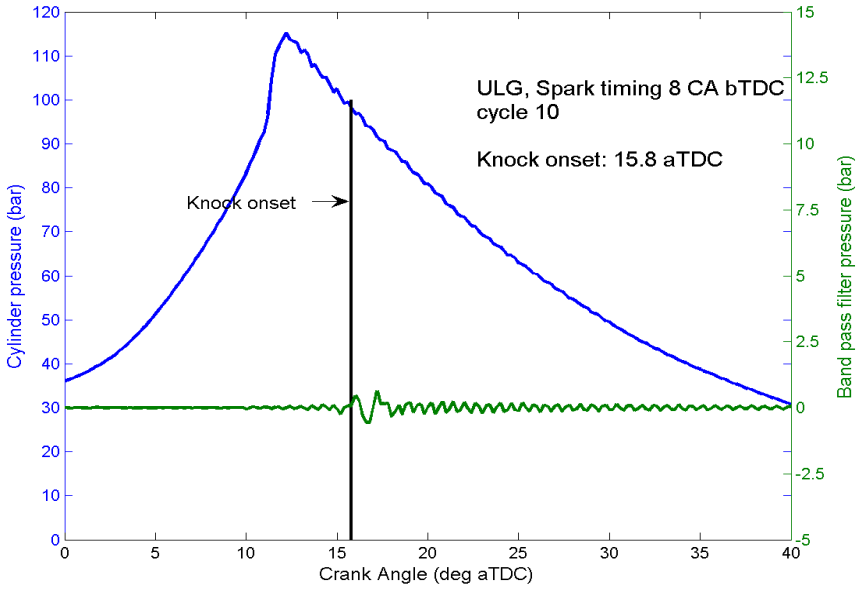

(b)

Figure 3.10: Typical band pass filtered pressure for knock onset estimation using the method of Worret superimposed upon the respective knocking pressure cycles of ULG measured at a spark timing of 8 CA bTDC (a) cycle number 13 (b) cycle number 10.

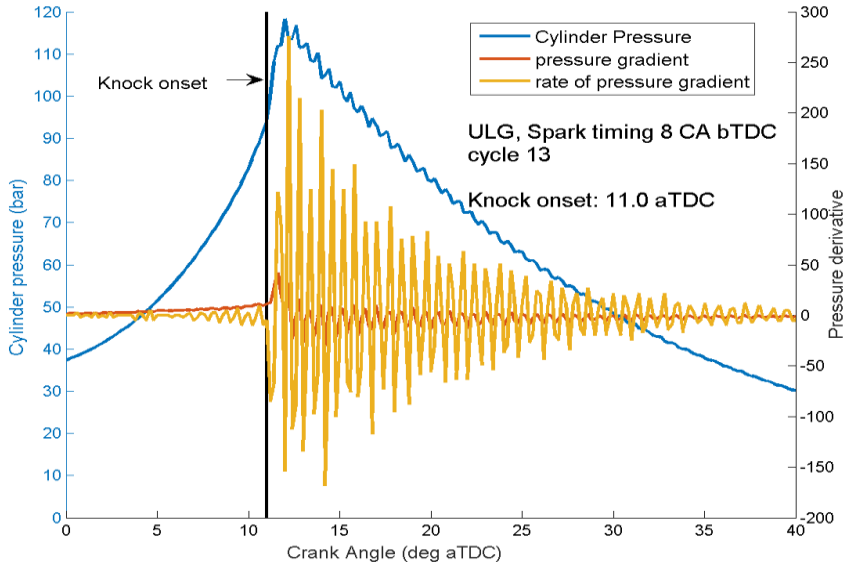

(a)

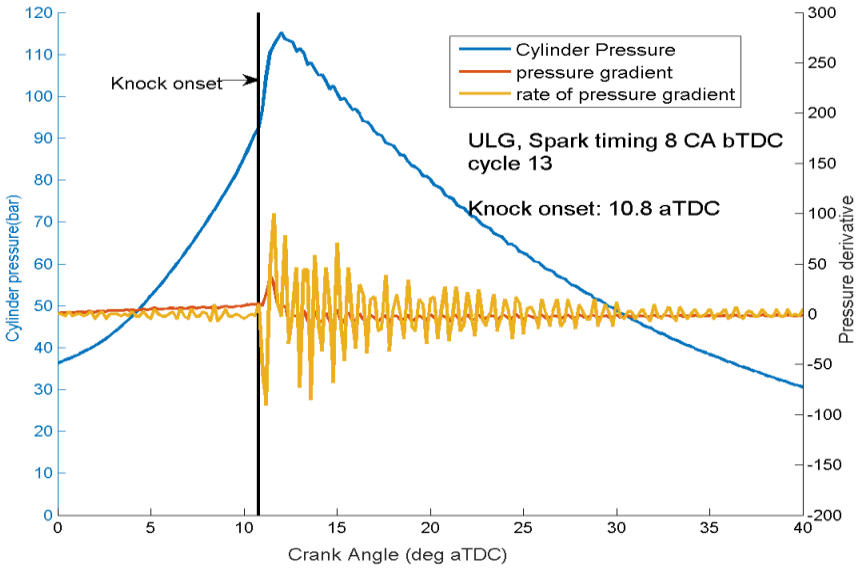

(b)

Figure 3.11: Typical second and first derivative of pressure computed using the method outlined in Liu superimposed upon the respective knocking cycles of ULG at a spark timing of 8 CA bTDC (a) cycle number 13 (b) cycle number 10.

3.3 Modelling and simulations

3.3.1 Chemical kinetic modelling of DME autoignition in an RCM

3.3.1.1 RCM modelling

The CANTERA software libraries (version 2.0.2)[71] were used within the Python environment to model the DME fueled RCM in line with the experimental conditions and data given in Mittal et al. [136]. The RCM modelled in this present study, has been described in detail by the author in a previous publication [152]. In the experimental setup modelled, DME/O_2/N_2 mixtures were investigated over the temperature range of 615-735 K, a pressure range of 10 - 20 bar, and an equivalence ratio range of 0.43 - 1.5. Most studies assume that the effect of the compression process on the predicted ignition delays is negligible. However, based on Computational Singular Perturbation (CSP) analysis carried out by Mittal and co-workers [136], it was concluded that the compression stroke could greatly influence post compression events such as ignition delay times due to production of small radical pools during the compression stroke. Therefore the modelling approach adopted is in line with that of Mittal, in which both compression and post compression events are accounted for. The compression stroke is modelled by varying the volume of the simulated RCM reactor chamber with time. The volume history during compression is computed from the geometric parameters (stroke, bore, acceleration time, deceleration time, total compression time etc.) of the RCM. The total time taken to complete the compression stroke is divided into three time stages given by:

$$t_{comp} = t_{accel} + t_{const} + t_{decel} \tag{3.8}$$

where t_{comp} the total time for compression is, t_{accel} is the uniform acceleration time, t_{const} is the constant velocity time and t_{decel} is the uniform deceleration time.

In this study, the effect of the compression stroke was also investigated by modelling only the post compression events and comparing predicted results with results predicted from the set up in which the full RCM event (entire compression stroke and post compression process) is modelled. In the setup in which only the post compression process is modelled, the initial pressure and temperature was taken to be the

thermodynamic state at TDC (i.e. P_c and T_c) while the initial mixture composition is taken to be the initial experimental reaction mixture. The effect of heat loss is however accounted for in both models. Heat loss effects during and after compression, are accounted for by specifying an effective volume as a function of time. Details of the procedure can be found in [152]. In summary, the model which defines the volume of the RCM reactor chamber with heat loss effect taken into account is given by:

$$\text{while } t \leq t_{comp}: V(t) = V_g(t) + V_{add} \tag{3.9}$$

$$\text{while } t > t_{comp}: V(t) = V(t_{comp}) * V_p(t) \tag{3.10}$$

where $V(t)$ is the time-dependent effective volume of the reactor chamber, $V_g(t)$ is the geometric volume of the reactor chamber, $V(t_{comp})$ is the volume at the end of compression and $V_p(t)$ is the volume expansion computed from the polynomial fit used in matching the volume expansion trace $V_{exp}(t)$ determined from the pressure trace of the non-reactive experiment. V_{add} is an empirical volume parameter that is added to the actual computed geometric volume of the reactor chamber $V_g(t)$ at any time in order to match the simulated pressure trace during the compression event with the experimental data. Based on an assumption of adiabatic expansion, $V_{exp}(t)$ is given by:

$$V_{exp}(t) = \left(\frac{P(0)}{P(t)}\right)^{1/\gamma} \qquad t \geq 0 \tag{3.11}$$

where γ is the specific heat ratio, P (0) is the initial pressure and P (t) is the measured non-reactive pressure.

The geometric parameters of the RCM and the empirical effective volume parameters (or heat loss parameters) used in modelling these specific experiments are available from the University of Connecticut Combustion Diagnostics Laboratory experimental database [180]. Appropriate tolerance criteria were chosen to ensure sufficiently stable and well converged solutions across the three selected kinetic schemes. Calculations of rate coefficients for pressure dependent reactions were performed in Cantera using both the Troe formulation given in equation 2.61 and the PLOG approach. The Troe formulation requires that the first three parameters (A, T_3, T_1) be specified in the kinetic scheme with the optional parameter T_2 defaulting to zero when it is not specified. In the

PLOG approach, calculations were performed in CANTERA by simply logarithmically interpolating between Arrhenius rate expressions specified at different pressures in the kinetic scheme [71].

3.3.1.2 Definition of ignition delay

In the RCM model, the computed ignition delay time is defined as the time from the end of compression (at TDC) to the point of maximum rate of pressure rise $\left(max\left({}^{dP}/_{dt}\right)\right)$

3.3.1.3 Chemical kinetic schemes

Three recent chemical kinetic mechanisms describing the low temperature oxidation of DME were adopted for the DME study and compared. The first scheme is comprised of 299 reversible reactions and 55 species and is known in this study as the "Liu2013" mechanism. The scheme was originally developed in [124] with several updates implemented as outlined in [126]. The major updates include, the replacement of the hydrogen subset with the model of Burke et al. [181], the revision of the rate parameters for a number of the pressure-dependent DME decomposition reactions [126], and updating of the thermodynamic parameters based on the thermodynamic database of Goos et al. [182]. The second chemical kinetic scheme is comprised of 251 reversible reactions and 49 species and is referred to in this study as the "LLNL" mechanism. The mechanism which was obtained from the Lawrence Livermore National Laboratory (LLNL) is fully described in Zheng et al. [123]. The third mechanism, known in the study as "Aramco' mechanism is a recently published detailed hierarchical scheme describing the oxidation of small hydrocarbons and oxygenated fuels. The Aramco mechanism was developed at NUI Galway [125] and is comprised of 766 reversible reactions and 125 species. The Aramco mechanism having been developed particularly for use in a general sense was validated across a large spectrum of initial conditions and experimental configurations such as shock tubes, flow reactors, jet-stirred reactors and flame setups. The three schemes which were obtained in CHEMKIN input format were first of all converted to CANTERA input file format (.cti) using a CANTERA subroutine before they were implemented in CANTERA simulations.

3.3.1.4 Local sensitivity analysis

Since in reality it is the uncertainties in only a few of the rate parameters in the mechanism that determine (influence) the overall predicted output uncertainties and the simulations to a very large extent are insensitive to the other rate parameters, a huge amount of computational time can be saved if these few reactions are identified for inclusion in global sensitivity analysis, whilst parameters of low sensitivity are retained at their nominal values. This allows for a smaller sample size to be used within the context of global sensitivity analysis without compromising the sparsity of the input space. Therefore a screening approach based on the Brute-force local sensitivity method was performed for a range of conditions (P, T, ϕ) across the conditions studied in Mittal et al. [136] to identify the key reactions that influence the predicted ignition delays at compressed (TDC) conditions of P = 10 - 20 bar, T = 615 K - 725 K and ϕ = 0.43 - 1.5.

The sensitivity analysis setup used for the analysis in this work is a specific-purpose Python script originally developed in [164], which was then modified in this work and coupled to our in-house CANTERA RCM code. In the Brute-force method employed, each rate constant (pre-exponential factor) in the mechanism was multiplied by a factor of 1.25 (representing 25 % increase from the nominal value) in turn and coupled with the RCM simulations for computation of the corresponding ignition delay (i.e. τ_{after}). The ignition delay computed before any of the reaction rates is perturbed is represented by τ_{before}. The sensitivity coefficient by definition is given by $S_i = \frac{\partial \tau}{\partial k}$, thus the ignition delay sensitivity to each reaction in the kinetic model was calculated as,

$$S_i = \frac{\tau_{before} - \tau_{after}}{\tau_{before}}. \quad (3.12)$$

In each of the conditions considered, the set of reactions that were deemed to exhibit high enough sensitivity to be included in the subsequent global uncertainty and sensitivity analysis were screened within the context of local sensitivity analysis based on a threshold criteria of $abs\,(S_i) > 2$ %. A total of 36, 25 and 35 reactions were screened out by the local method for the Liu2013, LLNL and Aramco mechanisms respectively and carried forward for further analysis by global uncertainty and sensitivity method. The results of the local sensitivity analysis showing the set of

reactions that were screened out and the normalised sensitivity indices are presented in the result section (section 4.2.3).

3.3.1.5 Uncertainty quantification and global sensitivity analysis

One of the objectives of the study is to assess the predictive accuracy and robustness of the three DME schemes adopted in the study by estimating and plotting the error bars predicted by each of the schemes while accounting for the uncertainties in the input parameters of the scheme. This is quite useful as it could provide information as to how reliable the model is and at the same time be a pointer to an existing structural defect in the model, especially in the instances when there is considerable disparity between experimental data and model prediction. Such a structural defect may arise in the scheme due to the absence of model sub components such as specific reaction steps, physical processes etc. Moreover, the estimated error bars could give insight into the range of conditions under which the model would produce the highest level of predicted uncertainties. An instance of the application of uncertainty quantification method can be found in the work of Hebrard et al [183] where higher levels of uncertainties of the predicted target were recorded in the NTC region for an *n*-butane oxidation model in comparison to the low and high temperature regions.

In the global uncertainty and sensitivity approach employed in this study, the uncertainties in the selected rate parameters were propagated across the model in order to provide error bars based on the predicted ignition delay distribution. In accomplishing this task, an open source CANTERA toolbox was coupled to a specific-purpose Python code for execution of automatic global sampling-based sensitivity simulations from which a set of output is generated for each individual sample of the input space. Furthermore, HDMR analysis is then further performed in order to determine and rank the contribution of each parameter uncertainty to the overall predicted output uncertainty. This method allows one to be able to investigate the impact of model input parameters (e.g. reaction rates) across their entire uncertainty range and also to account for the effect of parameter interactions. While only the forward rate input parameters were perturbed in the global uncertainty and sensitivity computations for the Liu2013 and Aramco mechanisms, both the forward and reversed were modified separately in the case of the LLNL scheme in order to explore the possibility of the influence of

thermochemistry based on the analysis of the relative importance of the forward vs. reverse reaction step.

Prior to performing global uncertainty and sensitivity analysis, uncertainty factors (G_i) were assigned to each set of screened reactions (see Appendix A for uncertainty table) based on values evaluated in the reviews of Baulch [184-186] and Tsang and coworkers [187, 188]. In the data evaluations mentioned above, the uncertainties are normally provided in log (k) and are represented by a log normal distribution in which the values are centrally located around the nominal value. For reactions without evaluated uncertainties, data available from the National Institute of Standard and Technology (NIST) website representing several studies was employed to estimate the uncertainty of the input parameter. In the case where no evaluation exists or insufficient studies exist on the NIST website (experimental or theoretical) to determine uncertainty from spread of data, an appropriate uncertainty value of 10 was then chosen for the sensitivity calculations in the present study. A factor of 10 was deemed to be an appropriate choice in this study as recent studies [189] indicate that for even high-level theoretical calculations involving complex reactions, the resulting uncertainties can be up to factor of 10. For the pressure-dependent reactions in the model such as the falloff reactions, uncertainty factors were assigned to the A-factors for both the low pressure and high pressure limit if found to be available from evaluations or estimation, otherwise both values were set to be the same. In the Aramco scheme pressure dependency of some the rates is characterised using the PLOG formulation. For such reactions, the same value of uncertainty was given to all the A- factors indicated for the various pressure points in the scheme as no further information could be obtained from the literature.

In the global technique employed in this work, the sampling of the rate parameters was implemented using a low-discrepancy sequence [163, 190], because of its effectiveness in generating samples that are uniformly spread across the entire input space. Among the several low-discrepancy sequences described in section 2.6.2.3, the Sobol's quasi-random sequence was selected for the sampling process because of its faster convergence capability compared to other low-discrepancy sequences (e.g. Faure, Halton) and the standard Monte Carlo random sampling [191-193]. Sobol's sequence represents a quasi-random set of numbers between 0 and 1 generated for each of the selected input parameters across the chosen sample size N. This sequence is then used

to create a sample of rate parameters within the uncertainty range (k_i/G_i, G_i x k_i) which is uniform in the space of log (k), where k_i is the original rate parameter in the scheme, k_i/G_i is the lower limit and G_i x k_i is the upper limit. The rate variables within the chosen uncertainty range are uniformly distributed, as they have all been assumed to have equal probability of being selected.

The global sensitivity indices were estimated using a HDMR method that is capable of expressing the input-output relationship of any complex model with a high-dimensional input space. The HDMR method is a very efficient and low computationally expensive surface response method (SRM) that allows a fully functional surrogate model (meta-model) to be constructed. The meta-model is fitted to the sample input-output distributions that are generated from simulations involving the full model runs. A total sample size of N = 256 was used for the uncertainty study while a sample size N ranging from 4096 - 8192 was used for the QRS-HDMR study in order to obtain an accurate HDMR meta-model (i.e. coefficient of determination R^2 > 80%) for ignition delay predictions.

3.3.2 Chemical kinetic modelling of *n*-butanol oxidation in an RCM and JSR

One of the major objectives of the study is to model alternative fuel effects under practical engine conditions and a primary focus of the study is to investigate the behavior of gasoline when blended with *n*-butanol. The evaluation of the Sarathy *n*-butanol mechanism was therefore considered to be very important as it was meant to provide useful insights that could assist the process of developing a suitable chemical kinetic scheme of a gasoline/*n*-butanol blend to be used in the context of simulating practical engines.

3.3.2.1 Ignition delay times modelling in RCM

The modelling of the *n*-butanol fueled RCM was accomplished using the CANTERA kinetic libraries (version 2.1.1) [71], in accordance with the experimental set up described in Weber et al. [194] and recent data obtained by Materego [195] using the Leeds University RCM. For the Weber data, ignition delay simulations of *n*-butanol/O_2/N_2 mixtures were performed over compressed temperature range of 679 - 925 K, compressed pressures of 15 and 30 bars, at equivalence ratios of 0.5, 1.0 and 2.0,

in order to assess the predictive capability of the Sarathy *n*-butanol scheme in terms of its agreement with the reference experimental data. Here, both the compression and post compression phases were modelled and volume traces which inherently account for the heat losses during both compression and post compression effect were used as input into the autoignition simulations of this study. As described in [194], the volume traces for the full event (compression and post compression) were determined from the measured pressure trace of the non-reactive experiment using the isentropic core relations and temperature-dependent mixture specific heat ratio. The volume profiles were implemented in our Cantera calculations at each time step during which the state of the RCM reactor is advanced. A python-based subroutine obtained from the GitHub account of Weber [196] was used alongside an in-house Cantera RCM code for this purpose. The volume traces used in this study are available from the University of Connecticut Combustion Diagnostics Laboratory experimental database [180].

The Leeds RCM, on the other hand, was modelled as a constant volume adiabatic reactor based on experimental data provided by [195], with heat loss effects of the reactants to chamber walls taken as negligible. *n*-butanol mixtures of different diluents ratio were modelled for compressed temperature ranges of 670 K - 865 K and compressed pressure of 20 bar under stoichiometric conditions.

The definition of the computed ignition delay time in the *n*-butanol RCM is the same with that used in section 3.3.1.2 for the DME RCM which is equivalent to the time from the end of compression (at TDC) to the point of maximum rate of pressure rise $max\left(\left({}^{dP}/_{dt}\right)\right)$.

3.3.2.2 Species concentration modelling in the JSR

The modelling of the JSR was also performed within the Python environment using a Cantera set of libraries according to the experimental specification of Dagaut et al. [20] at P = 10 atm, T = 800-1150 K and ϕ = 0.5 - 2.0. The JSR set up fully described in [20], is comprised of a 4 cm diameter sphere constructed from fused silica to reduce the effect of wall catalytic reactions and supplied with four 1 mm internal diameter nozzles which helps to admit the gases and at the same time facilitate the mixing of the gases with the reactants. The JSR was chosen for the study because of its relevance in fundamental

kinetics and its capacity for investigating fuel effects within the low temperature and intermediate temperature regime. The aim was to determine whether it provided a different set of constraints on the mechanism when compared to low temperature ignition delays. Moreover, the simplicity of the JSR model, which typically, makes it possible to attain high levels of homogeneity in the reactor during the steady state experiments, makes it computationally feasible when coupled with global sampling techniques even when the sample size required is in the order of many thousands.

For the sensitivity analysis of the JSR simulations, a constant residence time of 1.7 s was employed at a constant pressure of 10 atm, and $\phi = 1$ with an initial temperature of 800 K which was increased stepwise by 30 K. A time step of 0.2 s was utilised alongside appropriate tolerance limits in order to attain convergence to steady state. In the context of uncertainty and global sensitivity analysis, only the predicted steady state mole fractions of species carbon monoxide (CO) and formaldehyde (CH_2O) are considered for further investigation because of their key role as pollutants along with the parent fuel *n*-C_4H_9OH.

3.3.2.3 Chemical kinetic model

As mentioned earlier in the literature review (section 2.5.2), a number of studies addressing the chemical kinetic modelling of biobutanol combustion have been performed [20, 140, 141, 143-146]. Most of the mechanisms developed so far for biobutanol focus on the high temperature reaction classes and have not been specifically designed for application in the prediction of ignition behaviour at lower temperatures. As at the time of this study the mechanism of Sarathy [148], described in detail in section 2.5.2 was found to be the only mechanism that included both the low and high temperature reaction pathways for the four isomers of butanol and was therefore adopted in the main part of the study, being the only mechanism with the capacity to model the engine-relevant low temperature autoignition behaviour of *n*-butanol. The kinetic model was constructed based on the 1-butanol kinetic scheme of Black et al. [145] by upgrading the mechanism with the primary reactions of tert-butanol, 2-butanol, and iso-butanol and related radical reactions. As reported in [148], the mechanism contains a total of 433 species and 2551 reactions and was validated with reasonable agreement against a wide range of recently published experimental data which includes: speciation

data obtained in low pressure laminar premixed flames, premixed laminar flame velocities under atmospheric pressures, species data from a high pressure JSR, ignition delay times from a high pressure RCM and ignition delay times from an atmospheric and high pressure shock tubes (ST). The scheme is available at the Lawrence Livermore website and is described in detail in [148]. For the purpose of comparison, the model of Sarathy was evaluated against the high temperature mechanism of Black [145] and Moss [140]. Results of such a comparison are presented in chapter four.

3.3.2.4 Screening approach

A screening process utilising a local sensitivity method was first of all applied to the *n*-butanol kinetic scheme in order to reduce the number of input parameters involved in the global uncertainty/sensitivity analysis since only a few key reactions are likely to greatly influence the accuracy of the predicted targets. The screening of reactions in the *n*-butanol kinetic scheme was based on the Brute-force method discussed previously in section 3.3.1.4. Prior to running the Brute-force local sensitivity analysis on the *n*-butanol scheme, the *n*-butanol RCM model and volume profile subroutine was first of all coupled to our previous local sensitivity code and simulations were performed for conditions of pressure of 15 bar, temperature range of 678 K - 898 K and equivalence ratio of 0.5 - 2.0. The sensitivity of the target output to each reaction in the kinetic model was calculated based on 30 % increase of the reaction rates from their nominal value. Normalised changes to the target quantity were then calculated and based on a threshold of sensitivity coefficient $S_i > 2\%$, a total of 40 reactions were screened for the RCM study and 50 for the JSR. Both set of reactions were then taken forward for further analysis by global uncertainty and sensitivity methods. The set of screened reactions and their normalised local sensitivity indices for selected conditions are presented in the result section.

3.3.2.5 Uncertainty analysis and global sensitivity analysis

Uncertainties factors were assigned to the set of most dominant reactions (see Appendix A for the table of uncertainty factors) screened out in the local sensitivity analysis of the *n*-butanol kinetic model using the approach described in section 3.3.1.5. For the key reactions without available uncertainty data from the literature, an uncertainty factor of

2 was chosen for the sensitivity calculations. An uncertainty factor of 2 was specifically chosen for the RCM study as higher uncertainties resulted in situations where the model did not produce an ignition event or would produce ignition during compression. A factor of 2 may be optimistic for reactions with rates determined by theory, group additivity or estimation, but the results will show that it already leads to quite large uncertainties within the predictive targets. Our previous Python-based global sensitivity solver, which employs a quasi-random sample of the selected input rate parameters, generated using the Sobol's sequence over the adopted sample size, was then coupled to the *n*-butanol RCM simulations for computation of the predicted output distributions. A sample size of 256 was utilised in the uncertainty analysis while sample sizes ranging from 2048 - 4096 were utilised for construction of the HDMR meta model required for determination of global sensitivity indices and component functions of main reactions influencing predicted ignition delays and species profiles.

3.3.3 Chemical kinetic modelling of the autoignition of gasoline and gasoline/*n*-butanol blend in Leeds RCM

3.3.3.1 Reaction mechanism

The detailed kinetic model used in this study was developed in collaboration with the King Abdullah University of Science and Technology (KAUST) group headed by Mani Sarathy. The KAUST group was responsible for developing the TRF/*n*-butanol mechanism while the experimental data for validation of the mechanism was generated in the course of this work as described in section 3.2.1. The mechanism was derived from merging previously reported mechanisms for gasoline surrogates by Mehl [88] and *n*-butanol [148]. It was shown in our previous study [197] that the relative rates (branching ratios) for the hydrogen abstraction reactions of *n*-butanol by OH from the α and γ sites are critical for accurate prediction of *n*-butanol autoignition at low temperatures. Therefore, the mechanism of [148] was used with modifications to the rate constants for the H-abstractions of *n*-butanol by the OH radical according to rate constants suggested by McGillen et al. [198] to improve the reactivity at lower temperatures. The resulting detailed mechanism consists of 1944 species and 8231 reaction steps. A comparison of simulated ignition delay times using the updated *n*-butanol model compared with the original model of [199] is presented in Figure 3.12.

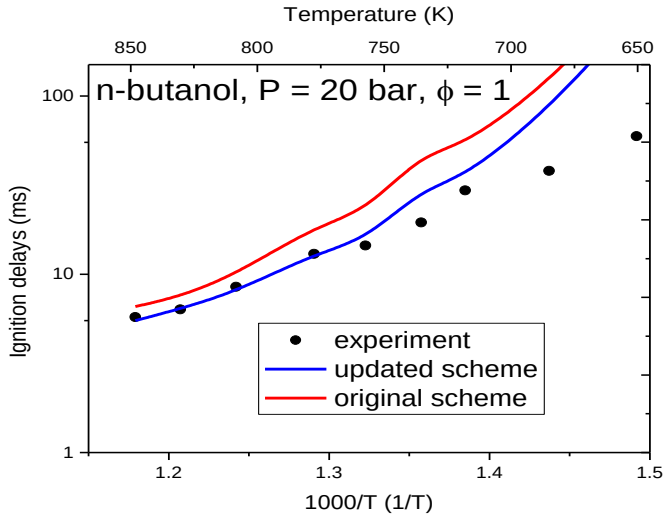

Figure 3.12: Comparison of original *n*-butanol scheme with the updated scheme.

3.3.3.2 Simulations and uncertainty/sensitivity analysis

It was not possible to get Cantera to successfully run the variable volume ignition delay simulations using the detailed TRF/*n*-Butanol mechanism as the number of reactions were beyond the capability of Cantera. Therefore ignition delay times measured in the RCM were simulated using CHEMKIN PRO [200] by running homogeneous variable volume history simulations accounting for heat loss in the experiments. The volume traces were determined from the measured pressure trace of the non-reactive experiment using isentropic core relations and a temperature-dependent mixture specific heat ratio [201].

In order to highlight the important reactions controlling the autoignition, Brute-force sensitivity analyses were conducted at 20 bar and various temperature conditions using the closed homogeneous batch reactor module in CHEMKIN PRO [200] and constant volume simulations. Since Brute-force analysis requires a simulation for each reaction tested, temperature sensitivities were first calculated at the time of ignition to identify the most important reactions. This method has been previously shown to identify the same reactions as a Brute-force sensitivity analysis on ignition delay times and hence provides a useful screening method [202]. The Brute-force sensitivity coefficients were then computed for the top 20 reactions from the screening by varying the reaction rates using the formula $\sigma = \log(\tau+/\tau-)/\log(2.0/0.5)$, where $\tau+$ and $\tau-$ are the computed ignition

delay times corresponding to an increase/decrease in the reaction rates by a factor of two [125, 203]. Therefore, negative sensitivities indicate that ignition delay times decrease when the reaction rate coefficient is increased. The values were normalised by the maximum sensitivity at each temperature and hence the most important reaction has a sensitivity index of 1.

In the course of the collaboration with the KAUST group, a skeletal TRF/*n*-butanol scheme comprising of 527 species and 2644 reactions was also developed from the detailed TRF/*n*-butanol blend scheme with an overall aim of providing a reliable kinetic mechanism that could be successfully used within the context of SI engine modelling. Figure 3.13 shows how the detailed mechanism compares with the skeletal scheme in terms of the predicted ignition delay times of stoichiometric *n*-butanol, TRF and a TRF/*n*-butanol blend at P = 20 bar, T = 678 - 858 K. As shown in Figure 3.13, the level of agreement between the detailed and skeletal model is excellent. Therefore the global uncertainty and sensitivity study involving the Leeds RCM data was performed using the skeletal TRF/*n*-butanol blended mechanism developed in collaboration with the KAUST group. The modelling of autoignition and knock in LUPOE-2D was also carried out using the same skeletal TRF/*n*-butanol blended mechanism.

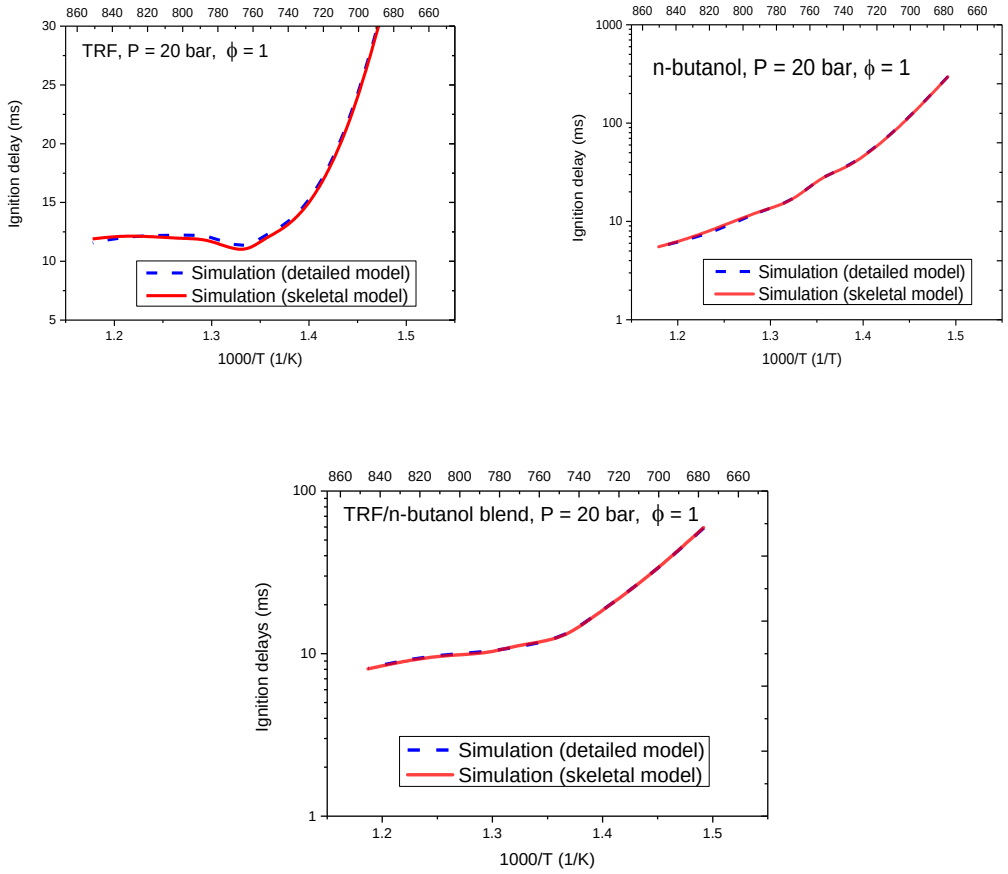

Figure 3.13: Comparison of detailed TRF/*n*-butanol scheme with skeletal scheme (a) TRF (b) *n*-butanol (c) TRF/*n*-butanol.

The global sampling technique described in detail in section 3.3.1.5, was further applied in the simulations in order to quantify the error bars of the ignition delays predicted by the TRF/ *n*-butanol scheme while incorporating the uncertainties of the input rate parameters in the simulations. Uncertainty factors obtained either from published evaluations and experimental data or from estimates made in the absence of sufficient data were assigned to the 42 most important reactions screened out across the three fuel mixture using a Brute-force local sensitivity analysis. An uncertainty factor of 10 was assigned to the reaction rates in the cases where there were no data on the uncertainty range of the reaction rate. The list of the uncertainty factors assigned to the set of reactions considered in the global analysis of the TRF/*n*-butanol mechanism can be found in Appendix A. In addition, a variance-based global sensitivity analysis using HDMR [163] is carried out to understand and rank the parameters responsible for the predicted uncertainties. Global sensitivity plots representing the first-order and second-

order response between sampled input rates and predicted output are presented and also discussed in the result section to explore and demonstrate how the choice of a parameter in the scheme impacts on the predicted ignition delay uncertainties.

3.3.4 Chemical kinetic modelling of the combustion, autoignition and knock behaviour of gasoline and gasoline/*n*-butanol blends in Leeds SI engine.

3.3.4.1 Introduction to LOGESOFT code

LOGESOFT [204] is a software suite developed by LOGE AB, Lund Combustion Engineering, a software development company based in the University City of Lund, Sweden. LOGESOFT is comprised of various specialised tools that use reaction mechanisms for simulating chemical and physical processes in various engineering applications. The tools in LOGESOFT are capable of handling gas phase chemistry, surface chemistry and soot chemistry through a suite of reactor models and reaction mechanisms. LOGESOFT contains both laboratory facility based models such as constant volume reactor, constant pressure reactor, PSR, plug flow reactor (PFR), equilibrium reactor and RCM as well as engine based models such as the SI and HCCI engine. Other models in the LOGESOFT code include the stochastic reactor model (SRM) for HCCI, SI, DICI engines, flame models (premixed or counter flow) and 1-D models (e.g. 1-D catalyst and diesel particulate filter models) for after treatment. LOGESOFT also comes with the capability for integrating detailed chemical kinetic modelling analysis with 1-D commercial engine simulation tools such as GT-Power and Ricardo Wave. A database of reaction mechanisms for various fuels also exist in LOGESOFT alongside various tools for mechanism development, reduction and export. The reaction mechanisms and thermochemical data for all the species in the mechanism, required for calculation of the forward and reverse reaction rates can be loaded into the software using the READ MECHANISM module and further preprocessed using the MECHANISM OVERVIEW module. There is also room to specify the transport properties of species when modelling a combustion system where transport processes are important. The two-zone homogenous SI engine model in LOGESOFT was employed for simulating the combustion of gasoline and gasoline/*n*-butanol blend in this work. Details of the model are presented in the next section while details of the

other models that make up the LOGESOFT code can be found in the LOGESOFT manual.

3.3.4.2 LOGESOFT two-zone combustion model for SI engines

The LOGESOFT SI engine combustion model is a two-zone thermodynamic model that assumes the combustion chamber to be made up of two separate homogenous zones (spatially homogenous in temperature and species concentrations) containing the unburned gas mixture and the burned gas respectively (Figure 3.14). In the two-zone model, each of the zones (unburned and burned zones) are separated by an infinitesimally thin spherically propagating flame front or reaction zone. During combustion, no heat is transferred between the two zones but mass is transferred from the unburned zone to the burned zone as the flame advances into the unburned gas mixture. The pressure in the entire combustion chamber is taken to be constant throughout the period of combustion while the volume of each zone changes with the movement of the piston. The behaviour of the homogenous mixture in each zone is assumed to follow that of a perfect gas and the conservation laws of mass and energy are applied to both the burned and unburned zones. The governing equations are fully described in the following sections.

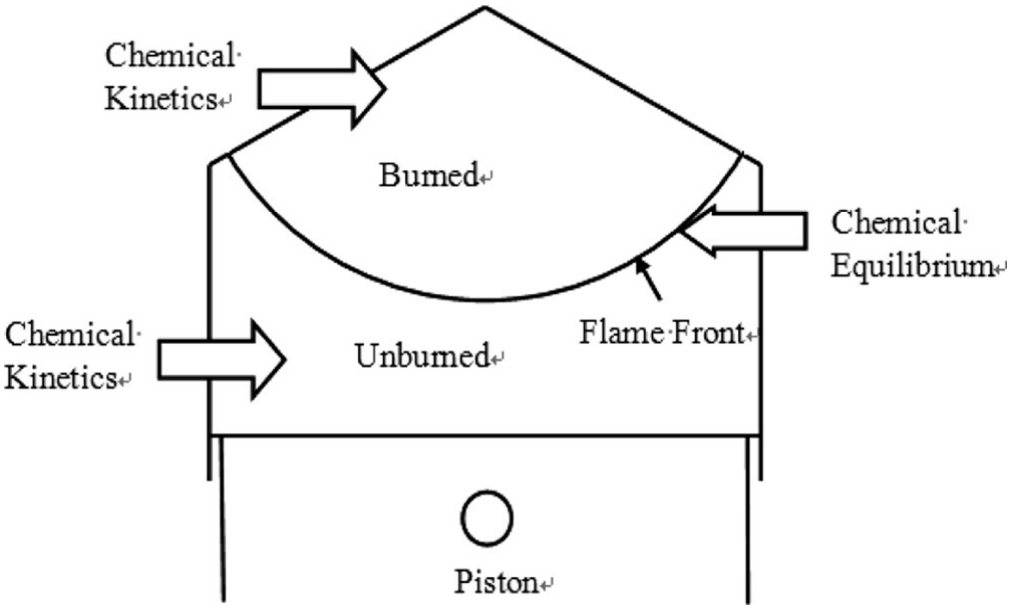

Figure 3.14: Schematic diagram of the two zone thermodynamic model.

Ideal Gas Law

The homogenous mixture in each of the zones obeys the ideal gas law which is given by,

$$P_i\, V_i = n_i\, R\, T_i \tag{3.13}$$

Where, P = pressure, V = volume, n = no of moles of gas, R = universal gas constant

T = temperature and i = zone index.

Conservation of mass

The total mass in the engine cylinder is defined by,

$$m = \sum_{i=1}^{N_z} m_i \tag{3.14}$$

where m_i = mass of zone i, N_z = number of zones which is equal to 2 in this case.

The change in the total mass in the cylinder is given by,

$$\frac{dm}{dt} = m_{out} \tag{3.15}$$

where m_{out} is the mass flow leaving the combustion chamber via blowby, crevice losses etc. Since blowby is considered negligible in the LOGESOFT model, equation 3.15 becomes,

$$\frac{dm}{dt} = 0 \tag{3.16}$$

During combustion, each zone operates as an open system with mass and species leaving the unburned zone and then entering the burned, resulting in the transfer of enthalpy between the two zones. The rate of change of mass in each zone is given by,

$$\frac{dm_i}{dt} = m_{in,\ i} - m_{out,\ i} \tag{3.17}$$

where $m_{in,\ i}$ is the mass flowing into the $i-th$ zone and $m_{out,\ i}$ is the mass flowing out of the $i-th$.

Conservation of species

Applying the law of conservation of mass to the unburned zone, the rate of change of the mass fraction of any specie Y_i in the unburn zone is given by,

$$\frac{dY_{i,u}}{dt} = \frac{M_i \dot{w}_i}{\rho_u} \tag{3.18}$$

where M_i and $\dot{w}_i$ are the molecular weight and rate of production of the species i respectively, ρ is the density of the unburned zone and u denotes unburn zone.

The rate of change of the mass fraction of a species in the burned zone is determined by two events, namely the species transferred from the burning zone (frame front) due to formation by the flame front reactions and the post flame species formation by the chemical reactions in the burned zone. This is expressed mathematically as,

$$\frac{dY_{i,b}}{dt} = \frac{\dot{m_{f,b}}}{m_b}\left(Y_{i,f} - Y_{i,b}\right) + \frac{M_i \dot{w}_i}{\rho_b} \tag{3.19}$$

where $Y_{i,f}$ is the mass fraction of species i in the mass $m_{f,b}$ transferred from the burning or reaction zone across the flame front into the burned zone, $Y_{i,b}$ is the mass fraction of the residue gas in the burned zone before the transfer from the flame front and m_b is the total mass in the burned zone.

Conservation of energy

Energy conservation based on the first law of thermodynamics can be applied to show the energy changes across the unburned and burned zones. For the unburn zone, this includes the heat transfer $\dot{Q}_{ht,u}$ due to temperature differences between the zone (engine volume) and surrounding atmosphere, the work done $\dot{W}$ due to changes in volume via piston motion and the heat release due to chemical reactions (last term on the RHS of Equation 3.20).

$$m_u c_{p,u} \frac{dT_u}{dt} = \dot{Q}_{ht,u} - \dot{W}_u + V_u \sum_{l=1}^{N_s} \dot{w}_{i,u} . M_i . h_{i,u} \tag{3.20}$$

where c_p is the specific heat capacity at constant pressure, h is the specific enthalpy, T is the temperature of the zone, V is volume of the zone and N_s is the number of species in the reaction mechanism.

The work due to volume change $\dot{W}_u$ and heat transfer $\dot{Q}_{ht,u}$ are given by,

$$\dot{W}_u = -P \frac{dV}{dt} \tag{3.21}$$

$$\dot{Q}_{ht,u} = \alpha_g A_{wall}(T - T_{wall}) \tag{3.22}$$

where P is the cylinder pressure, A_{wall} is the cylinder wall area, T_{wall} is the cylinder wall temperature and α_g is the heat transfer coefficient.

Substituting equation 3.21 and 3.22 into equation 3.20 gives,

$$m_u c_{p,u} \frac{dT_u}{dt} = \alpha_g A_{wall}(T - T_{wall}) - P \frac{dV}{dt} + V_u \sum_{l=1}^{N_s} \dot{w}_{i,u} . M_i . h_{i,u} \tag{3.23}$$

In the case of the burned zone, the effect of the energy transfer from the burning zone on the temperature changes, which is given by the enthalpy difference between the resident gas and the gas flow from the burning zone, must be taken into consideration. Therefore, the energy balance for the burned zone becomes,

$$m_b c_{p,b} \frac{dT_b}{dt} = \alpha_g A_{wall}(T - T_{wall}) - P \frac{dV}{dt} + m_{f,b} \sum_{i=1}^{N_s} Y_{i,b} \left(h_f - h_b\right) + V_b \sum_{l=1}^{N_s} \dot{\omega}_{i,b} . M_i . h_{i,b} \tag{3.24}$$

where h_f is the specific enthalpy of the inflow mixture and h_b is the specific enthalpy of the residue gas.

Heat transfer

The heat transfer term $\dot{Q}_{ht,u}$ (equation 3.22) is modelled in LOGEengine using the Woschni correlation [31, 205] in which the heat transfer coefficient α_g is given by,

$$\alpha_g = 3.26 B^{-0.2} P^{0.8} T^{-0.53} w^{0.8} \tag{3.25}$$

where w is the characteristic speed.

Volume and in-cylinder pressure calculation

The total cylinder volume at any instant in time is a function of the crank angle degree travelled and can be computed using the expression given in Heywood [31].

$$V = V_c + \frac{\pi B^2}{4}(L_{cr} + R_c - L_{cr}\cos(\theta) + \sqrt{{L_{cr}}^2 - {R_c}^2 sin^2(\theta)} \quad (3.26)$$

where V_c is the clearance volume, B is the engine bore, L_{cr} is the length of the connecting rod and R_c is the crank radius.

The total pressure in the cylinder is calculated as a weighted average using the temperatures and gas masses of the burned and unburned zones. The total pressure is therefore given by

$$P = \frac{m_u R\, T_u + m_b R\, T_b}{V} \quad (3.27)$$

The mass and energy losses as a result of leakages and flow into crevices are assumed to be negligible in the LOGESOFT model.

Flame propagation model for SI engine

In the LOGEengine two-zone SI engine model, the effect of flame propagation on combustion is modelled using either the non-predictive Wiebe function or the predictive turbulent flame propagation (TFP) models. Both models control the movement of mass from the unburned zone to the burned zone. The Weibe function gives the mass fraction burned by flame propagation as a function of crank angle travelled using the equation,

$$m_b = 1 - \exp\left(-b\left(\frac{\theta-\theta_0}{\Delta\theta}\right)^{n+1}\right) \quad 3.28)$$

where θ is the instantaneous crank angle, θ_0 is the crank angle at the start of combustion and $\Delta\theta$ is the combustion duration for which $0.0 \leq m_b \leq 0.9$. The adjustable parameters b and n are usually unknown but can be determined by fitting the mass fraction burn (MFB) profile, calculated through a burn rate analysis of measured cylinder pressure, to the Weibe function.

The TFP model employed in LOGEengine SI engine model for determining the mass burn rate (Figure 3.15) is a quasi-3D turbulent flame propagation (TFP) model in which the flame is assumed as spherically expanding and limited by the cylinder walls. The turbulent flame speed S_T is computed based on the knowledge of the laminar flame speed S_L using the correlation of Peters [206, 207] which is given by,

$$\frac{S_T}{S_L} = 1 + C\left(\frac{u'}{S_L}\right)^n ; 0.5 < n < 1 \tag{3.29}$$

where u' is the root mean square velocity while *n* and *C* are adjustable constants with *n* ranging from 0.5-1.0 [206, 208].

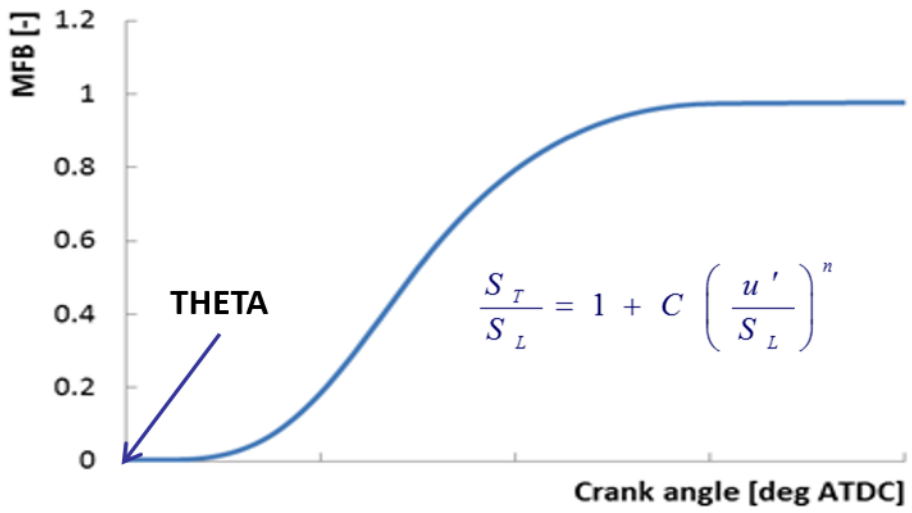

Figure 3.15: Typical burn rate profile based on the turbulent flame propagation model. Taken from [208]

The laminar flame speed S_L is obtained from a laminar flame speed library for pure iso-octane, covering the wide range of conditions (temperatures, pressures, equivalence ratios and EGR rates) as shown in Table 3.8. During the simulations, the particular value of the flame speed required under a set of conditions is retrieved more quickly with the help of an advanced correlation function implemented in the LOGEengine code. Figure 3.16 shows a comparison of the library data and the correlation function for laminar flame speed at 10 bar and 10 % EGR. In this work, all engine computations were performed using the default values of *C* = 2.5 and *n* = 0 in order to keep the complexity

of the simulation process to the minimum. The root mean square velocity u' is calculated using the relation,

$$u' = \frac{l}{\tau_t} \tag{3.30}$$

where l_l is the integral length scale of the flow and τ_t is the turbulent mixing time. The root mean square velocity (rms) is a good indicator of the level of turbulence in the engine. The time evolution of the integral length scale is only slightly dependent on the engine operation [30]. Therefore a constant value of l = 0.04 was used in the calculation of u' similar to the value reported by previous studies involving the LUPOE engine [40, 209].

Table 3.8: Range of parameters for the laminar flame speed library. Adapted from [210]

Parameter	Value
Equivalence ratio	0.2-0.4
Temperature	300 K- autoignition
Pressure	1-130 bar
EGR	0 – 50 %

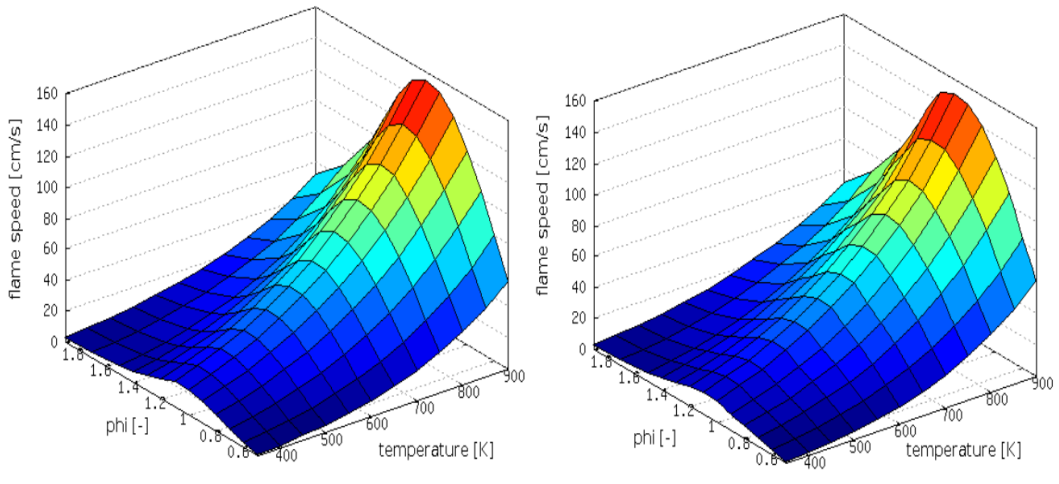

Figure 3.16: Library data (Left) and correlation function (right) for laminar flame speed at *P* = 10 bar and 10 % EGR [210].

The turbulent mixing time, by the definition given in Equation 3.31, is inversely proportional to the turbulent intensity, therefore a large turbulent mixing time is an indication of a very small turbulent intensity. The turbulent mixing time can also be defined as the time taken to transport the turbulent kinetic energy (TKE) of the large eddies (scales) to the small eddies where it is dissipated as heat due to the effect of viscosity. The turbulent mixing time can be obtained from 3D CFD computations (*k*-ε turbulence model) using the equation,

$$\tau_t = \frac{l}{u'} = \frac{k}{\varepsilon} \tag{3.31}$$

where k is the turbulent kinetic energy and ε is the turbulent kinetic energy dissipation rate.

The combustion process in an SI engine occurs in a 3-D time dependent turbulent flow field which is quite difficult to model. The use of empirical sub-models (correlations) to account for the effect of turbulence is highly limited by the lack of experimental turbulence data as it is quite difficult to measure turbulence in practical engines. While turbulence data can be obtained from CFD calculations for use in 0-D thermodynamic based modelling, it is however difficult to extrapolate this data from a 3-D domain to a 0-D space without losing the accuracy of the data. Therefore the turbulent mixing time which accounts for the effect of turbulence is modelled in LOGEengine using an optimisation approach where it is calibrated against a set of measured pressure data.

In this work, the simple but predictive quasi dimensional TFP model was used instead of the non-predictive zero dimensional Weibe model. The TFP model gives a better representation of the effect of engine geometry and operating conditions on combustion compared to the Weibe function. The turbulent intensity or turbulent mixing time helps to account for the physical process of turbulent mixing which is a function of engine geometry. The laminar flame velocity, used in computing the turbulent flame velocity is determined as a function of engine operating conditions such as pressure and temperature. The fuel effect (chemistry effect) is modelled by the chemical kinetic mechanism employed in the simulations.

3.3.5 Introduction to LOGEengine optimisation code

3.3.5.1 Setting up an SI engine simulation test case in LOGEengine

LOGEengine is a fully integrated software that incorporates both the LOGESOFT SI and DI-CI thermodynamic engine models (both homogenous and SRM models) with an optimisation tool for calibration of initial conditions and tuning of mixing time. The LOGEengine software comes with an inbuilt initial condition calibration tool and a turbulent flame propagation optimisation tool. One of the advantages of LOGEengine is its capacity for fast full cycle engine simulations with detailed and reduced reaction mechanisms, allowing the effect of the chemistry-flow interaction in the engine to be accounted for to a reasonable extent. Inhomogeneity and cyclic variation within the engine can also be modelled using the SRM. The SRM is a probability model that models the in-cylinder mixture (both the burned and unburned zones) as an ensemble of particles which are capable of exchanging heat and mass among themselves within a zone. Depending on the number of particles used, one closed cycle engine simulation on a personal computer using the SRM model may take up to one full day to complete and for a cyclic variability study involving 30 cycles, this may last up to a month to complete. The computational cost of one operating point (OP) simulation could be far greater considering that the optimisation process may require parameters (ie. mixing time) to be tuned several times and simulations repeated before a good match between measured and predicted data is obtained. The basic two zone SI engine combustion model was therefore adopted in this study instead of the SRM model in order to cut down on the computational cost required for the full engine calculations.

Before running an engine simulation test case in LOGEengine, the chemistry files of the fuel are first of all read into LOGESOFT, where they can also be post processed and checked for incompatibilities. Once the chemistry files have been successfully read into LOGESOFT, the files are automatically converted into the REDKIN format required for engine simulations and optimisation in LOGEengine.

3.3.5.2 Heat release analysis and compression phase matching

The first step in setting up and running a simulation test case of the spark ignition engine model in LOGEengine involves the tuning and calibration of the initial conditions

through a heat release analysis and matching of the compression phase with experimentally obtained pressure data. The various engine design and engine operating parameters used for the calibration process are shown in Table 3.9.

In performing of initial condition calibration in LOGEengine, the following specific steps were performed using the setup wizard on the graphical user interface.

- Loading of experimental pressure data and checking of units for consistency
- Selection of optimisation limits for pressure offset, cylinder head temperature, compression ratio, temperature and pressure at IVC.
- The advanced option is normally utilised for optimum compression phase matching if the correct mass flow of fuel before compression in kg/s/cylinder as well as atomic fractions of fuel components are known. The advanced option was not utilised in this work as the exact mass flow of fuel in LUPOE is not known due to the effect of blow by.
- Running of several heat release and compression phase matching set ups with different ranges of input parameters such as pressure offset, pressure multiplier, cylinder head temperature, cylinder wall temperature, compression ratio, EGR, temperature and pressure at IVC until a good match is achieved between the simulated and experimental pressure of the compression phase.
- Exporting of optimised initial conditions from heat release setup wizard to the YAGA tool for engine simulation and combustion model calibration via optimisation of mixing time.

Figure 3.17 shows the result of the heat release analysis obtained based on the LOGEengine SI engine sample data. The results obtained based on the Leeds engine data are presented in the results chapter (chapter 6).

Table 3.9: Basic input for SI engine calculations

Simulation parameters	
Engine parameters	
SPEED	750 RPM
PINOFFSET	0.0
BORE	0.08 (m)
COMPRESSION RATIO	11.5
STROKE	0.110(m)
ROD LENGTH	0.232 (m)
STARTCAD	-108.0 (CAD)
STOPCAD	100.0 (CAD)
EGR_AMOUNT	3 %
EGR_NCYCLES	1
Heat Transfer parameters	
Wall temperature	450.0 (K)
Woshni_AP0	1.37000004768372
Initial conditions	
Temperature	0.323E+03 (K)
Pressure	0.160E+06 (N/m^2)

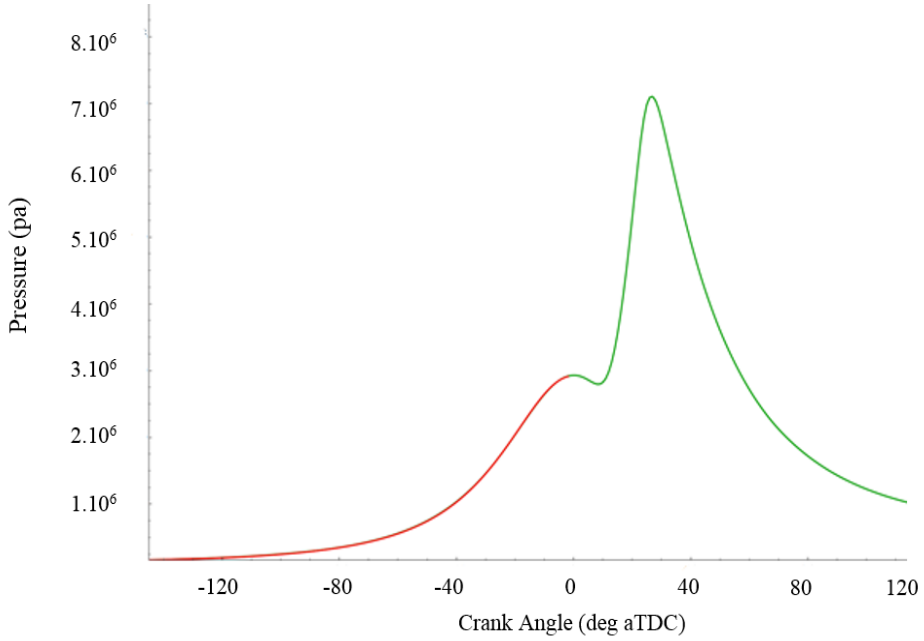

(a)

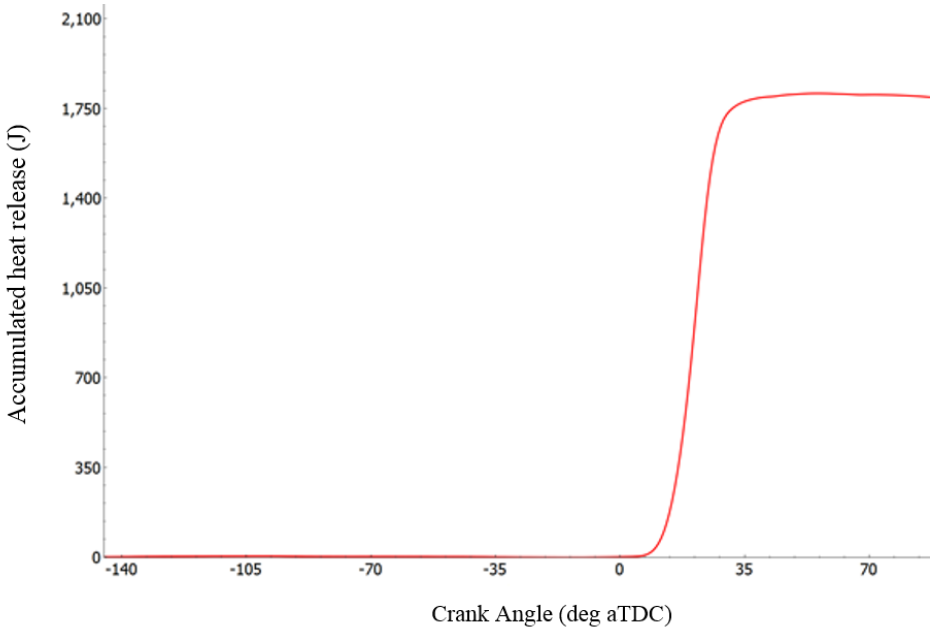

(b)

Figure 3.17: Heat release analysis and compression phase matching obtained using LOGEengine sample data (a) matched pressure trace-the red line represents the calculated pressure while the green line represents the measured pressure (b) cumulative heat release.

3.3.5.3 Generation of cylinder profile and combustion phase matching in LOGEengine

If the predictive TFP in LOGEengine is chosen for modelling of flame effect, the user is required to also provide a cylinder geometry input file which contains a set of two dimensional co-ordinates providing detailed information on the shape of the engine cylinder head and position of the spark plug. The path to this file can be specified using one of the tabs in the graphical Interface (GUI) of the optimisation tool and for the file to run successfully in LOGEengine, the user must ensure that the format of the file is consistent with the right format recognised in LOGEengine. The cylinder profile is required for modelling the evolution of the flame during the combustion process. In calculating the flame evolution, the engine cylinder profile is implemented within a Monte Carlo geometry model which assumes a spherically propagating flame and gives a description of the shape and position of the flame at any particular time step within the specified cylinder [210]. The Monte Carlo model is also very useful within the framework of developing advanced flame quenching models as it is capable of computing the fractions of the flame volume at any location relative to the cylinder walls [211].

As pointed out in the results chapter (section 6.3.1), the use of a correct cylinder geometry and spark plug position is very important for correct modelling of the flame propagation. For example, if the cylinder profile gives a calculated volume that is relatively too large, then by the time the flame has gone a few crank angles, its radius would have been equal to the cylinder radius and flame is quenched. This could lead to the simulation of inaccurately low pressures or result in non-ignition of the fuel mixture during the simulations. Based on the methodology outlined in the LOGEengine manual, and using the relevant dimensions of the engine cylinder head and spark plug as well as the information on spark plug location, an appropriate cylinder profile was generated for the cylinder clearance volume of the Leeds University Ported Optical engine (LUPOE) and prepared in a text file in line with the format recognised by LOGEengine. All data for the cylinder head profile were normalised against the cylinder radius such that the same original profile can be used in engine simulations where the dimension of the cylinder bore is changed. The definition of each line of data in the cylinder geometry

file is fully described in the LOGEengine manual. Figure 3.18 shows the cylinder profile developed for the cylinder head of LUPOE in the course of this research.

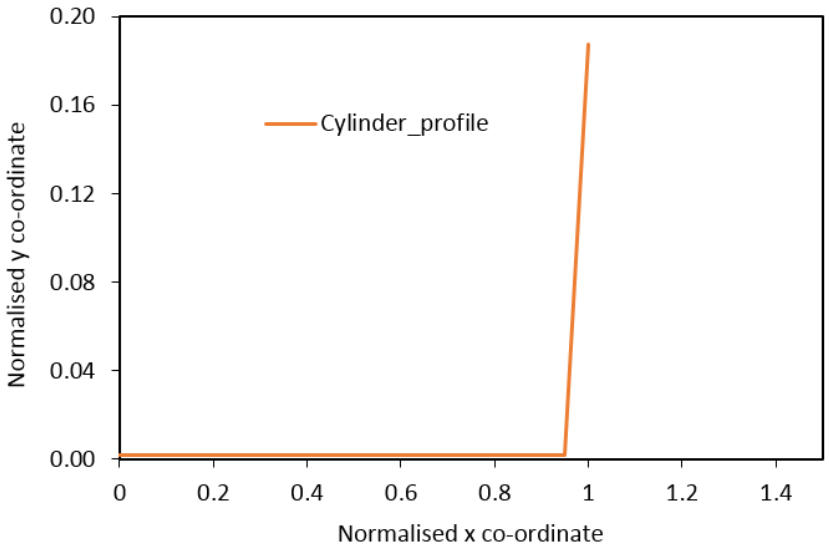

Figure 3.18: Cylinder profile for LUPOE-2D engine.

3.3.5.4 Combustion phase matching and autoignition modelling in LOGEengine

Various physical and chemical processes contribute to the full engine cycle event occurring in an engine and these processes can be modelled or represented considerably well by the mathematical equations presented in section 3.3.4.2. Matching of the combustion phase is a crucial step in the calibration of the SI engine model and modelling of autoignition in LOGEengine. Matching of the combustion phase in the LOGEengine application is a rigorous part of the simulation process and requires some experience with tuning of the mixing time. The concept behind the LOGEengine optimisation code is based on the understanding that if the experimental and simulated in-cylinder pressure traces during the combustion phase are effectively matched through the tuning of the mixing time, the temperature history of the end gas ahead of the flame can be matched and as a result the influence of chemical processes can then be decoupled from the impact of all other parameters. Autoignition and knock in an SI engine originates from the unburned zone as a result of end gas compression by the propagating flame. Therefore the predicted autoignition onset (knock onset) is detected in LOGEengine by analysis of the unburned zone heat release and species concentration

profiles. Since the experimental and simulated pressure profile and consequently temperature history have been matched for the combustion phase, the differences between the predicted and measured autoignition onset would then be solely dependent on the chemistry model employed in the engine simulations.

The following specific steps were followed in setting up of engine simulations in the YAGA optimisation interface for matching of the combustion phase.

- Loading of cylinder profile and all chemistry files into set wizard (YAGA tool)
- Selection of appropriate turbulent flame propagation model
- Selection of appropriate tuning limits for turbulence theta and mixing time and running of engine calculations for optimal matching of combustion phase.
- Tracking of optimisation parameter development and target parameter development for improvement of simulation results.

Figure 3.19 shows a typical result of the parameter tuning carried out in LOGEengine for matching of the combustion phase using the SI engine gasoline sample pressure data, cylinder profile and gasoline chemistry files in LOGEengine while Figure 3.20 shows the rate of heat release profile obtained using the same set of data. Fig 3.21 presents the heat release profile and temperature profile calculated for the unburn zone. The first peak in Figure 3.21a occurring after the induction or ignition delay period represents the low temperature ignition and heat release due to the cool flame chemistry. The time between the TDC and the point of hot ignition leading to the high temperature heat release is taken as the onset of knock.

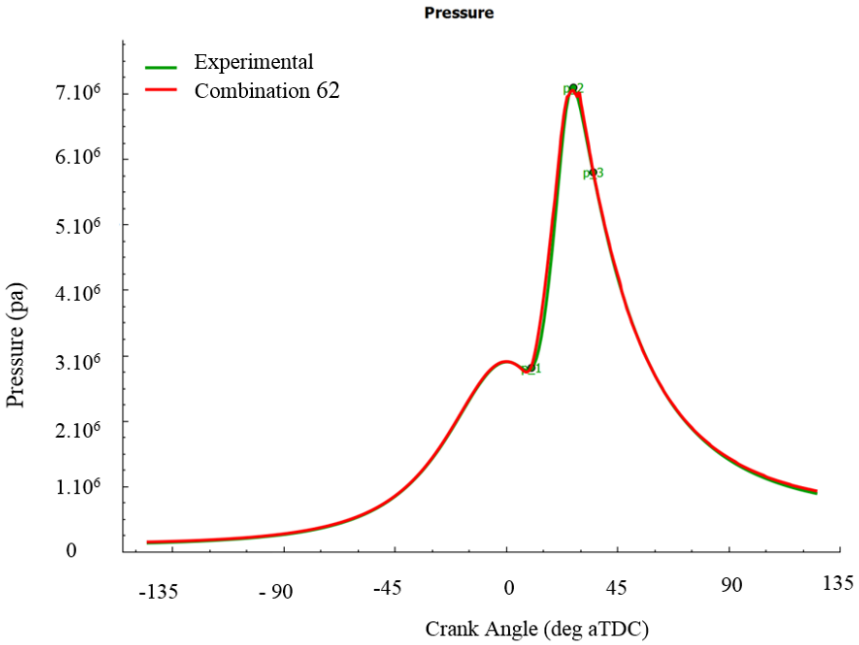

Figure 3.19: Comparison of simulated and measured in-cylinder pressure with mixing time optimisation using LOGEengine sample data.

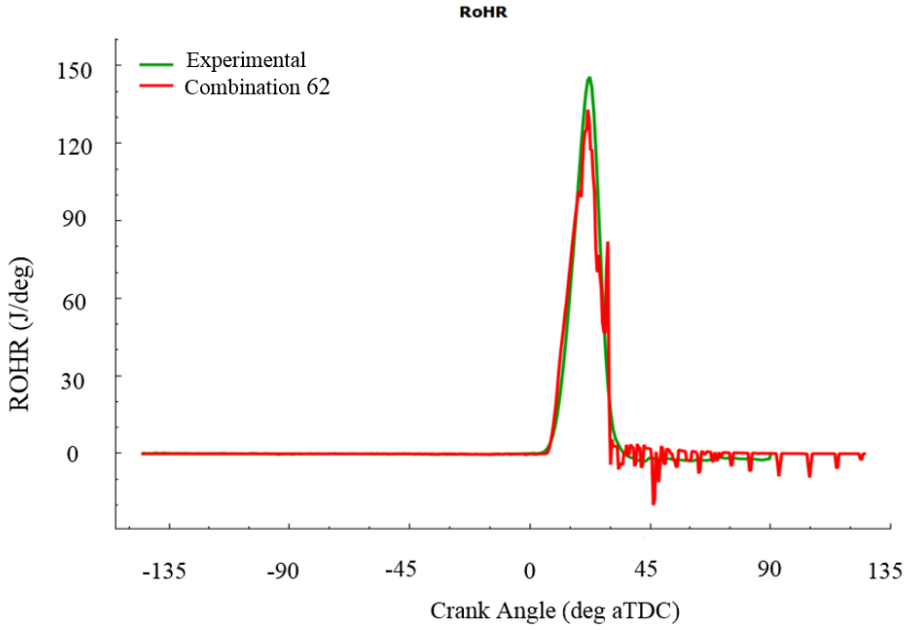

Figure 3.20: Comparison of simulated and measured in-cylinder rate of heat release with mixing time optimisation using LOGEengine sample data.

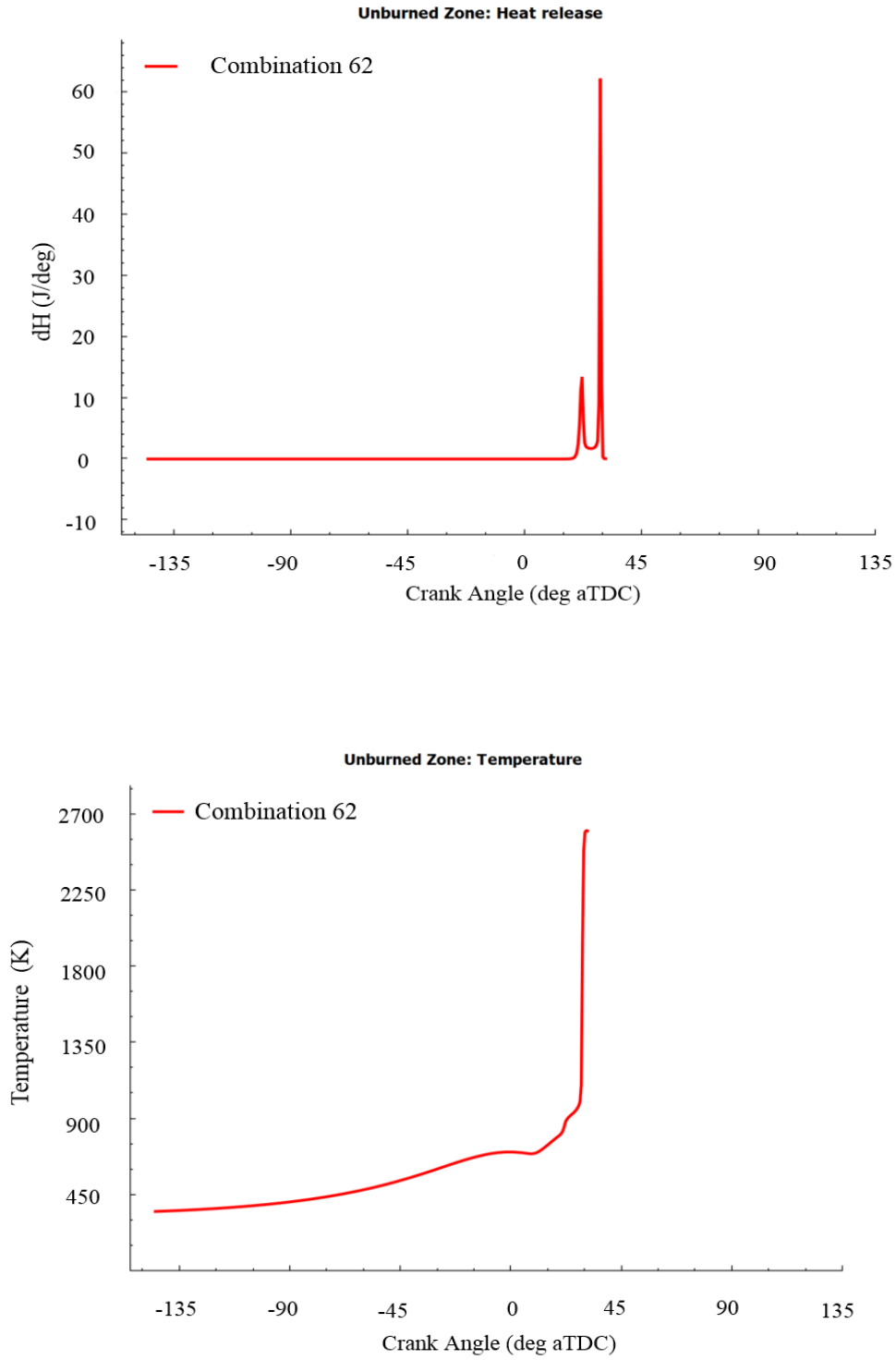

Figure 3.21: Simulated unburned conditions using LOGEengine default data (a) heat release profile (b) temperature profile.

Chapter 4

Chemical kinetic modelling study of DME and *n*-butanol oxidation in fundamental systems.

4.1 Introduction

4.1.1 Background and motivation

Computer modelling and simulation of fuel combustion in internal combustion engines has in recent time become an indispensable tool used in aiming to meeting today's energy needs especially in the area of optimising automotive engines and developing future cleaner fuels. However, to simulate practical combustion systems such as spark ignition and HCCI engines, accurate and reliable chemical kinetic models of fuel oxidation are needed as input into engine simulations. Due to the need to cut down on the computational cost and complexities involved with engine simulations, much effort is now being focused towards reducing the detailed chemical kinetic schemes into simpler reduced forms, using various available techniques before they are then applied in engine simulation studies. Therefore, it is imperative that available detailed chemical kinetic models of Dimethyl Ether (DME) and *n*-butanol be reliable and accurate as much as possible because of their key role in the development of simplified schemes required for use in the context of simulating practical combustion systems.

However, kinetic models of complicated fuels are usually made up of a large set of elementary reactions which are quantitatively described by the rate parameters. A large number of the rate parameters are determined using semi-empirical approaches (e.g group additivity methods) because of the difficulties associated with the experimental measurement of such large number of rate parameters. This however has the disadvantage of introducing large uncertainties in the determined parameter values and consequently the model as a whole [212] and the model could quite easily fail when utilised under practical engine conditions that are outside the range in which it is validated or constrained. Although the use of local sensitivity methods for importance ranking of key reactions that mostly influence the predicted target quantities is quite common in most reaction mechanism studies, the evaluation of the impact of the

inherent uncertainties in the input rate parameters on the overall predictive uncertainties is usually not addressed. In contrast to local sensitivity methods, global uncertainty and sensitivity methods provide an understanding of the predictive output uncertainties as well as details on their main contributing parameters, even where the relationship between the input parameters and predicted target output are highly nonlinear [212, 213]. In addition, since they are based on estimating the contribution of uncertainties to predictive variance, selecting particular experimental observations as predictive targets allows the use of global sensitivities in exploring the extent to which a particular observable can constrain key parameters.

This current work is fundamentally motivated by the search for suitable chemical kinetic models of alternative fuels such as DME and *n*-butanol that can be used for subsequent development of reduced schemes needed for simulations of the combustion of DME and *n*-butanol, and also their blends with conventional fuels, in compression ignition and spark ignition engines. Reducing uncertainties in the predicted ignition properties and concentrations of minor species from the combustion of alternative fuels is one major way the predictive accuracy of these kinetic schemes can be improved upon but achieving that is still currently a very challenging task for the kinetic community especially for oxygenated fuels. In the context of the above, DME being one of the simplest representations of oxygenated fuels is therefore considered here as a starting point and an appropriate reference case for other oxygenated fuels [118].

With a view to providing useful information needed to assist the process of reducing uncertainties in these kinetic schemes, the sensitivity of the selected predictive target (ignition delays and species concentration profiles) to possible uncertainties within the input data of these schemes (i.e. rate parameters) is herein investigated using both local and global uncertainty/sensitivity methods. This is important in order to identify the model parameters that mostly contribute to the predictive uncertainties of the key target outputs. This can help focus effort on the parameters (e.g. rate constants) with largest influence on predictions through more detailed experimental and theoretical studies in order to improve model parameterisation, thus helping to improve the predictive accuracy and robustness of the schemes. Information provided via sensitivity analysis on the detailed schemes is also very useful for further development of simplified

schemes that can be used optimally within the framework of simulating combustion in internal combustion engines with huge gains in computational cost.

4.1.2 Objective of the current chapter

This chapter presents the results of the chemical kinetic modelling study of DME and *n*-butanol combustion carried out within the framework of ignition delay times modelling in RCM and species concentrations prediction in homogenous reactors. The numerical methods employed in generating all the simulated data presented in this chapter are fully described in chapter 3.

In this chapter, various chemical kinetic models of Dimethyl ether (DME) and *n*-butanol combustion obtained from the literature are investigated. Comparison between model predictions and target experimental data is a significant aspect of the model validation and evaluation process. Therefore a primary objectives of this chapter is to assess the robustness and predictive capabilities of selected kinetic models of alternative fuels (DME and *n*-butanol) in terms of their ability to accurately reproduce the autoignition properties and species concentration profiles of the target fuels across a wide range of chosen conditions by comparing predicted data from simulations with measured data from experimental studies. For both the DME and *n*-butanol studies, results from simulations using the adopted kinetic schemes are compared with previous experimental data obtained from the literature. The *n*-butanol kinetic scheme is also validated against recent ignition delay times measurements of *n*-butanol obtained from the University of Leeds RCM by Materego [195]. Furthermore, the sensitivity of predicted ignition delays within the RCM and species concentrations in the JSR to possible uncertainties within the input data of the kinetic schemes (in this case, rate parameters) are also investigated via local and global uncertainty/sensitivity analyses in order to identify the key reactions influencing the predictive targets as well as evaluate the constraints provided by different experimental set-ups on the key reaction rate parameters.

4.2 Chemical kinetic modelling study of DME oxidation in a rapid compression machine

4.2.1 Introduction

Based on the review presented in section 2.5.1, it is clear that many detailed chemical kinetic models of DME oxidation already exist in the open literature that could provide the foundation for the development of reduced and skeletal DME schemes needed for simulating practical combustion systems. However, these models may contain considerable differences in terms of their parameterisation or structure due to missing chemical pathways within the mechanism. Therefore it is imperative to perform an evaluation and comparative analysis of these schemes and to investigate how the inherent uncertainties in their rate parameters impact on the overall predictive capability of the schemes in comparison with available experimental data.

Out of the large number of kinetic models that have been proposed so far for DME oxidation in the open literature, the three most recent models referred to in this study as Liu2013 mechanism, LLNL mechanism and Aramco mechanism and described in section 2.5.1 were adopted for the study. It is important to state that while the three schemes mentioned above, particularly the Aramco mechanism, have been validated across a wide range of experimental data as reported in the referenced papers, a detailed comparison of the three mechanism has however not be performed. Therefore a key aim of this study is to compare the three mechanisms in terms of their capability to reproduce the low temperature ignition properties of DME and to establish how the differences in their rate constant parameterisation and inherent uncertainties influence the predictive target and their sensitivities.

4.2.2 Comparison of model predictions with experimental data

Figure 4.1 illustrates a typical pressure trace for the ignition of a DME/O_2/N_2 mixture (1/4/30 by mole) at initial conditions of T = 297 K and P = 430 Torr. The first-stage (τ_1) and overall (τ) ignition delays are defined as the total time between the end of compression stroke (t = 0) and the point of maximum pressure rise. Figure 4.2 shows both the experimental and simulated pressure trace diagrams obtained from our current modelling work for the ignition of DME/O_2/N_2 mixture (1/4/30 by mole). As indicated

in Figure 4.2, the measured pressure and the deduced temperature at the end of compression (t = 0) are P = 10 bar and T = 634.6 K respectively. At the conditions studied, the result of the current RCM modelling is in reasonable agreement with the experimental pressure trace in terms of predicting the well-known two-stage ignition feature of DME. However, compared to experimental data for the condition given, the simulated pressure trace obtained using the three selected chemical kinetic schemes over predicts the first-stage and overall-ignition delays with the difference more pronounced with the LLNL mechanism.

Figure 4.3 and Figure 4.4 show the results of the two modelling approaches employing the Liu2013 kinetic scheme, in which the post compression event (constant volume simulation) and full event comprising both the compression and post compression phase (variable volume simulation) are modelled separately. For the compressed conditions of P = 10 bar and T = 634.6 K (Figure 4.3), the two modelling approaches gave overall ignition delay times of 48.00 ms and 43.16 ms respectively, leading up to a difference of about 11 %. The difference in the predicted ignition delay times is however quite significant at experimental conditions resulting in shorter ignition delays, i.e. at very reactive conditions of P = 20.1 bar and T = 720 K (Figure 4.4). In this case, the predicted overall ignition delay times for the two modelling approaches are 3.90 ms and 2.47 ms respectively, leading to a difference of about 60 %. As reported in [136], the lower ignition delay times predicted when accounting for the compression phase through variable volume simulations, is as a result of the effect of the radical pool formed during the compression stroke. The second-stage ignition delay may be defined as the time interval between the end of first-stage ignition delay and the point of hot (second) ignition. By comparing the computed pressure history of Figure 4.3 and Figure 4.4, we observed that while the radical pool produced in the compression stroke has a significant effect on the first-stage ignition delay, the impact on the second-stage ignition delay is however negligible.

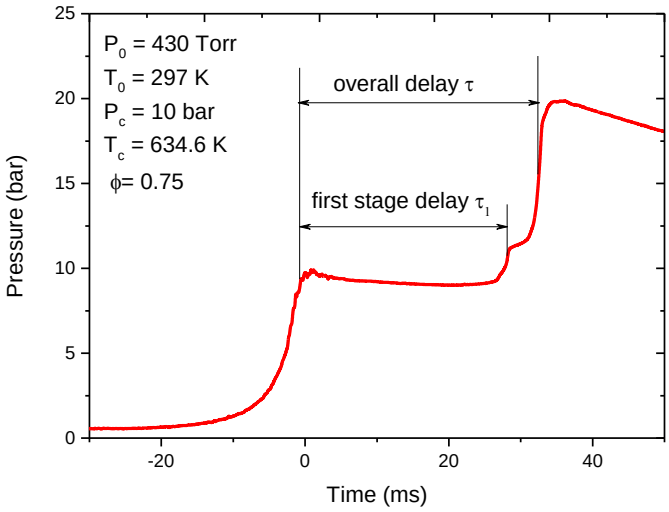

Figure 4.1: Typical pressure trace illustrating the definition of first stage and overall delay used in this study.

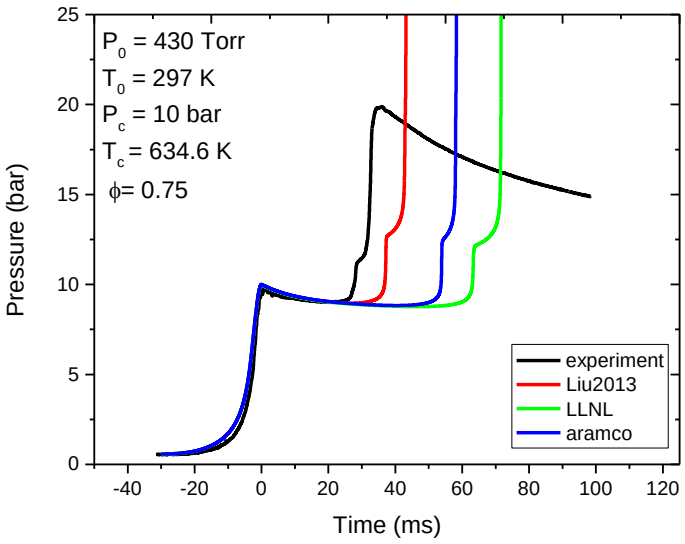

Figure 4.2: Comparison of experimental data with results predicted by the three DME mechanisms.

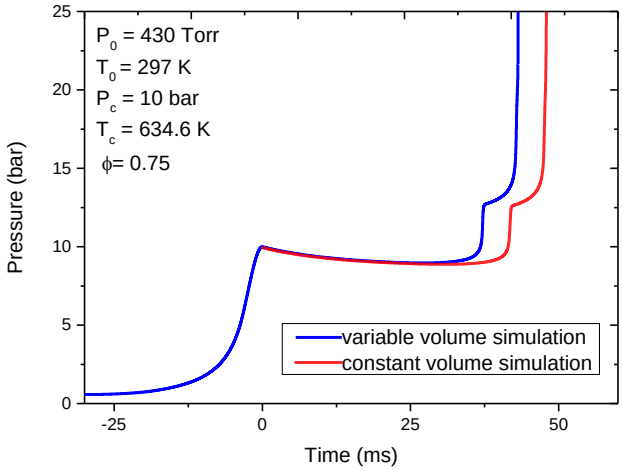

Figure 4.3: Pressure trace diagram showing result of two modelling approaches and illustrating the effect of the compression stroke using the 'Liu2013' mechanism for conditions P = 10 bar and T = 655 K.

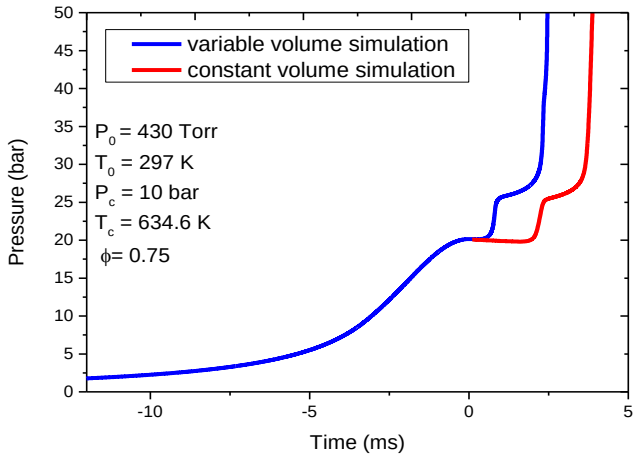

Figure 4.4: Pressure trace diagram showing results of two modelling approaches and illustrating the effect of the compression stroke using the 'Liu2013' mechanism for conditions P =20 bar and T = 720 K.

Figure 4.5 shows a direct comparison of the predicted ignition delays from each kinetic scheme with the experimental data of Mittal [136]. The results show that for the three schemes, there is reasonable agreement between the predicted and experimental data across a large part of the temperature range. However significant discrepancies of up to a factor of 5 also exist for the rich case of ϕ = 1.5, P = 10 bar both at the high and low temperature region.

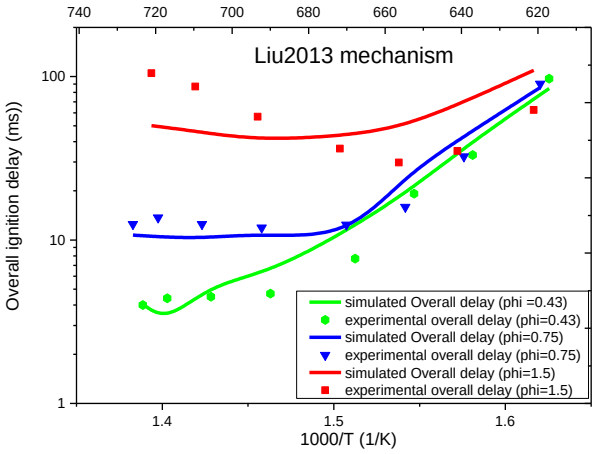

(a)

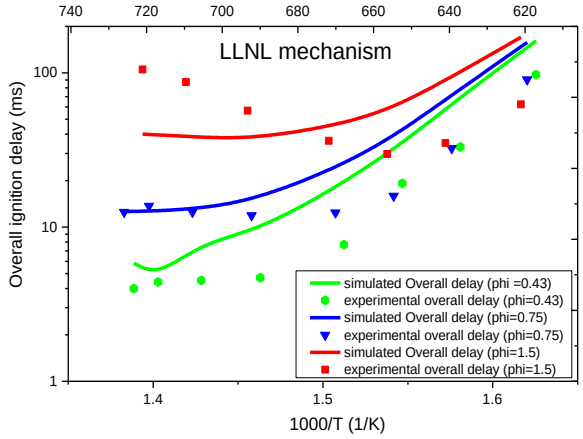

(b)

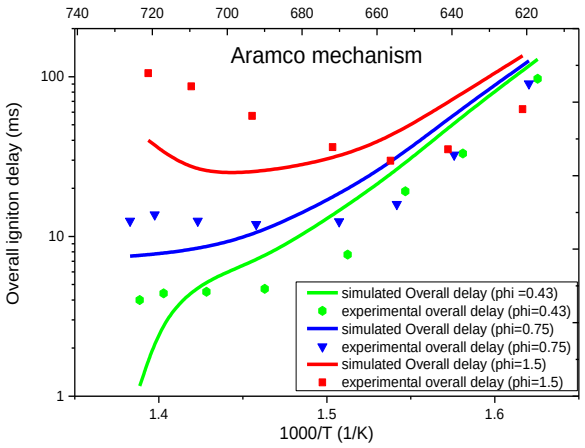

(c)

Figure 4.5: Comparison between experimental [136] and simulated DME ignition delays (a) Liu2013 mechanism (b) LLNL mechanism (c) Aramco mechanism. In all cases P = 10 bar.

4.2.3 Local sensitivity analysis

Local sensitivity analysis was performed in order to identify the key reactions driving the predicted ignition delays at conditions of P =10 bar, ϕ = 0.75 and T = 615 K - 723 K. Figure 4.6a shows the normalised local sensitivities of the 12 most dominant reactions for the Liu2013 mechanism alongside sensitivities of the same reactions for the LLNL and Aramco kinetic schemes at T = 649 K, representing the impact of 25% increase of *A*-factors on the ignition delay output. The reactions captured in the local sensitivity analysis are quite consistent across the three schemes with little differences in the relative size of the sensitivity indices. The results of local sensitivity analysis shows that across the three chemical kinetic models employed, the overall ignition delays are most sensitive to the isomerisation of methoxymethyl-peroxy radical, $CH_3OCH_2O_2$, producing a hydro-peroxy-methoxymethyl radical, $CH_2OCH_2O_2H$. The hydro-peroxy-methoxymethyl radical formed is consumed through two different reaction pathways: one is through β scission leading to the formation of two molecules of formaldehyde and a hydroxyl radical ($CH_2OCH_2O_2H = CH_2O + CH_2O + OH$) and the other route is via oxygen addition leading to the formation of peroalkylhydroperoxide ($CH_2OCH_2O_2H + O_2 = O_2CH_2OCH_2O_2H$) which reacts further by a second isomerisation to yield two OH radicals formed via the reactions of $O_2CH_2OCH_2O_2H = HO_2CH_2OCHO + OH$ and $HO_2CH_2OCHO = OCH_2OCHO + OH$. At the low temperature condition, the oxygen addition step is the key reaction route promoting chain branching and consequently autoignition leading to a 'cool flame' while the β scission pathway leading to the formation of only one OH radical, is the key ignition-inhibiting reaction step [136, 214]. The term 'cool flame' is used in the sense that the supposed flame is unable to attain its adiabatic temperature, resulting in the incomplete oxidation of the reactive mixture [214]. Based on the result of the local sensitivity analysis shown on Figure 4.6b, the beta scission reaction step has increased dominance across the three schemes at higher temperatures (i.e. T = 723 K) thus explaining the reason for the observed decrease in reactivity and formation of the NTC region in the intermediate temperature range. While the low temperature reactions captured at T = 723 K is quite consistent across the three schemes, a good number of the reactions involving the smaller molecules that are important in the Liu2013 mechanism are not selected in the LLNL and Aramco mechanism.

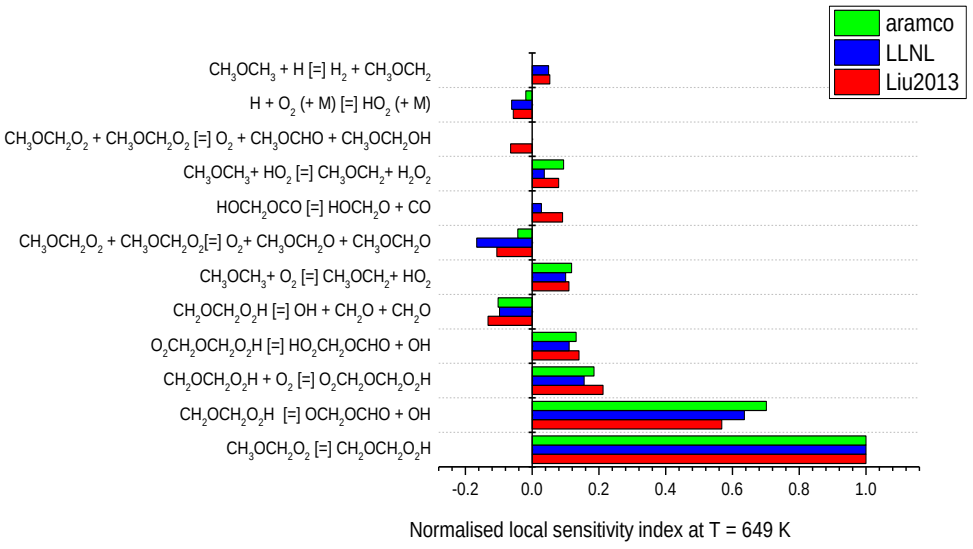

(a)

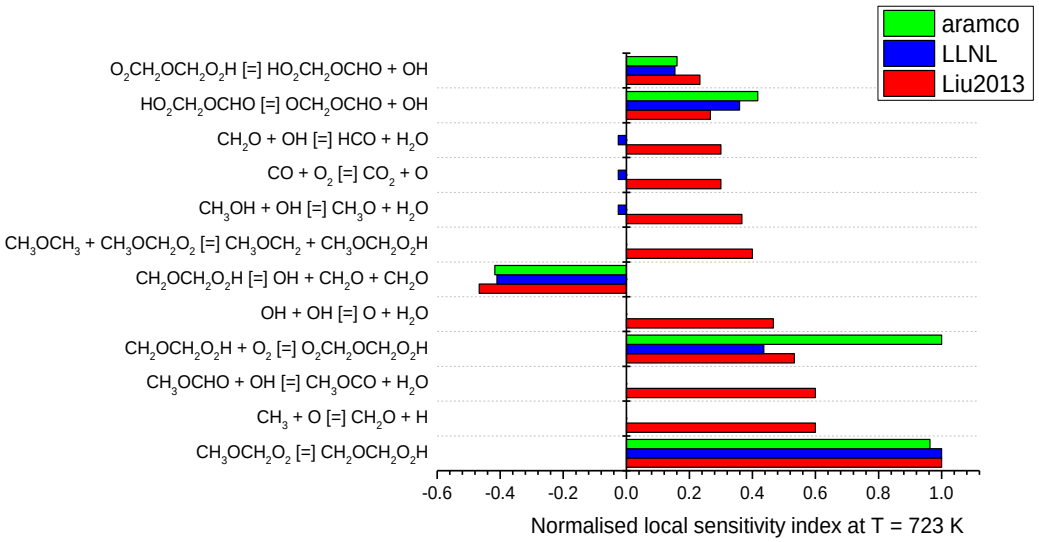

(b)

Figure 4.6: Normalised local sensitivities of overall ignition delay times to reaction rates for DME/O_2/N_2 mixture at P = 10 bar, ϕ = 0.75 using the three DME schemes (a) T_c = 649 K (b) T_c = 723 K.

4.2.4 Uncertainty quantification

Figure 4.7 shows the results of the uncertainty propagation in the ignition delays predicted by the three mechanisms at ϕ = 1 and P = 10 bar. In Figure 4.7, we can see that although the ignition delays predicted by the three mechanisms based on their

original parameterisation are in reasonable agreement with measured data, the predicted ranges of the output uncertainties are large, spanning up to three orders of magnitude under some conditions. While this seems contrary to common-sense expectation, a valid explanation could however be provided for the observed discrepancies in the uncertainty study. It should be noted that the parameterisation of key reactions in the mechanism may have not been based on fundamental data of chemical kinetic studies but by available experimental data such as those of ignition delays measurements in the RCM. Within the framework of ignition delay prediction, the ratio of the propagation to branching fluxes is quite important and must be captured correctly in the computation in order to obtain an accurate predicted output. However in the approach employed in the uncertainty analysis of this study, each key reaction rate is varied independently and this could potentially alter the balance between these important reaction steps. A study on DME, focused on the uncertainty analysis of predicted concentration profiles of CH_2O, CH_3OCHO and H_2O_2 in a flow reactor, at a temperature range of T = 50 – 750 K, ϕ = 0.6 and P = 1 bar was carried out side by side with this work and was reported in [166]. In the work [166], the experimental data of Guo [128] involving flow reactor measurements of the concentration profiles of various species relevant to combustion studies was used a reference. It is worth pointing out that the original parameterisation for the three mechanisms also led to a significant spread in the predicted uncertainties within the flow reactor simulations (Figure 4.8). As shown in Figure 4.8, particularly at low temperatures, the uncertainties spanned several orders of magnitude for predicted mole fractions of all species and within this temperature region, the experimental profiles for CH_2O were within the range of the 95^{th} percentile of the predicted CH_2O distribution. Since the level of agreement of the model with measured data is relatively poor for both sets of chosen output data (species concentrations and ignition delay times) it will therefore be useful to examine if a similar set of reactions dominates the predicted output variance in the HDMR analysis of both cases. The disparity between the mean and median values of the predicted distributions shown in Figure 4.7 indicates that the data does not follow a normal distribution but rather a skewed distribution (lognormal distribution). Further discussions elucidating this point and the possible reason for such behaviour is presented in section 4.3.1.3 where a typical distribution from the high dimensional model representation (HDMR) analysis is shown for the predicted *n*-butanol ignition delays.

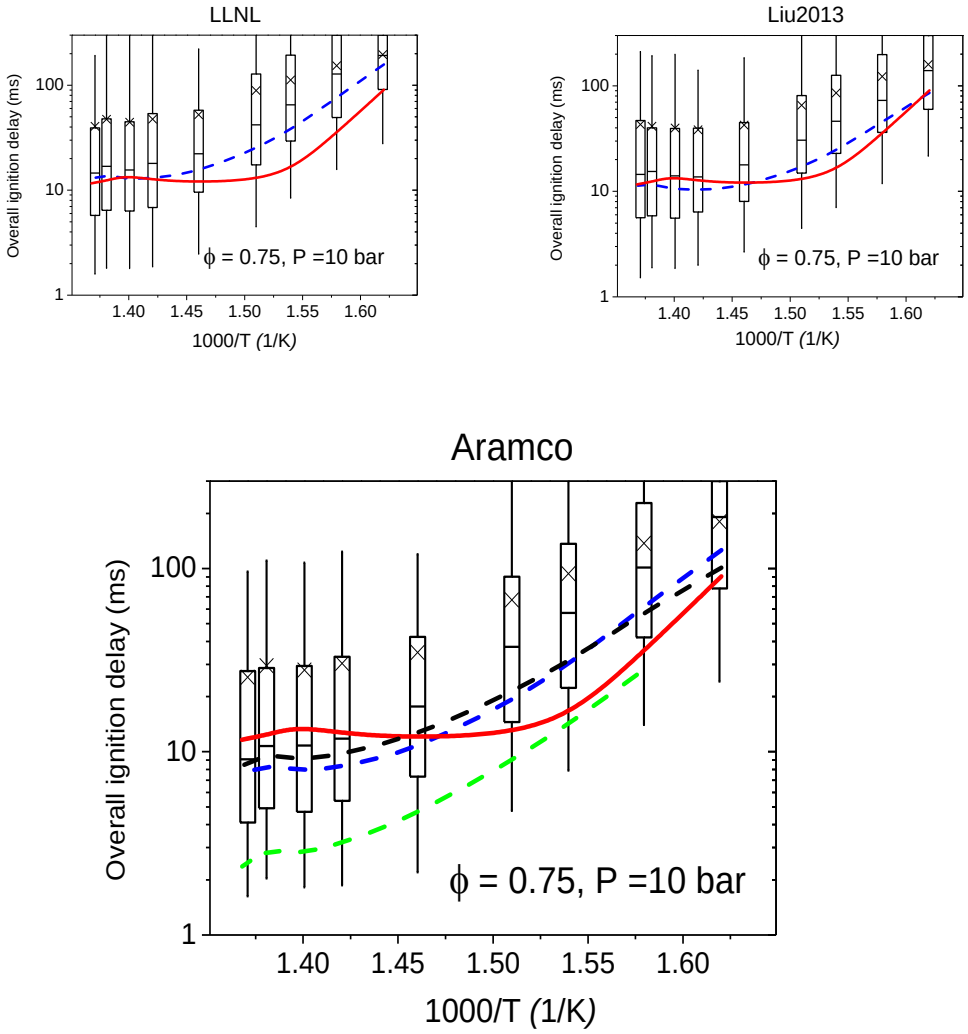

(c)

Figure 4.7: Comparison between experimentally measured DME ignition delays (red solid line) and simulated profiles for the RCM data [136]. The dashed blue line represents the model simulations with unperturbed parameter values. The whiskers represent 5th and 95th percentiles while the box represents 25th and 75th percentiles respectively based on a quasi-random sample of 256 model runs. The large crosses and horizontal lines represent the mean and median of the predicted output from the 256 simulations respectively (a) LNNL mechanism (b) Liu2013 mechanism (c) Aramco mechanism. In (c) the dashed green line represents the effect of modifications of the $RO_2 \rightarrow QOOH$ and $QOOH \rightarrow 2CH_2O + OH$ channels based on the data of Eskola et al. [215]. The dashed black line represents further modification of the chain-branching step $QOOH+O_2$ by a factor of 5.

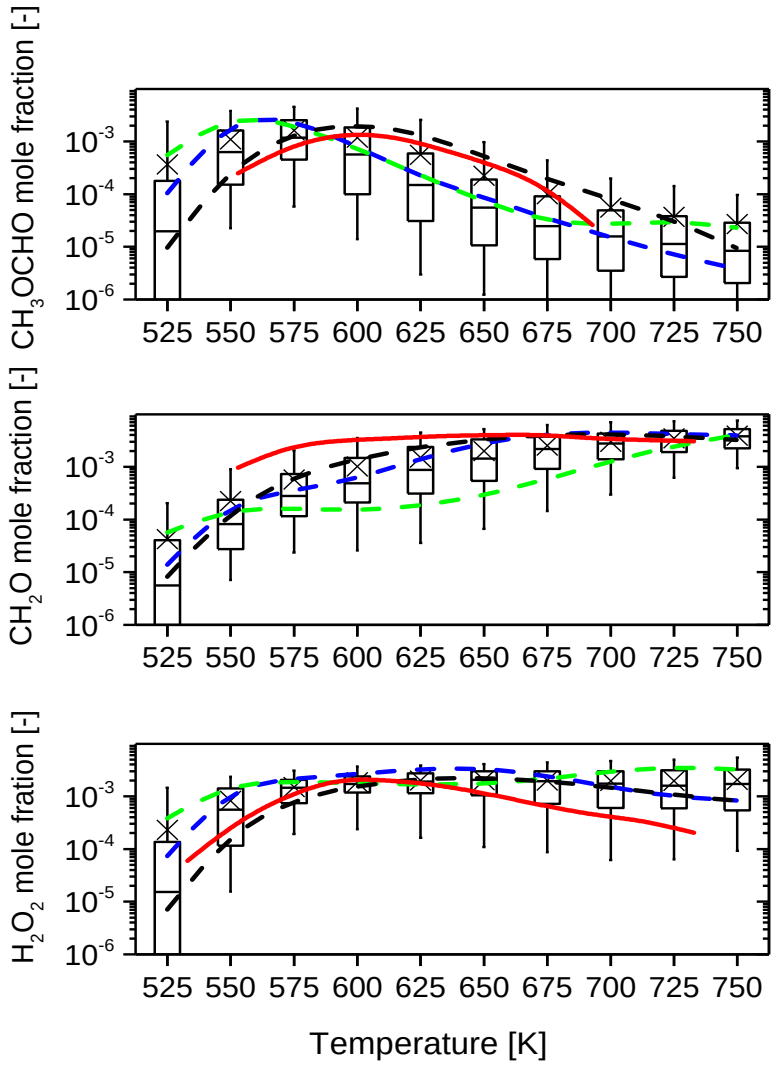

Figure 4.8: Comparison between experimentally measured DME species profiles (red solid line) and simulated profiles for the Princeton flow reactor data [128] for the Aramco mechanism. The dashed blue line represents the model simulations with unperturbed parameter values. The whiskers represent 5th and 95th percentiles while the box represents 25th and 75th percentiles respectively based on a quasi-random sample of 256 model runs. The large crosses and horizontal lines represent the mean and median of the predicted output from the 256 simulations respectively. The dash green line represents the effect of modifications of the $RO_2 \rightarrow QOOH$ and $QOOH \rightarrow 2CH_2O + OH$ channels based on the data of Eskola et al. [215]. The dashed black line represents further modification of the chain-branching step $QOOH+O_2$ by a factor of 10.

4.2.5 Global sensitivity study

Figure 4.9 shows the main first-order and second-order global sensitivity indices obtained from the HDMR analysis for ignition delay simulations carried out at some selected conditions of temperature and equivalence ratio. The shading for each reaction or pairs of reactions is explained in the legend. Sensitivity indices of up to second-order were estimated to a good accuracy (i.e. coefficient of determination $R^2 > 80\%$) within the context of HDMR analysis based on simulation of 4096 samples for the Liu2013 and LLNL mechanism and 8192 samples for the Aramco mechanism. The data for sample cases in which ignition was either predicted during the compression phase or not captured at all by the model were eliminated and not included as part of the data for constructing the meta-model fit as their inclusion would normally result in a very poor fit.

In Figure 4.9, we can see that the sensitivity indices of the selected reactions in the HDMR analysis are relatively similar across the three schemes in line with the results obtain using the local sensitivity approach (section 4.2.3). At the condition of $\phi = 0.75$ and T= 649 K, the isomerisation reaction of methoxymethyl-peroxy radical, $CH_3OCH_2O_2$ dominated in terms of its contribution to the overall variance in the predicted ignition delay with its contribution amounting to over 60 % across the three kinetic schemes. The other key routes contributing to the overall variance but to a lesser degree includes the $CH_2OCH_2O_2H + O_2 = O_2CH_2OCH_2O_2H$, $O_2CH_2OCH_2O_2H = HO_2CH_2OCHO+OH$ and $HO_2CH_2OCHO = OCH_2OCHO + OH$. Therefore the reaction of hydroperoxymethyl formate, HO_2CH_2OCHO is a very important reaction step in the current form of the three schemes in terms of the production of OH which is crucial for autoignition at low temperature. Gao and Nakamura [216] however reported that there could possibly be other OH formation routes present, based on their detection of some non-negligible species concentrations such as HCHO, HCOOH, and CH_3OCHO in the low temperature region. At higher temperatures, the relative importance of hydroperoxymethyl formate, HO_2CH_2OCHO decreases due to the increase in the competition between the chain branching step $CH_2OCH_2O_2H + O_2 = O_2CH_2OCH_2O_2H$ and chain propagation step $CH_2OCH_2O_2H = CH_2O + CH_2O +OH$. As mentioned previously in section 4.2.3, the increase in dominance of the propagation step at higher temperatures has a suppressive effect on the chain branching pathway. While Figure 4.9

shows the presence of a few second-order terms, their contribution to the overall predicted ignition delay distribution is however quite small.

In the case of the flow reactor (Figure 4.10), a higher number of reactions (a total of 15) were found to be important and accounted for between 60 % - 85 % of overall variance compared to just nine reactions in the case of the RCM ignition delays. In addition a higher percentage of the total variance is accounted for by second-order effects at the high temperature point. Across the three chemical kinetic schemes, the isomerisation reaction of $CH_3OCH_2O_2$ dominated the predicted uncertainties in both ignition decays and CH_3CHO production across all temperatures. Across all three species (CH_2O, CH_3OCHO and H_2O_2) the isomerisation reaction was however dominant only at the lowest temperature of 550K. As we can see in Figure 4.10, over 40 % of the uncertainties in the predicted species concentrations can be accounted for by the uncertainties in the isomerisation rate at 550 K, implying that low temperature experimental measurements involving key species such as those reported in [128] could well provide relevant constraints on the forward rate of the isomerisation step at the low temperature region. The main pathways that dominate the uncertainty in predicted ignition delays and species mole fractions for CH_2O, CH_3OCHO and H_2O_2 at low temperatures are shown in Figure 4.13.

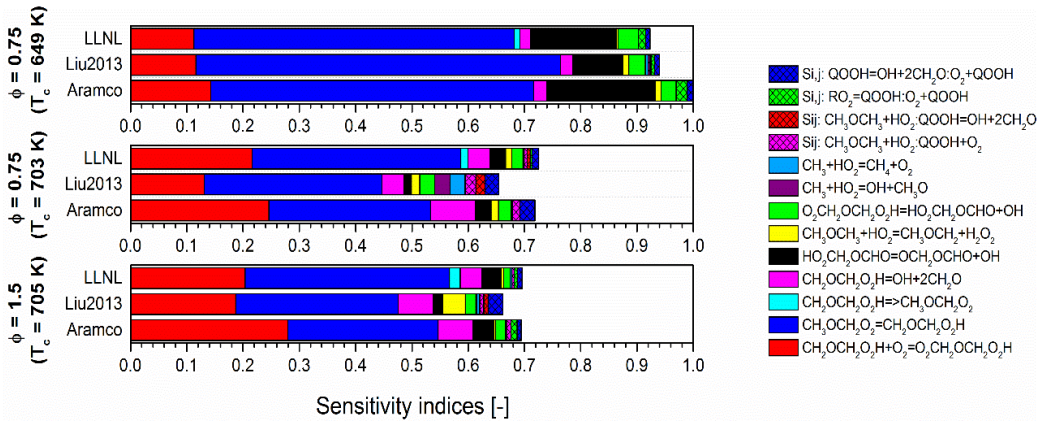

Figure 4.9: Main sensitivity indices (first- and second-order) for simulated DME ignition delays with respect to reaction rates at selected temperatures and pressures. A comparison between each mechanism is given and shading for each reaction or pair of reactions is shown in the legend.

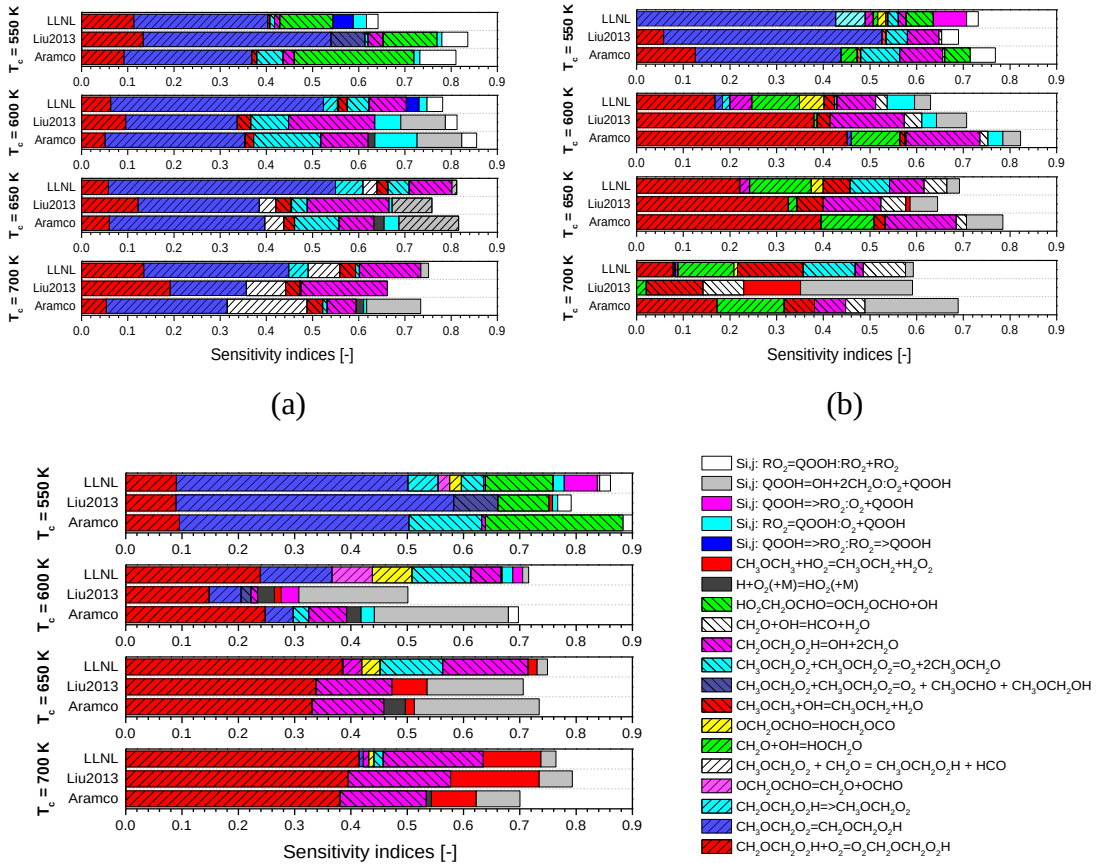

Figure 4.10: Main sensitivity indices (first- and second-order) for flow reactor simulations with respect to reaction rates at selected temperatures. A comparison between each DME mechanism is given and shading for each reaction or pair of reactions is shown in the legend. (a) CH_2O mole fraction (b) H_2O_2 mole fraction (c) CH_3OCHO mole fraction (d) legend.

Figure 4.11 shows the HDMR first-order component functions (solid) of predicted ignition delays using the Aramco mechanism for three of the most dominant reactions at a representative condition of ϕ = 1, P = 10 bar and T = 703 K (middle case in Figure 4.9), superimposed upon the scatter plots caused by uncertainties in the rest of the important input parameters while Figure 4.12 shows the second-order component function for a combination of the chain propagation and branching routes. While the first-order component function represents the impact of the changes in a single reaction A-factor, the second-order component function gives an idea of the second order effects caused by interaction of a pair of the input parameters upon the predicted delays over

the entire input parameter range. As shown in Figure 4.11a, the first-order component response for the isomerisation route is negative, meaning that the predicted ignition delays would decrease as the rate of the isomerisation route is increased. As the rate of isomerisation is increased, the scatter in the predicted ignition delays also becomes much wider (up to three orders of magnitude) implying that the predicted ignition delay distribution would vary for every selected value of the rate constant for the isomerisation reaction. The reason for the widening of the predicted ignition delay distribution could be attributed to the increase in the relative importance or dominance of other competitive reaction routes as the isomerisation rate is increased. For example, a faster isomerisation rate would lead to an increase in the rate of formation of QOOH which in turn would increase the dominance of the competition between the branching and propagation steps. The inability of the model to accurately represent the balance in the rate of the above two competing steps (branching ratios), would obviously lead to higher predicted uncertainties as the isomerisation rate is increased, and as a result, the width of the predicted ignition delay distribution becomes much wider as shown in Figure 4.11a. The value of the logarithm of the ignition delay measured for these conditions is just over 1, therefore it is clear that all of the two orders of magnitude span in the rate constant of the forward isomerisation step (Figure 4.11a) could enclose the experimental data depending on the rates of other routes.

As expected, the component function for the branching step QOOH + O_2 (Figure 4.11b) gives a negative gradient, meaning that reducing the rate will result in longer ignition delays. Based on the uncertainty factor of 10 that was chosen for this step, the first-order effect on the predicted ignition delays spans an order of magnitude within the range of the input parameter while that of the competing propagation step (Figure 4.11c) extends over a factor of about 0.5. A complex second-order relationship is observed between the chain branching and propagation routes as presented in Figure 4.12. Although this second-order term accounts for less than 3 % of the total variance, the complex nature of the correlation implies that significant order of magnitude changes in the predicted ignition delay distribution can occur depending on the parameter pair that is chosen in the mechanism for both channels. As a result, an attempt to tune the input rate parameters to give better agreement with measured data could prove extremely difficult as pointed out in Mittal [217].

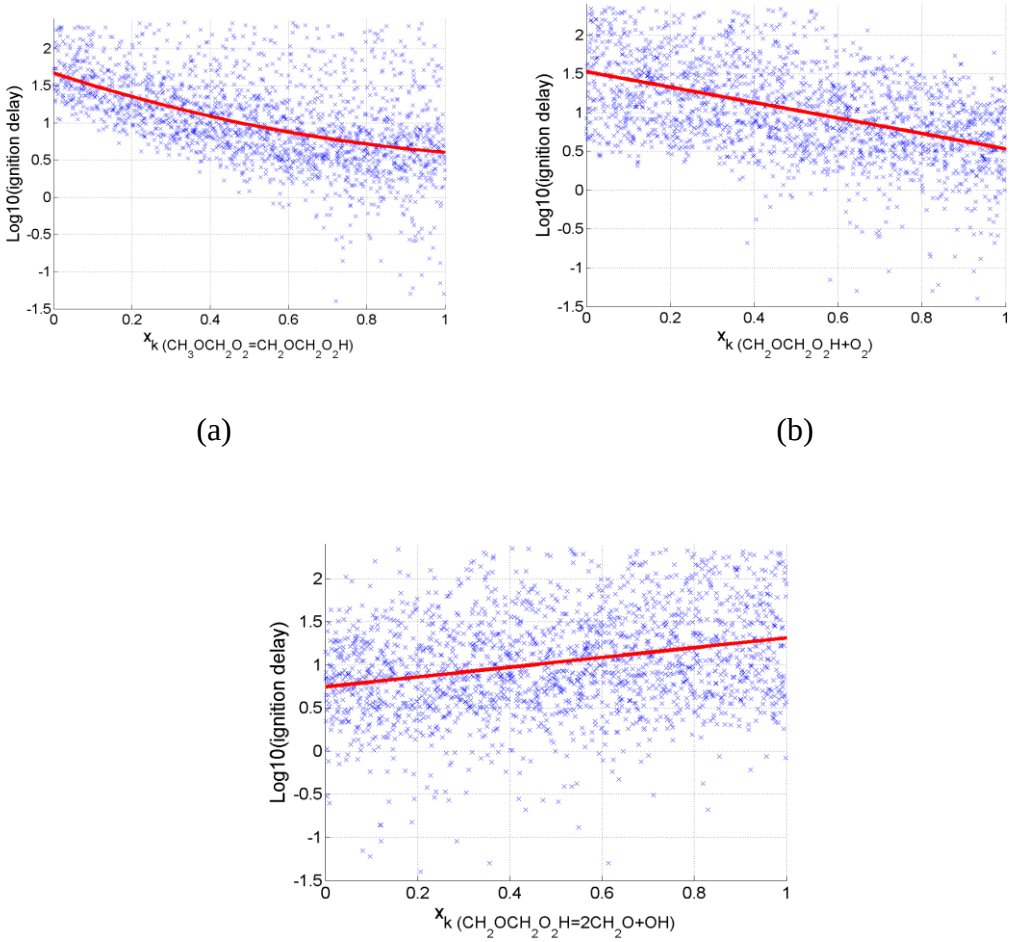

Figure 4.11: HDMR component functions (solid line) of simulated DME ignition delays shown on-top of the scatter resulting from the quasi-random sampling in the case of first-order functions. P = 10 bar, ϕ = 0.75, T = 703 K. Sensitivity with respect to (a) forward rate of RO_2 = QOOH (b) forward rate of QOOH + O_2 (c) forward rate of QOOH = $2CH_2O$ + OH. Results are based on the Aramco mechanism.

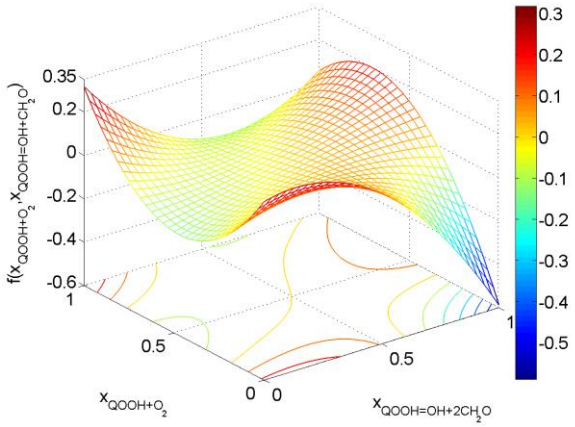

Figure 4.12: Second-order component function of simulated DME ignition delays representing the interactive effect of forward rates for QOOH + O_2 and QOOH = $2CH_2O$ + OH. Results are based on the Aramco mechanism.

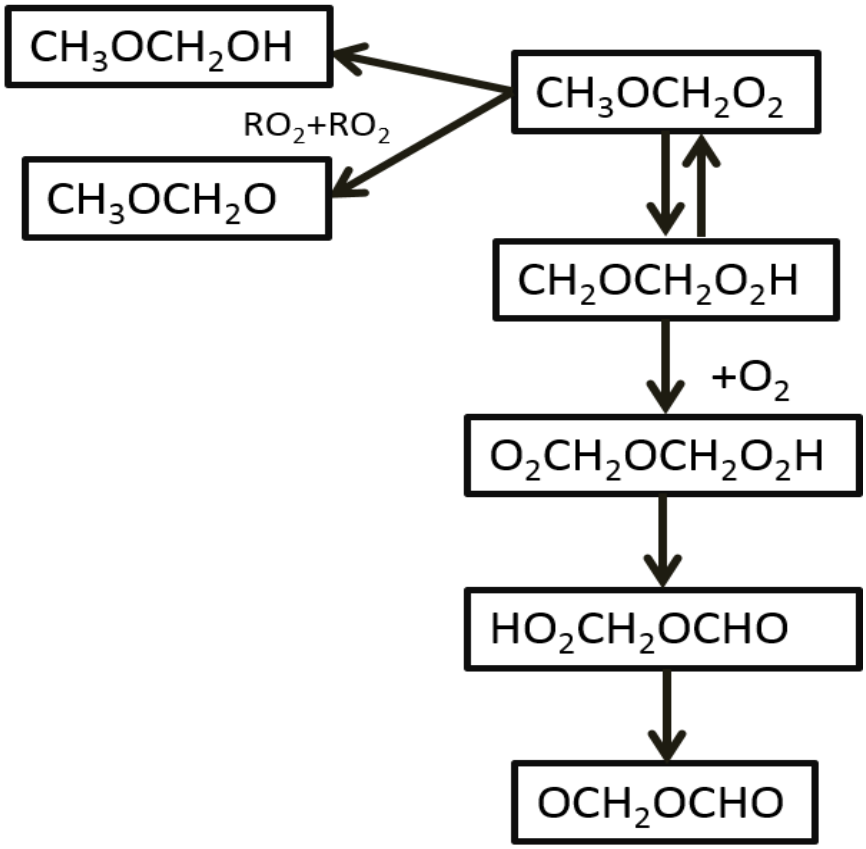

Figure 4.13: Main pathways that dominate the uncertainty in predicted DME ignition delays and species mole fractions for CH_2O, CH_3OCHO, H_2O_2.

4.2.6 Impact of updates on chemical kinetic model

It is clear from the uncertainty and sensitivity study that it would be very challenging to tune the kinetic model to match with experimental data as no single reaction channel dominated the predicted uncertainties across all temperature. A comprehensive optimisation study such as the one reported in Turanyi [218] might not even suffice as the optimised rate constants would still be subject to large uncertainties. Further fundamental detailed kinetic studies of the key channels captured in the study would therefore be highly beneficial in order to reduce the predicted uncertainty range and improve the accuracy and robustness of the model. A recent study carried out by Eskola et al. [215] was found to contain useful data for a number of reaction routes that were considered to be very significant in this study. In the study of Eskola, pressure- and temperature-dependent rate constants were determined for the various reaction routes using a combination of master equation calculations and experimental data of the overall rate constant and also OH yields measured at low temperature. A comparison of the original rate constants in the DME scheme for the isomerisation reaction $CH_3OCH_2O_2 \rightarrow CH_2OCH_2O_2H$ (Figure 4.14a) and the chain-propagation step $QOOH \rightarrow OH + 2CH_2O$ (Figure 4.14b) with values obtained from the study of Eskola for the same set of reaction is presented in Figure 4.14. As shown in Figure 4.14, the data of Eskola display a pressure dependency for the two reaction routes in line with the recommendation of previous studies [219], whereas in the case of the Aramco mechanisms the current rate parameters for the two reactions are independent of pressure. The current rate in the mechanisms for the isomerisation step is considerably slower than that in the study of Eskola across all temperatures and pressures with the difference rising up to about an order of magnitude at low temperatures. In the case of the chain-propagation step, although the pressure dependency of the Eskola data is not captured by the parameterisation of this rate in the kinetic model, the model's data however lay in-between that of Eskola. Also, the temperature dependency of the Eskola rate data is significantly different from that of the original mechanism, with the value of the rate constant for the mechanism approaching the upper pressure limit at higher temperatures and 1 bar data at lower temperatures. The study of Eskola also supplied data for well skipping channels in which the alkyl + O_2 step proceeds directly to RO_2, QOOH or $2CH_2O + OH$, and RO_2 directly forms $2CH_2O + OH$. In all, about nine

pressure and temperature dependent rate constants were made available from the study of Eskola [215] for the $CH_3OCH_2 + O_2 \rightarrow CH_3OCH_2O_2$ system in the form of Chebyshev polynomials.

In order to assess the impact of the Eskola data on the predictions of the DME scheme, the Aramco scheme was updated with rate constants from the study of Eskola. The update on the Aramco scheme lead to larger discrepancy in the predicted ignition delays (shown as dashed green line in Figure 4.7c) for condition of P = 10 bar and ϕ = 0.75 across the temperature range as the agreement with experiment is worsened. We saw previously from Figure 4.11a that the scatter in the predicted ignition delays increased with increase in the rate of isomerisation due to the fact that the influence of other reactions became more significant with the increase in this rate. It is obvious that the current DME mechanism contains correlations that were introduced in the model as a result of tuning it to fit with several experimental data sets due to the unavailability of the required detailed fundamental chemical kinetic studies. Therefore updating only a subset of the dominant rates could potentially alter the equilibrium between the branching and propagation step thereby worsening the agreement with experimental data and this should therefore be accounted for. The difference between the updated rate parameter for the propagation step and that of the Aramco mechanism is quite small at around the low temperature region at 10 bar and hence further changes to the predicted ignition delay could be accomplished by adjustment to the branching step. Whilst normally tuning mechanisms to match experimental data is not recommended, further modifications were however made to the rate of $QOOH + O_2$ just for demonstrative (illustrative) purposes. The effect of reducing the rate constant of $QOOH + O_2$ by a factor of 5 on the predicted ignition delay (dashed black line) at a pressure of 10 bar is shown in Figure 4.7c. Interestingly, the update on the branching step led to very significant improvement in the agreement with the experimental data. Similarly updates for the atmospheric pressure flow reactor simulations, reported in [166], are highlighted in Figure 4.8 (dashed black line) but in this case a reduction by a factor of 10 gives very good agreement with the measured data for all the species considered.

The fact that different degree of modification was needed in order to bring the predicted output of both the high pressure RCM and low pressure flow reactor in very good agreement with the respective measured data, suggests that some level of pressure

dependency might exist in the QOOH + O_2 system. Notwithstanding, the above submission is still subject to validation as previous studies on QOOH + O_2 in other systems have only reported a weak pressure dependency in contrast to a very strong pressure dependency for the decomposition channel [220, 221].

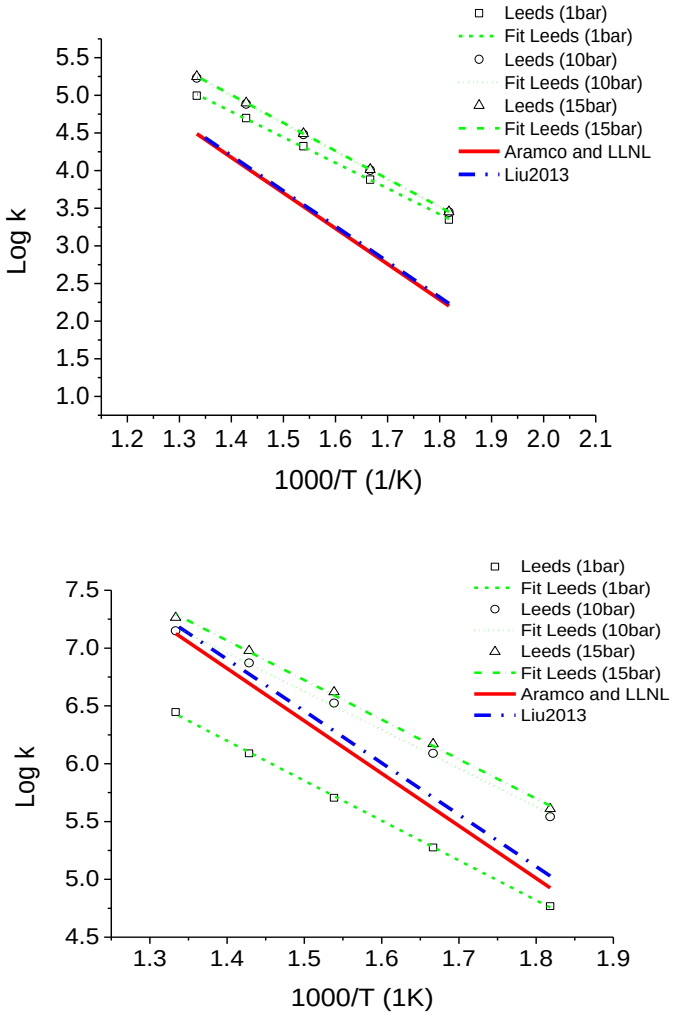

(b)

Figure 4.14: Comparison of current data within the LLNL, Liu2013, and Aramco mechanisms compared to new data from a recent study of Eskola et al. [215]: (a) RO_2 →QOOH and (b) QOOH→$2CH_2O$ + OH.

4.3 Chemical kinetic modelling study of *n*-butanol oxidation in a rapid RCM and JSR

4.3.1 *n*-butanol RCM Studies

4.3.1.1 Comparison of model prediction with experimental data

Figure 4.15 shows the comparison of Weber data [194] with the variable volume pressure traces simulated using the mechanism of Sarathy [148] and the high temperature mechanisms of Moss [140] and Black [145] for stoichiometric *n*-butanol/O_2/N_2 mixture at compressed conditions of T = 737 K and P = 15 bar. Across the range of temperatures investigated, only the Sarathy mechanism demonstrated the capability to reproduce the ignition delays within the experimental time frame. However, the pressure traces predicted by the mechanism of Moss and that of Black, gave very good agreement with the measured pressure trace during the compression phase and post compression phase (pre-ignition phase). In other words, both mechanisms very well described the lack of chemical reactions. For the purpose of comparing the three mechanisms with the experimental data in terms of the predicted ignition delays, constant volume simulations were performed with the simulation duration extending well beyond that of the experimental measurements. Figure 4.16 shows the result of the predicted constant volume ignition delay times for the three mechanisms in comparison with Weber data. The ignition delays predicted by the kinetic model of Moss and that of Black are significantly longer than the measured data. Although the level of discrepancy between the measured data and the two models (Black and Moss models) is unexpectedly large, it is important to note that both mechanisms have not been validated within the condition space of the measured data. The modelling results and analysis presented in the rest part of this work are based on the Sarathy model. In Figure 4.17 we observe that the predicted ignition delays decrease with increases in temperature across the entire temperature range in line with the experimental observations. The absence of the NTC region captured in the measured data is also accurately predicted by the Sarathy mechanism.

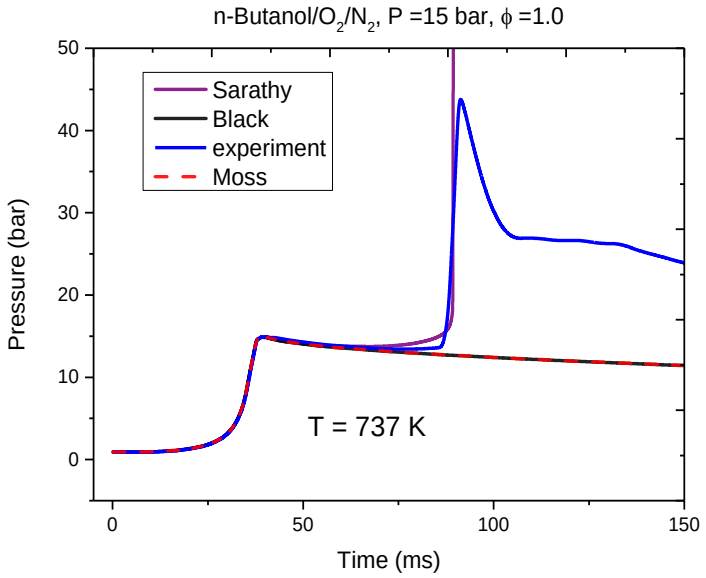

Figure 4.15: Comparison of experimental pressure trace with variable volume simulations for three mechanisms [140, 145, 148].

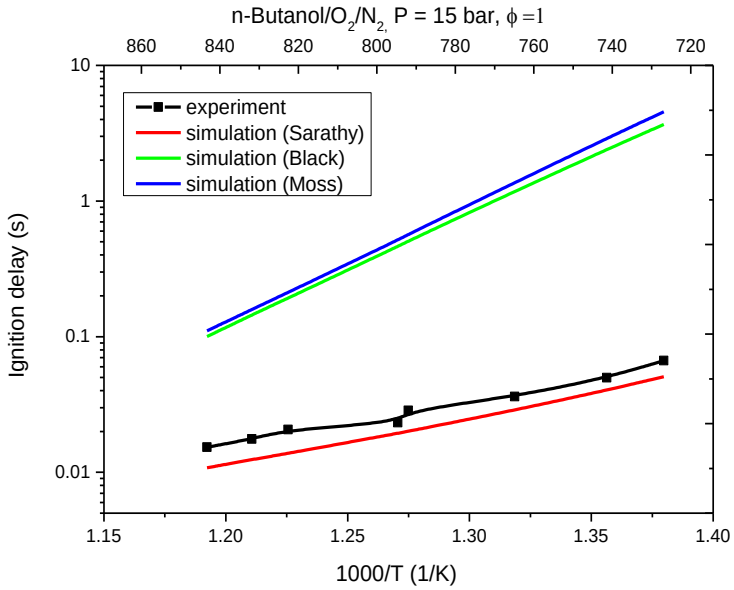

Figure 4.16: Comparison of experimental pressure trace with constant volume simulations for three chemical kinetic models [140, 145, 148].

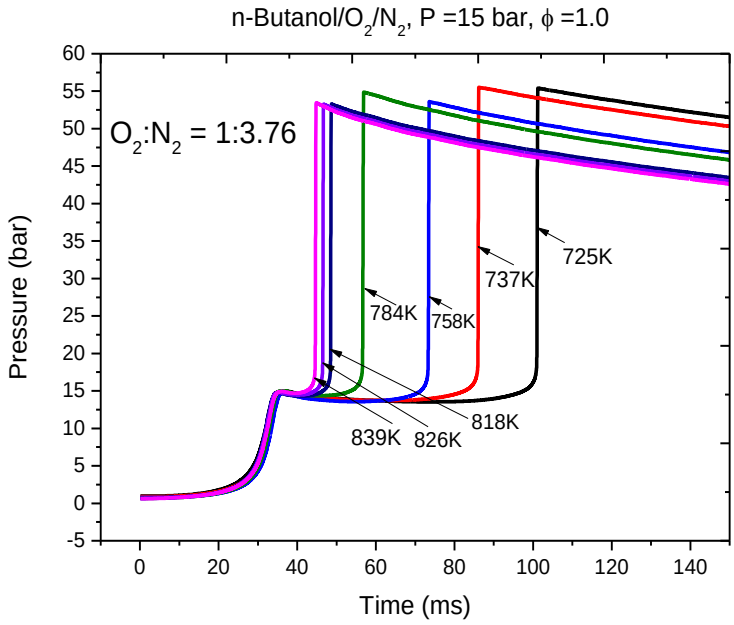

Figure 4.17: Pressure traces simulated for *n*-butanol/O_2/N_2 at different compressed temperatures using the model of Sarathy [148].

Figure 4.18 shows a comparison of predicted ignition delays with the data from Weber et al. for a compressed pressure of 15 bar, T = 678 – 925 K and ϕ = 0.5 -2.0. In common with Sarathy et al. and Weber et al. [148, 194], we find in Figure 4.18 that under these conditions, the RCM data is predicted to a reasonable level of accuracy across the entire equivalence ratio range. However, under rich conditions, the model's over-prediction of the ignition delay data could be over a factor of 5 for the low temperature region (i.e. T < 700 K). Under stoichiometric conditions, at a higher pressure of 30 bar (Figure 4.19), which is above the pressure range at which the model was constrained by ignition delays, the model over-predicts the Weber data by a factor of about 2 across a major part of the temperature range. In addition, the decrease in ignition delays when pressure is increased from 15 - 30 bar is under-represented by the model. It is also apparent from Figures 3.18 and 3.19 that *n*-butanol does not exhibit the well-known two-stage, NTC behaviour commonly seen for linear alkanes and shown for DME ignition delays in our previous work [166].

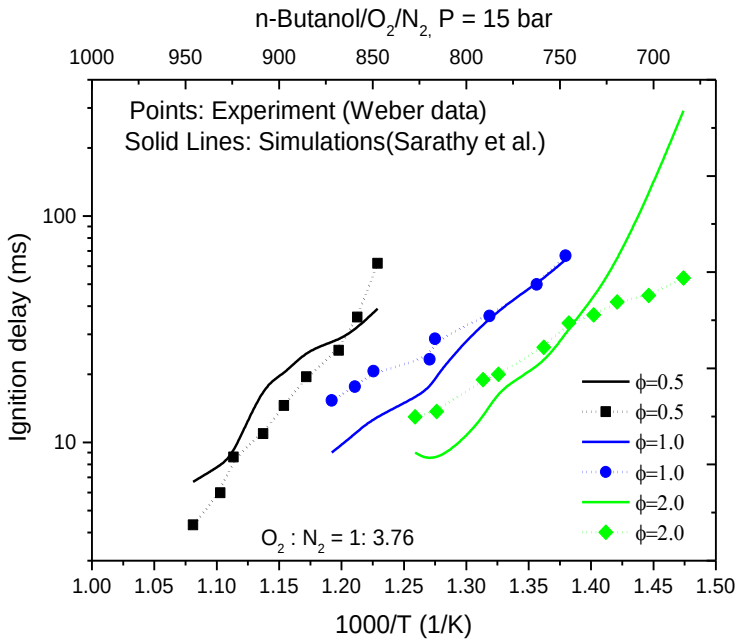

Figure 4.18: Comparison of ignition delays predicted by the Sarathy model [148] with Weber et al. data [194] for conditions of P = 15 bar and equivalence ratios ϕ = 0.5 and 2.0.

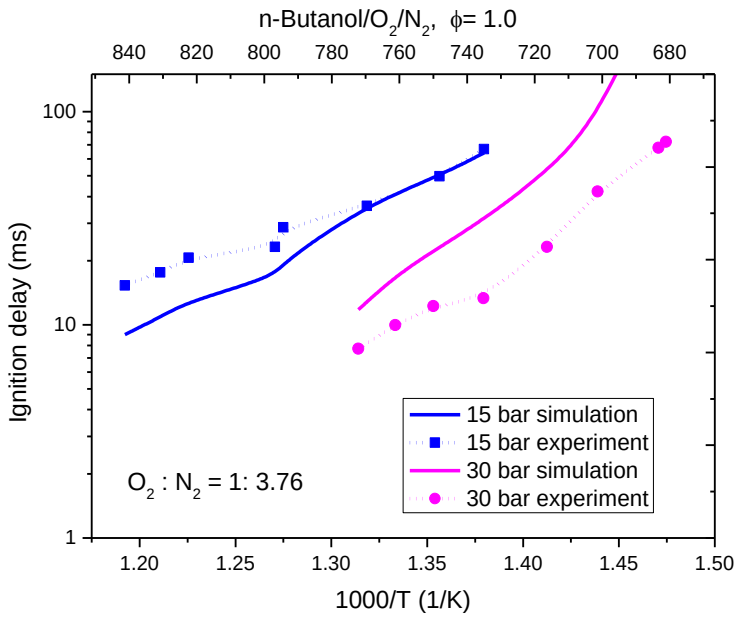

Figure 4.19: Comparison of ignition delays predicted by the Sarathy model [148] with Weber et al. data [194] under stoichiometric conditions at P = 15 bar and 30 bar.

Figure 4.20 shows that under constant volume stoichiometric simulation conditions of 20 bar, the kinetic model predicts the Leeds data quite well at high temperatures but over predicts the experimental data by about a factor of 2 at lower temperatures below T = 700 K. The discrepancy is smaller than that shown at 30 bar in Figure 4.19 but is still significant. It is obvious from Figure 4.18 that a linear fit to both the measured and simulated data at stoichiometric conditions would result in the model's over-prediction of the measured data at low temperature condition in agreement with the modelling result of the Leeds data shown in Figure 4.20.

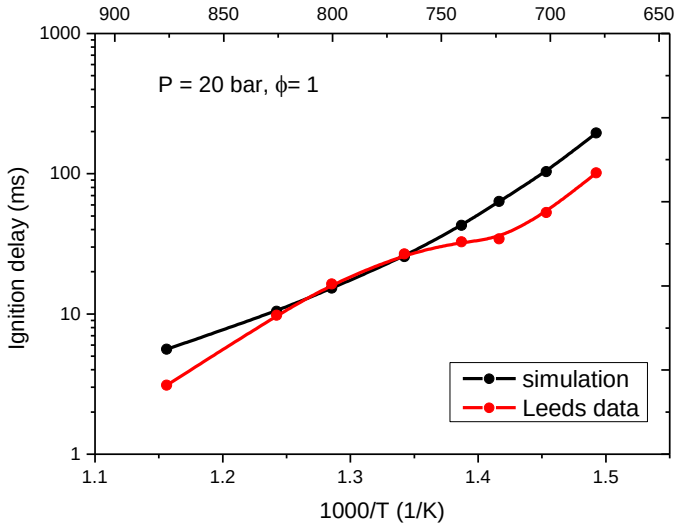

Figure 4.20: Comparison of predicted ignition delays of *n*-butanol with Leeds data for conditions of P = 20 bar under stoichiometric conditions of ϕ = 1.

4.3.1.2 Local sensitivity analysis

Local sensitivity analysis employing the Brute-force method was conducted for *n*-butanol for a range of conditions across T = 678 - 898 K, ϕ = 0.5 - 2.0 and P = 15 bar. The results of such analysis are illustrated in Figure 4.21 for fifteen (15) of the most sensitive reactions at T = 725 K, ϕ =1 and P = 15 bar. The results show that the most sensitive reactions at low to intermediate temperatures are the branching fractions of the main fuel H abstraction reactions via OH with the abstraction from the α[1] carbon

[1] α, β, γ and δ represents the hydrogen atom attached to the first, second, third and fourth carbon atom respectively.

site playing the most dominant role. These same reactions were also reported in [148, 222] to be the most sensitive reactions at conditions of low temperature. The α–hydroxybutyl radical formed via hydrogen abstraction from the α site reacts very quickly with oxygen to produce butanal (*n*-C_3h_7CHO) and HO_2. This reaction route which has a similar sensitivity to the OH abstraction route from the γ site, is similar to the termination (inhibiting) step in the low temperature oxidation of alkanes leading to the formation of alkenes and HO_2 radicals that compete with the isomerisation and chain branching reactions by direct elimination from RO_2. As reported in [148], the current rate parameterisation of this reaction (1-hydroxybutyl + O_2 = *n*-C_3H_7CHO + HO_2) is based on the theoretical evaluation of Silva and Bozzelli [223] and is majorly responsible for the very slow reactivity exhibited by the model across the low temperature range (Figures 4.18 and 4.19) especially under rich conditions and high pressures. Figure 4.22 shows the plot of the normalised local sensitivities for 20 of the most dominant reactions at T = 814 K, P = 15 bar and ϕ = 0.5 alongside the sensitivities of the same reactions at T = 898 K. Figure 4.22 clearly indicates that as temperature is increased, the reactions of *n*-C_4H_9OH + HO_2 and H_2O_2 become more important in terms of the accurate prediction of autoignition in the high temperature region. This is in agreement with the local sensitivity result of [222] where the fuel specific reaction of *n*-C_4H_9OH + HO_2 = H_2O_2 + C_4H_8OH-1 and H_2O_2 = 2OH were identified as the reactions with the most influence on ignition delays at higher temperatures (above T = 1000 K).

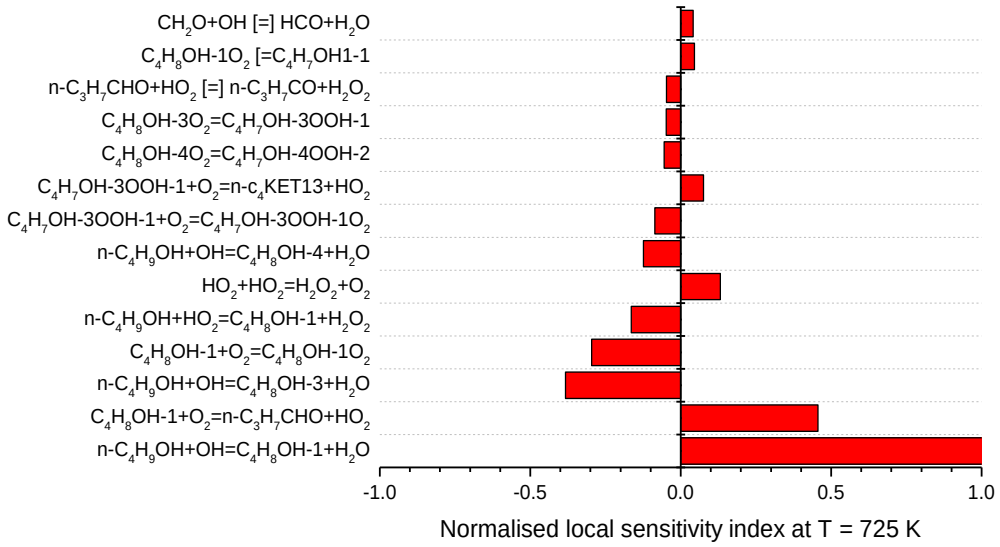

Figure 4.21: Normalised local sensitivity analysis for predicted log (ignition delay) of *n*-butanol at P = 15 bar, T = 725 K and ϕ = 1.

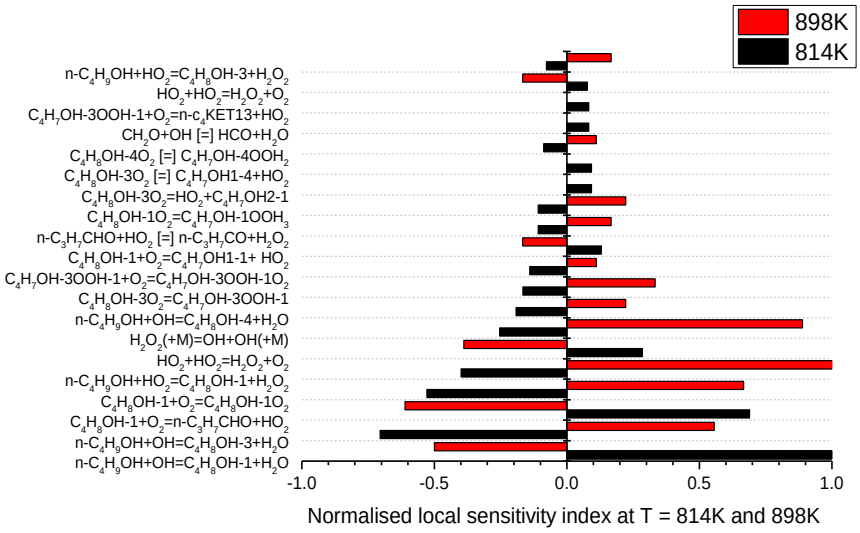

Figure 4.22: Result of local sensitivity analysis for predicted log (ignition delay) of *n*-butanol at P = 15 bar, T = 814 K and 898 K and ϕ = 0.5.

4.3.1.3 Uncertainty study

Figure 4.23 shows the predicted ignition delay distributions based on the propagated uncertainties in the model for the case of ϕ =1, at P =15 bar, and T = 725 - 839 K. Although the original model appears to predict the ignition delay data quite well at

lower temperatures, with the experimental values close to the median of the predicted distribution, uncertainties in the predicted ignition delays are quite large in this region; up to at least plus or minus one order of magnitude. At higher temperatures, the agreement at nominal parameter values is less good, although the predicted uncertainty distributions are much smaller (up to about 50 % less) and the experimental values do lie close to the mean predictions. Overall, within the suggested uncertainties for the model, there is agreement with the experiments across the temperature range. The large uncertainties in predicted delays especially at the lower temperature region do however, indicate the need for a more accurate knowledge of the dominant rate parameters in the scheme if the scheme were to be reliably utilised for autoignition predictions under real engine conditions. Particular focus should be paid to temperature dependencies of the rate parameters. Via a global sensitivity study we can determine first of all, which parameters contribute most to these predictive uncertainties. Secondly we can determine how the experimental measurements constrain these parameters under the different conditions studied.

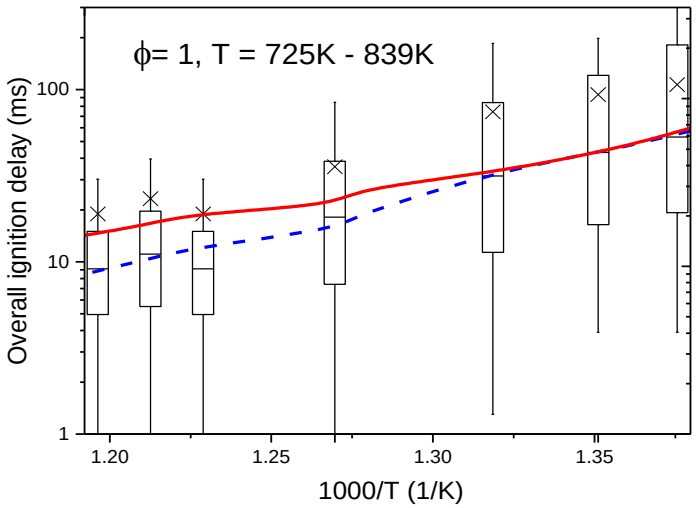

Figure 4.23: Comparison of predicted *n*-butanol ignition delays (dashed blue) with Weber et al data [194] (red line). Boxes represent 25th and 75th percentiles while whiskers represent 5th and 95th percentiles. The large crosses and horizontal lines represent the mean and median of the predicted distribution from the 256 simulations respectively.

The differences in the location of the mean and median of the predicted output also reveal that the data represent a non-Gaussian distribution. Figure 4.24 shows a typical distribution of the predicted log ignition delays of *n*-butanol at T = 787 K and ϕ = 1 for the 256 runs from the quasi-random sample. The data is skewed to the left with a tail and conforms more to a lognormal distribution rather than a normal distribution. This means that in a low number of samples very short ignition delays are predicted leading to the whiskers and outliers of the data set shown in Figure 4.23. Such tails are often an indication of interactions between parameters driving large variability in the predicted targets. On the face of it, the predicted output uncertainties shown in Figure 4.23 seem large, particularly since they are based on input uncertainties of no greater than a factor of 2 (see supplementary material) in many cases. The reason is that within the sampling we are allowing each rate parameter to vary across its whole range without assuming any correlations between input data. The prediction of ignition delays is strongly influenced by the relative rates that lead to chain branching compared to those that lead to chain propagation or termination. Therefore the relative rates of the H abstraction from the fuel at different sites are likely to be influential and if competing reaction channels are allowed to vary across their whole range, tails in the predicted distribution of target outputs such as ignition delays may result from the pairing of extreme values of the input parameters for the competing channels.

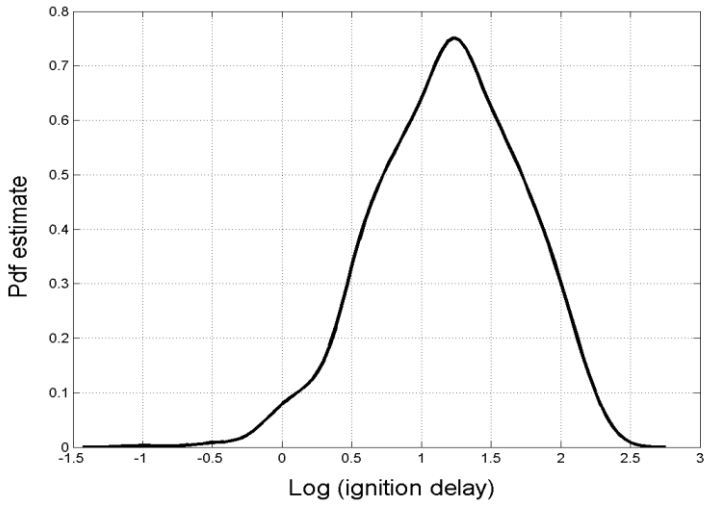

Figure 4.24: Typical distribution of predicted log (ignition delay (ms)) of *n*-butanol at T = 787 K and ϕ = 1.

4.3.1.4 Global sensitivity study

Figure 4.25 shows the main first-order sensitivity coefficients calculated in the HDMR study. The low temperature conditions of T = 650 K and 678 K are obtained under rich condition of ϕ = 2. The shading for each of the selected reactions is shown on the legend. If all the variance in the predicted output was accounted for by the individual effects of each parameter, then the sum of the S_i would be 1 (equivalent to 100 % of the variance). The selected reactions are the seven most important reactions influencing the predicted *n*-butanol ignition delay and account for over 85 % of the predictive uncertainties highlighting that the uncertainties are dominated by the first-order effects of just a few reactions.

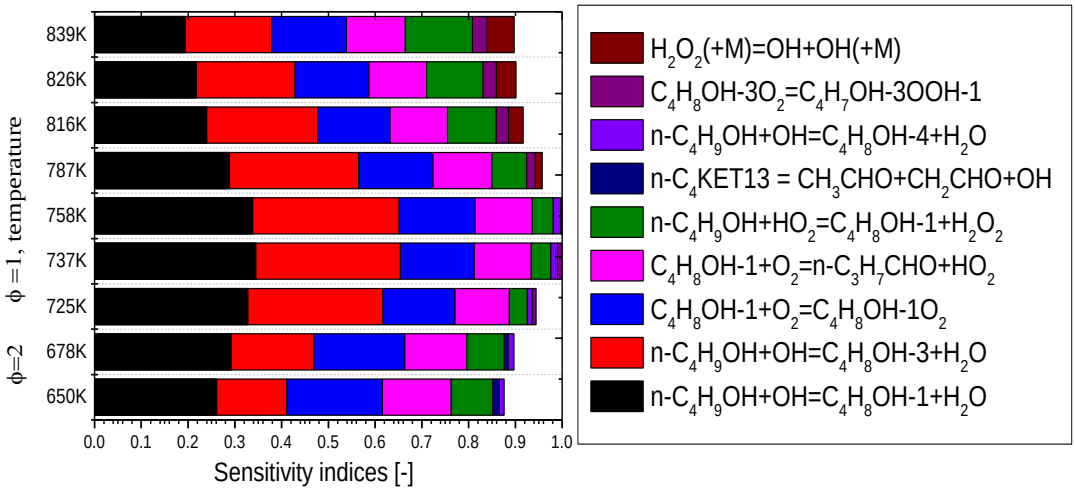

Figure 4.25: Main first-order sensitivity indices for simulated ignition delays of *n*-butanol with respect to reaction rates at selected temperatures and P = 15 bar. (Left) Sensitivity coefficients (Right) and legend.

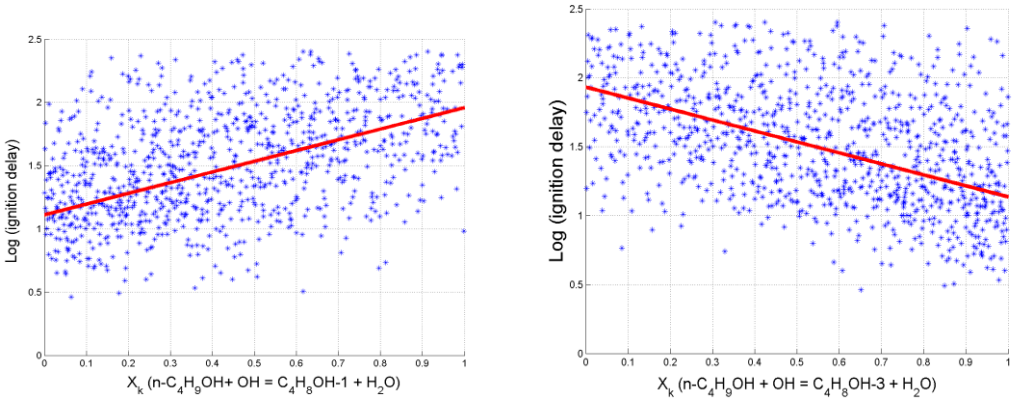

Figure 4.26: HDMR component functions (solid line) of simulated ignition delays of *n*-butanol shown on-top of the scatter for (a) *n*-C_4H_9OH + OH = C_4H_8OH-1 + H_2O (b) for *n*-C_4H_9OH + OH = C_4H_8OH-3 + H_2O, P = 15 bar, ϕ = 1, T = 725 K.

For the stoichiometric conditions studied, the branching fractions of Fuel + OH hydrogen abstraction reactions dominate the predicted uncertainties across the entire temperature range (e.g. low-intermediate temperatures). The hydroxybutyl radicals produced as a result of the main fuel oxidation reactions are consumed via two different type of reaction pathways. One is the oxygen addition reaction (α-hydroxybutyl +O_2) leading to the formation of peroxy radical (RO_2) that drives autoignition and the other is the termination step that inhibits autoignition due to the formation of HO_2. Although it is well known that the isomerisation reaction of the peroxy radical (RO_2) dominates autoignition chemistry in general low-temperature mechanisms, the dominance of the main fuel hydrogen abstraction reactions is as a result of its key role in determining the amount of fuel that goes to the termination steps compared with how much is available for the chain branching and propagation steps. The contributions from the hydrogen abstraction reactions however diminishe with increasing temperature while contribution from HO_2 chemistry and formation route for H_2O_2 become more significant.

The sensitivities highlight that constraints on the reaction rate coefficients for the H abstraction reactions by OH are better provided by ignition delays at stoichiometric lower temperature conditions since their uncertainties contribute to a larger percentage of the predictive variance. However, no single rate constant dominates, with the two main H abstractions from the α and γ sites showing first-order sensitivities of 0.32 and

0.29 respectively. This means that a wide range of chosen rate constants for these reactions could reproduce the experimental ignition delays with reasonable accuracy.

Figure 4.26 shows the HDMR component functions which highlight the individual response of the predicted targets to changes in the *A*-factor for these reactions. The data points in these figures represent the individual responses from the quasi-random sample whereas the line (component function) illustrates the individual effect of the chosen parameter. If a single parameter dominated the uncertainties in the output, then there would be no scatter about the line in such a plot and the sensitivity index for the parameter would be close to 1. However, what we see is a high degree of scatter about the component function, indicating a strong influence from the uncertainties in the other selected input parameters. Measured ignition delay times therefore offer only weak constraints on the abstraction rates from the individual sites.

Sarathy et al. report [148] discrepancies between the ab initio studies for abstraction from the α site between the studies of Zhou et al. [224] and Zádor et al. [225] and adopted the temperature dependence of [225] to give better agreement with experimental data. H abstraction from the γ site is critical to correctly determining the amount of chain branching which drives low- temperature autoignition. The rate constant for this reaction was however, subject to large discrepancies between [224] and [225] and hence corrections were made in [148]. The low temperature ignition delays at ϕ = 1 provide some constraints on this reaction channel (S_i = 0.29) but there is still a large influence of uncertainties in other key rates (Figure 4.26b).

However, if we plot predicted log ignition delay against a scaled ratio of the log reaction rates for these main abstractions reactions from the α and γ sites, leading to C_4H_8OH-1 + H_2O and C_4H_8OH-3 + H_2O respectively, we see an almost linear relationship (Figure 4.27), with the scatter resulting from uncertainties in the other main reactions listed in Figure 4.25. The sensitivity index for this branching ratio is 0.7 i.e. twice that for the individual rates. On the contrary the sensitivity index for the sum of reaction rates for H abstraction by OH is < 0.1. The analysis therefore demonstrates that ignition delay measurements provide much stronger constraints on the branching ratio than on the overall rate constant for this reaction class. There is still scatter in Figure 4.27 however, due to the influence of uncertainties in other channels such as R + O_2. At lower

temperatures and richer conditions (ϕ = 2), where discrepancies between model and experiment were seen in Figure 4.18, R + O_2 reactions are equally as important as H abstraction (Figure 4.25). The reaction to form butanal + HO_2 is included as a high temperature pathway in [148] but actually shows a higher sensitivity at low temperature rich conditions (Figure 4.25).

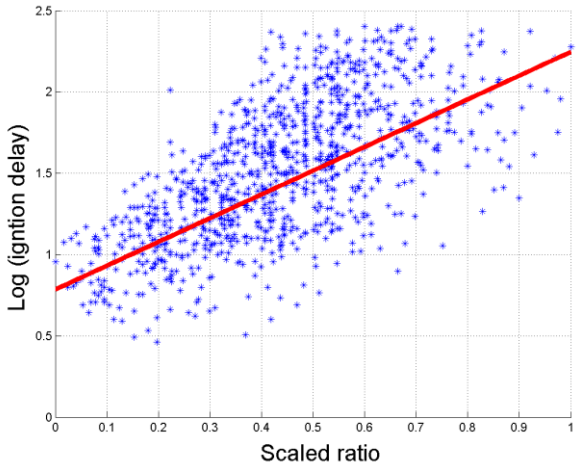

Figure 4.27: Scatter plot and HDMR component function for predicted log (ignition delay) of *n*-butanol against the scaled branching ratio for the two main H abstraction reactions by OH, taking into account uncertainties in the 40 main reactions, T = 725 K, ϕ =1, P = 15 bar.

4.3.2 *n*-Butanol JSR Studies

4.3.2.1 Comparison with experimental data

Figure 4.28 reveals how the experimental species mole fractions measured in the JSR compare with the predicted species profiles using the mechanism of Sarathy [148] at ϕ = 1 and P = 10 bar. The solid line indicates the measured data while the dash line represents the predicted profiles based on the original parameterisation of the Sarathy scheme. Similar to what was reported in Dagaut et al. [20], we see here that the predicted species concentrations of CO and CH_2O are in very good agreement with the measured profiles across a major part of the temperature range except for temperatures below 830 K where the model significantly over predicts the experimental values up to a factor of 9 for CO and 8 for CH_2O. *n*-butanol species profiles were predicted reasonably well in the temperature range of 800 - 920 K but not at higher temperatures (above 920 K)

where the model displayed higher levels of reactivity compared to the measured data. In general, the model prediction of the peak point for the three species considered in the study is very good. The possible causes of the discrepancies between the simulations and experimental data will be discussed further in the subsequent sections.

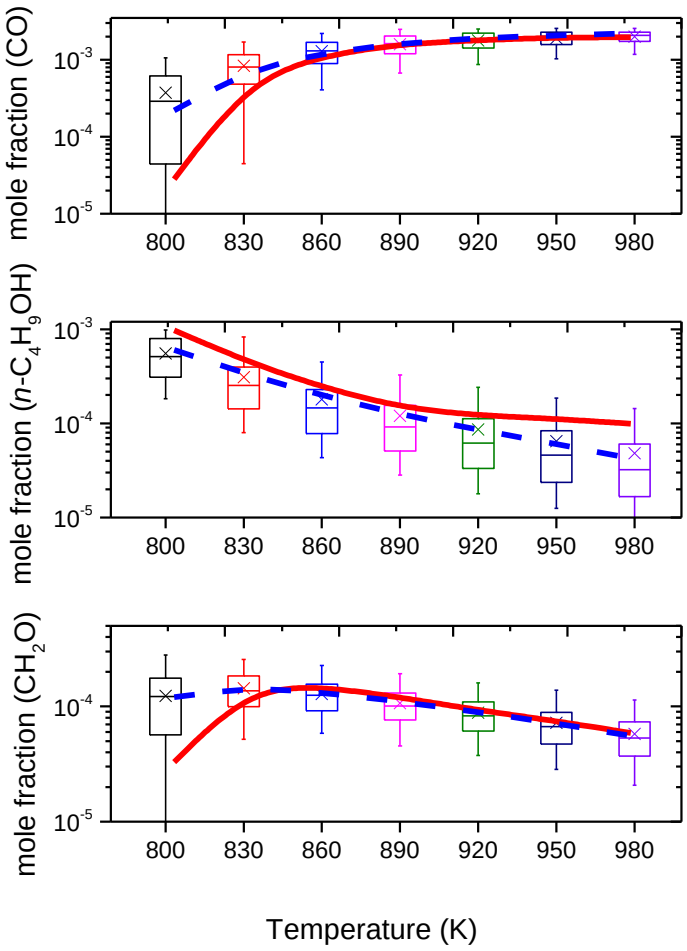

Figure 4.28: Comparison between experimentally measured species profiles (solid line) and simulated profiles in the JSR (dashed line).The boxes represent 25th and 75th percentiles while whiskers represent 5th and 95th percentiles. The large crosses and horizontal lines represent the mean and median of the predicted output based on a quasi-random sample of 256 model runs respectively.

4.3.2.2 Local sensitivity analysis

Figure 4.29 shows the normalised local sensitivity indices for the first 20 most important reactions influencing the predicted concentration profiles of *n*-C_4H_9OH, CH_2O and CO at 830 K. While the high temperature decomposition reaction of H_2O_2 (H_2O_2 (+M) = OH +OH) is found to dominate the predicted concentration profiles of the three chosen species at 830 K, H abstraction reactions from the α and γ sites of *n*-C_4H_9OH alongside reactions involving HO_2, (*n*-C_4H_9OH + HO_2 = C_4H_8OH-1 + H_2O_2, HO_2 + HO_2 = H_2O_2 + O_2) are also found here to play key roles in the prediction of *n*-C_4H_9OH and CO. Interestingly, the H abstraction reactions, particularly the ones from the α–carbon site are also the ones that dominated the predicted ignition delay times within the RCM. In terms of the predicted formaldehyde concentrations, the H abstraction reactions from the γ and δ site alongside reactions involving CH_2O and HO_2 are among the most important reactions at 830 K.

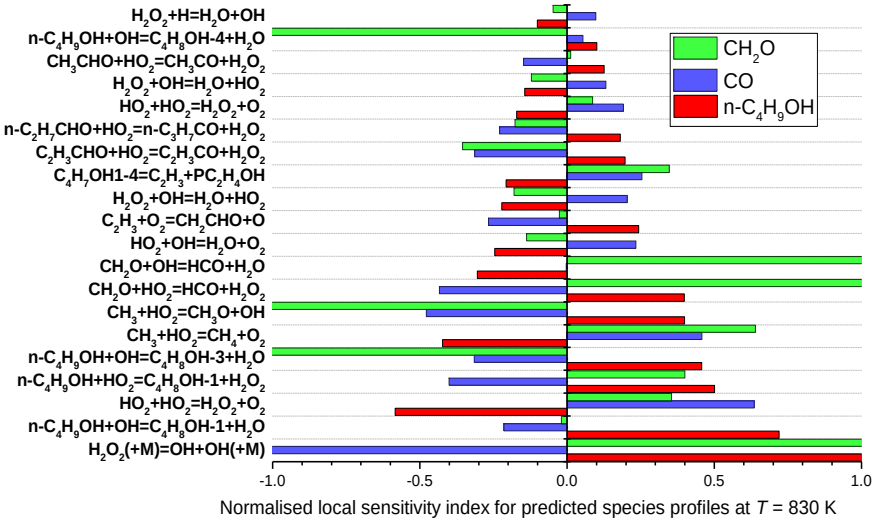

Figure 4.29: Result of local sensitivity analysis for predicted species profiles of *n*-butanol/air mixtures in the JSR at P = 10 bar, T = 830 K and ϕ =1.

4.3.2.3 Uncertainty quantification

Figure 4.28 also presents the predicted distribution of the concentration profiles of CO, CH_2O and *n*-C_4H_9OH while incorporating the uncertainties of the most dominant input

parameters in the simulations, superimposed on the predicted single profiles of the same species. The box in the figure represents the 25th and 75th percentiles while the whiskers indicate the 5th and 95th percentiles. Figure 4.28 shows that for CO and CH_2O, the experimental data fall well around the mean of the predicted output distributions except for the lower temperature region (T < 860 K) where the experimental data lie within the 25th percentile of the predicted output distributions. For *n*-butanol, the experimental data is close to the 75th percentile for most part of the temperature range. In terms of the uncertainty quantification, the predicted uncertainty distributions for CO and CH_2O are quite small at temperatures above 860 K where the model is in good agreement with the measured data but could be up to two orders of magnitude at the lower temperature of 800 K. For *n*-butanol, the predicted uncertainty distributions are largest at the higher temperatures and are within the range of one order of magnitude. In the next section, a global sensitivity approach is employed alongside a HDMR response surface to identify the key reactions driving the predicted output uncertainties.

4.3.2.4 Global sensitivity analysis

Figures 4.30 and 4.31 show the main first-order and second-order sensitivity indices obtained from the HDMR analysis for the simulated JSR data. Sensitivity coefficients were estimated in the HDMR analysis based on simulations involving 2048 samples. Results shown in Figure 4.30 and Figure 4.31 represent the sensitivity coefficients for the 10 most important reactions influencing the predicted uncertainties for *n*-C_4H_9OH and CH_2O at two selected temperature points (800 K and 830 K) where the model displayed a very high level of discrepancy in terms of the predicted species profiles. Interestingly, these are also the temperature points that overlap with the temperature conditions studied in the RCM. Looking at the calculated sensitivity indices from the HDMR model (Figure 4.30 and Figure 4.31), we can see that the selected ten key reactions account for about 55-70 % of the overall predicted uncertainties, with the hydrogen abstraction reaction by HO_2 leading to formation of C_4H_8OH and H_2O_2 (contributing over 30 %) dominating the predicted uncertainties in both *n*-C_4H_9OH and CH_2O profiles at T = 800 K. This same abstraction route for *n*-C_4H_9OH + HO_2 was found to be the most dominant reaction in [148] in terms of the ignition delay sensitivity at 800 K, and ϕ = 1 but this was at a much lower pressure of 1 atm. In the HDMR analysis of predicted ignition delay times (Figure 4.25), over 85 % of the uncertainties

were however accounted for by only seven reactions, and the H abstraction reaction by OH dominated the predicted ignition delay uncertainties across the temperature range in contrast to *n*-C_4H_9OH + HO_2 as found in the case of the JSR. Heufer et al. [222] suggested the use of estimated rate coefficients for the dominant *n*-butanol + HO_2 system based on alkanes, and this could be the reason for the large discrepancies between the predicted target outputs and measured data. According to Heufer [222], the current parameterisation of this rate is still very poor as variation of the rate coefficients for this same reaction in the mechanisms of Black and Moss [140, 145] could be up to a factor of 20, suggesting the need for more detailed and accurate studies of this reaction across a wide range of temperatures and pressures in order improve on the level of agreement with experimental data.

As temperature is increased to 830 K, the contribution from abstraction by HO_2 diminishes in importance (Figures 4.30 and 4.31) while abstraction reactions by OH become more significant with abstraction from particularly the α site leading in terms of the predicted *n*-butanol uncertainties. This sensitivity behaviour is in agreement with the results of local sensitivity analysis carried out in [20] where H-abstraction reactions by OH from the α and γ carbons were captured as the reactions for which *n*-butanol concentrations are most sensitive at high temperatures (T = 1050 K). The sensitivities demonstrate as well that H abstraction from the α site is not important at high temperatures for the predicted distribution of CH_2O concentrations, but the reactions of CH_2O + OH and H abstraction from the δ site are significant contributors. It is also clear from the HDMR study that no single reaction dominates the uncertainties at higher temperatures as most of the key reactions are equally significant. A stronger level of constraint is however provided by the measured species profiles of *n*-C_4H_9OH and CH_2O on the *n*-C_4H_9OH + HO_2 abstraction rate at the lower temperature given their estimated sensitivities of 0.34488 and 0.35203 respectively.

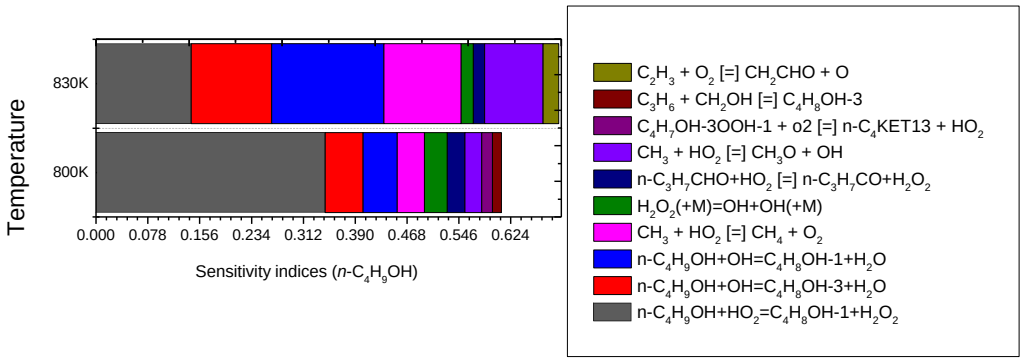

Figure 4.30: Main first-order sensitivity indices for simulated *n*-C_4H_9OH species profiles in the JSR with respect to reaction rates at selected temperatures and P = 10 bar (Left) Sensitivity coefficients (Right) legend.

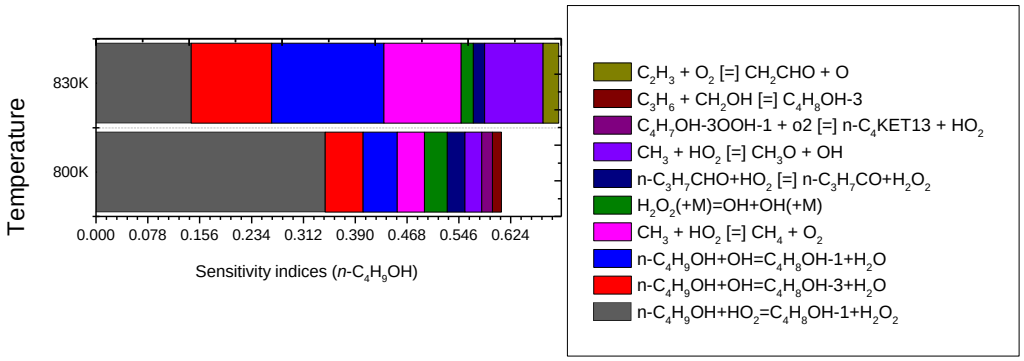

Figure 4.31: Main first-order sensitivity indices for simulated CH_2O species profiles in the JSR with respect to reaction rates at selected temperatures and P = 10 bar (Left) Sensitivity coefficients (Right) legend.

Figure 4.32 shows the plots of the four most important first-order component functions with respect to *n*-butanol concentrations, and gives an overview of the relationship existing between these input parameters and the predicted output. In each case shown, the middle point on the x-axis (0.5) represents the current nominal value of the *A*-factor used in the model. Firstly, we can see a nonlinear response to changes in the rate of all three hydrogen abstraction reactions demonstrating the need to compute the model's sensitivities across the entire range of input uncertainties rather than just at the nominal value as seen in local sensitivity analysis. For example in the local sensitivity method

employed here prior to the global sensitivity analysis, the reaction of H_2O_2 + (M) = OH + OH + (M) was captured as the most dominant reaction at T = 800 K across all target species but here in the HDMR analysis (Figures 4.30 and 4.31), the reactions α-*n*-C_4H_9OH + HO_2, α-*n*-C_4H_9OH + OH and γ-*n*-C_4H_9OH + OH are more dominant. From Figure 4.32b and Figure 4.32c, we can see that the gradients at the nominal input rate for the reactions indicated are less steep (indicating low sensitivity) compared to that in the upper part of their input range. The same is true for H_2O_2 + (M) = OH + OH + (M) (Figure 4.32d) and this is one reason that local sensitivity indices, computed using the nominal parameter values can be misleading. Another reason is that the local method does not account for the degree of uncertainty in the parameters and so does not represent the contribution of input uncertainties to the output variance. The response of the predicted *n*-butanol mole fractions to the *n*-butanol abstraction reaction by HO_2 is strongly negative across the entire input uncertainty range (Figure 4.32a) indicating that a decrease in this rate could potentially lead to better agreement of the model output with measured data but this is still subject to the influence of the uncertainty in the other rate parameters in the system. As the rate of the abstraction reaction by HO_2 is reduced, the impact uncertainties in other reaction rates including the branching fractions of *n*-C_4H_9OH + OH increases, as indicated by the broadening of the scatter.

The functional relationship between the abstraction reaction of *n*-C_4H_9OH + OH from the α and γ site (Figure 4.32b and 3.32c) shows a strong negative response at the upper part of the input space but the effect however saturates at the lower half, indicating that adopting different rate parameters outside the nominal rate for these channels is unlikely to reduce the discrepancy between the model and the measured data. However, it was shown in section 4.3.1.4 that ignition delay measurements provide much stronger constraints on the branching ratio than on the overall rate or individual rate constant for this set of abstraction reactions. The first-order sensitivity component functions with respect to formaldehyde mole fractions at T = 800 K are presented in Figure 4.33 for the abstraction reaction of *n*-butanol + HO_2 and *n*-butanol + OH abstraction from the γ site. A nonlinear response is also observed in both cases similar to that involving *n*-butanol mole fractions but in this case, the response for *n*-butanol + HO_2 is positive for most of the lower uncertainty range and slightly negative at the upper end. Also, the contribution from the other important parameters to the predicted uncertainty band decreases

drastically across the upper part of the input range as indicated by the narrowing of the scatter. For the γ abstraction reaction of *n*-butanol + OH (Figure 4.33b), a very low gradient is seen at the lower end indicating low sensitivity but the response becomes slightly stronger as we move from the lower part of the input range to the upper part. The experimentally measured log of CH_2O mole fraction is around -4.52 and looking at Figure 4.33a, the rate of the abstraction reaction *n*-butanol + HO_2 would have to be in the lower part of the input parameter range in order to bring the model's prediction in close agreement with the measured data.

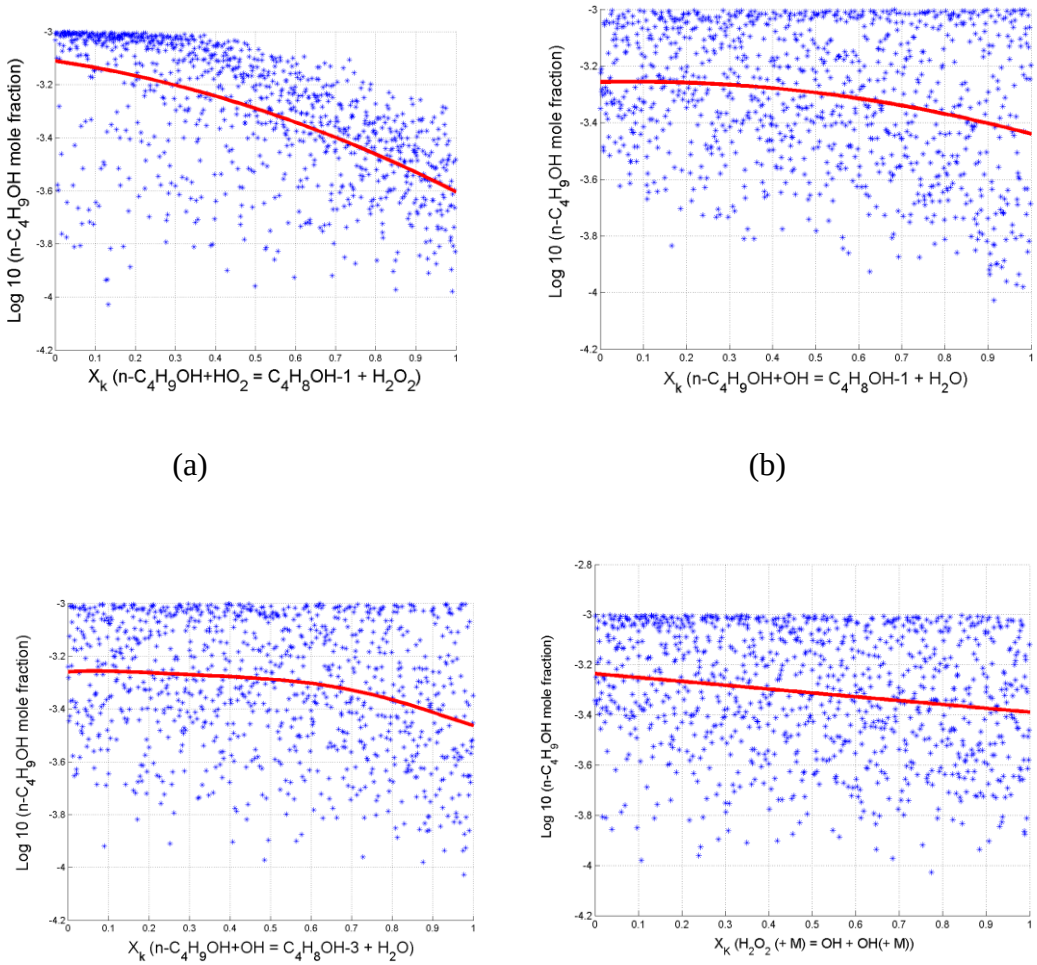

Figure 4.32 First-order component function (solid line) of simulated species profile and scatter at T = 800K, sensitivity of *n*-butanol to changes in *A*-factor for reaction (a) *n*-C_4H_9OH + HO_2 = C_4H_8OH-1 + H_2O_2 (b) *n*-C_4H_9OH + OH = C_4H_8OH-1 + H_2O (c) *n*-C_4H_9OH + OH = C_4H_8OH-3 + H_2O (d) H_2O_2 + (M) = OH + OH + (M).

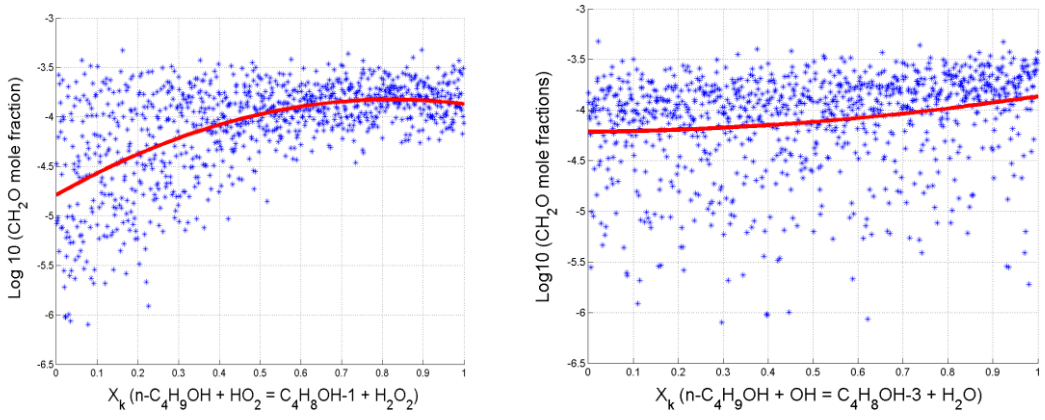

(a) (b)

Figure 4.33: First-order component function (solid line) of simulated species profile and scatter at T = 800 K, sensitivity of CH_2O to changes in A-factor for reaction (a) *n*-C_4H_9OH + HO_2 = C_4H_8OH-1 + H_2O_2 (b) *n*-C_4H_9OH + OH = C_4H_8OH-3 + H_2O.

At a higher temperature of 830 K, the prediction of *n*-C_4H_9OH and CH_2O is relatively less sensitive to the abstraction reaction by HO_2. At 830 K, *n*-butanol mole fraction is most sensitive to the abstraction reaction by OH from the α site (Figure 4.34a) while CH_2O mole fraction is driven mainly by the reaction of CH_2O + OH (Figure 4.34b). The reaction CH_2O + OH was found to be the most influential reaction contributing about 16 % of the uncertainties in the predicted mole fractions of CH_2O at 830K and increasing the rate of this reaction (Figure 4.34b) could lead to a reduction in the predicted CH_2O mole fractions to give a better match with the experimental data. Another key reaction route on which the accuracy of the predicted CH_2O concentration depends is CH_2O + OH = HCO + H_2O with its uncertainty contributing to over 10% of the variance in predicted CH_2O mole fractions.

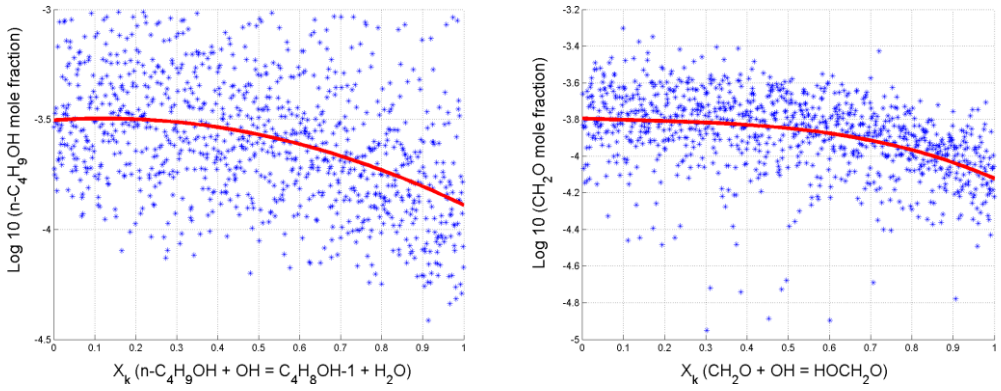

(a) (b)

Figure 4.34: First order component function (solid line) of simulated species profile and scatter at 830K, ϕ = 1. (a) Sensitivity of *n*-C_4H_9OH to changes in *A*-factor for reaction *n*-C_4H_9OH + OH = C_4H_8OH-1 + H_2O (b) Sensitivity of CH_2O to changes in *A*-factor for reaction CH_2O + OH = $HOCH_2O$.

4.3.3 Impact of update on H abstraction reactions based on new data

We have shown that the H abstraction routes by OH in the investigated *n*-butanol mechanism, especially those from the α and γ carbon sites, are important for accurate prediction of ignition delay times in the RCM and species concentrations in the JSR. A recent study by McGillen [198] provided updated site specific rate constants for each site, albeit based on measurements at lower temperatures than of interest here. As a final sensitivity test the four H abstraction rate constants by OH were updated based on the new rate data from [198]. Figure 4.35 showed the results obtained with the updated mechanism in comparison with predictions from the original mechanism and Weber data [194] for ϕ = 0.5 - 2 and *P* = 15 - 30 bar. The update led to a decrease in the predicted ignition delay times across all conditions studied and therefore better agreement with the measured data under lean conditions at higher temperatures and 15 bar. This is consistent with the findings in [65] where the same updates to the Sarathy mechanism led to significant improvement in the reactivity of *n*-butanol at lower temperatures. While there is also significant improvement in the predicted reactivity under stoichiometric conditions, particularly at *P* = 30 bar (Figure 4.36), the agreement with the measured data is worsened at lower pressures (i.e. *P* = 15 bar) under stoichiometric conditions (Figure 4.36).

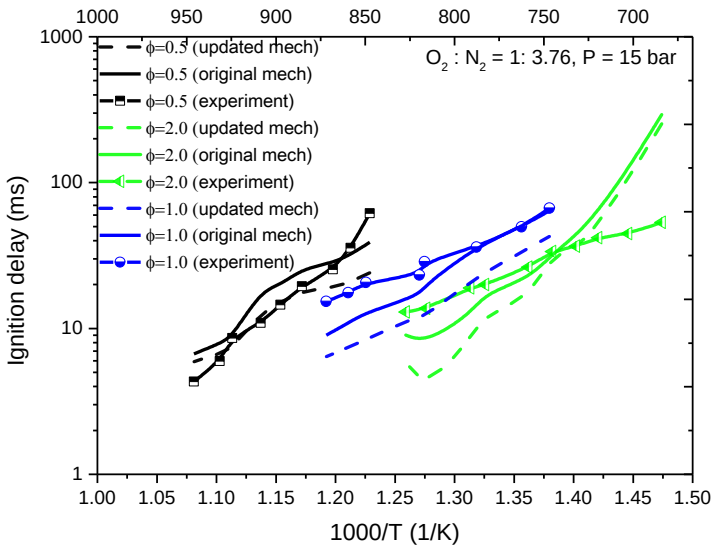

Figure 4.35: Comparison of ignition delays predicted by the Sarathy model with Weber et al. data [194] for conditions of P = 15 bar and ϕ = 0.5 and 2.0.

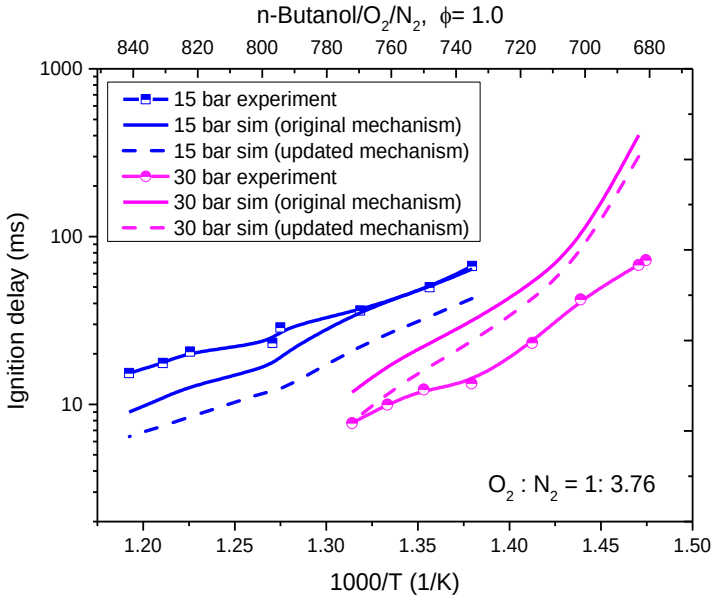

Figure 4.36: Comparison of ignition delays predicted by the Sarathy model [148] with Weber et al. data [194] under stoichiometric conditions at 15 bar and 30 bar.

4.4 Summary

In this chapter three recently developed chemical kinetic mechanisms describing the low temperature oxidation of DME have been investigated using both local and global uncertainty and sensitivity methods with ignition delays as the predicted output for a temperature range of 615 - 735 K, pressure range of 10 - 20 bar, and equivalence ratios of 0.43 - 1.5. A similar approach has been employed to evaluate a current chemical kinetic model of *n*-butanol combustion within the context of ignition delay time prediction in an RCM over a temperature range of 678 - 898 K, pressure range of 15 - 20 bar and equivalence ratios of 0.5 - 2.0 as well as species concentration modelling in JSR, over a temperature range of 800 – 1150 K, equivalence ratios of 0.5 - 2.0 at a pressure of 10 atm. The study incorporates the effects of uncertainties in the rate constants of the adopted mechanisms on the predicted target outputs, based on a global approach, in order to quantify errors bars which provide information on the robustness of the mechanism over a range of operating conditions. In addition, a variance-based global sensitivity analysis using high dimensional model representation (HDMR) has been carried out to understand and rank the rate parameters driving the predicted uncertainties.

Firstly, the study has shown that predicted error bars (uncertainties) currently existing within the low temperature DME oxidation system, while incorporating the uncertainties in the input rates, are quite large, spanning several orders of magnitude. These uncertainties however, are driven by a few important reactions within the reaction mechanisms studied and the parameterisations of these reactions are quite similar across the three mechanism studied except for a few minor reaction steps for which significant disparity exist in the choice of rate parameters. Global sensitivity plots representing the first-order and second-order responses between sampled input rates and predicted output, show that tuning input rate parameters to give better agreement with target experimental data would be a very difficult task as no individual reaction accounts for the overall predicted uncertainties across the entire range of condition studied. Recent rate data obtained from the study of Eskola for the isomerisation and propagation steps show a pressure dependency which is not reflected in the current parameterisation of these channels. However, updates on the Aramco scheme based on the data of Eskola, lead to larger discrepancies between the measured data and predicted target outputs

when used in isolation for both the RCM and flow reactor. Further modifications to the rate of the chain-branching step $CH_2OCH_2O_2H + O_2 = O_2CH_2OCH_2O_2H$ led to improvement in the models simulations in both the RCM and flow reactor. The study demonstrates that further studies on the temperature and pressure dependency of the chain branching pathway, $CH_2OCH_2O_2H + O_2 = O_2CH_2OCH_2O_2H$ are required in order to reduce uncertainties within DME mechanism for low temperature conditions. This is imperative in order to improve on the accuracy and robustness of the DME low temperature mechanism which is critical for the design of combustion devices which can use alternative fuels such as DME optimally.

Finally, the key reactions that dominate the uncertainties in the predicted low-intermediate temperature of target properties of *n*-butanol (ignition delays and species concentrations), have been identified through global sampling-based HDMR analysis. Calculated sensitivity indices show that in the context of ignition delay prediction, the dominant reaction pathways are H abstraction via OH. The study indicates that low temperature ignition delay measurements provide a high level of constraint on the branching ratio for abstraction from the α and γ sites but not on the total rate constant. For rich conditions, $R + O_2$ and subsequent pathways are equally as important as H abstraction. In the HDMR analysis of the predicted *n*-C_4H_9OH and CH_2O concentration profiles at low temperatures (i.e. 800 K), about 55 - 70 % of the overall predicted uncertainties are accounted for by about ten reactions as against seven which accounted for over 85 % of the predicted uncertainties in the case of the RCM. Also, H abstraction reaction by HO_2 (*n*-$C_4H_9OH + HO_2 = C4H_8OH\text{-}1 + H_2O_2$) dominated the predicted *n*-butanol and formaldehyde uncertainties in contrast to H abstraction reaction by OH which was more important in the case of the RCM. In addition, a reasonable amount of contribution also comes from the abstraction reaction from the γ and α site with abstraction from the alpha site dominating the predicted *n*-C_4H_9OH profiles at higher temperatures. In general, better constraint is provided on the *n*-$C_4H_9OH + HO_2$ abstraction rate by the measured species profiles of *n*-C_4H_9OH and CH_2O at lower temperatures. Current uncertainties in the rate of $C_4H_9OH + HO_2$ system suggest the need for detailed and more accurate studies of this reaction rate across a wide range of temperatures and pressures in order to bring predicted targets in better agreement with experimental data.

Chapter 5

Experimental and chemical kinetic modelling study of the influence of *n*-butanol blending on the ignition delay times of gasoline and its surrogate at high pressures

5.1 Introduction

5.1.1 Background and Motivation

Bio-derived alcohols are considered as viable blends for petroleum derived fuels in order to reduce their overall carbon footprint [226]. As mentioned in the introduction of this thesis, the similarity of their physical and chemical properties to those of fossil-derived fuels make them compatible with modern engines, particularly when used as blends [199, 227]. This means that fewer modifications have to be made to the existing hardware, and additional costs for infrastructure and maintenance can be lower than for other biofuels. Ethanol has been used extensively and can be used at low blending ratios with gasoline without requiring engine modifications. Butanol isomers have been less commonly used in practice but may offer the potential for higher blending ratios due to having more similar properties to gasoline than ethanol.

A key property of any fuel under consideration for blending is its ability to auto-ignite. If a fuel is less able to auto-ignite under engine relevant conditions than gasoline, then higher compression ratios may be able to be used in the engine, allowing more power to be delivered efficiently and economically [199]. It is therefore important to understand the autoignition behaviour and chemistry of proposed replacement fuels over a variety of temperatures and pressures. The combustion occurring in the engine is quite complex, therefore the RCM provides a good environment to test the chemistry of these fuels because of its similarity with the engine. However, there is currently very little data on the impact of blending butanol isomers with gasoline and their surrogates on key properties such as ignition delay times. Mixtures of other butanol isomers (2-butanol and tert-butanol) blended with TRF mixtures have previously been studied under shock tube conditions [228] demonstrating that at lower temperatures, these butanol isomers lengthened ignition delays of the mixtures, thus acting as octane boosters. Similar

studies have not yet however been performed for *n*-butanol blending with gasoline, or in the lower temperature conditions of the RCM as at the time of this study and this work fills that void.

Gasoline's complexity makes it practically impossible to model its chemistry exactly, so an appropriate 3-component toluene reference fuel (TRF) surrogate is formulated in this work. Methods have recently been developed to predict the octane numbers of TRF mixtures, via correlations with homogeneous gas-phase fuel/air ignition delay times for conditions covering both the RON and MON [229]. Hence it is important to establish that TRF mixtures can be representative of the ignition behaviour of gasoline, not only for pure gasoline, but also under blending with alternative fuels. Therefore in this work, the ability of the TRF surrogate to represent the ignition delay behaviour of the reference gasoline at low temperatures is first of all investigated experimentally, both alone, and when blended with *n*-butanol. The method used for formulating the TRF surrogate as well as its composition are presented in section 3.2.1.3. If observed ignition delays can then be successfully modelled using surrogate chemical mechanisms, it allows the estimation of octane numbers over wide ranges of conditions for use in engine development and optimisation. Therefore, in addition, a combined gasoline surrogate and *n*-butanol scheme is evaluated in terms of its ability to accurately reproduce the low temperature ignition behaviour of *n*-butanol, TRF, and a TRF/*n*-butanol blend from T = 678 - 858 K, ϕ = 1, at P = 20 bar. The reaction mechanism as described in section 3.3.3.1, is based on the *n*-butanol mechanism of Sarathy [148] investigated in chapter 4 and the recent gasoline surrogate mechanism of Mehl [88]. The methods employed in acquiring all the experimental and simulated data presented in this chapter were fully described in chapter 3.2.1 and 3.3.4 respectively.

One of the objectives of this work is to provide an understanding of the underlying chemistry responsible for the observed ignition delay behaviour of the gasoline/butanol blends. This goal is achieved in this chapter through local sensitivity analysis, using the Brute-force local sensitivity approach. It serves to highlight the important reactions driving the influence of *n*-butanol when blended with gasoline on ignition delay times at low temperatures providing useful information for kinetic studies that will improve model robustness. Moreover, global uncertainty and sensitivity analysis are carried out in order to explore the impact of the inherent uncertainties in the combined gasoline and

n-butanol scheme on the predicted ignition delay times of *n*-butanol, TRF and a TRF/butanol blend. Sensitivity indices calculated within the global analysis, based on the application of a HDMR metamodel, further helps to appropriately identify the key reaction rates that mostly influence the predicted target uncertainties.

5.1.2 Objective of the current chapter

The main objective of this chapter is to present and discuss the results of the chemical kinetic modelling analysis of the influence of *n*-butanol blending on gasoline performed in the context of ignition delay time prediction in the RCM, alongside the experimental validation data obtained from the Leeds RCM. Section 5.3.1 of this chapter discusses the performance of the TRF in comparison with a reference gasoline in terms of the ignition delay times measured in the RCM while section 5.4 discusses the performance of the TRF under blending condition with gasoline. Typical pressure traces indicating the experimental reproducibility of the data obtained from the Leeds RCM at selected temperature and pressure conditions are presented in section 5.2. The results of the simulated ignition delay times of TRF in comparison with the measured data as well as the results of the local sensitivities of the reaction rates in the TRF/*n*-butanol mechanism to the predicted ignition delay times of the TRF are presented in section 5.3.2. Section 5.3.3 presents the results of the global uncertainty/sensitivity analysis of the scheme based on the predicted ignition delay times of TRF. In section 5.4.1, the simulated ignition delay times of TRF/*n*-butanol blend are presented in comparison with the measured data, as well as the results of the local sensitivity while section 5.4.2 presents the results of uncertainty/ sensitivity analysis based on the global methods. The final section of this chapter (section 5.5) presents the results of the update made on the rate of the phenol + CH_3 = toluene + OH reaction pathway in the mechanism based on the gap identified in the local and global sensitivity analysis of the scheme.

5.2 Experimental pressure traces and reproducibility

Figure 5.1 shows typical pressure traces for TRF indicating the experimental reproducibility for both the reactive and nonreactive case at T = 729 K in addition to the reactive case at the lower temperature of T = 679 K. Figure 5.2 shows reactive pressure traces for the gasoline/*n*-butanol blend at T = 702 K and non-reactive pressure traces for

the TRF/*n*-butanol blend at T = 678 K respectively, demonstrating the experimental reproducibility at the indicated temperature points. Figure 5.3 shows a typical pressure trace for a TRF/*n*-butanol blend at compressed conditions of P = 20 bar and T = 702 K alongside the definition of ignition delay used in this work. Additional pressure traces covering various compressed temperature conditions at P = 20 bar and ϕ = 1 are also presented for TRF and TRF/*n*-butanol in Figures 5.4 –5.6. The figures show very good agreement between the measured traces for gasoline and TRF at the higher temperature and under conditions of blending. The TRF surrogate exhibits a slightly shorter ignition delay times than that for gasoline at the lower temperature as discussed further in the results section 5.3.1.

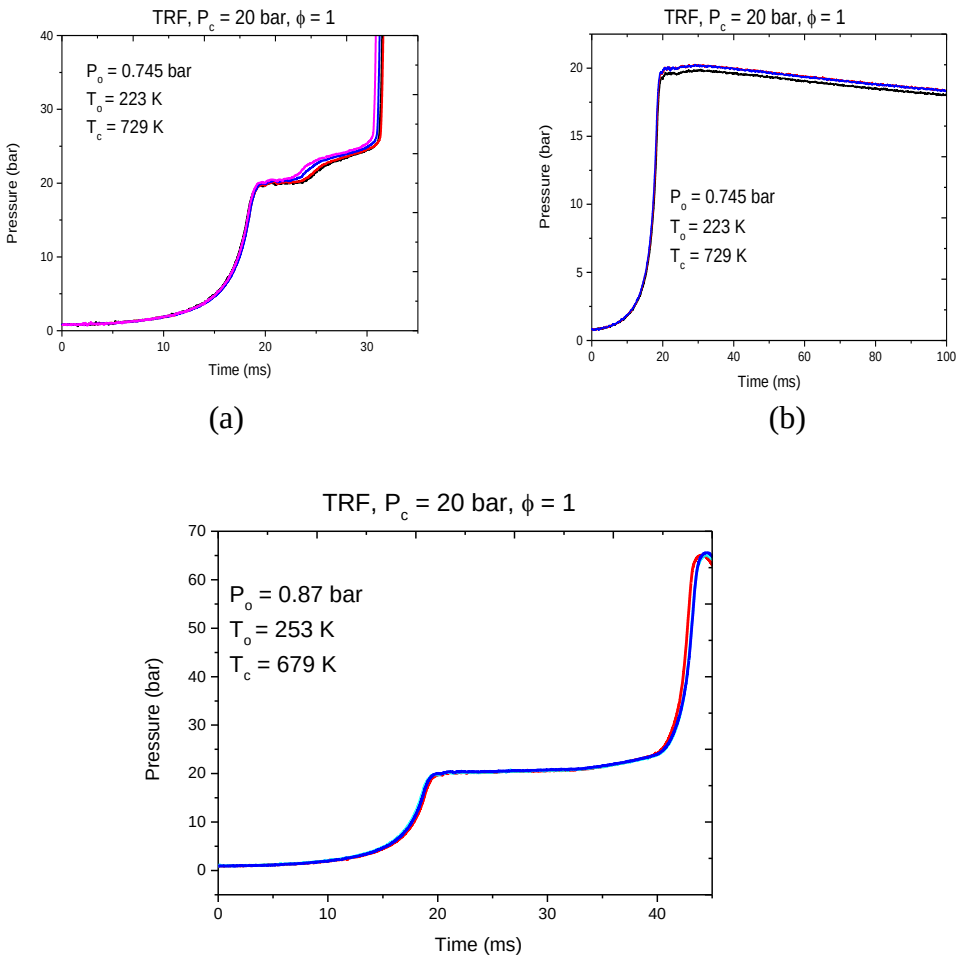

Figure 5.1: Pressure traces for TRF illustrating experimental reproducibility at some selected conditions a) reactive, two-stage ignition (b) non-reactive (c) reactive, one-stage ignition.

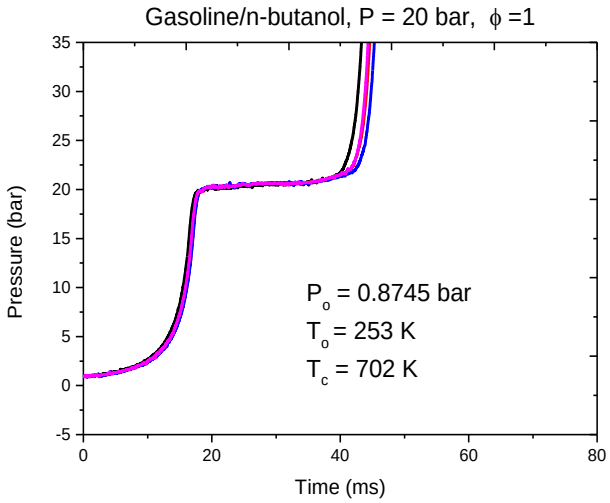

(a)

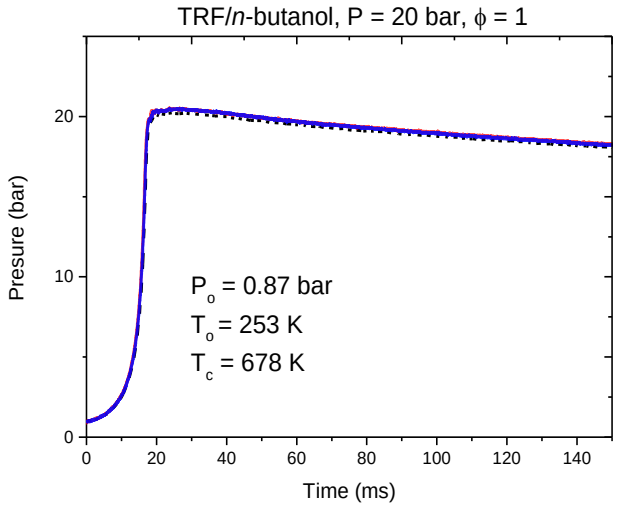

(b)

Figure 5.2: Pressure traces for gasoline/*n*-butanol and TRF/*n*-butanol illustrating experimental reproducibility at some selected conditions (a) reactive, one-stage ignition (b) non-reactive.

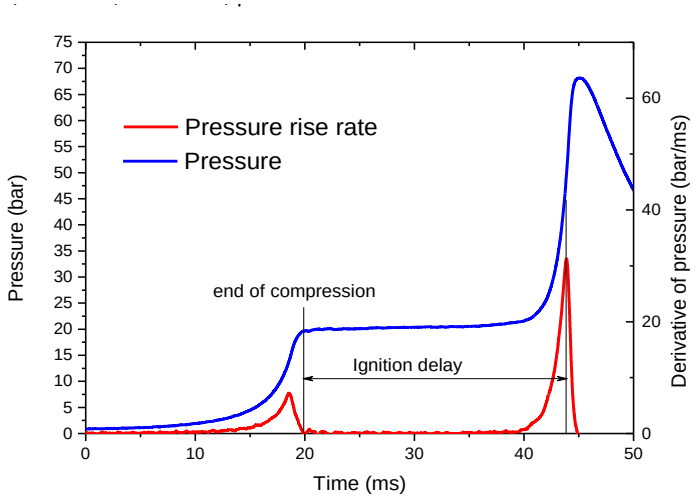

Figure 5.3: Typical pressure trace illustrating the definition of ignition delay reported in this study.

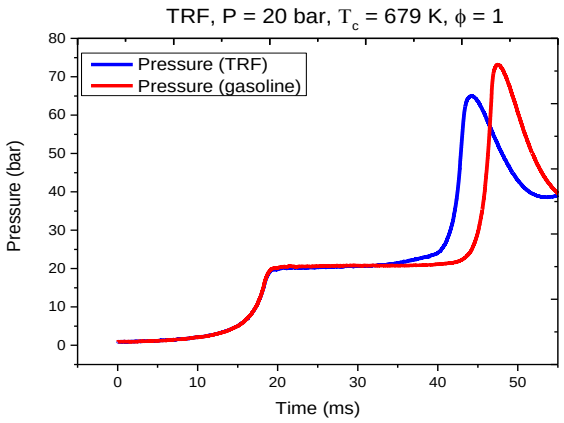

(a)

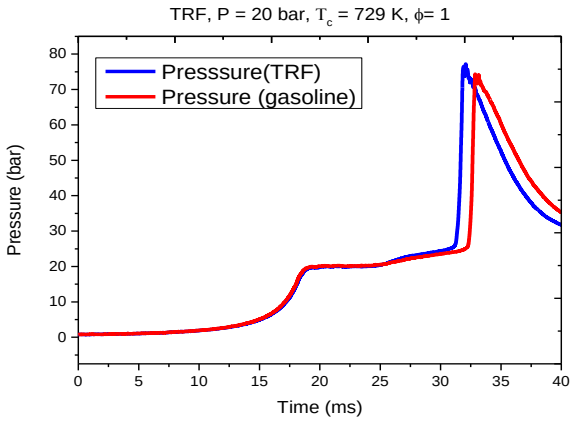

(b)

Figure 5.4: Experimental pressure traces showing how TRF compares with gasoline at (a) T = 679 K (b) T = 729 K.

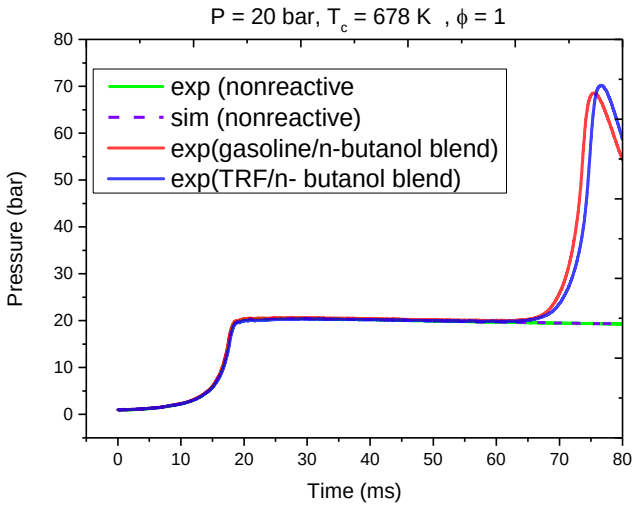

Figure 5.5: Experimental pressure traces showing how gasoline/*n*-butanol blend compares with TRF/*n*-butanol and how the simulated non-reactive case matches the experimental case.

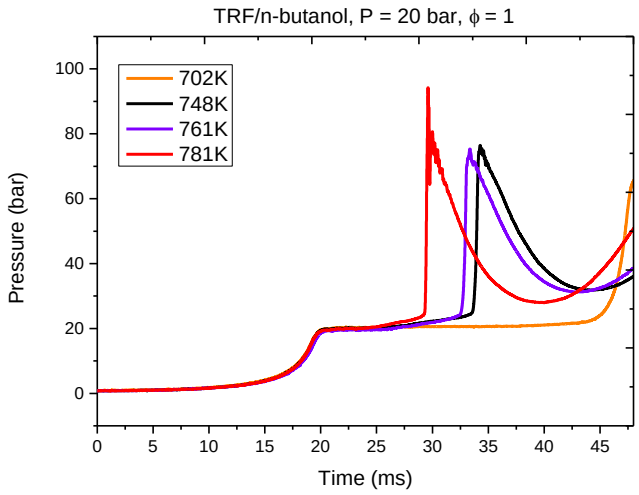

Figure 5.6: Comparison of experimental pressure traces for gasoline/*n*-butanol blend at various temperature conditions.

5.3 Investigation of ignition delay times of gasoline and its surrogate

5.3.1 The representation of the reference gasoline via TRF surrogate

Figure 5.7 shows that the 3-component TRF surrogate provides a good representation of the ignition delay data in comparison to the reference gasoline for the conditions

studied. Both fuels show weak negative temperature coefficient (NTC) behaviour as has been previously noted by Kukkadapu and co-workers [97, 104]. The ignition delays measured for the TRF surrogate are consistently slightly lower than those of the reference gasoline. The disparity between both data sets is higher in the lower temperature region and this can be attributed to the difficulty in carrying out the ignition delay measurements at lower temperatures as well as slight differences in the autoignition sensitivities. It was suggested in [97] that adding an additional component, 2-pentene, to *n*-heptane, iso-octane, and toluene gave a closer match to the ignition delay data for the research grade gasoline (RD387). However, in this study it is found that a 3-component TRF surrogate provides adequate representation of the ignition delay data for the reference gasoline under the conditions of the RCM, and hence the same TRF mixture is used in the butanol blending study.

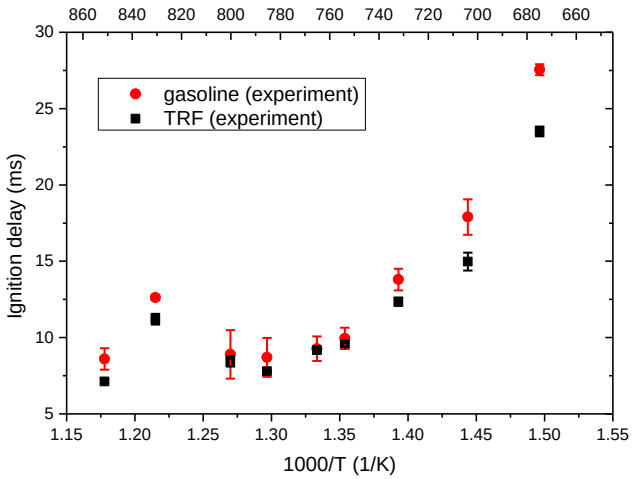

Figure 5.7: Experimental ignition delays showing how TRF surrogate compares with reference gasoline. Error bars are also shown, P = 20 bar, ϕ = 1.

5.3.2 Simulations and local sensitivity analysis

Simulations of the Leeds RCM data for TRF were achieved using the combined LLNL gasoline surrogate mechanism [88] and the updated *n*-butanol scheme of Sarathy et al. [199] developed in partnership with the KAUST group in the course of this study. More information on the TRF/*n*-butanol blended mechanism including the updates made on the *n*-butanol scheme can be found in section 3.3.3. The ability of the LLNL surrogate gasoline mechanism [88] to capture the low temperature ignition delay data is demonstrated in Figure 5.8. The mechanism captures the general temperature

dependence fairly well, although the NTC region predicted by the model is shallower and narrower than that seen in the experimental data. The cause of this slight discrepancy can be attributed to the model itself rather than the surrogate formulation, since the experimental data for the surrogate mixture shows a similar NTC behaviour to the gasoline. At low temperatures there is a slight over estimation of ignition delay times, although experimental uncertainties are expected to be larger for these longer delays. Both linear and global sensitivity analyses were carried out to determine the main reactions driving uncertainties in predicted ignition delays across the temperature range. Figure 5.9 presents the result of the local sensitivity analysis for predicted ignition delay times of TRF for the temperatures range of T = 679 – 858 K.

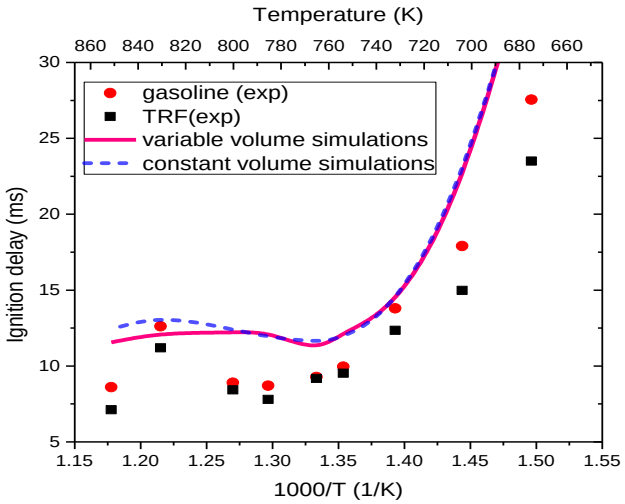

Figure 5.8: Experimental and simulated ignition delays for gasoline and TRF. ϕ = 1, P = 20 bar.

The local sensitivity analysis demonstrates that the most dominant reactions below temperatures of 761 K are those of OH reacting with either iso-octane, *n*-heptane or toluene with the sensitivity indices for the H abstraction reaction from *n*-heptane by OH being the lowest for these set of reactions. The absolute values of the normalised sensitivity indices for H-abstraction reactions from the α, β and γ sites are 0.739, 0.631 and 1.000 respectively for iso-octane while those for *n*-heptane are 0.389, 0.581 and 0.512 respectively. The only H abstraction reaction for toluene highlighted by the sensitivity analysis of the LLNL scheme is via HO_2 radical. The main toluene + OH route captured in the sensitivity analysis is expressed as the reverse rate constant leading to the formation of CH_3 and C_6H_5OH and its sensitivity index was estimated as 0.918.

In contrast to both *n*-heptane [127] and iso-octane [152, 230], toluene does not exhibit NTC behaviour [231], and the sensitivity analysis shows the reaction of toluene + OH is almost as important as that of iso-octane at low temperatures.

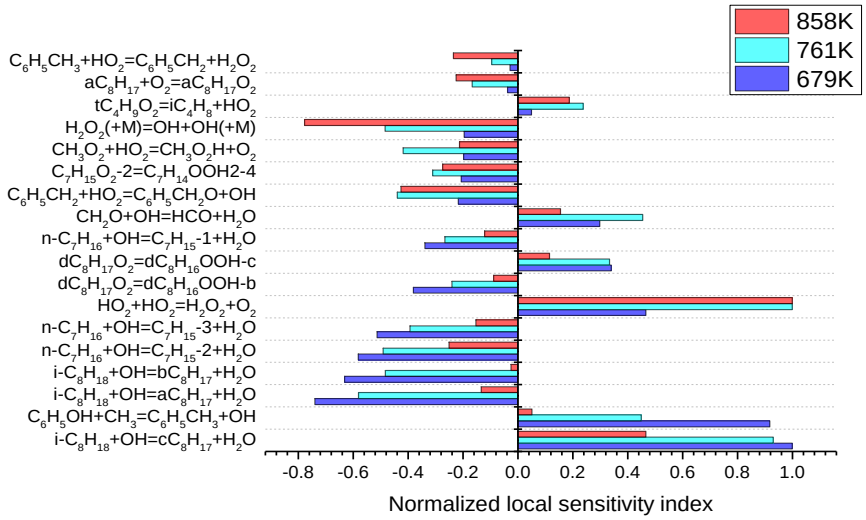

Figure 5.9: Normalised local sensitivity indices for simulations of ignition delay time for TRF at 3 different temperatures. ϕ = 1, P = 20 bar.

A high temperature shock tube study for toluene was reported in [232] where the reaction of toluene + H was noted as the most dominant abstraction channel in simulations carried out at P = 10 atm and T =1600 K. Large discrepancies in toluene mechanisms were noted in [231] for stoichiometric toluene ignition delay data at high pressure (P = 45 bar) and T = 1045 K in an RCM. Their work also showed substantial discrepancies in local sensitivities between the different mechanisms, with toluene + OH and toluene + H reaction channels ranking very highly for one of the mechanisms and then very poorly for another of the mechanisms [231]. Hence the relative importance of different product channels for these reactions could be important for the accurate prediction of the behaviour of surrogate mixtures. The main kinetic study of toluene + OH of relevance to combustion temperatures is a transition state theory study from Seta et al. [233]. There are likely to be large uncertainties in this system which will clearly impact on the robustness of TRF mechanisms. This point is addressed further in the next section involving the global sensitivity approach where the predictive error bars based on the inherent uncertainties in the rate parameters are determined. In addition, the main

reactions contributing to the predictive uncertainties are identified and ranked in the next section.

At slightly higher temperatures, iso-octane + OH is the more dominant reaction when compared to that of toluene. This reaction was also dominant in the analysis of a 4-component surrogate mixture in [97], at T = 780 K for stoichiometric conditions, followed by the toluene + OH pathways and to a lesser extent *n*-heptane + OH as seen here. Here, the reaction of formaldehyde + OH is important across the whole temperature range, but particularly so at the highest temperature. The sensitivity analysis also shows that the reactions of HO_2 dominate above T = 780 K. Nagy et al. [234] highlighted uncertainties of a factor of 2.5 in the reaction rate for $HO_2 + HO_2 = H_2O_2 + O_2$ for temperatures above 700 K. A similar level of uncertainty was suggested for OH + OH (+M) = H_2O_2 (+M) which ranks highly here for temperatures above 780 K.

The isomerisation reactions from RO_2 to QOOH are of lower importance here than fuel + OH which contrasts with the behaviour of smaller molecules [183]. However, they do feature for both iso-octane and *n*-heptane channels across the range of temperatures studied, and thus uncertainties in the temperature dependence of these reactions could affect the prediction of NTC behaviour. Nevertheless, since overall the predictions from the LLNL surrogate mechanism provide a reasonable representation of the temperature dependence of the gasoline ignition delay data, the mechanism was therefore employed as the basis for modelling blending in section 5.4.

5.3.3 Global uncertainty and sensitivity analysis

Figure 5.10 presents the uncertainty plot for predicted TRF ignition delays at ϕ = 1 and temperature range of 679 - 858 K using the blend mechanism while accounting for the effect of uncertainties in the input rate parameters. The uncertainty factors adopted in the uncertainty analysis of the TRF/*n*-butanol blended mechanism are given in Appendix A3. Figure 5.10 shows that the error bars currently existing within the TRF system are quite large rising above an order of magnitude in the NTC region where the model performance is weakest. However, the experimental data points overlap fairly well with the predicted error bars indicating that reasonable values of uncertainty factors have been adopted for the key rates in the blend scheme. This also indicate that the model is reasonably sound in terms of its structure or mechanistic framework despite

the parametric deficiency. Within the NTC region, the measured ignition delays are in closest agreement with the 25th percentile of the predicted distribution suggesting that some key input parameters would need to be fairly close to the limit of their input uncertainty range in order to improve the level of agreement of the model with experimental data.

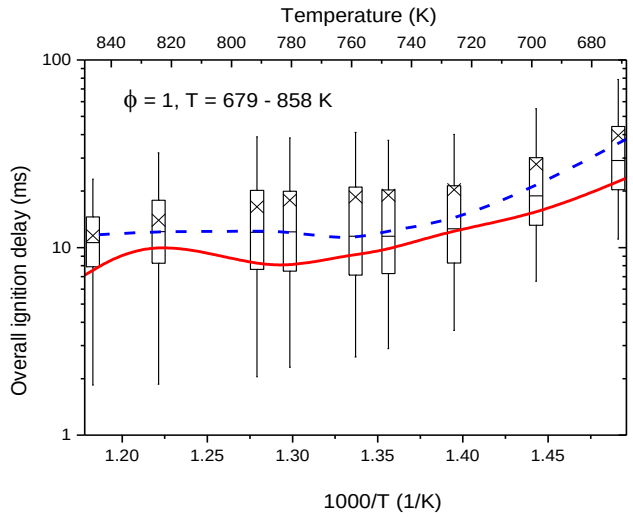

Figure 5.10: Comparison of predicted TRF ignition delays with experimental data (red line) obtained in this study. Boxes represent 25th and 75th percentiles while whiskers represent 5th and 95th percentiles. The blue dashed line represents model simulation with nominal parameter values. The large crosses and horizontal lines represent the mean and median of the predicted output from the 256 simulations respectively.

Figure 5.11 highlights the first–order global sensitivity indices computed for ignition delay times using the variance based HDMR method for three representative temperature conditions at ϕ = 1 and P = 20 bar. This approach provides a ranking of each input parameter in terms of their contribution to the overall output variance. Figure 5.11 shows that at the lower temperature (i.e. 679 K), a total of seven reactions involving fuel + OH contribute to over 80% of the predicted error bars. The most dominant reaction at lower temperatures is that of OH + toluene expressed as the reverse (CH_3 + C_6H_5OH = $C_6H_5CH_3$ + OH) with its contribution being about 30 % of the overall predicted uncertainties. This is somewhat surprising since a recent theoretical study by Seta et al. [233] suggested this to be significantly slower than the hydrogen abstraction route via OH. Further investigation performed in this study to understand why the H abstraction is not the dominant route is presented in section 5.4. Hydrogen abstraction

reactions by OH from the α, β and γ sites of iso-octane and *n*-heptane were also found to play a significant role in agreement with the local sensitivity study presented in Figure 5.9. At higher temperatures, the contribution from the reaction CH_3 + C_6H_5OH = $C_6H_5CH_3$ + OH diminishes considerably (disappearing at T = 858 K) with the H abstraction reaction from the γ site for iso-octane via OH becoming far more dominant. The main first-order global sensitivities shown in Figure 5.11 indicates that the alkyl + HO_2 reactions for toluene are also quite important for the predicted TRF ignition delays at high temperatures. Also, for toluene a growing importance is observed for the isomerisation reaction from RO_2 to QOOH as the temperature increases. The white portion in Figure 5.11 represents the contribution from reactions that are not displayed in the legend or the combined effect from higher order terms.

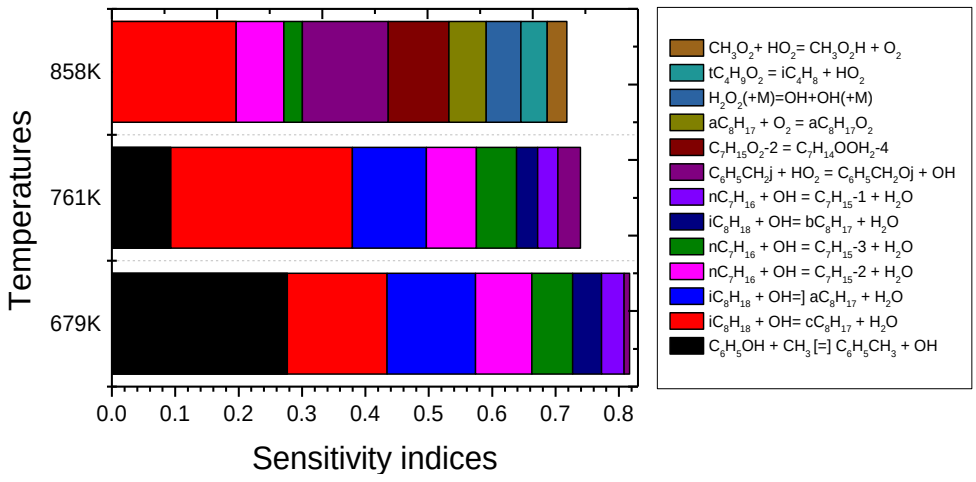

Figure 5.11: Main first-order sensitivity indices for simulated ignition delays of TRF at ϕ =1 and P = 20 bar with respect to the key reaction rates at selected temperatures and pressures. The shading for each reaction is shown in the legend.

The analysis of the first-order component functions plots further helps to explore the shape of the relationship between the input parameters and the target output. The first-order component plots (Figure 5.12) show that at T = 679 K, a nonlinear relationship exists between the target output and input rates across a large portion of the input space for all three most important reactions dominating the predicted uncertainties. Decreasing the rate of the phenol route (CH_3 + C_6H_5OH = $C_6H_5CH_3$ + OH) would likely improve the agreement with the experimental data at low temperature (Figure 5.12a) due to the attendant increase in reactivity while reducing the rate of the H abstraction reaction for

iso-octane from the γ site, would have no significant effect on the predicted uncertainties (Figure 5.12c) as the effect saturates in the lower part of the input space. On the other hand, increasing the rate of the abstraction reaction from the α site for iso-octane could potentially lead to an increase in reactivity of the TRF system at low temperature (Figure 5.12b) and better agreement with experiment but this is still dependent on the influence of second-order and higher order interactions. One interesting thing we observe in Figure 5.12b is that the influence of the uncertainties from all other reactions reduces considerably in the upper part of the input range as shown by the scatter which narrows down in this region and this would suggest that some reasonable level of constraint is provided by the ignition delay measurements on this iso-octane H abstraction rate by OH.

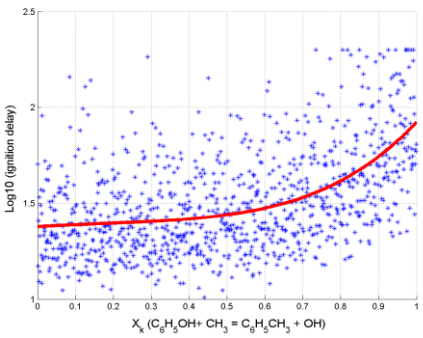

(a)

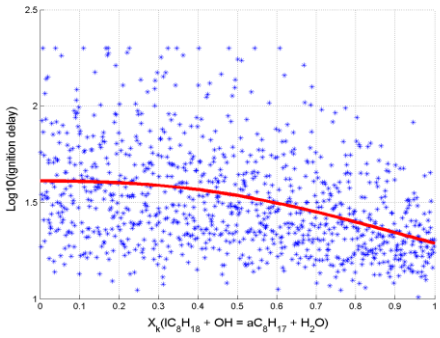

(b)

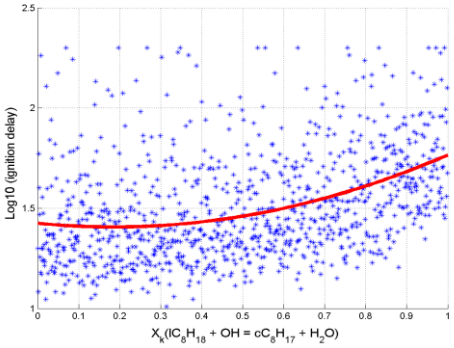

(c)

Figure 5.12: HDMR component functions (solid line) of simulated TRF ignition delays shown on-top of the scatter. P = 20 bar, ϕ = 1, T = 679 K. Sensitivity with respect to (a) CH3 + C_6H_5OH = $C_6H_5CH_3$ + OH (b) IC_8H_{18} + OH = aC_8H_{17} + H_2O (c) IC_8H_{18} + OH = cC_8H_{17} + H_2O.

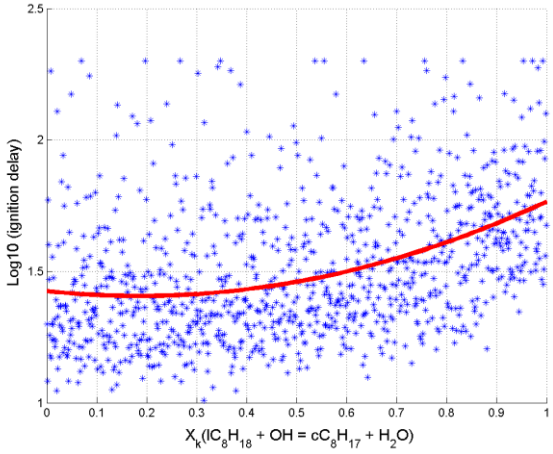

Figure 5.13: HDMR component functions (solid line) of simulated TRF ignition delays shown on-top of the scatter. P = 20 bar, ϕ = 1, T = 761 K. Sensitivity with respect to $IC_8H_{18} + OH = cC_8H_{17} + H_2O$.

Within the NTC region, specifically at T = 761K, the iso-octane H abstraction reaction by OH from the γ site, dominates the predicted uncertainties (Figure 5.11) with the reactions $CH_3 + C_6H_5OH = C_6H_5CH_3 + OH$, $iC_8H_{18} + OH = aC_8H_{17} + H_2O$ and $nC_7H_{16} + OH = C_7H_{15}\text{-}2 + H_2O$ also contributing to a smaller degree. However, looking at the functional relationship between the rate of this reaction $IC_8H_{18} + OH = cC_8H_{17} + H_2O$ and the predicted ignition delays (Figure 5.13), no significant constraint is provided by the measured delays on this rate in the lower region of the input space where better agreement may be obtained as the slope of the first-order response is very close to zero in that region. On the other hand, a plot of the predicted log ignition delay against the scaled ratio of the log reaction rates for the iso-octane H abstraction reactions by OH from the α and γ site results in an almost linear relationship as shown in Figure 5.14. The computed sensitivity index of this branching fraction for iso-octane is 0.622 which is about three times the value of sensitivity for the individual reactions. Again, similar to what was observed for the *n*-butanol + OH system, this demonstrates the importance of the relative rates of the hydrogen abstraction reactions of iso-octane from the different sites that lead to chain branching compared to the competing reaction channels that lead to chain propagation or termination, on the accurate prediction of the ignition delay times of TRF in the RCM. Therefore better constraint is provided by the measured ignition delay data on the branching ratio for iso-octane than on the individual abstraction rates via OH from the and γ site.

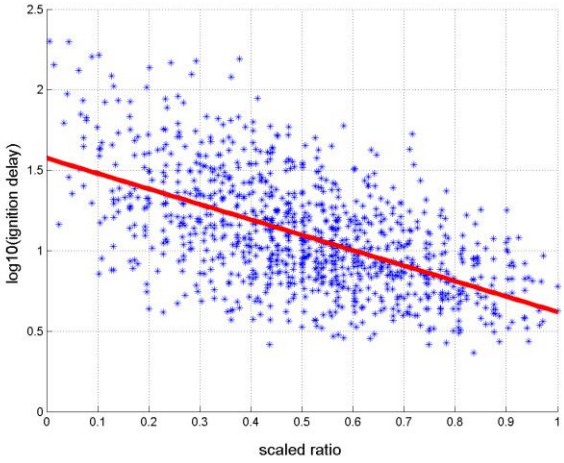

Figure 5.14: Scatter plot and HDMR component function for predicted log (ignition delay) of TRF against the scaled branching ratio for the two iso-octane main H abstraction reactions T = 761 K, ϕ = 1, P = 20 bar.

5.4 The influence of *n*-butanol blending on gasoline and its surrogate

20% *n*-butanol by volume was blended with both the gasoline and TRF surrogates to determine its influence on ignition delay times. The chosen TRF formulation is seen to behave very similarly to gasoline and therefore appears to provide a reasonable representation of the effects of blending across the temperature range (Figure 5.15). Figure 5.16 shows that both for the gasoline and the TRF, the ignition delays of the blend lie somewhere in between those of the unblended fuels across the temperature range. However, an interesting feature emerges at the lowest temperatures studied, where the ignition delays for the blend lie very close to those of pure *n*-butanol despite it being only 20 % of the mixture. At these lower temperatures the *n*-butanol clearly acts as an octane booster. The addition of *n*-butanol also has the effect of smoothing out the NTC region when compared to the gasoline/TRF behaviour. A similar effect was reported in Frassoldati et al. [235] for ethanol, where ethanol addition to a PRF mixture was observed to result in the disappearance of the NTC region. As highlighted in this work (Figure 5.16) and in [235], the inhibiting effect of alcohols, however disappears at high temperatures as the observed delays are quite similar for both the gasoline and the alcohol blend. The effect of blending a single stage ignition fuel such as *n*-butanol with a two-stage fuel (i.e. *n*-heptane, PRF or gasoline) was also reported in Saisirirat et al. [236]. In their work, similar to the findings in this study, it was shown that at low to

intermediate temperatures, the cool flame delay and the main combustion stage delay of *n*-heptane are increased with increasing 1-butanol addition to *n*-heptane.

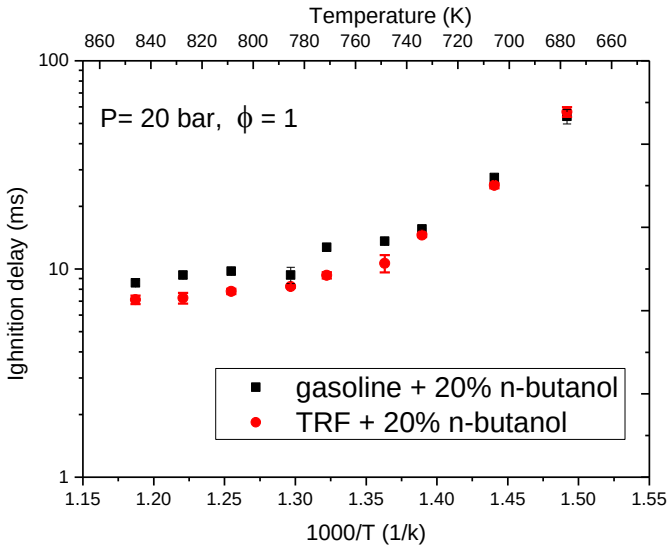

Figure 5.15: Experimental ignition delays showing how TRF/*n*-butanol surrogate blend compares with gasoline/*n*-butanol. Error bars are also shown , P = 20 bar, ϕ = 1.

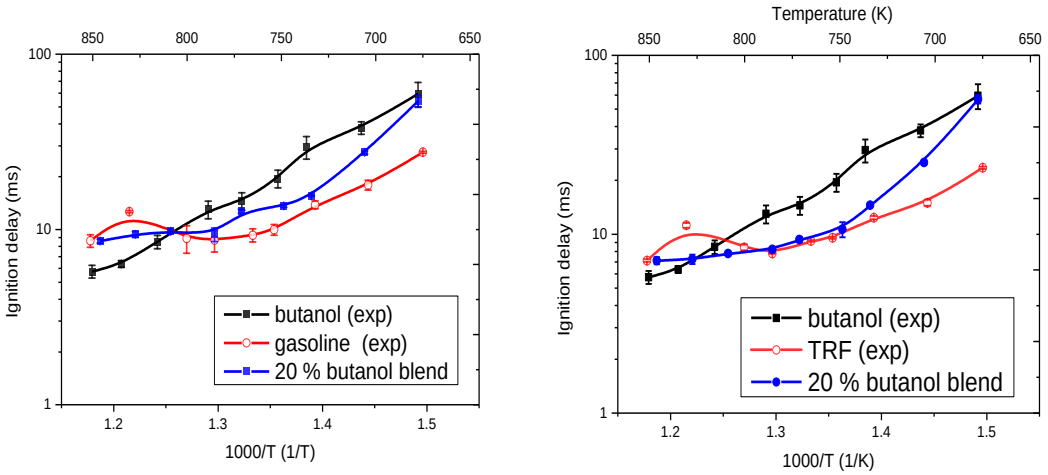

(a) (b)

Figure 5.16: Experimental ignition delays for a) gasoline and b) TRF on blending with 20% *n*-butanol by volume. Error bars are also shown , P = 20 bar, ϕ = 1.

5.4.1 Simulations and local sensitivity analysis

Simulations of the blend were also achieved using the combined TRF/*n*-butanol mechanism mentioned in section 5.3.2. The scheme reproduces the temperature dependence of the ignition delays well for the blends (Figure 5.17), with the predicted delays lying between those for TRF and *n*-butanol across the temperature range (Figure 5.18). However, at the lowest temperatures, the simulated delays for *n*-butanol are significantly longer than the measured data (triangle symbols in Figure 5.18). Hence the combined model seems to better predict the delays for the blends than for *n*-butanol. The reason for this behaviour of the mechanism is unclear as it does not seem like a case of cancellation of errors since both the TRF and *n*-butanol are overpredicted on their own. The sensitivity analyses presented in Figures 5.19 and 5.20 highlight possible reasons for the discrepancy.

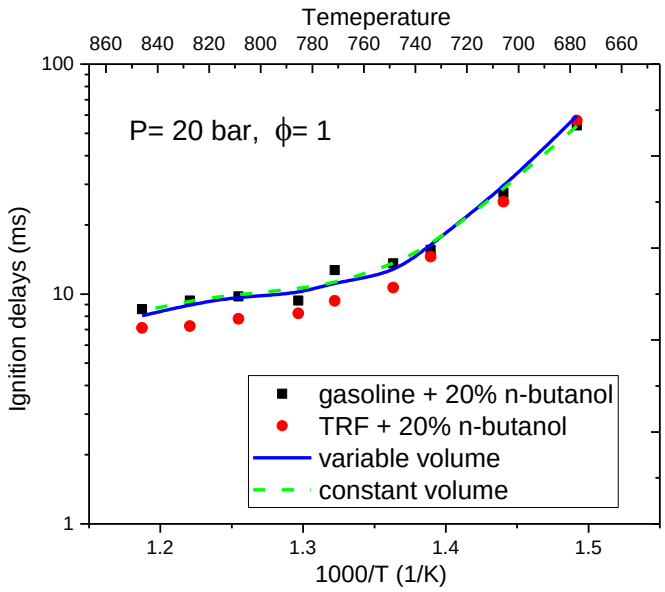

Figure 5.17: Experimental ignition delays for gasoline/*n*-butanol and TRF/*n*-butanol mixtures and simulated ignition delays for TRF/*n*-butanol mixtures. ϕ = 1, P = 20 bar.

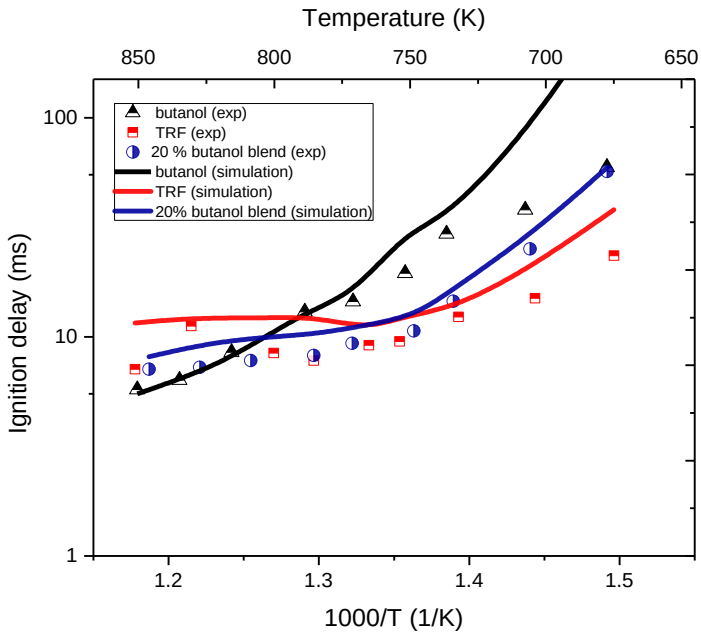

Figure 5.18: Comparison of simulated and experimental ignition delays for TRF on blending with 20% *n*-butanol by volume with those of stoichiometric TRF and *n*-butanol. P = 20 bar.

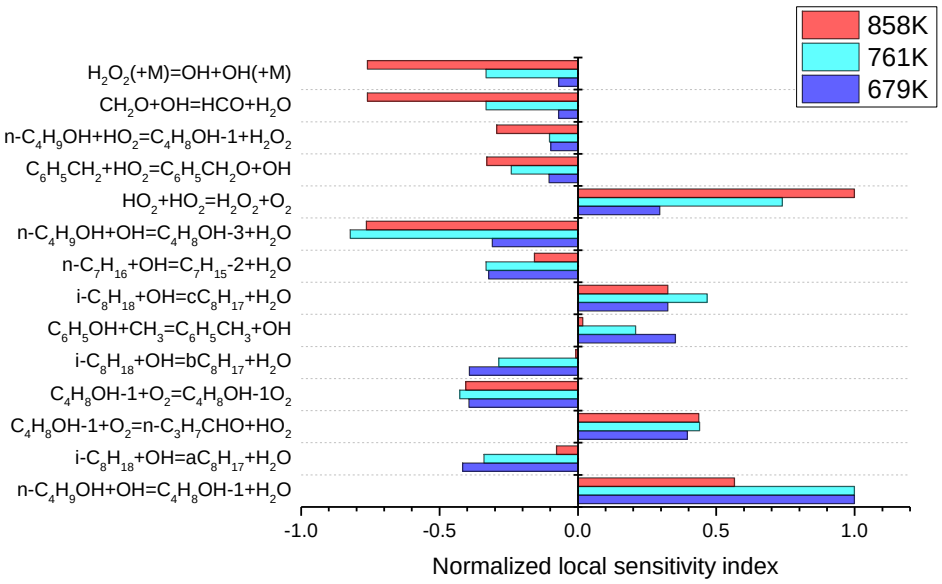

Figure 5.19: Normalised local sensitivity indices for simulations of ignition delay time for TRF/*n*-butanol blend at 3 different temperatures. ϕ = 1, P = 20 bar. *n*-butanol is 20% by volume.

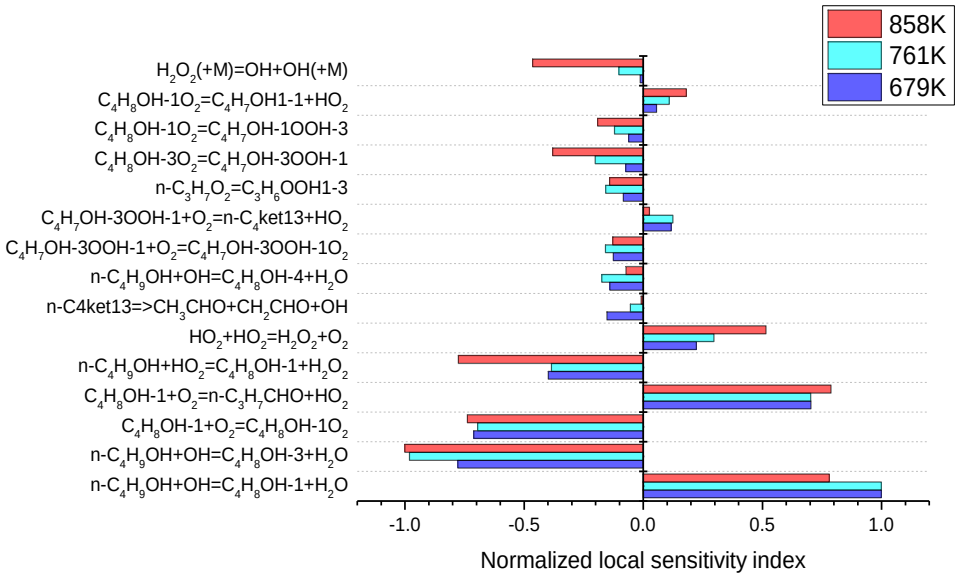

Figure 5.20: Normalised local sensitivity indices for simulations of ignition delay time for *n*-butanol at 3 different temperatures. ϕ = 1, *P* = 20 bar.

The first interesting feature is that, despite forming only 20% of the mixture by volume, it is the *n*-butanol + OH channels that dominate the predictions for the blends across the temperature range studied (Figure 5.19). Similar to the findings in Frassoldati et al. [235], the sensitivity analysis of Figure 5.19 also reveals the role of *n*-butanol in scavenging OH radicals from the system particularly leading to the formation of H_2O and hydroxybutyl radicals. For the blend mixture, H abstraction from the α site dominates at the lowest temperatures. Abstraction from the γ site increases in relative importance as temperature increases. For *n*-butanol (Figure 5.20), the γ pathway is relatively more important at the lowest temperature compared to the blend (Figure 5.19). It is this low temperature region for *n*-butanol where the biggest discrepancies occurred between the simulated and experimental results. The temperature dependence for the overall reaction rate suggested in [198] is based on a fit to both low temperature measurements below 400 K and the high temperature shock tube measurements of [237] (888 − 1178 K). Thus, the uncertainty in the overall rate may be larger in the temperature region of interest here. In addition, the global sensitivity study of predicted ignition delays for *n*-butanol at *T* = 725 K and *P* = 15 bar [197] carried out in chapter 4 (section 4.3.1.4), demonstrated that the sensitivity to the relative rates of abstractions from the α and γ sites was much higher than that to the overall rate constant. McGillen et al. suggest

higher uncertainties for the site specific channel for the γ site compared to the α site [198]. Hence uncertainties in the relative rates could be significant.

The sensitivity analysis shows that the hydroxybutyl radicals produced via the main fuel hydrogen abstraction reactions from the α sites are the most dominant compared to those from the other abstraction sites both in terms of RO_2 and HO_2 formation. The α-hydroxybutyl radical is consumed via two different reaction pathways: the oxygen addition reaction (α-hydroxybutyl + O_2) leading to the formation of the peroxy radical (RO_2) that drives autoignition; and the competing oxygen addition reaction (α-hydroxybutyl + O_2) leading to the formation of HO_2, a termination step that inhibits autoignition. As already mentioned in section 4.3.1.4, the dominance of the main fuel hydrogen abstraction reactions in the blended TRF-butanol scheme, in contrast to the well-known isomerisation reaction of RO_2, may be due to its key role in determining the amount of *n*-butanol that goes to termination steps compared with how much is available for chain branching and propagation. The ability of the reaction mechanism to correctly predict the low temperature delays for both *n*-butanol and the blend requires that the balance between the two dominant abstraction channels for *n*-butanol + OH is known for a wide range of temperatures and significant uncertainty still exists requiring further study.

5.4.2 Global uncertainty and sensitivity analysis

Figure 5.21 and Figure 5.22 show the calculated error bars for the simulated ignition delay times of TRF/*n*-butanol and neat *n*-butanol using the combined TRF and *n*-butanol scheme adopted in this study. Looking at Figure 5.21, we see that the predicted uncertainties for the TRF/*n*-butanol mixtures are largest (i.e. above an order of magnitude) in the temperature region 761 – 834 K where the discrepancy between the model's prediction and measured data is most pronounced. However, the experimental data falls well within the median (50^{th} percentile) of the predicted ignition delay distribution. In contrast to the experimental data, at the lowest temperatures, the simulated ignition delay profiles for *n*-butanol fall close to the outliers far away from the median of the distribution. In the uncertainty analysis, at very low temperatures, certain combinations of the sampled input rates resulted in extremely long ignition delay times and such results were therefore truncated in order to reduce the required

computational time. This explains why the simulated delay times at the nominal rate (blue line) are now shifted closer to the outliers of the distribution rather than the median of the distribution. This explanation is also true for the predicted TRF/*n*-butanol distribution shown in Figure 5.21 but in this case the effect is less pronounced compared to that of pure *n*-butanol due to the lower predicted ignition delay times of the blend. For *n*-butanol, the predicted uncertainties (Figure 5.22) are the largest and are over two orders of magnitude in the low temperature region where the models agreement with the measured data is also worse. The discussion in the next section is centred on the global HDMR analysis carried out in order to highlight the most important reactions influencing the predicted *n*-butanol and TRF/*n*-butanol output distribution.

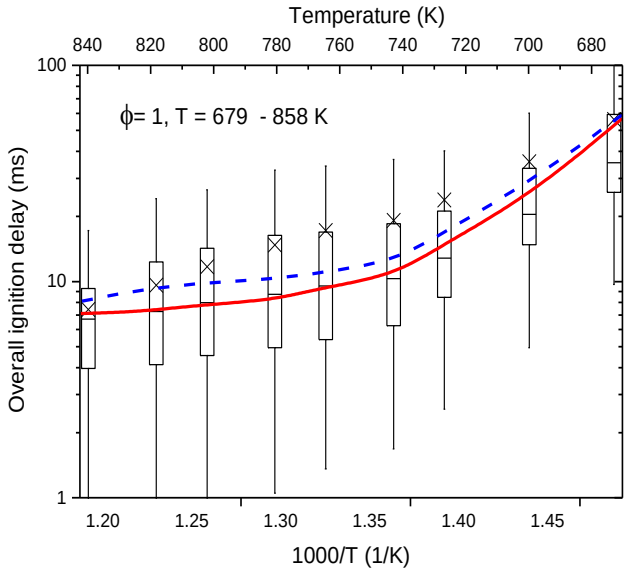

Figure 5.21: Comparison of predicted TRF/*n*-butanol ignition delays (blue) with experimental data (red) obtained in this study. Boxes represent 25th and 75th percentiles while whiskers represent 5th and 95th percentiles. The large crosses and horizontal lines represent the mean and median of the predicted output from the 256 simulations respectively.

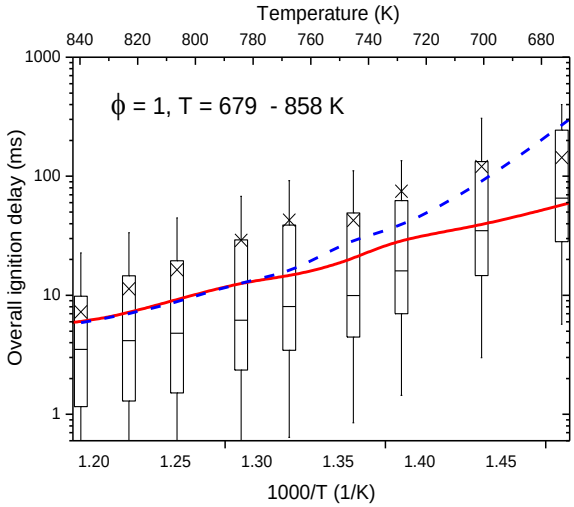

Figure 522: Comparison of predicted *n*-butanol ignition delays (blue) with experimental data obtained (red) in this study. Boxes represent 25th and 75th percentiles while whiskers represent 5th and 95th percentiles. The large crosses and horizontal lines represent the mean and median of the predicted output from the 256 simulations respectively.

Figure 5.23 shows the first-order sensitivity indices calculated in the HDMR analysis for predicted *n*-butanol + TRF ignition delay times. At lower temperatures, the *n*-butanol + OH hydrogen abstraction reaction from the α site is found to be the most dominant reaction in terms of its contribution to the predicted uncertainties. Other key reactions contributing to the predicted uncertainties include $C_4H_8OH\text{-}1 + O_2 = C_4H_8OH\text{-}1O_2$, $IC_8H_{18} + OH = aC_8H_{17} + H_2O$ and $C_6H_5OH + CH_3 = C_6H_5CH_3 + OH$. As the temperature is increased to 858 K, the relative dominance of the *n*-butanol + OH abstraction reaction from the α site becomes significantly smaller while that of abstraction from the γ site conversely increases with abstraction from the γ site dominating the predicted uncertainties at T = 858 K. The trend observed within the global sensitivity framework for the TRF/*n*-butanol system is similar to that obtained using the local sensitivity approach except that in the local sensitivity analysis, at T = 858 K, the reaction involving hydroperoxyl, leading to the formation of H_2O_2 ($HO_2 + HO_2 = H_2O_2 + O_2$) was slightly more dominant compared to the *n*-butanol + OH abstraction reaction from the γ site.

For the *n*-butanol system, the results of the HDMR analysis (Figure 5.24) show that at the lower temperature (i.e. T = 679 K), the chain branching pathway (alpha-

hydroxybutyl + O_2) leading to the formation of the peroxy radical (RO_2) (γ -C_4H_8OH-1 + O_2 = C_4H_8OH-1O_2) is the most dominant reaction, being responsible for over 20 % of the predicted uncertainties. This was not the case for the local sensitivity analysis of *n*-butanol where the hydrogen abstraction from the γ site of the *n*-butanol + OH channel dominated the uncertainties in the predicted ignition delay times. In the *n*-butanol system, a smaller fraction of the overall uncertainties (about 10 % and 12 %) is also accounted for by the α and γ branching fractions of *n*-butanol + OH respectively. The slight difference between the most dominant reaction channel obtained in the local sensitivity analysis and that captured in the global sensitivity analysis can be attributed to the impact of the input uncertainty range adopted for the chain branching pathway relative to that of the H abstraction reaction from *n*-butanol by OH (see Appendix A3 for table of uncertainty range). The impact of the chain branching reaction however diminishes with increases in temperature while the contribution from *n*-butanol + OH abstraction reaction from the γ site, becomes more significant similar to the result obtained for the local sensitivity analysis. At high temperature, the H abstraction reaction from *n*-butanol by HO_2 leading to the formation of C_4H_8OH-1 and H_2O_2 is shown to be equally as important as the abstraction reaction from the γ site.

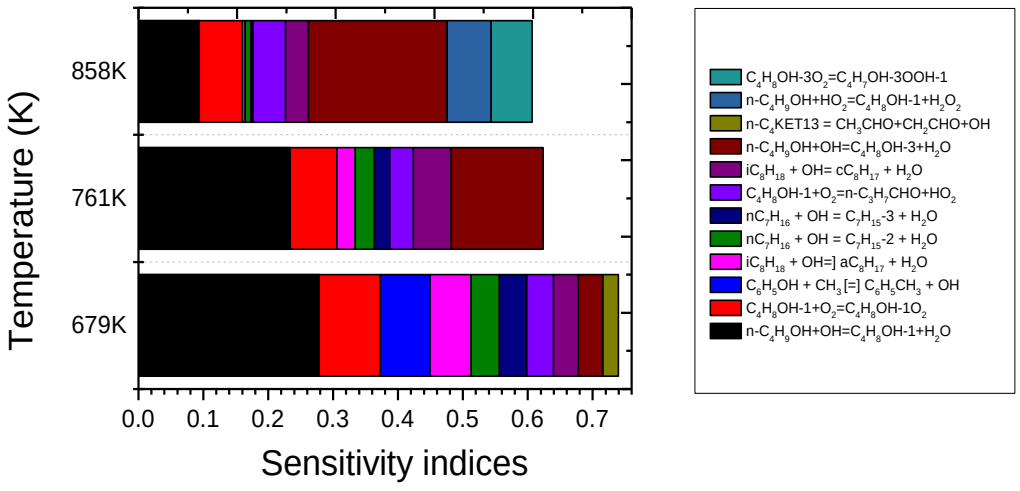

Figure 5.23: Main first-order sensitivity indices for simulated TRF/*n*-butanol ignition delays with respect to reaction rates at selected temperatures and pressures. The shading for each reaction is shown in the legend. P = 20 bar, ϕ = 1.

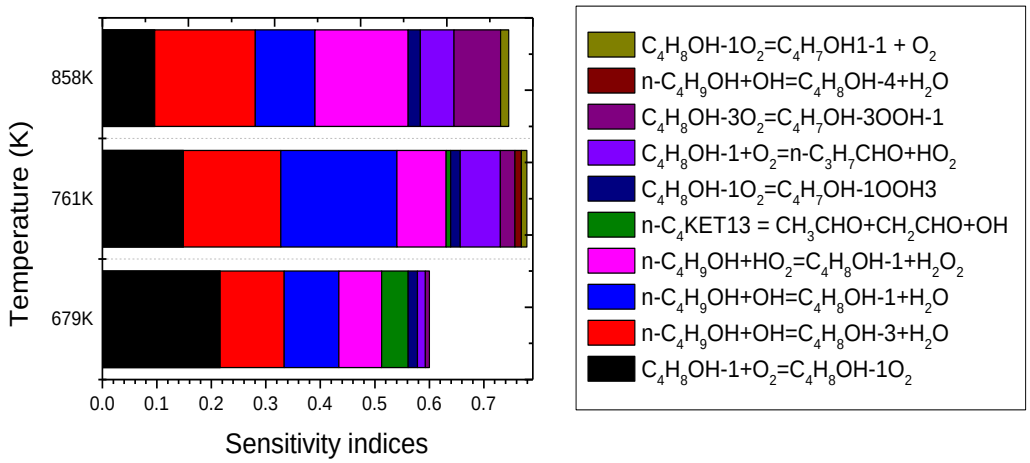

Figure 5.24: Main first-order sensitivity indices for simulated *n*-butanol ignition delays with respect to reaction rates at selected temperatures and pressures. The shading for each reaction is shown in the legend. P = 20 bar, ϕ = 1.

Based on the computed sensitivity indices from the HDMR analysis (Figure 5.23) it is clear that the branching fractions of *n*-butanol + OH (α and γ site) with global sensitivity indices of 0.234 and 0.142 respectively are important for the TRF/*n*-butanol system at 761 K as they account for about 40 % of the predicted output uncertainties in this region where the highest discrepancy occurred. Figure 5.25 presents the first-order component plots for these two abstraction reactions at T = 761 K with the scatter in the figure representing the impact of the uncertainties in the other parameters within the mechanism. The overall response of these two parameters to the predicted delays is nonlinear and the overall slopes are opposite to one another. While a reasonable level of constraint is provided in the individual rate of the two abstraction reactions by the measured data as indicated by the computed sensitivities, none of them solely dominates the predicted output uncertainties meaning that different combinations of these two rates could lead to different levels of improvement in terms of the agreement with the experimental data. The high temperature component plot for the TRF/*n*-butanol system (Figure 5.26) shows that a decrease in the γ abstraction rate of *n*-butanol + OH could potentially also lead to improvement in the model's prediction at high temperatures.

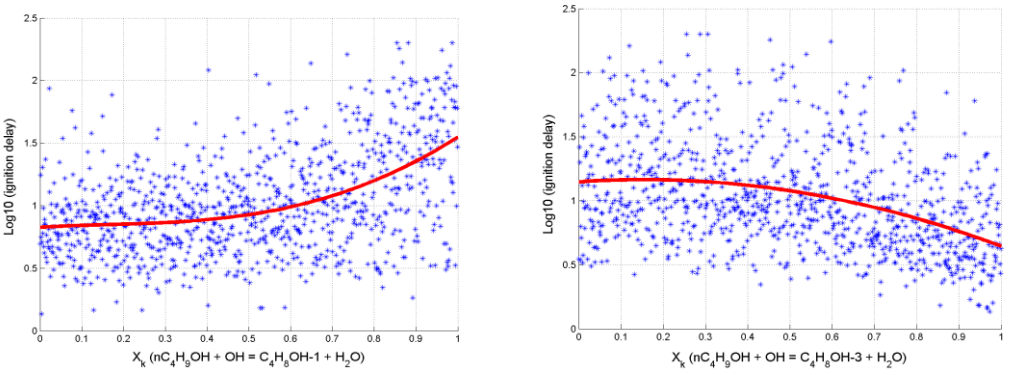

(a) (b)

Figure 5.25: Component function for TRF/*n*-butanol mixture at *T* = 761 K with respect to (a) *n*-C_4H_9OH + OH = C_4H_8OH-1 + H_2O (b) *n*-C_4H_9OH + OH = C_4H_8OH-3 + H_2O.

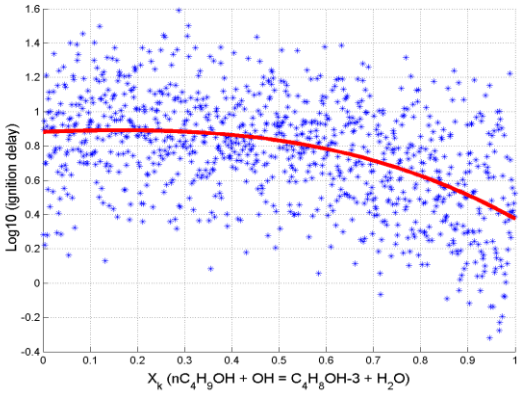

Figure 5.26: Component function for TRF/*n*-butanol mixture at *T* = 858 K with respect to *n*-C_4H_9OH + OH = C_4H_8OH-3+ H_2O.

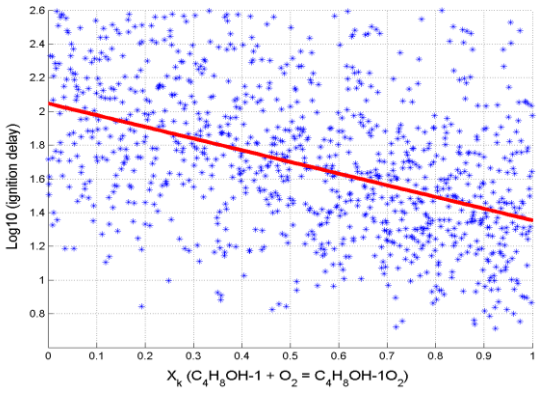

Figure 5.27: Component function for *n*-butanol mixture at 679 K with respect to C_4H_8OH-1 + O_2 = C_4H_8OH-1O_2.

Figure 5.27 shows that the predicted *n*-butanol ignition delays are well correlated to the O_2 addition pathway and a large increase in this rate could potentially lead to a considerable decrease in the predicted *n*-butanol delays at lower temperatures. The large scatter however indicates that other reaction pathways such as the competing termination step leading to the formation of HO_2 ($C_4H_8OH\text{-}1 + O_2 = n\text{-}C_3H_7CHO + HO_2$), could become more significant as the rate of this reaction is increased.

5.5 Analysis of toluene + OH system

5.5.1 Comparison of Arrhenius parameters

The results of the local and global sensitivity analysis described in section 5.3.3 and reported in [65] for predicted TRF ignition delays using the combined TRF/*n*-butanol mechanism, showed a strong sensitivity to the reaction toluene + OH = phenol + CH_3 rather than the hydrogen abstraction channels by OH (toluene + OH = $C_6H_4CH_3 + H_2O$). This was however not expected as a recent study by Seta et al. [233] on the reaction of OH radicals with benzene and toluene suggested that the hydrogen abstraction route (toluene + OH = $C_6H_4CH_3 + H_2O$) is significantly faster than the toluene + OH route leading to the formation of phenol. Figure 5.28 shows the Arrhenius plot in which the temperature dependence of the forward rates of the toluene + OH = $C_6H_4CH_3 + H_2O$ and toluene + OH = phenol + CH_3 reaction pathways, obtained from the study of Seta are compared. In Figure 5.28, we see that the OH abstraction routes could be over ten times faster than the phenol route across the temperature range.

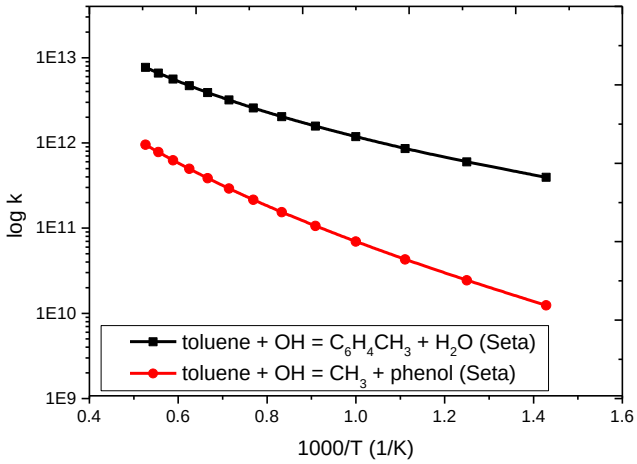

Figure 5.28: Comparison of the forward rates of toluene H abstraction route (toluene + OH) and the phenol route from a recent study of Seta et al. [233].

In order the understand why the H abstraction channel is not the dominant route, a critical investigation of the sources of the data for the current parametrisation of the two toluene + OH routes in the available version of the LLNL TRF mechanism was therefore carried out. It was found in the course of the investigation that the current parametrisation of the H abstraction route (toluene + OH = $C_6H_4CH_3$ + H_2O) in the LLNL TRF mechanism, is based on the recent data from the theoretical study of Seta. The H abstraction reactions in the LLNL scheme were updated from the paper of Seta et al. [233], but for some reason which is not clear as at the time of this study, it appears that the toluene + OH channel leading to the formation of phenol (toluene + OH = phenol + CH_3) was not updated from the same source. In the update of Mehl et al. [88], all attacks on the toluene ring by OH including the reaction toluene + OH = $C_6H_4CH_3$ + H_2O in the mechanism were taken to be the same with the ones estimated by Seta [233] for benzene.

In order to test the impact of the differences between the rate parameterisation of the reversed form of the phenol route (phenol + CH_3 = toluene + OH) which is included in the TRF/*n*-butanol mechanism and that of Seta [233], on the predicted ignition delays, a new set of reaction rates were computed for the reversed reaction based on the forward rate data obtained from the paper of Seta. The method employed for the computation of the reversed reaction rates is described briefly in the following section.

5.5.2 Calculation of reversed rate based on data of Seta

In Cantera, the temperature dependence of the forward rate constants k_f follows the Arrhenius expression given by:

$$k_f = A_f T^{n_f} \exp\left(-E_f/RT\right) \tag{4.6}$$

where A_f is the A -factor (pre-exponential factor), n_f is the temperature exponent, E_f is the activation energy, T is the absolute temperature and R is the universal gas constant.

By using Equation 2.11 and 2.12 in chapter 2 of this thesis, the reversed rates of any reaction can be calculated if the forward rates are known. The temperature-dependent reversed rates for the phenol route were determined using the value of the forward rates of the reaction given in the paper of Seta alongside the equilibrium rate constants estimated using the NASA polynomials in the TRF/*n*-butanol mechanism for the involved species. Table 5.1 gives the values of the equilibrium constant and reversed rates calculated across the temperature range 700 -1900 K using equations 2.11-2.15.

Table 5.1: Calculated equilibrium constant and reversed rates

Temperature (K)	k_f(T)[c]	$k_{eq}(T)$	$k_r(T)$
700	1.24×10^{10}	6.94×10^{2}	1.79×10^{7}
800	2.43×10^{10}	3.53×10^{2}	6.90×10^{7}
900	4.28×10^{10}	2.09×10^{2}	2.05×10^{8}
1000	6.95×10^{10}	1.38×10^{2}	5.02×10^{8}
1100	1.06×10^{11}	9.85×10^{1}	1.08×10^{9}
1200	1.54×10^{11}	7.42×10^{1}	2.07×10^{9}
1300	2.15×10^{11}	5.83×10^{1}	3.69×10^{9}
1400	2.91×10^{11}	4.73×10^{1}	6.16×10^{9}
1500	3.84×10^{11}	3.95×10^{1}	9.72×10^{9}
1600	4.95×10^{11}	3.37×10^{1}	1.47×10^{10}
1700	6.26×10^{11}	2.93×10^{1}	2.14×10^{10}
1800	7.78×10^{11}	2.57×10^{1}	3.02×10^{10}
1900	9.53×10^{11}	2.27×10^{1}	4.20×10^{10}

[c] Values obtained from the paper of Seta et al. [233]

The associated reversed rate parameters required in the CANTERA input file for the simulations such as the temperature exponent *n*, frequency factor *A* and activation energy *E* were further estimated using a least square fit to the reversed rate data.

As presented in Figure 5.29, a comparison of the rates of the reversed form of the phenol route (toluene + OH = phenol + CH_3) captured in the LLNL mechanism with those estimated from the data of Seta shows a significant difference in their temperature dependence. Although both rate constant parametrisation are closely matched at high temperature, the disparity is quite large at lower temperatures.

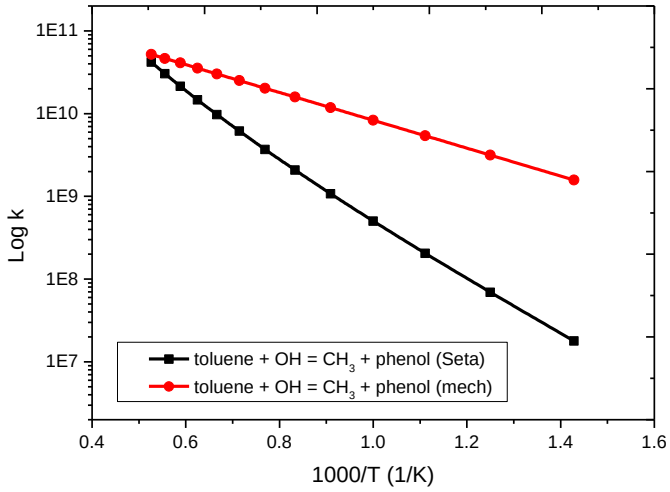

Figure 5.29: Comparison of the reversed rates of the phenol route (toluene + OH = phenol + CH_3) captured in the LLNL mechanism with those estimated from the data of Seta et al. [233].

5.5.3 Impact of update on reaction mechanism based on new data

The rate of the phenol route in the mechanism was finally updated to that in the paper of Seta and variable volume ignition delay simulations were repeated based on the new set of data. Figure 5.30 shows the result of the predicted ignition delays based on the updated mechanism. Interestingly, as shown in Figure 5.30, the updated mechanism gives a better agreement with the experimentally measured ignition delays at P =20 bar under stoichiometric conditions. Also, we see that the NTC region is now predicted to a higher level of accuracy and this is important for accurate prediction of autoignition and knock in practical engines. The update also leads to a reasonable improvement in the predicted ignition delays of the TRF, *n*-butanol blend (Figure 5.31) mainly within the lower to intermediate temperature region.

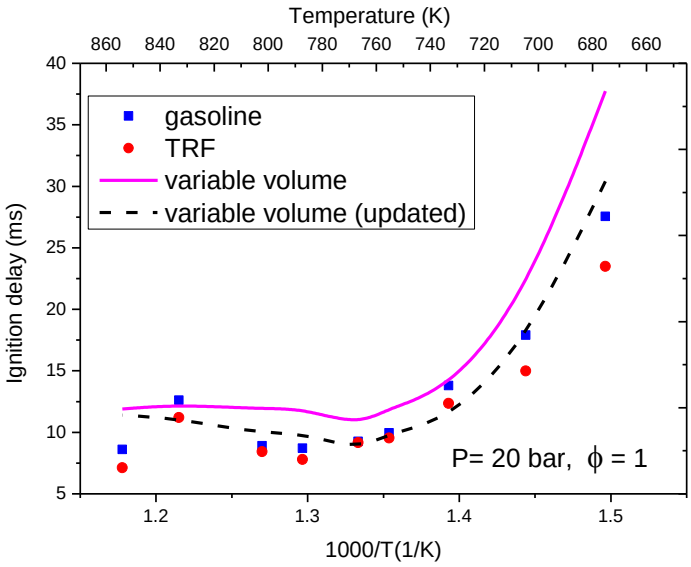

Figure 5.30: Ignition delay simulations showing how the updated mechanism compares with original LLNL data, TRF mixtures at P = 20 bar, ϕ = 1.

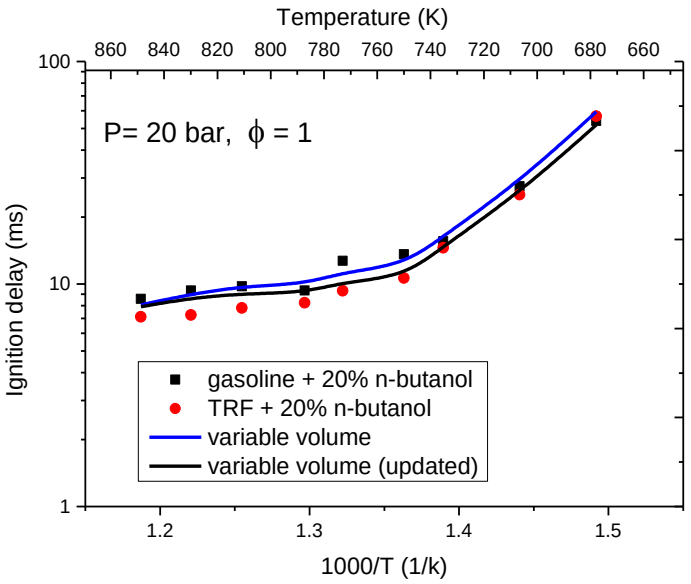

Figure 5.31: Ignition delay simulations showing how the updated mechanism compares with original LLNL data, TRF, *n*-butanol blend at P = 20 bar, ϕ = 1.

Furthermore, local sensitivity analysis was repeated for the TRF mixture using the updated scheme to see if the importance of this channel will now be replaced by the H abstraction route. The result of local sensitivity analysis based on the updated mechanism is presented in Figure 5.32 for fifteen (15) of the most sensitive reactions. As expected the toluene + OH hydrogen abstraction route is now captured as one of the

most important (dominant) reactions for low temperature ignition delay prediction of TRF mixtures while the phenol route is shown to be relatively unimportant as it is not among the set of reactions identified in the sensitivity analysis. Interestingly, this is in agreement with the analysis of the component plot presented in Figure 5.12a (section 5.3.3) where the sensitivity of the phenol route is shown to be quite low at the lower end of the adopted input range.

It is also worth pointing out that based on the update, the iso-octane chemistry, specifically the iso-octane + OH hydrogen abstraction reaction from the γ site now dominates the predicted ignition delays of TRF. Also the alkyl + HO_2 route for toluene which was prominent at higher temperatures in the local sensitivity result based on the original TRF/*n*-butanol mechanism has now disappeared.

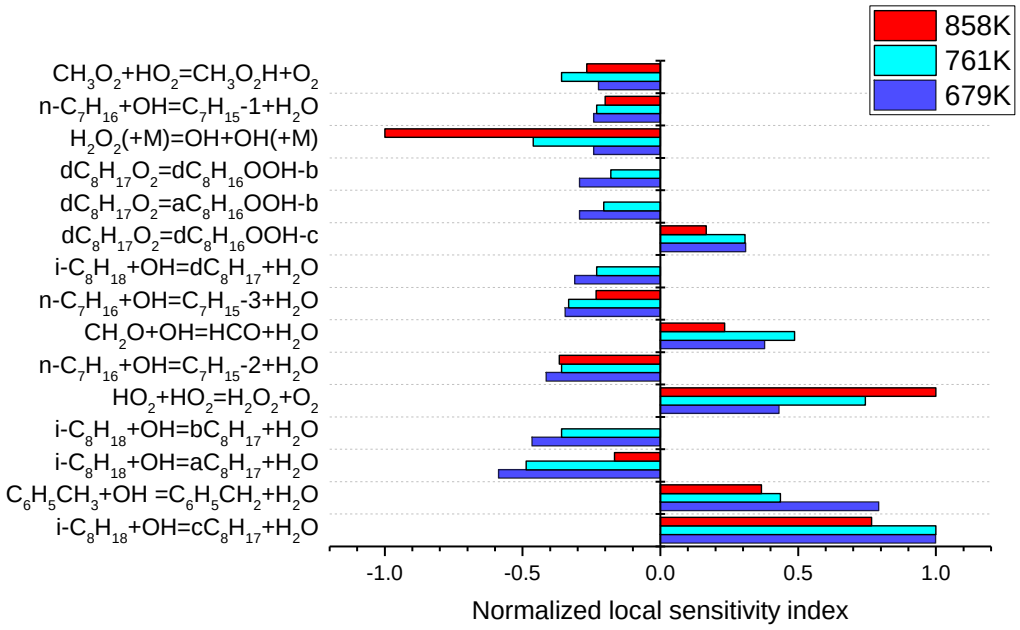

Figure 5.32: Brute-force local sensitivity result based on updated mechanism for TRF mixtures at P = 20 bar, ϕ = 1.

5.6 Summary

The influence of blending *n*-butanol at 20% by volume on the ignition delay times for a reference gasoline was studied in a rapid compression machine (RCM) at 20 bar from 678 - 858 K. Delay times for the blend lay between those of gasoline and *n*-butanol

under stoichiometric conditions across the temperature range. At lower temperatures, delays for the blend were much closer to those of *n*-butanol than gasoline, despite *n*-butanol being only 20% of the mixture, showing that *n*-butanol acts as an octane enhancer over and above what might be expected from a simple linear blending law. At higher temperatures the delay times for the blend were slightly shorter than those for gasoline and TRF within the shallow NTC region, although similar at the highest temperatures tested here. Whether the addition of *n*-butanol leads to octane enhancing qualities will therefore be highly dependent on local engine temperature conditions with a particularly sensitive region around 775 - 850 K. Experimentally, the 3-component TRF surrogate was able to capture the gasoline trends well across the temperature range. This was the case for both pure gasoline and on blending with *n*-butanol at 20%. The TRF formulation used therefore appears to be fairly robust but would need to be tested over wider ranges of blending conditions in future work. Local and global sensitivity analysis of the mechanism based on predicted ignition delays for stoichiometric TRF mixtures showed the phenol + CH_3 = toluene + OH route to be among the top dominant pathways but an update on the mechanism based on recent data from the study of Seta resulted in the toluene + OH channel becoming the most dominant reaction as expected. For the TRF/*n*-butanol blend, hydrogen abstraction reactions by OH from *n*-butanol appear to be key in predicting the effect of blending. Uncertainties in the temperature dependence of relative abstraction rates from the α and γ sites may still be present within current mechanisms, and in particular may affect the ability of the mechanisms to capture the low temperature delay times for *n*-butanol. Further studies of the product channels for *n*-butanol + OH for temperatures of relevance to combustion applications could help to improve current mechanisms. At higher temperatures, the reactions of HO_2 and that of formaldehyde with OH also became critical and attempts to reduce uncertainties in the temperature dependent rates of these reactions would be useful.

Overall, the global sensitivity study demonstrates that there is need to capture the relative rates for the different abstraction routes in the TRF/*n*-butanol mechanism and not just the overall fuel + OH rate in order to improve the capability of the TRF/*n*-butanol mechanism in predicting the ignition delay times of TRF, *n*-butanol and their blends.

Chapter 6

Experimental and chemical kinetic modelling study on the combustion, autoignition and knock properties of gasoline, its surrogate and blend with *n*-butanol in an SI engine

6.1 Introduction

6.1.1 Background and motivation

Engine downsizing which aims at reducing the engine swept volume and consequently fuel consumption without penalising power output is currently considered as a viable option for achieving a low carbon footprint in the transportation sector. In order for a downsized engine to achieve the same amount of power as the original engine, a boosting system (supercharging) is usually required to increase the density of inlet air. However, supercharging and the use of high compression ratios are currently limited by the phenomena of knock [228]. There is now an increased demand for fuels with high anti-knock quality as blending agents (octane boosters) [228] and this has also triggered a renewed interest to better understand the knock behaviour of new and alternative fuels for the purpose of optimising engine design and control strategies (i.e. ignition timing optimisation). Knock in an SI engine is predominantly caused by the autoignition of the end gas (unburned mixture of air and fuel) ahead of the propagating flame which results in the formation of high pressure gradients that propagate in the form of pressure oscillations (waves) across the combustion chamber. Depending on the amplitude of the pressure oscillations, engine knock could be potentially damaging to engine parts (piston, valves etc.) and must therefore be avoided. Autoignition and knock in an engine are governed by chemical kinetics and depend on the chemical composition of the fuel and on the evolution of pressure, temperature and equivalence ratio [92]. It would be helpful to be able to use computer simulations employing chemical kinetic mechanisms of fuels in main engine combustion models to reliably predict and understand autoignition and consequently knock in an engine. The ability to predict autoignition and knock in an engine can be quite beneficial to engine designers as it provides the opportunity to better understand the engine design parameters, engine operating conditions and fuel types or fuel blends with the highest potential for knock free engine

operation. Computer modelling, by providing information on the main parameters controlling engine combustion processes, can also be used as a tool to guide future experimental work and also aid the modelling of engine processes across a wide spectrum of operating conditions [238]. In the past, attempts have been made to predict autoignition using various simple empirical models. Two of such correlations are the popular Douaud and Eyzat (D&E) model [47] derived from the Arrhenius function and the Livengood-Wu integral [51] both of which are fully described in section 2.2.4.1. In terms of chemical kinetic modelling, the prediction of autoignition in the engine has been limited to the use of very basic global chemical reaction mechanisms developed for a limited number of fuels, e.g. the 'Shell model' [54] comprised of 5 species and 8 generalised reactions representing chain/degenerate branching and termination steps and the skeletal Hu and Keck model [56]. However these global kinetic models just like the empirical models, have been proven to be grossly inaccurate in terms of agreement with measured data. The various unique features of combustion such as the cool flame and two stage ignition as well as the long ignition delay times exhibited by certain hydrocarbons fuels can only be reasonably explained by the intermediate elementary reactions that make up the detailed reaction mechanism. Therefore the use of detailed or reduced reaction mechanisms that are coupled to main engine combustion models offers a far greater capability to predict autoignition in an engine to a higher level of accuracy and therefore forms the basis for this study. It should be noted that chemical kinetic models are however generally developed and validated within fundamental engine-like setups such as RCM, JSR, shock tubes etc., where the effects of fluid dynamics and turbulence are suppressed [30, 36, 179] and where the prevailing *P-T* conditions are much more representative of the *P-T* conditions occurring before autoignition in a HCCI and or controlled autoignition (CAI) engines rather than in SI engines. In SI engines, higher *P-T* conditions prevail in the end gas due to high compression induced in the end gas by the propagating flame. Therefore it crucial to test the applicability of these models under practical engine conditions in order to establish the impact of the chemistry-flow (fuel-engine) interactions and higher *P-T* conditions prevalent in SI engines on the predictability and robustness of these chemical kinetic models.

Thus one of the objectives of this study is to assess the ability of a recently developed reduced TRF/*n*-butanol blended mechanism [65], employed previously in the Leeds RCM modelling work (see chapter 5), to accurately predict the autoignition and knock behaviour of gasoline and gasoline/*n*-butanol blend under practical SI engine conditions. A further objective of the study is to link the fundamental understanding developed from the chemical kinetic modelling of the auto-ignition of alternative fuels carried out within the RCM and presented in the previous chapter, with the performance of the TRF/*n*-butanol scheme in terms of the autoignition and knock onset predicted by the scheme under real engine conditions. The chemical kinetic modelling of the knock onsets of TRF and TRF/*n*-butanol fuels have been carried out using the recently developed commercial engine simulation software known as LOGEengine, while the knock onsets of unleaded gasoline (ULG), TRF, gasoline/*n*-butanol and TRF/*n*-butanol blends have been measured using the Leeds University Optical Engine (LUPOE) for validation of the modelling work. Details of the experimental setup and the LOGEengine code used in the modelling work are fully described in section 3.2.2 and section 3.4.4 respectively while the chemical kinetic model employed in the simulations is described in section 3.3.3. As mentioned in section 3.3.4.1 of the methodology, the current engine modelling work is based on the spark ignition (SI) engine multi-zone thermodynamic model of the LOGEengine code. The multi-zone thermodynamic engine model has been chosen in this work as it is currently the best trade-off between the use of accurate but highly computationally expensive CFD models which can be coupled with only skeletal mechanisms, and the use of a very fast and efficient but fairly inaccurate single-zone homogenous engine model that can be coupled with very large and detailed reaction mechanisms.

6.1.2 Objective of the current chapter

The influence of *n*-butanol as an alternative fuel on the knocking behaviour of gasoline has been investigated in a spark ignition engine using both experimental and modelling approaches. The goal of this chapter is to present and discuss the results obtained from the experimental and modelling work carried out in the engine in comparison with the results obtained in the RCM. The first part of this chapter (section 6.2) presents and discusses the experimental results of the in-cylinder combustion properties of gasoline, a gasoline/*n*-butanol blend and their surrogates (TRF, TRF/*n*-butanol blend) measured

in LUPOE-2D under both normal and knocking combustion conditions. Section 6.2.1 presents the peak pressures and mean in-cylinder pressures measured in LUPOE- 2D under normal combustion while the knock onsets, knock intensities and peak pressures measured under knocking conditions are presented in section 6.2.2. The last part of this chapter (section 6.3) presents and discusses the results of the chemical kinetic modelling of TRF and a TRF/*n*-butanol blend in comparison with the measured data. Also in section 6.3, the performance of the Sarathy chemical kinetic scheme within the current modelling work involving the SI engine is compared with the results obtained in the RCM modelling framework (chapter 5). Finally in section 6.3.4, the results obtained with the updated version of the Sarathy TRF/*n*-butanol blended scheme are presented in comparison with the results from the original scheme.

6.2 Measured combustion characteristics of gasoline, a gasoline/*n*-butanol blend and their surrogates in LUPOE-2D

6.2.1 Measured combustion characteristics of gasoline, a gasoline/*n*-butanol blend and their surrogates under normal combustion

Figure 6.1 shows the crank angle resolved cycle-by-cycle pressure traces collected in LUPOE-2D for the four fuel mixtures under normal combustion at a knock free spark timing of 2 CA bTDC. The procedure used in collecting the pressure data is described in detail in section 3.3.2. Figure 6.2 presents a comparison of the crank angle resolved mean pressure cycle of each set of 39 pressure cycles shown in Figure 6.1 for the four fuel mixtures. Under normal combustion, the 20% *n*-butanol/gasoline blend showed higher burning rates with higher peak pressures compared to gasoline, TRF and the TRF/*n*-butanol blend (Figure 6.2). The faster burning velocity of the gasoline/*n*-butanol blend can be attributed to the impact of the 20% by volume of *n*-butanol in the mixture as alcohols have been generally reported [91, 239] to display higher burning velocities. Ethanol, olefins (i.e. 1-hexene) and *n*-heptane were shown in [240] to have higher burning velocities compared to iso-octane and toluene. The TRF surrogate showed slightly lower burning velocities and consequently lower peak pressures compared to the reference gasoline. Looking at the composition of the TRF mixture presented in section 3.2.1.3 (Table 3.1), over 65 % by volume of the mixture is accounted for by slower burning iso-octane and this is mainly responsible for the observed lower burning

velocity of TRF. The lower burning rate of TRF compared to gasoline can also be partly explained by the absence of faster burning fuel components such as ethanol and olefins which are present in the reference gasoline at about 5 % and 8 % by volume respectively. The burning velocity of the TRF/*n*-butanol blend was the lowest as given by the lowest value of the mean peak pressure (Figure 6.2). Therefore the trend shown on blending TRF with *n*-butanol is also opposite to that shown for the blend involving gasoline. This is however surprising as the peak pressure of the TRF/*n*-butanol blend was expected to be higher than that of the TRF mixture due to the influence of the 20% by volume addition of the relatively fast burning *n*-butanol in the blend. Although the amount of fast burning *n*-heptane in the TRF mixture is reduced from about 11.5 % by volume to about 9 % by volume in the TRF/*n*-butanol blend, it is not clear as at the time of this study if that is mainly responsible for the considerably lower peak pressure recorded by the TRF/*n*-butanol blend (TRFB20). Investigation of the spark discharge showed that this was consistent across the four fuels and therefore unlikely to be the cause. This requires further study in order to explore and understand the underlying cause of the observed behaviour in the TRFB20 blend. At a more advanced spark timing of 4 CA bTDC (Figure 6.3), the TRF mixture displayed a slightly higher burning rate (i.e. higher peak pressure) compared to the other fuel mixtures due to the influence of knock

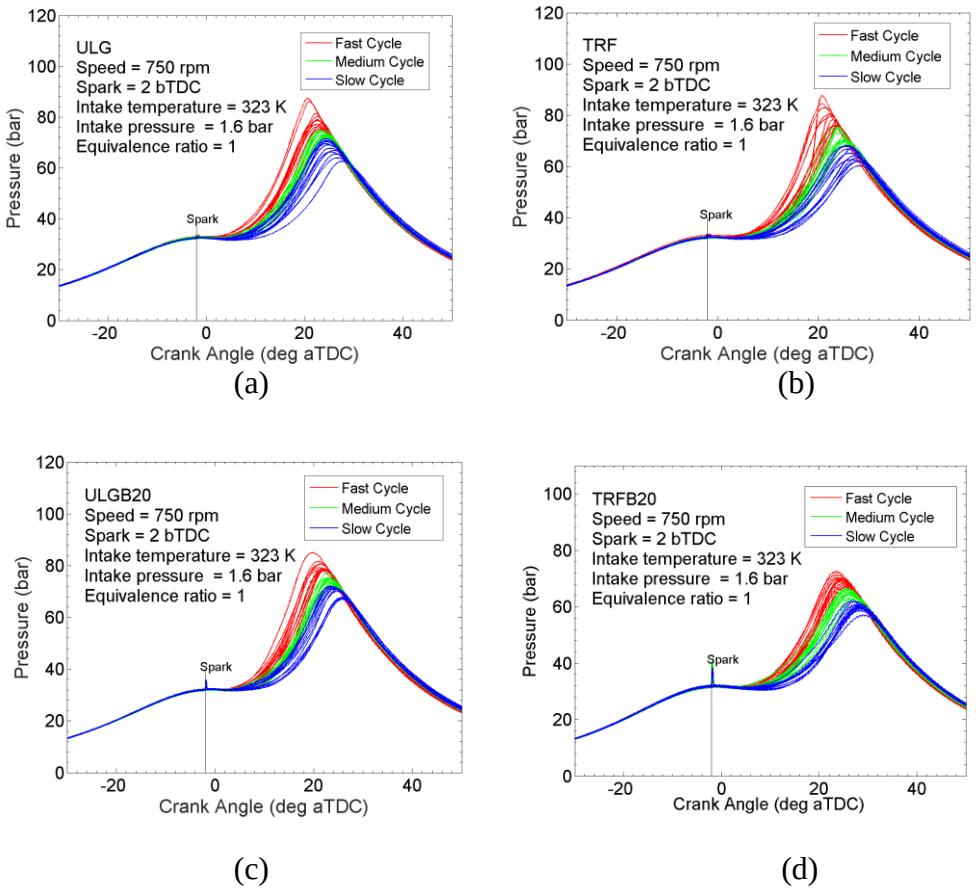

Figure 6.1: Typical pressure traces collected in LUPOE-2D under normal combustion for the four fuels at a spark timing of 2 CA bTDC. Shown are 39 cycles each for (a) ULG (b) TRF (c) ULGB20 (d) TRFB20.

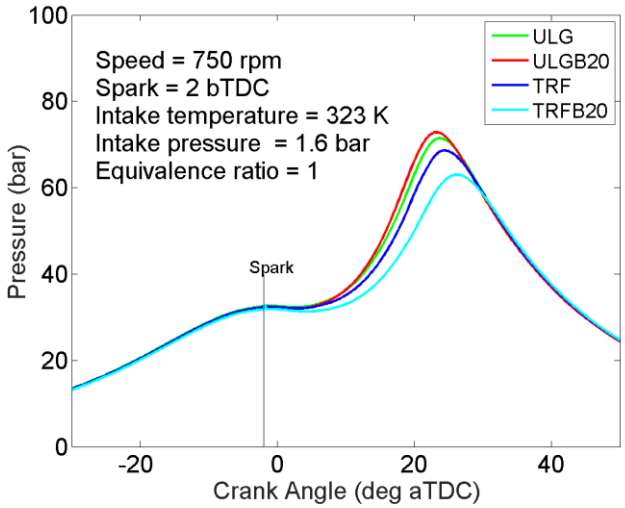

Figure 6.2: Mean pressure cycle for ULG, TRF, ULGB20 and TRFB20 at a spark timing of 2 CA bTDC.

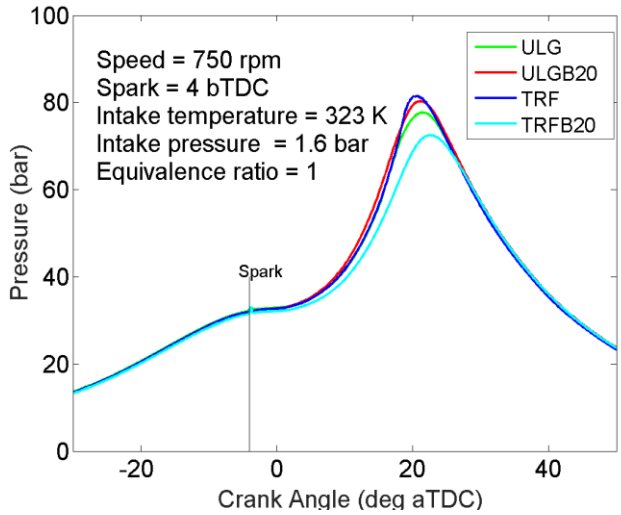

Figure 6.3: Mean pressure for ULG, TRF, ULGB20 and TRFB20 at a spark timing of 4 CA bTDC.

Figure 6.4 presents the cycle-by-cycle analysis of the peak pressures as a function of the crank angle at which they occur at a spark timing of 2 CA bTDC. In general, the relationship between the measured peak pressures and the crank angle of occurrence is linear across the set of fuels investigated with the higher peak pressures occurring at a corresponding earlier crank angle. In order to compare the magnitude of variability in the set of peak pressures collected under normal combustion, the coefficient of variation (COV) in the peak pressures for the 39 cycles recorded at a spark timing of 2 CA bTDC for each of the four fuels has been computed and presented in Table 6.1. The COV is given by the ratio of the standard deviation to the mean of the data. Although the TRF surrogate reproduces the range of peak pressures of the reference gasoline reasonably well as shown in Figure 6.4, the degree of cyclic variability is higher compared to gasoline (Table 6.1). While a higher disparity exists between the range of peak pressures measured for the gasoline/*n*-butanol blend and the TRF/*n*-butanol blend (Figure 6.4), compared to that between gasoline and TRF, the coefficient of cyclic variability (Table 6.2) between the blends is reasonably closer. Interestingly, the cyclic variability of the measured peak pressures for the gasoline/*n*-butanol blend and the TRF/*n*-butanol blend are lower than those of gasoline and TRF respectively (Table 6.1), indicating the impact of blending on cyclic variability. Minimal cyclic variability is desired in engine operation as a high cyclic variability has the potential to narrow down the engine operating range as well as reduce the engine performance [30].

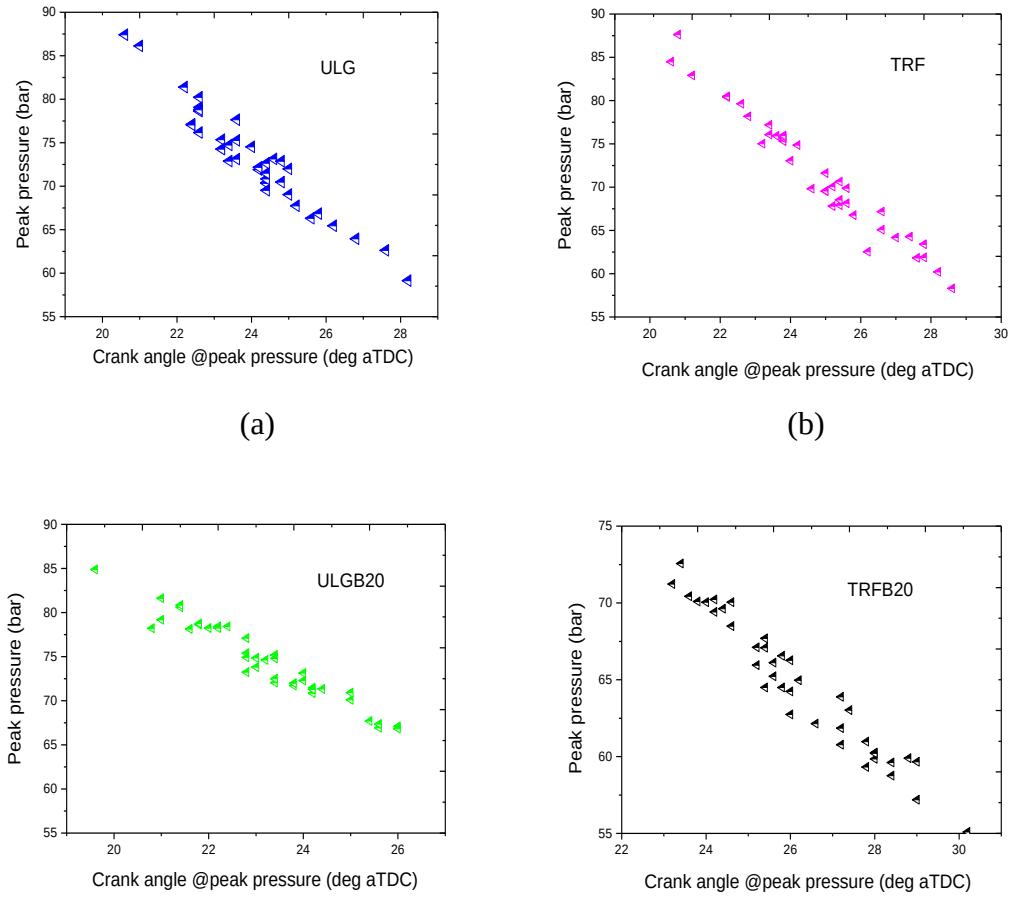

Figure 6.4: Cyclic variability of peak pressures versus corresponding crank at its occurrence measured at a spark timing of 2 CA bTDC (a) ULG b) TRF (c) ULGB20 (d) TRFB20.

Table 6.1: Coefficient of variation of peak pressures for the four fuels at 2 CA bTDC

Fuel	COV (%)
ULG	7.98
TRF	9.85
ULGB20	6.02
TRFB20	6.87

6.2.2 Measured combustion properties of gasoline, TRF and their surrogates under knocking conditions

The study of fuel effect on the knock boundary performed for the set of chosen fuels under similar engine conditions showed an earlier knocking regime (spark advance 4 CA bTDC) for the formulated TRF compared to the rest of the fuels. While gasoline exhibited a similar knock boundary (spark advance 6 CA bTDC) with the blended fuels, for TRF, a far higher number of measured cycles (over 98 %) were knocking with higher knock intensities at the knock boundary compared to the blends in which only a few cycles exhibited knock with very low intensities.

6.2.2.1 Measured in-cylinder pressures

Typical knocking pressure cycles for the four fuels recorded at an advanced spark timing of 8 CA bTDC are presented in Figure 6.5 while the mean pressure based on the cycles shown in Figure 6.5 for each of the fuels are compared with one another in Figure 6.6. Again, similar to the result obtained under non-knocking conditions, the gasoline/*n*-butanol blend exhibited the fastest burning velocity with the highest mean pressure. At the more advanced spark timing of 8 CA bTDC, the mean pressure of the TRF mixture (Figure 6.6) is in very good agreement with that of gasoline and only slightly higher indicating that the disparity between gasoline and the formulated surrogate reduces as the spark timing is well advanced.

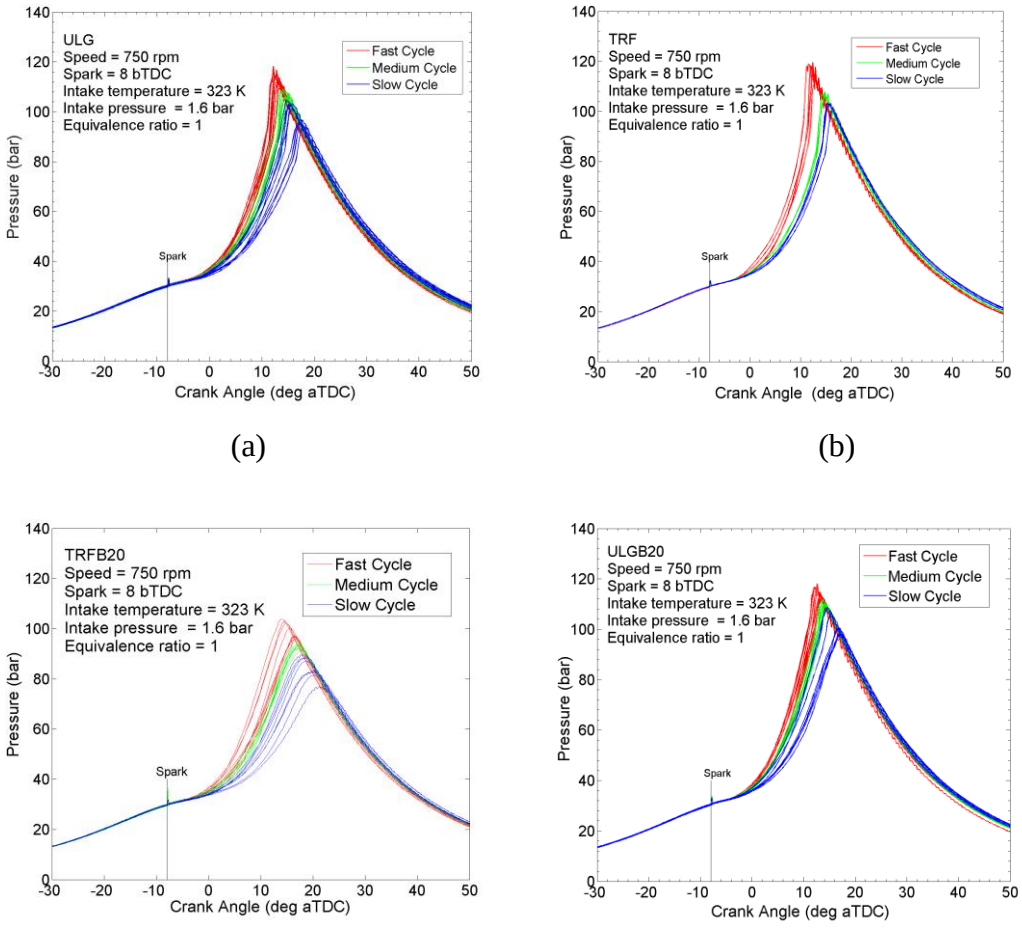

Figure 6.5: Typical pressure traces collected in LUPOE-2D under knocking combustion for the four fuels at a spark timing of 2 CA bTDC. Shown are 26 cycles each for (a) ULG (b) TRF (c) TRFB20 and 12 cycles for (d) ULGB20.

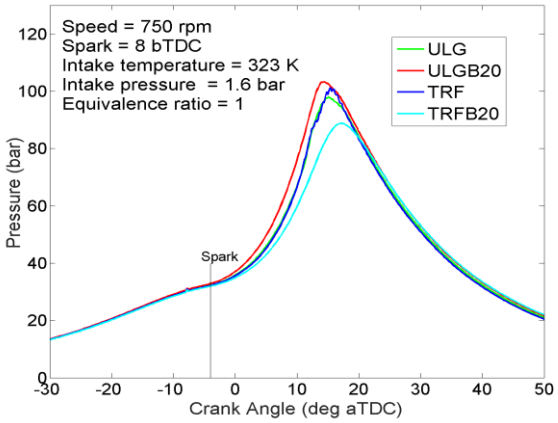

Figure 6.6: Mean pressure for ULG, TRF, ULGB20 and TRFB20 at spark timing 8 CA bTDC.

6.2.2.2 Measured knock onsets and knock intensities

The knock onsets and knock intensities exhibited by the four fuels across the knocking conditions tested were computed from the measured pressure data using the method described in section 3.2.2.7. Figures 6.7 and 6.8 show a statistical variation of the knock onsets as well as a comparison of the knock onsets for the four fuels at a spark timing of 6 CA bTDC and 8 CA bTDC. At a spark timing of 6 CA bTDC (Figure 6.7), the TRF fuel knocks earlier than the reference gasoline and blended fuels while the ULGB20 blend knocks slightly later than gasoline (ULG). This indicates that blending an oxygenated fuel such as *n*-butanol with gasoline could possibly lead to improvement in the knocking performance of gasoline. While the behaviour exhibited under blending conditions does not get worse in terms of the knock resistance performance, it is hard to conclude on the overall blending impact of *n*-butanol on gasoline since only one blend has been investigated in this study. The results obtained here at the lower temperatures (lower spark timing of 6 CA) shown in Figure 6.7, are also in agreement with the findings within the RCM (section 5.3.1) where for example, across the temperature of interest (Figure 5.7), the ignition delays for TRF are shorter compared to those of the reference gasoline. Similar to the result observed under normal combustion in terms of variation in peak pressures, the spread in knock onset is slightly larger for TRF and slightly smaller for ULGB20 compared to gasoline. At a more advanced spark timing of 8 CA bTDC (Figure 6.8) where the in-cylinder *P*-*T* conditions are higher, the TRF also knocks earlier than gasoline, but the difference between the knock onsets of the earliest knocking cycle as well as the mean knock onsets of both fuels is considerably smaller compared to that recorded at a spark timing of 6 CA bTDC (Figure 6.7).

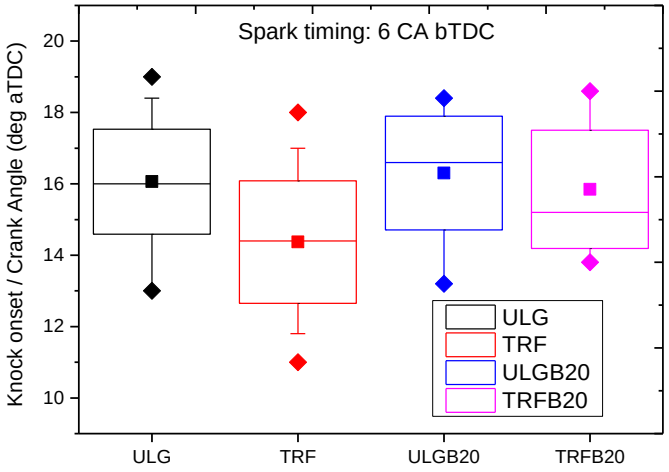

Figure 6.7: Variation of measured knock onsets across the four fuels tested at 6 CA bTDC. Boxes represent 25th and 75th percentiles while whiskers represent 5th and 95th percentiles. The squares and horizontal lines represent the mean and median of the measured distribution.

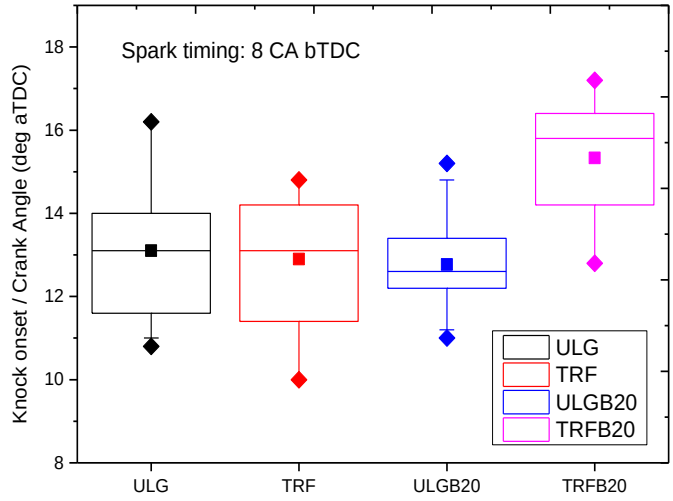

Figure 6.8: Variation of measured knock onsets across the four fuels tested at 8 CA bTDC. Boxes represent 25th and 75th percentiles while whiskers represent 5th and 95th percentiles. The squares and horizontal lines represent the mean and median of the measured distribution.

Based on the results obtained in this study, it is clear that compared to gasoline, TRF would lead to a reduction in the knock limited spark advance (KLSA) as well as a

decrease in the power output from the engine. The study shows that although the TRF is not a terrible surrogate for gasoline, it is however not a perfect representation of the combustion behaviour of gasoline. In general, the TRF/*n*-butanol blend gave a fairly poor agreement with the gasoline/*n*-butanol blend across the conditions studied. This study would however benefit from further SI engine studies on the impact of *n*-butanol blending ratios on the knocking behaviour of gasoline as well as further studies on the representation of gasoline/*n*-butanol blend with TRF/*n*-butanol blend or with a different surrogate employing a 4 component surrogate (e.g. TRF and 2-pentene) for gasoline.

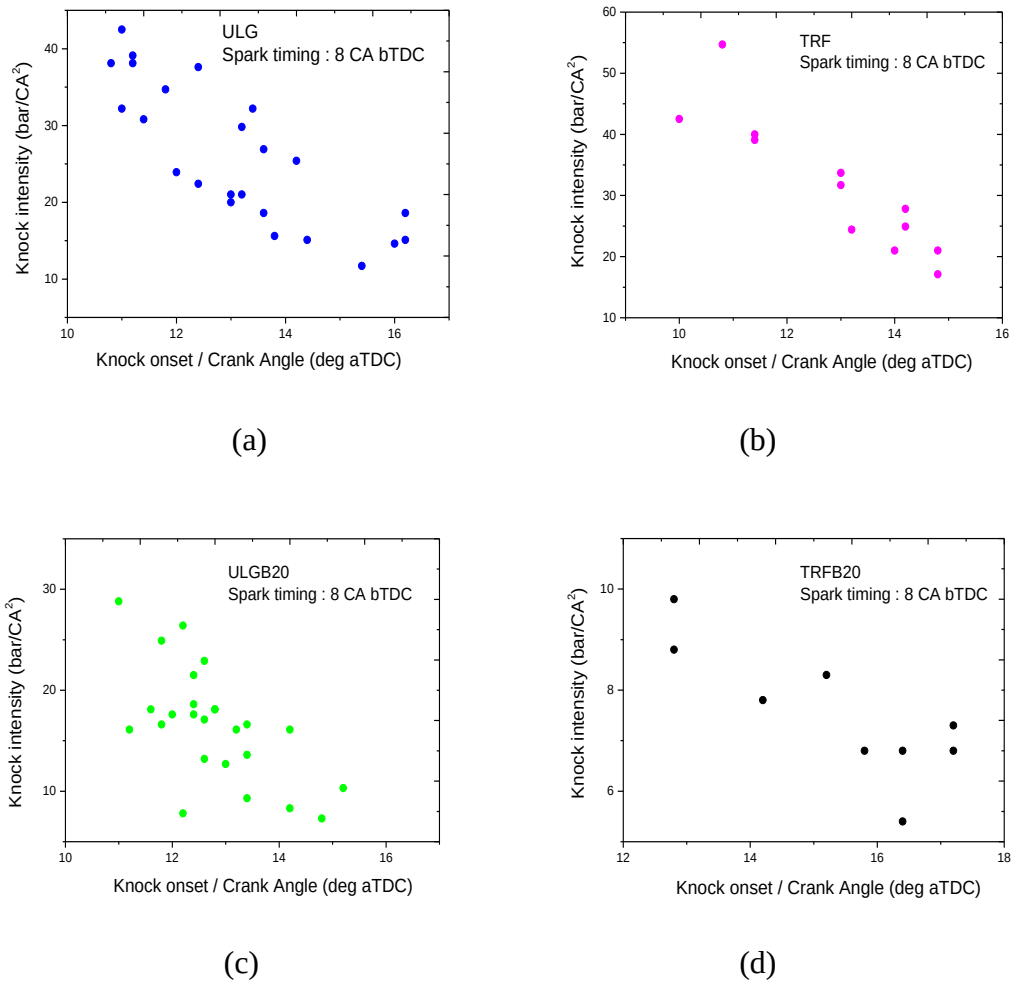

Figure 6.9: Knock intensities versus corresponding knock onsets of the identified knocking cycle at 8 CA bTDC (a) ULG (b) TRF (c) ULGB20 (d) TRFB20.

Figure 6.9 shows a linear relationship between the knock intensity defined by the maximum amplitude of the pressure rise rate, and knock onset. Figure 6.10 also depicts a linear relationship between the in-cylinder peak pressures and knock onsets. In both

figures, the knock intensity and peak pressures generally increase as the knock onsets decrease, i.e. as the point of autoignition of the end gas advances towards top the dead center (TDC). This is understandable since the closer the pressure waves are to the engine top cylinder, the higher the impact (intensity) it is expected to have on the metallic top cylinder surface in the form of engine knock. Similar to the trend observed for the cyclic variation of peak pressures measured under normal combustion, it is also clear from Figures 6.9 and 6.10 that blending leads to a reduction in cyclic variability of measured knock onsets.

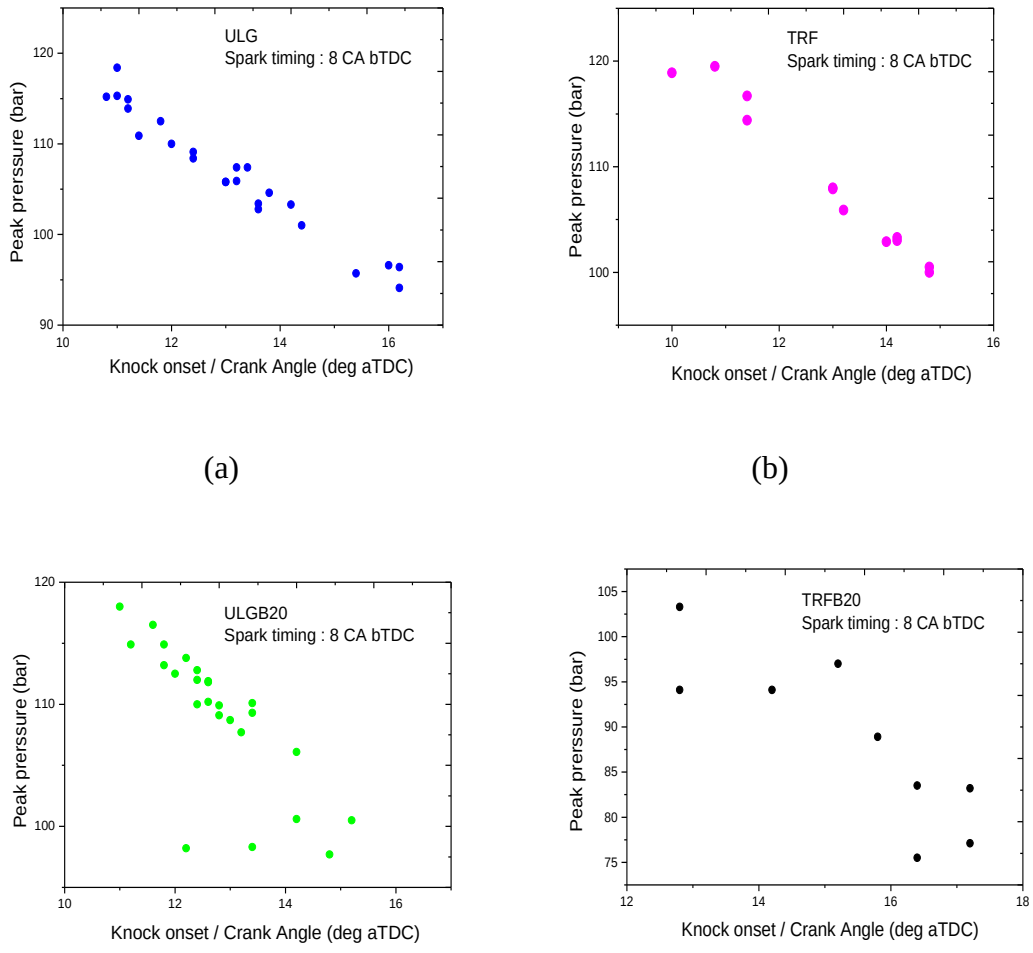

Figure 6.10: Peak pressures versus corresponding knock onsets of the identified knocking cycles (a) ULG b) TRF (c) ULGB20 (d) TRFB20.

6.2.2.3 Effect of spark timing on mean peak pressure, knock onset and knock intensities

Figures 6.11 - 6.13 show how the mean values of the peak pressures, knock onsets and knock intensities vary with spark timing across the four sets of fuels. In the test, knock did not occur for the non-TRF fuels at the spark timings of 4 CA and 5 CA bTDC and as a result, no data is shown for the non-TRF fuels at those conditions. Also, as mentioned in section 3.2.2.5 no knock data was collected for TRF above the spark timing of 8 CA bTDC in order to avoid damaging the engine cylinder head due to the excessive in-cylinder pressures developed at those conditions. Across all fuels, retarding the spark timing advances the knock onset location away from TDC (Figure 6.11) and consequently leads to a reduction in the impact (intensity) of knock (Figure 6.12). Also, retarding the spark timing leads to a reduction in the in-cylinder peak pressure (Figure 6.13). However, if the knock limited spark advance (KLSA) is retarded (later) than the maximum brake torque (MBT) timing required to produce the maximum brake torque (MBT), then the engine performance will be limited by knock. This is where the role of anti-knock fuels such as ULGB20 and TRFB20 becomes very crucial in pushing the spark advance towards the MBT timing while at the same time avoiding the problem of knock. The results shown in Figures 6.11-6.13 also clearly indicate that at lower spark timing (e.g. lower temperatures), TRF does not seem a good representation of gasoline.

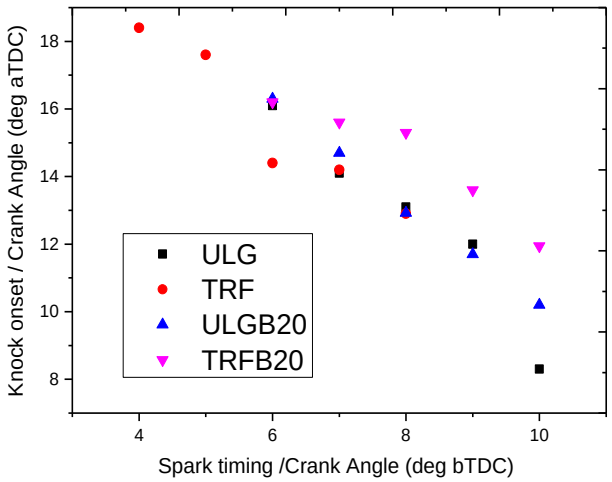

Figure 6.11: Mean knock onsets at various spark advances (effect of spark timing on mean knock onsets).

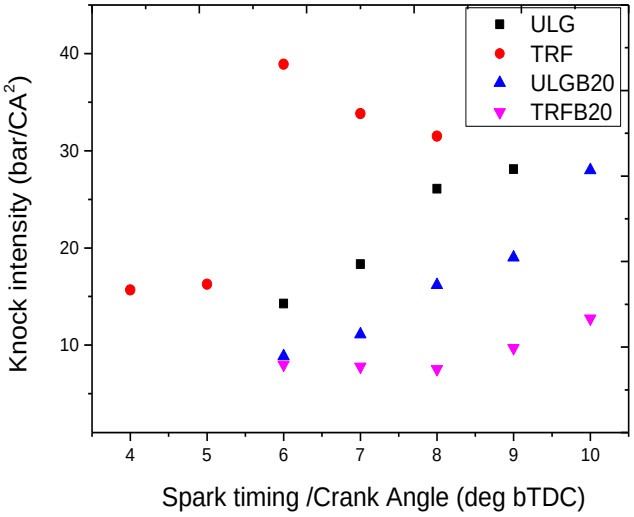

Figure 6.12: Mean knock intensities (MAPO) at various spark advances (effect of spark timing on knock intensities).

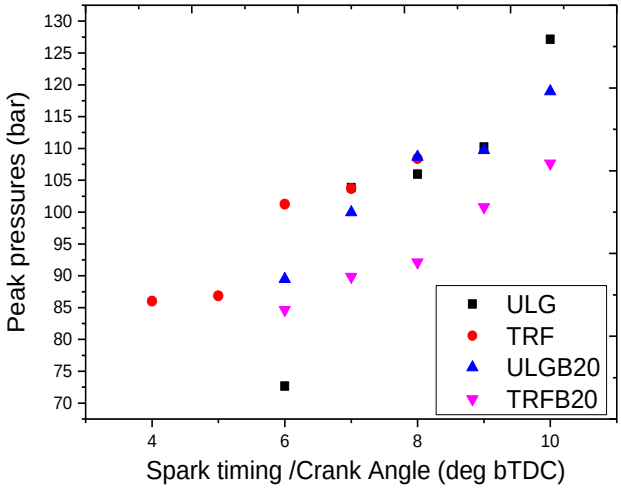

Figure 6.13: Mean peak pressures at various spark advances (effect of spark timing on mean peak pressures).

6.3 Simulations and comparison with experimental data

The overall aim of this work is to investigate fuel (chemistry) effects on autoignition and knocking combustion. Therefore it is imperative to ensure that there is no significant difference between the thermodynamic state of the simulated condition and experimental condition and also across the set of fuels being compared such that the end

gas is subject to the same pressure-temperature (*P-T*) history across all fuels. According to [30] and in line with the findings of [195], the heat loss characteristics of the fuels under consideration are significantly independent of the fuel composition as they exhibit very similar heat loss profiles or characteristics under the same pre-knock *P-T* conditions. Therefore matching the in-cylinder pressure would largely result in a match of the pre-knock temperature history of the end gas ahead of the propagating flame. Similar to the approach employed in [30], the mean experimental pressure cycle of the reference gasoline was selected and matched across the spark timing of 6 CA, 7 CA and 8 CA. This approach was mainly employed since a cycle-by-cycle comparison of all fuels is not possible due to the different levels of cyclic variability exhibited by all the fuels studied. Therefore, the mean pressure cycle of the reference gasoline which is representative of the *P-T* conditions across all four fuels at a particular spark timing, was employed for calibration of initial engine conditions required as input in the engine simulations. Across the four fuels (ULG, TRF, ULGB20 and TRFB20), experimental pressure cycles with pre-knock values very close to the mean pressure cycle of reference gasoline were then selected for knock onset averaging (Figure 6.13). The estimated average knock onsets of the selected cycles for ULG, TRF, ULGB20 and TRFB20 presented in Figure 6.14 is considered here as representative of the overall average across the respective fuels.

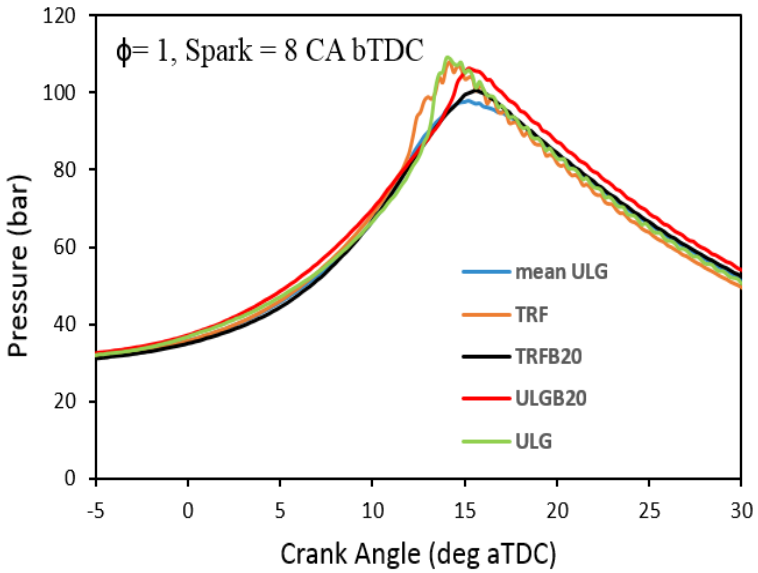

Figure 6.14: Selected experimental pressure cycles of four fuels with pre-knock values close to that of the mean cycle for gasoline.

6.3.1 Prediction of the average knocking combustion properties of gasoline

Figure 6.15 shows a comparison of the experimental pressure trace and the simulated pressure trace for TRF at an intake temperature and pressure of 320 K and 1.6 bar respectively at a spark timing of 6 and 8 CA bTDC. As shown in Figures 6.15a and 6.15b, the simulated pressure traces are in good agreement with the measured pressure traces. The level of agreement was obtained with an optimised turbulence mixing time of 0.022 s and an integral length scale of 0.04 m. An EGR of 3 % was employed in all simulations based on the assumption that the combustion chamber is highly free of exhaust products based on the high skip firing ratio employed in the experiments. The deviation between the measured and simulated pressure traces during the expansion phase after around 35 CA aTDC can be explained on the basis of the approximated cylinder profile and spark plug position employed in the simulation.

As reported in [30, 40, 241], three temperature regimes namely, low (T< 800 K), intermediate (T = 800 - 1100 K) and high (T > 1100 K) are usually used to classify the different phases of oxidation chemistry in the combustion process. In the combustion of hydrocarbons fuels in an engine, different elementary reactions involving a set of species would dominate at different temperature intervals until the constituent hydrogen and carbon are completely oxidised. It should be noted that while certain reaction pathways are mainly dominant within a specific temperature region, such pathways might also be present at other temperature intervals but with a lower impact on the autoignition and knock response.

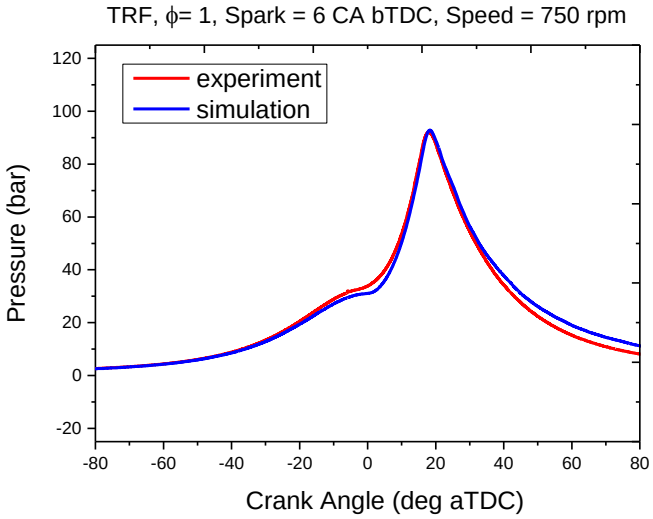

(a)

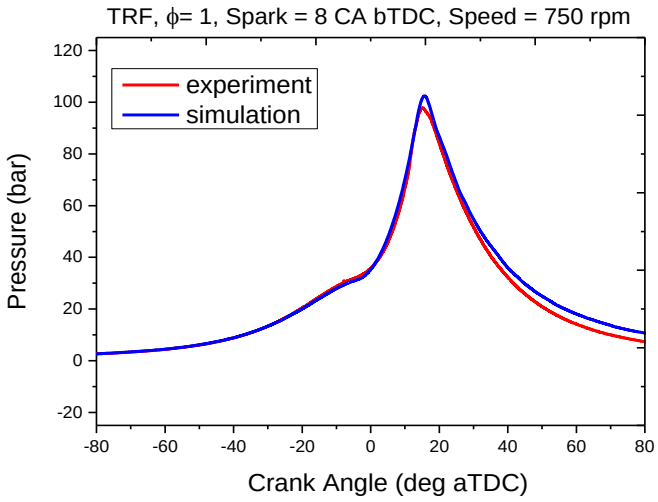

(b)

Figure 6.15: Comparison of experimental and simulated pressure trace for TRF (a) 6 CA bTDC (b) 8 CA bTDC.

Engine experiments show that gasoline exhibits low temperature heat release (LTHR), intermediate temperature heat release (ITHR) and high temperature heat release (HTHR) depending on operating conditions [104]. Figure 6.16 presents the predicted unburned gas temperature history superimposed upon the simulated heat release profile for spark advances of 6 and 8 CA bTDC. A two-stage ignition feature which is common to hydrocarbon fuels, and which was also observed in our RCM study [65] for gasoline and TRF under certain conditions is well predicted by the mechanism. The NTC

behaviour is also well captured in line with the behaviour observed in [65] but in this case, it's given by the sharp decrease in heat release rate as temperature slightly increases. The first stage ignition represents the start of low temperature (cool flame) heat release and occurs after the induction period (period of slow oxidation) measured from TDC. At a spark timing of 6 and 8 CA bTDC, the first stage ignition occurred at 14.5 CA aTDC and 10 CA aTDC respectively at around T = 800 K while the maximum first stage heat release occurred at 17 CA aTDC and 13 CA aTDC respectively. The earlier start of the first stage ignition at the spark timing of 8 CA bTDC is due to the higher unburned gas temperatures obtainable at the higher spark advance of 8 CA bTDC compared to 6 bTDC. According to [82], an increase in the temperature of the end gas leads to a decrease in the induction period as well as an increase in the magnitude of the cool flame (i.e. heat release) mainly due to the disappearance of the peroxy radical (Equation. 6.1) that drives the low temperature chemistry.

During the low temperature heat release, low temperature hydrocarbon oxidation reactions dominate and the gasoline fuel mixture is partially oxidised to form a large variety of stable and fairly stable intermediate products including alkenes, oxygenated molecular intermediates (e.g alcohols, aldehydes and ketones), water, oxides of carbon etc. and a small amount of heat release results [82, 208, 241]. Reactions involving further oxidation of the partially oxidised fuel and oxidation of formed oxygenated compounds also occur during the low temperature heat release- the rates of these reactions increase with increase in *P-T* conditions giving rise to higher heat release as seen in Figure 6.16b. The term cool flame is used based on the understanding that the system's temperature is lower than the adiabatic flame temperature due to incomplete combustion of the fuel mixture. Fundamentally, the mechanism for the complete oxidation of hydrocarbon fuels as explained in section 2.4, begins by first of all initiation reactions involving H abstraction reactions by O_2 ($RH + O_2 = R. + HO_2$) and then mainly by OH radicals resulting in the formation of alkyl radicals. The alkyl radicals then add to oxygen to form the peroxy radical, RO_2 according to Equation 6.1 given below. The alkyl/alkyl peroxy equilibrium is very significant in autoignition chemistry as the direction of the reaction at different temperature regimes determines to a large extent what chemistry would follow or become dominant.

$$R + O_2 = RO_2 \quad (6.1)$$

Because of the negligible activation energy for the forward rate of Equation 6.1, at low temperatures, RO_2 is increasingly formed and further undergoes isomerisation to QOOH. QOOH in a second O_2 addition reaction combines with oxygen to promote chain-branching pathways that results in the occurrence of a cool flame.

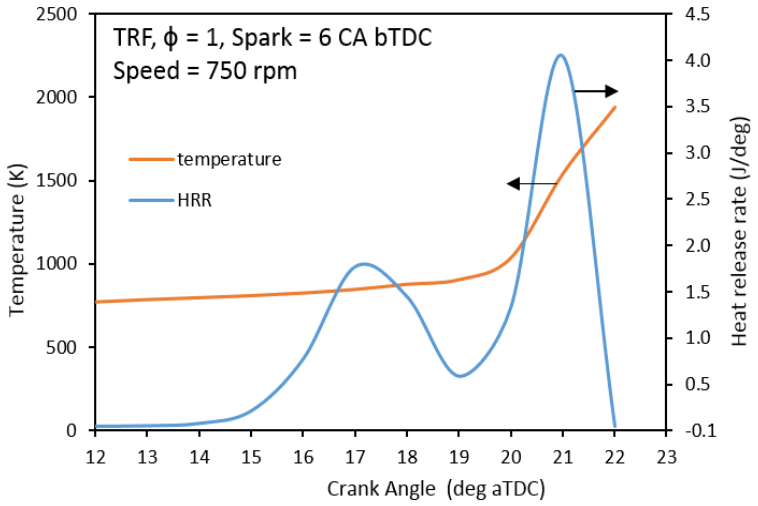

(a)

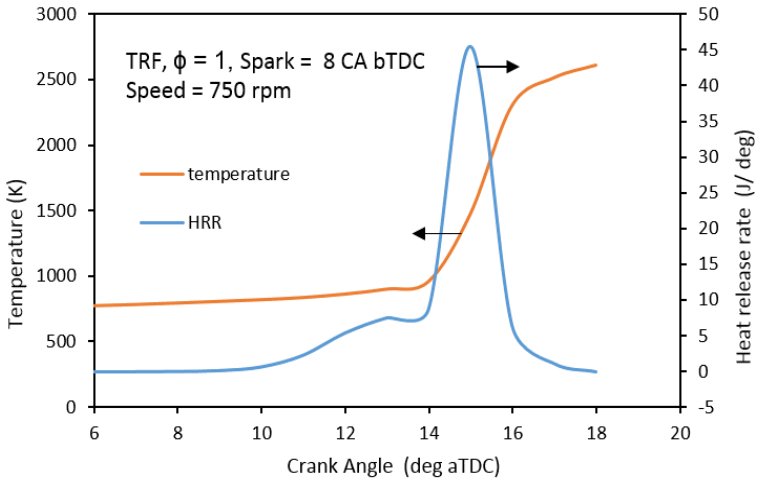

(b)

Figure 6.16: Heat release rate (HRR) and temperature histories in the unburned zone simulated for TRF mixture (a) 6 CA bTDC (b) 8 CA bTDC.

As shown in Figure 6.17 only a small amount of the fuel (TRF) is consumed during cool flame heat release but the net heat release in the first stage ignition raises the temperature of the unburned gas and as a result, the average compressed gas temperature attained is greater than that resulting from adiabatic compression alone. With increase in

temperature the equilibrium of Equation 6.1 now shifts towards the reactants favouring the inhibiting pathway involving the formation of HO_2 and the conjugated alkenes over the low-temperature chain branching sequence. Also, competing unimolecular decomposition reactions via Beta scission of QOOH leading to the formation of two molecules of formaldehyde (QOOH = 2 CH_2O +OH) now begins to play a prominent role with an attendant decrease in reactivity. The decomposition reaction of QOOH can also lead to the product channel Q + HO_2, therefore both HO_2 and CH_2O are increasingly formed during the NTC heat release. The NTC behaviour which is typical of alkanes now sets in due to decrease in reactivity and results in a decrease in heat release as shown by the deepening of the heat release curve at the locations between 13 CA and 14 CA aTDC for the spark timing of 8 CA bTDC (Figure 6.18a) and between 15 CA aTDC and 17 CA aTDC for the spark timing of 6 CA bTDC (Figure 6.18b). Interestingly as shown in Figure 6.19 for the spark timing of 8 CA bTDC, we observe from the simulated species concentrations in the unburned zone that most of the alkyl peroxy radicals peak at slightly above 12 CA bTDC and decrease in the NTC region thus providing an explanation for the suppression of reactivity and also the observed reduction in heat release at higher temperatures. The HO_2 formed during the NTC phase is however consumed in the combination reactions of HO_2 (HO_2 + HO_2 = H_2O_2 + O_2) and propagating reactions of HO_2 (HO_2 + RH = H_2O_2 + R) leading to the formation of H_2O_2. Therefore during the NTC stage there is a noticeable sharp rise in the production of formaldehyde (CH_2O) and hydrogen peroxide (H_2O_2) (Figure 6.18).

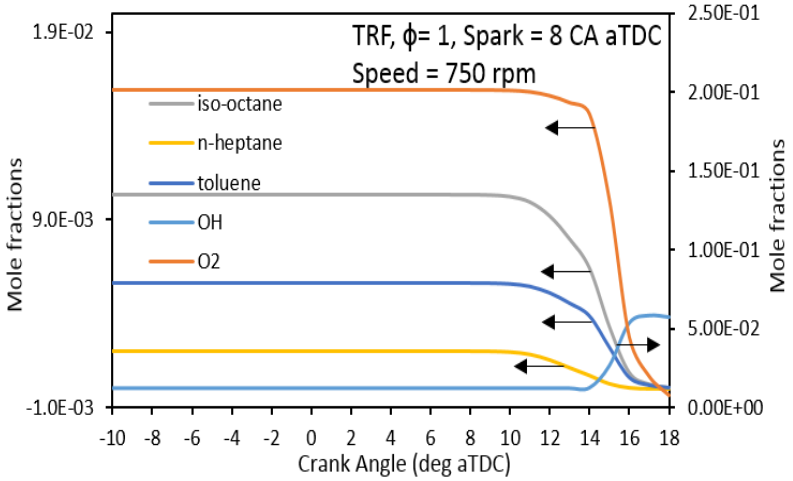

Figure 6.17: Simulated species concentrations of the reactants TRF/O_2 mixture and OH histories in the unburned zone.

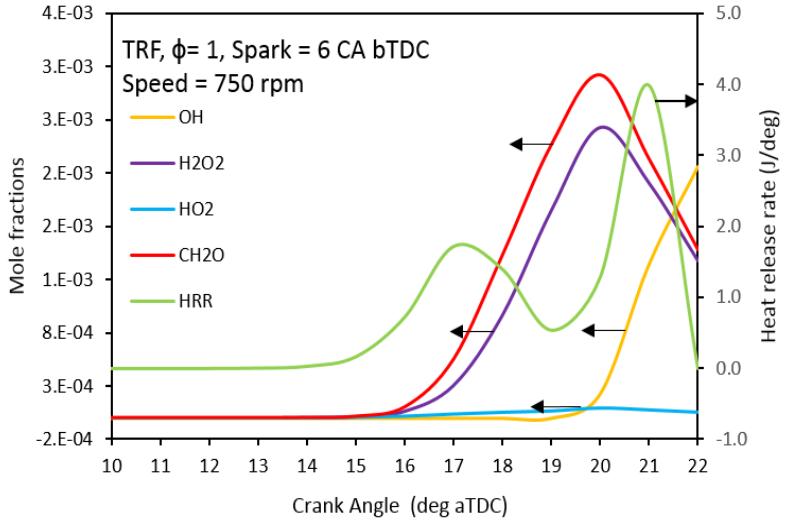

(a)

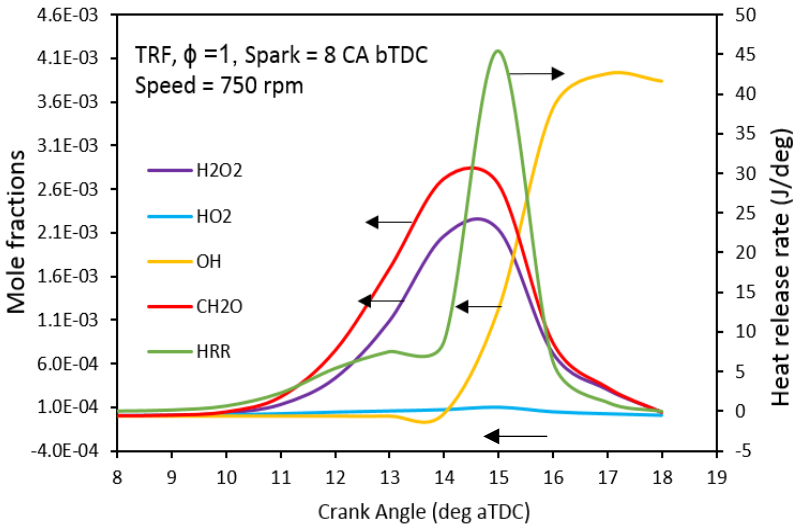

(b)

Figure 6.18: Rate of heat release in the unburned zone and species concentrations simulated for TRF mixture (a) 6 CA bTDC (b) 8 CA bTDC.

We also observe from Figure 6.19 that the concentrations of alkyl peroxy radicals (RO_2) peaks where the mole fractions of CH_2O and HO_2 are still quite small indicating the start of the dominance of QOOH decomposition reactions and termination reactions forming HO_2 over RO_2 chemistry just after the low temperature heat release. At higher temperatures the H_2O_2 formed during the low temperature heat release is consumed in a decomposition reaction forming OH radicals. The formed OH radicals are responsible for the rapid consumption of the fuel at high temperatures in chain branching reactions in which more and more OH radicals are generated in the process. The chemistry of H_2O_2 is responsible for the main stage ignition and high temperature heat release leading to the occurrence of knock.

The NTC phase predicted at a spark timing of 8 CA bTDC (Figure 6.18b) is flatter and narrower compared to that predicted at a spark timing 6 CA bTDC (Figure 6.18 a) and this can be attributed to the higher prevailing in-cylinder *P*-*T* condition at the spark advance 8 CA aTDC that results in a higher heat release and consequently higher maximum temperature of the end gas. With higher end gas temperatures, high temperature decomposition reactions (chemistry) involving the decomposition of H_2O_2 (H_2O_2 (+M) = 2 OH) are favoured over unimolecular QOOH decomposition and termination reactions forming alkenes and HO_2 and the main stage ignition occurs much earlier resulting in a smaller predicted NTC region as well as shorter predicted knock onset.

Also, it should be noted at this point that the occurrence of a first stage ignition in the engine has serious implications in the sense that pre-conditioning of the air-fuel mixture (end gas) by the first stage heat release leads to a reduction in the subsequent time required for the knock related second stage ignition to occur [38, 123]. Since the overall impact of the presence of a low temperature hydrocarbon oxidation (first-stage heat release) in an engine is the enhancement of knock, methods that could suppress or eliminate the first-stage low temperature reactions could therefore potentially help in controlling the occurrence and intensity of knock. The use of oxygenated fuels such as *n*-butanol has been proposed as a viable strategy for achieving desired higher engine efficiencies and lower carbon footprint while at the same time avoiding the dilemma of knock. It was found in [242] that the knock propensity of a given fuel can be effectively altered by modifying the low temperature heat release through the application of

blending fuels or additives. It was shown in the RCM section that the blend does not display a significant NTC behaviour and is almost Arrhenius-like. This point would be addressed further in the next section involving the use of the blended fuel in order to explore and understand the NTC behaviour of gasoline when blended with a single-stage fuel such as *n*-butanol under practical engine conditions.

According to Faraz [30], the autoignition phenomena can be linked to the build-up of critical intermediate species and it's distinguishable from the resulting heat release and temperature rise or from the point where the species attain certain concentration levels. In previous studies [136, 207, 208], the occurrence or onset of knock in the engine has been identified by the analysis of the unburned zone heat release rate and species profiles. A sharp rise in the second stage heat release rate and temperature of the unburned mixture is caused by the autoignition of the end gas and high temperature exothermic oxidation of intermediate fuel species such as CO, C_2H_4 etc. as well as the various oxygenated intermediate products (i.e.) produced during the cool flame phase. From the heat release profile shown for the unburned zone in Figure 6.18, the predicted knock onset at a spark timing of 6 and 8 CA bTDC are 19 and 13.8 CA aTDC respectively while the maximum heat release occurs at locations of 21 and 15 CA aTDC respectively. The point of rapid rise in heat release coincides well with the point of rapid rise in OH radical formation which is expected as a lot of OH radicals as discussed previously are produced during chain branching reactions leading to the rapid consumption or oxidation of the parent fuel at high temperature. According to [241], the hot flame ignition or chemistry is marked with a strong presence of OH radicals. Yang et al. [243] reported in their study that a high wavelength aldehyde photon was emitted during the cool flame (low temperature hydrocarbon chemistry) while hydroxide species were detected close to the end of the low temperature hydrocarbon chemistry. However the hydroxide radical concentrations increased across the main heat release stage. It is also clear from Figure 6.18 that hydrogen peroxide (H_2O_2) peaks near the point of hot ignition. The dominance of the chain branching step involving the decomposition reaction of H_2O_2 (H_2O_2 (+M) = 2 OH) at high temperature is responsible for the consumption and decrease in the mole fractions of H_2O_2 during the main heat release stage [241].

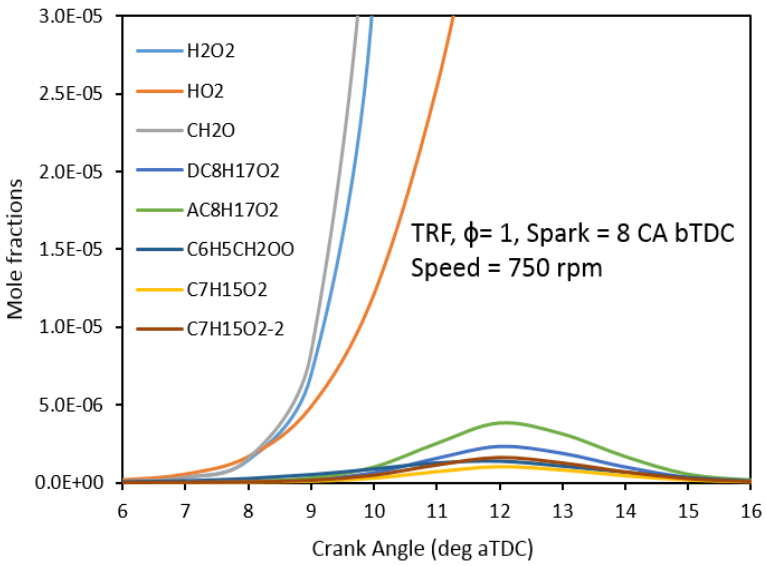

Figure 6.19: Simulated species concentrations of some peroxy radicals in the unburned zone for TRF.

Figure 6.20 shows how the predicted knock onsets of TRF compare with the experimental knock onsets across the spark timing of 6 - 8 CA aTDC. The knock onsets predicted by the TRF/*n*-butanol blended mechanism using the TRF fuel formulated in this study are consistently higher than the measured TRF knock onsets across the spark timing tested with the discrepancy between the measured and predicted data being more pronounced at the more retarded spark timing of 6 CA bTDC. Within the RCM (section 5.3.2), the autoignition delay times of TRF predicted by the mechanism across the range of temperature investigated were also significantly higher compared to the measured data. We also observe in Figure 6.20 that the disparity between the simulated and measured knock onsets decreases as the spark timing is advanced indicating that the mechanism performs better under higher in-cylinder *P*-*T* conditions. Within the RCM, the mechanism was also seen to perform better at the intermediate-high temperature region although it should be kept in mind that the highest temperatures in the RCM are here representative of the temperatures at the most retarded spark timing. It was shown previously in Figure 6.16 that the low temperature chemistry, in which the mechanism's performance is most deficient, is more dominant at the more retarded spark timing than at a well advanced spark timing (i.e. at higher in-cylinder *P*-*T* conditions) and this explains why the agreement of the predicted knock onset with the measured data is

poorest at the more retarded spark timing. Generally, the kinetic model captures the decrease in knock onsets observed in the measured data as spark timing is advanced.

Sensitivity analysis carried out within the RCM (section 5.3.2) revealed that the hydrogen abstraction reactions by OH from the α, β and γ sites of iso-octane, *n*-heptane and toluene as well as the decomposition reaction of hydrogen peroxide (H_2O_2 (+M) = OH + OH (+M)) are quite important for accurate prediction of autoignition delay times of TRF mixtures at the higher temperatures prevalent in the engine and the parameterisation of these reactions are currently ridden with significant levels of uncertainty. Therefore more detailed fundamental studies focused on these reactions are required in order to bring the predicted data in better agreement with the measured data. Similar to the experimental results presented in section 6.2.2.3, the predicted knock onsets also decrease as the spark timing is advanced indicating the robustness and fidelity of the scheme based on its mechanistic structure and showing that the mechanism could be used to a reasonable degree for knock onset prediction of TRF fuels within certain operating regime of the SI the engine. Overall the mechanism performed best at the more advanced spark timing where the impact of knock is more significant and where chemical kinetic modelling of fuels is of higher relevance.

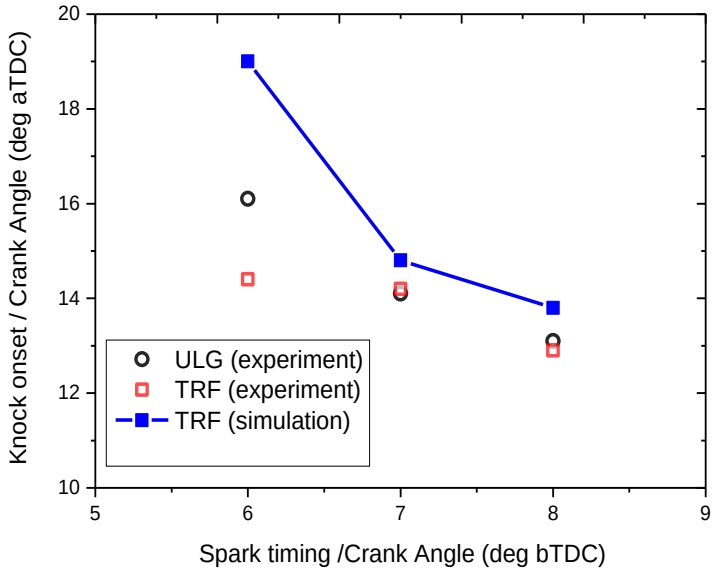

Figure 6.20: Predicted knock onsets of TRF mixture in comparison with the experimental knock onsets for ULG and TRF fuels.

6.3.2 Prediction of the influence of *n*-butanol blending on the average knocking combustion properties of gasoline

Figures 6.21a and 6.21b show a comparison of the experimental and simulated pressure traces for stoichiometric TRF/*n*-butanol blend at a spark timing of 6 and 8 CA bTDC respectively under in-cylinder pressure and temperature conditions of 1.6 bar and 320 K respectively while Figure 6.22 shows the predicted heat release profile of the unburned zone alongside the predicted unburned zone temperature profile for the TRF/ *n*-butanol blend at the spark timing of 6 and 8 CA bTDC. Similar to the results obtained for TRF (Figure 6.15a and Figure 6.15b), the simulated pressure traces match the experimental pressure traces very closely (Figure 6.21a and Figure 6.21b) except for after a crank angle degrees of 35 aTDC where the simulated pressure trace deviates from the measured trace. As explained previously in section 6.3.1, this is caused mainly by the error in the employed cylinder profile. In Figure 6.22, we see that the chemical kinetic model captures the influence of *n*-butanol blending on gasoline observed in the RCM measurements, which is shown by the suppression and smoothening out of the cool flame/NTC region compared to that of TRF. In the modelling work involving the Leeds RCM [65] it was also observed that the NTC region of the ignition delay times predicted by the scheme is suppressed due to the influence of *n*-butanol chemistry on gasoline. Autoignition or knock will occur in an engine when the end gas which is under additional compression and heating by the spark-initiated propagating flame is unable to delay or resist autoignition before it is completely consumed by the advancing flame front. Therefore, fuel mixtures with longer delays are more probable to avoid the occurrence of knock. In the early stages of the compression phase of the end gas, very slow reactions occur leading to the production of a radical pool (i.e. OH radicals) that promotes the low temperature cool flame chemistry and consequently the occurrence of knock. In the previous section (section 6.3.1) it was noted that fuels that inhibit the cool flame ignition have the potential to eliminate or reduce the impact of knock. That *n*-butanol exerts an inhibiting influence on the cool flame heat release of gasoline by scavenging of the OH radicals produced during the induction phase [65] is apparent from Figure 6.22a but the impact diminishes at the higher spark advance (8 CA bTDC) where the end gas temperatures are higher (Figure 6.22b).

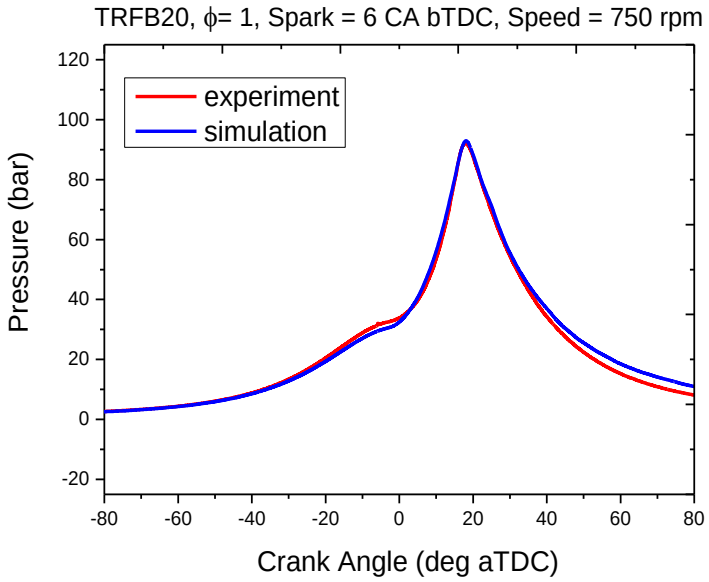

(a)

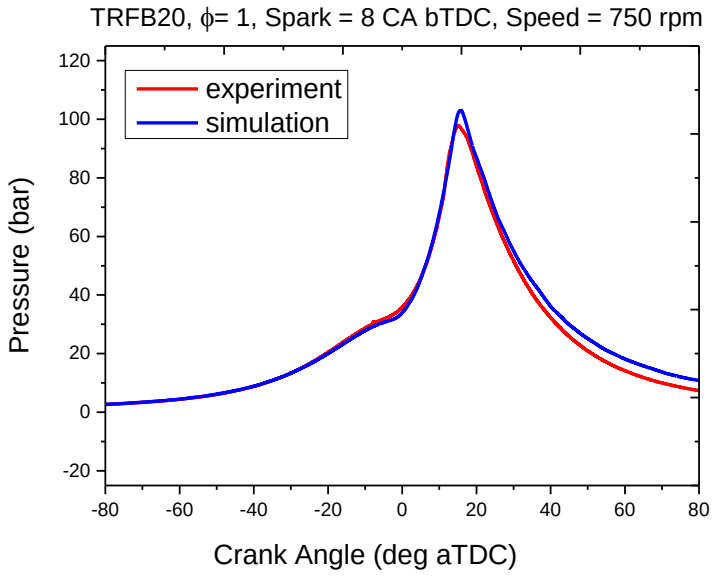

(b)

Figure 6.21: Comparison of experimental and simulated pressure trace for TRF/*n*-butanol blend (a) 6 CA bTDC (b) 8 CA bTDC.

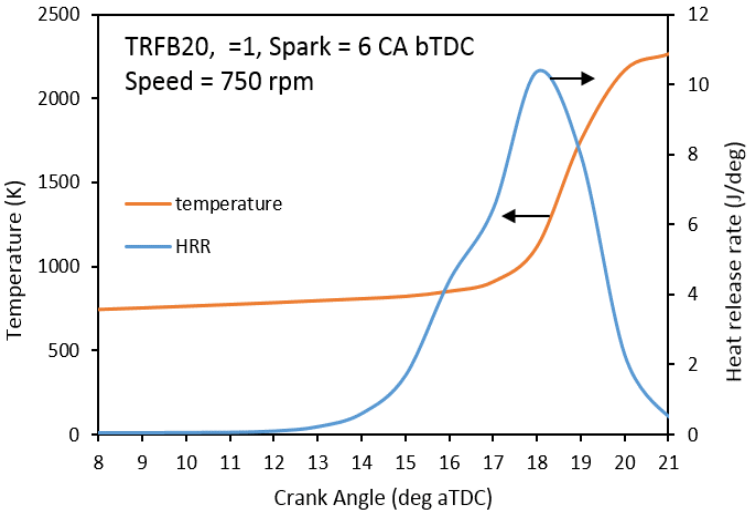

(a)

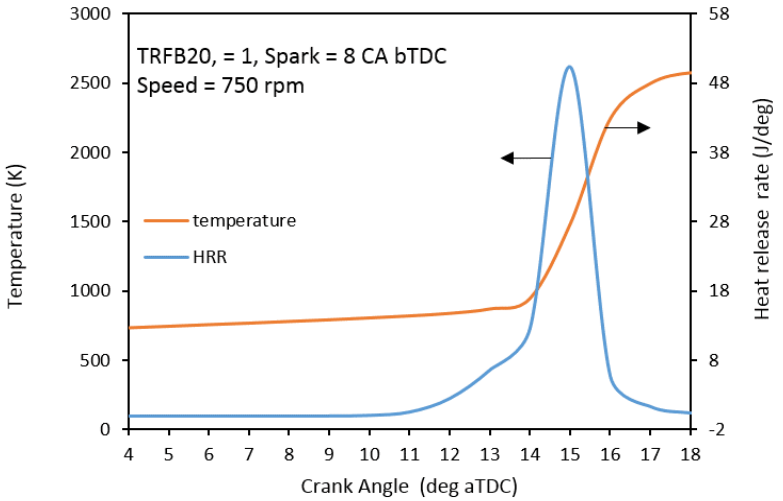

(b)

Figure 6.22: Rate of heat release and temperature histories in the unburned zone simulated for TRF/*n*-butanol blend (a) 6 CA bTDC (b) 8 CA bTDC.

The predicted autoignition onset of the end gas for the TRF/*n*-butanol mixture given by the location of the sharp rise in OH and heat release rate (Figure 6.23) at spark timing of 6 and 8 CA aTDC are 18 and 13.6 CA aTDC respectively. The knock onsets of the TRF/*n*-butanol blend predicted by the mechanism are slightly lower than those predicted for TRF- the knock onsets predicted by the scheme across all the fuels investigated including neat *n*-butanol are presented and further discussed in the concluding part of

this section. In Figure 6.23, similar to what was observed between the predicted knock onsets of TRF and TRF/*n*-butanol, the predicted peak concentrations of key species such as hydrogen peroxide (H_2O_2), formaldehyde (CH_2O) and OH for the TRF/*n*-butanol mixture are also slightly lower than those predicted for TRF (Figure 6.18) confirming that the concentrations of the above key species are closely linked to the autoignition of the end gas. In both Figures 6.16 and 6.22 for TRF and TRF/*n*-butanol respectively, we observe that the prevalent engine temperatures predicted in the modelling work prior to the main stage autoignition (T = 920 - 980 K) are much higher than the highest temperature attained in the RCM. Therefore, at a spark timing of 8 CA bTDC, the differences between the predicted knock onset (autoignition delay) for TRF and TRF/*n*-butanol blend in the engine are quite small since as was observed in section 5.4.1, the impact of *n*-butanol blending on gasoline diminishes significantly as temperature is increased.

For the TRF/*n*-butanol blend, the predicted species concentration profiles of the alkyl peroxy radicals in the unburned zone at 8 CA bTDC (Figure 6.24) peak 13 CA aTDC as against 12 CA aTDC in the case of TRF. The slightly prolonged dominance of the chain branching reactions in the low temperature heat release phase of the TRF/*n*-butanol blend is responsible for the slightly lower knock onset predicted for the blend compared to TRF.

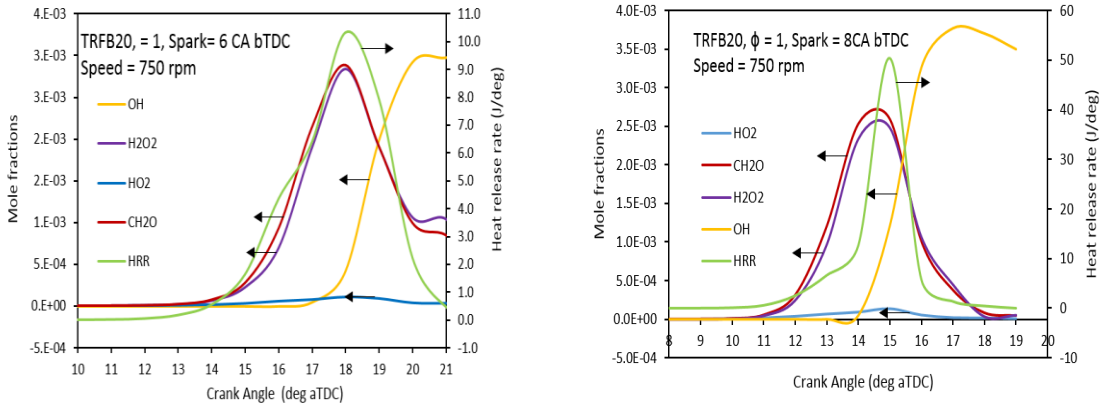

(a) (b)

Figure 6.23: Heat release rate (HRR) in the unburned zone and species concentrations simulated for TRF/*n*-butanol blend (a) 6 CA bTDC (b) 8 CA bTDC.

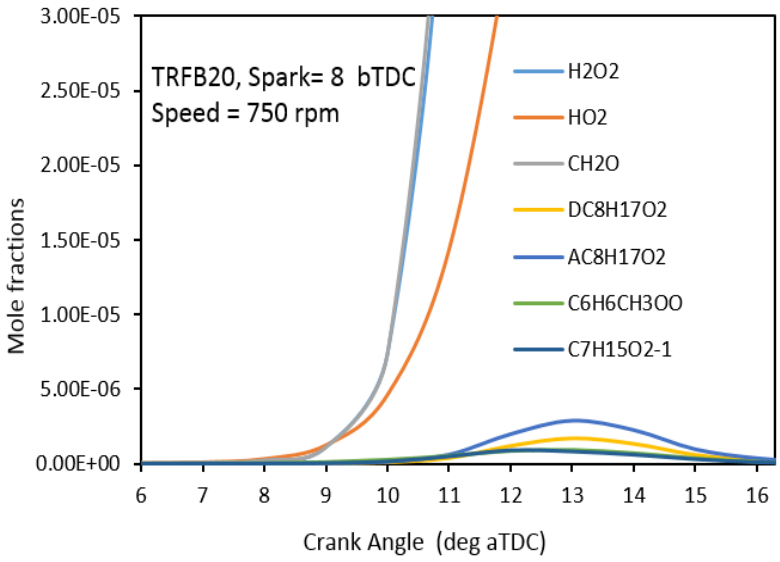

Figure 6. 24: Simulated species concentrations of some peroxy radicals in the unburned zone for TRFB20.

Figure 6.25 shows how the predicted mean knock onsets for TRF/*n*-butanol compare with the measured mean knock onset across the spark timing of 6 - 8 CA bTDC. Because of the unexplainable discrepancy in the measured knock onsets for the TRF/*n*-butanol blend, the predicted knock onsets were therefore compared with only the gasoline/*n*-butanol blend to facilitate a reasonable and fair assessment of the adopted kinetic model. Again, similar to the results obtained for TRF, the predicted knock onsets for the TRF/ *n*-butanol blend are higher compared to the measured knock onsets and the discrepancy is also highest at the retarded spark timing of 6 CA bTDC. Figure 6.25 also shows that the near linear inverse relationship between the measured knock onsets and spark advance is also well replicated by the mechanism

In the sensitivity analysis carried out in section 5. 4.1 and 5.4.2, for predicted TRF/*n*-butanol ignition delay times, the *n*-butanol + OH abstraction reaction from the γ site was found to be the most significant reaction influencing the predicted ignition delay times of TRF/*n*-butanol at higher temperatures (T = 858 K) with some reasonable contribution also coming from the abstraction reaction from the α site. The reactions of $HO_2 + HO_2 = H_2O_2 + O_2$ and H_2O_2 (+M) = 2 OH were also identified to be equally as important as the abstraction reaction from the γ site. It is worth mentioning that the uncertainties in the parameterisation of the rates of these reactions, particularly the uncertainties in the

relative rates of *n*-butanol + OH abstraction reaction from the α and γ site were identified in [65] to be very important for autoignition prediction in the temperature of interest. Therefore a more accurate quantification of these rates could lead to significant improvement in the robustness and accuracy of the scheme across the temperatures prevalent in the engine particularly at the more retarded spark advance.

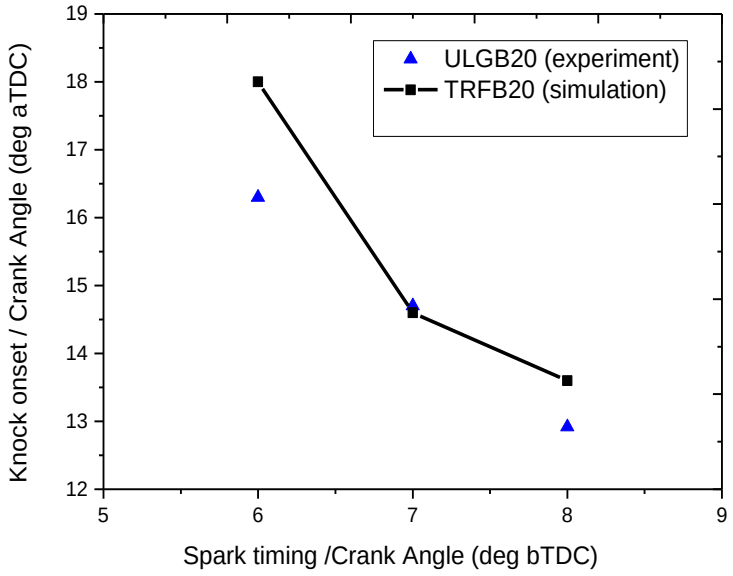

Figure 6.25: Comparison of predicted knock onsets of TRF blended with 20 % *n*-butanol by volume with measured knock onsets of gasoline blended with 20 % *n*-butanol by volume.

Although engine experiments were not performed for pure *n*-butanol, the modelling of the autoignition onset of a pure *n*-butanol mixture was also carried out in this work using the same initial conditions that are based on the reference pressure data of gasoline in order to explore the potential of the mechanism in reproducing the lower ignition delay times predicted for *n*-butanol in the RCM at high temperatures compared to the TRF and TRF/*n*-butanol blend. Figure 6.26 shows a comparison of the predicted pressure profile of stoichiometric *n*-butanol and the measured pressure data of reference gasoline while Figure 6.27 shows the predicted heat release profile of the unburned zone superimposed upon the temperature history of the unburned end gas. The result showing the variation of the predicted knock onsets of *n*-butanol with spark timing is presented alongside those of TRF, TFRB20 and their measured data in Figure 6.28.

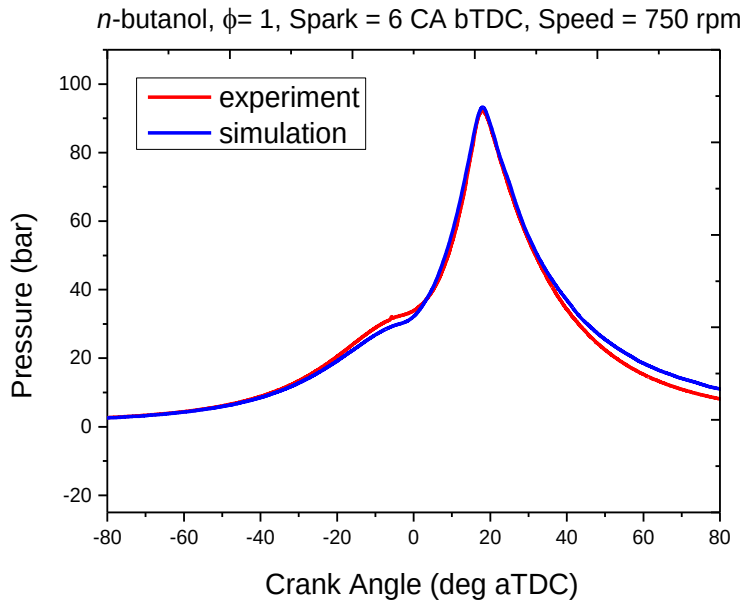

(a)

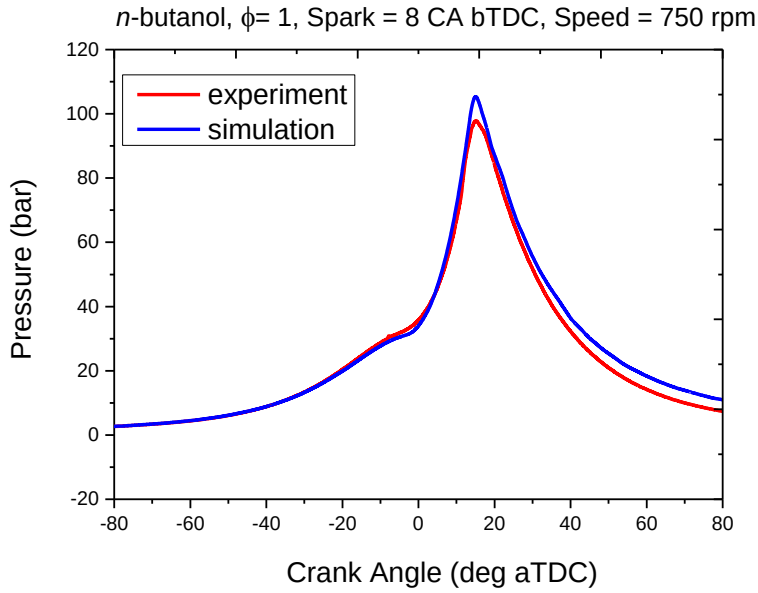

(b)

Figure 6.26: Comparison of experimental and simulated pressure trace for *n*-butanol (a) 6 CA bTDC (b) 8 CA bTDC.

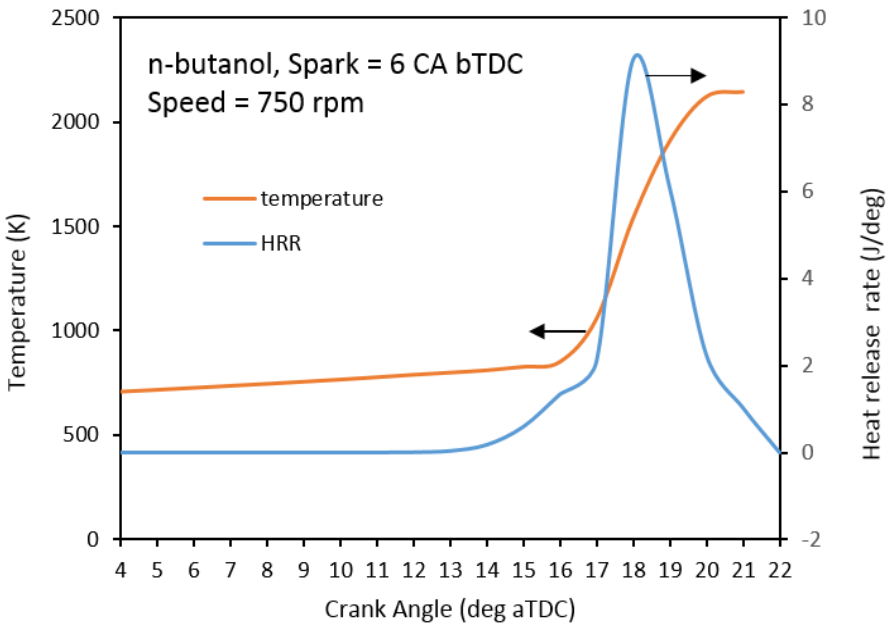

(a)

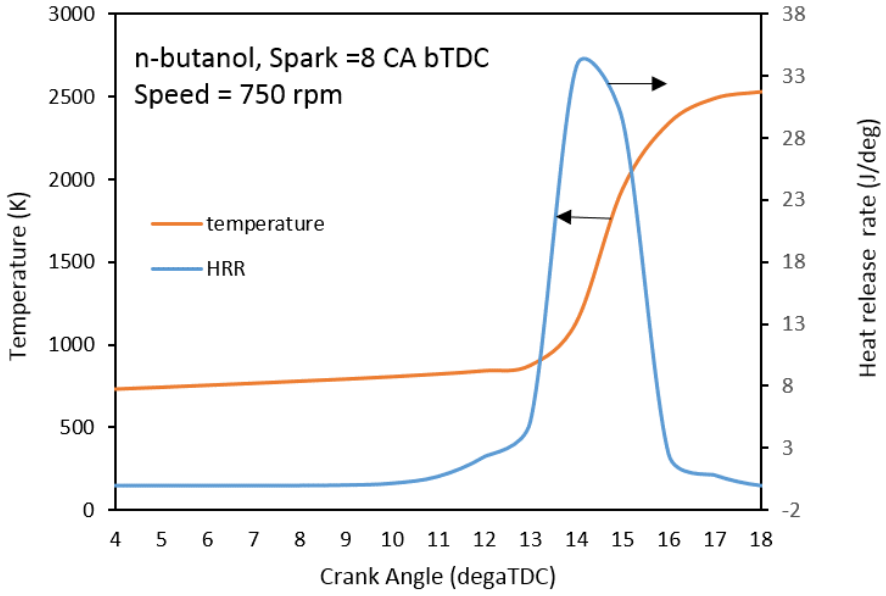

(b)

Figure 6.27: Heat release rate (HRR) and temperature histories in the unburned zone simulated for *n*-butanol using the Sarathy mechanism (a) 6 CA bTDC (b) 8 CA bTDC.

Figure 6.28 clearly shows that the autoignition predictions of the blend mechanism are lowest for *n*-butanol across the spark timing tested and consistent with the predictions in the RCM at high temperatures (Figure 5.18). While the TRF/*n*-butanol blended mechanism reproduces the trend between the measured knock onsets of TRF and gasoline/ *n*-butanol blend to a high level of accuracy at the more advanced spark timing of 8 CA bTDC, at the retarded spark timing of 6 CA bTDC, the prediction of the influence of *n*-butanol on the knock onset of TRF is less good as the predicted knock onsets of TRF are unexpectedly higher than those of the gasoline/*n*-butanol blend in reverse to the trend observed between the measured data of both fuels. This result is however in agreement with the observation in the RCM modelling work where the predicted ignition delays for TRF/*n*-butanol blend were significantly lower than that predicted for TRF within the NTC region and at slightly higher temperatures.

Overall, while the TRF/*n*-butanol mechanism developed in the course of this work still requires a far more accurate quantification of its key rate parameters to improve its predictive capability, it definitely could form a starting point for application in detailed chemical kinetic modelling of autoignition of alternative fuels (specifically TRF/*n*-butanol blended fuels) within the SI engine framework.

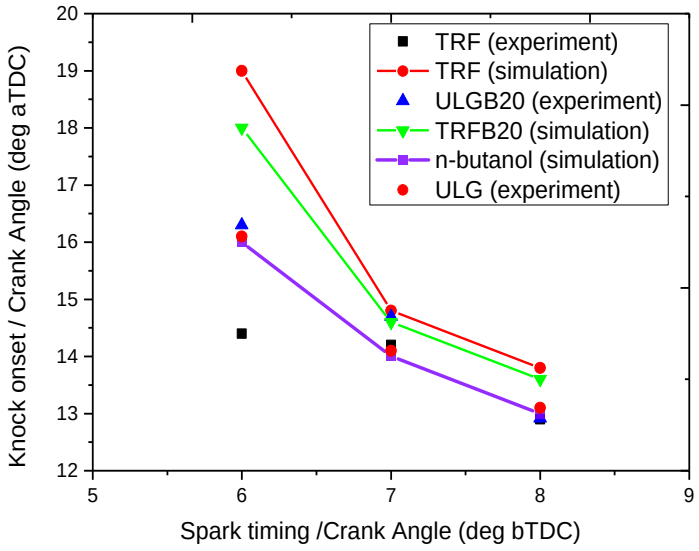

Figure 6.28: Comparison of predicted and measured knock onsets of TRF blended with 20 % *n*-butanol by volume with those of TRF, gasoline and *n*-butanol.

6.3.3 Evaluation of the chemical kinetic model based on individual cycles

In order to test the ability of the mechanism to reproduce the cycle-by-cycle variation of autoignition onset in the engine caused by engine conditions such as in-cylinder temperature and pressure, turbulent burning velocity, mixture compositions etc. at a specific spark timing, two sets of reference pressure cycles representing the fast cycles and moderate cycles were chosen from the set of measured pressure traces for gasoline at a spark timing of 8 CA bTDC for calibration of the initial conditions and chemical kinetic modelling of knock onsets in LOGEengine. In line with the methodology already described in section 6.3, pressure traces matching the selected medium and fast cycles of reference gasoline at a spark timing of 8 CA bTDC, were then chosen across the four set of fuels (ULG TRF, TRFB20, ULGB20) for knock onset averaging and comparison with the predicted data. Figures. 6.29a and 6.29b presents the set of similar pressure cycles selected across the four sets of fuels under the separate groups of medium and fast cycles respectively. Figure 6.29 shows how well the selected pressure cycles of the fuels match that of the reference gasoline indicating that the knock onsets for all fuels considered have been compared under similar conditions.

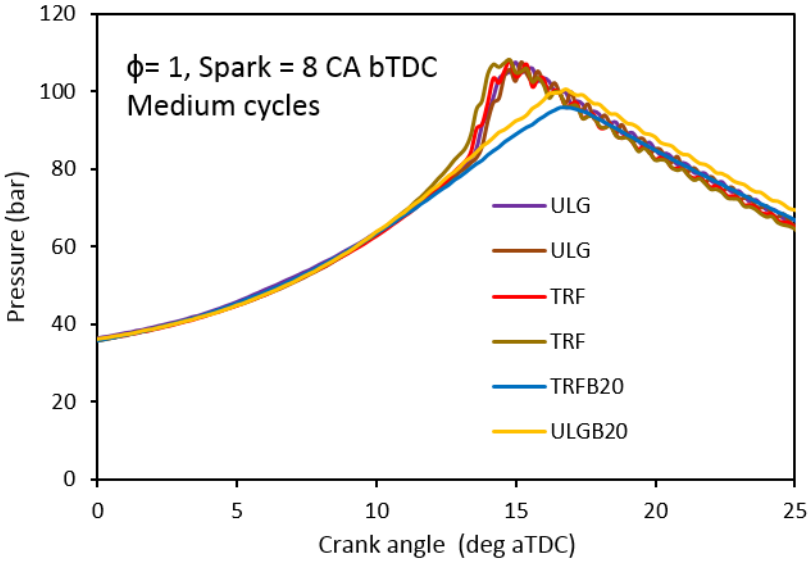

(a)

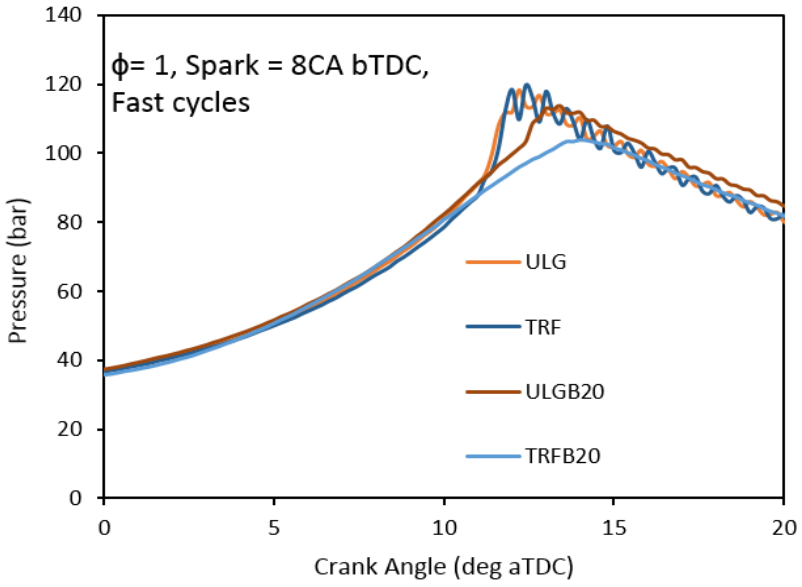

(b)

Figure 6.29: Selected experimental pressure cycles of four fuels with pre-knock values close to that of (a) medium cycles for gasoline, (b) fast cycles for gasoline.

Figure 6.30 shows how the simulated pressure traces of TRF compare with the measured pressure data for both the medium (Figure 6.30a) and fast cycles (Figure 6.30b) while Figures 6.31a and 6.31b show the predicted heat release profiles of the unburned zone of the selected medium and fast cycles superimposed upon their respective temperature histories. For the representative conditions of both the medium and fast cycles studied, the simulated pressure traces are in good agreement with the experimental pressure traces as was also seen in previous calculations involving the modelling of the average in-cylinder conditions. Looking at Figure 6.31, we clearly see that the negative temperature coefficient (NTC) heat release is more dominant within the medium cycle compared to the fast cycle. Similar to the explanation given in section 6.3.1, this disparity is caused by the higher temperature conditions prevalent during the fast cycles with the NTC chemistry being suppressed by the more favoured high temperature chemistry. Figure 6.32a presents a comparison of the predicted and experimental knock onsets for the selected medium and fast cycles at a spark timing of 8 CA bTDC. Although the predicted knock onsets are consistently higher than the experimental knock onsets across both the medium and fast cycles, the level of agreement with the measured data is reasonably good. Interestingly, the mechanism predicts the fast cycle better than it does the medium cycle for TRF. Therefore, the mechanism can potentially predict the knock limited spark advance (KLSA) for TRF to a reasonable level of accuracy since it is the cycle with the fastest burning velocity that knocks before the slower burning cycle and also determines the knock limited spark advance (KLSA).

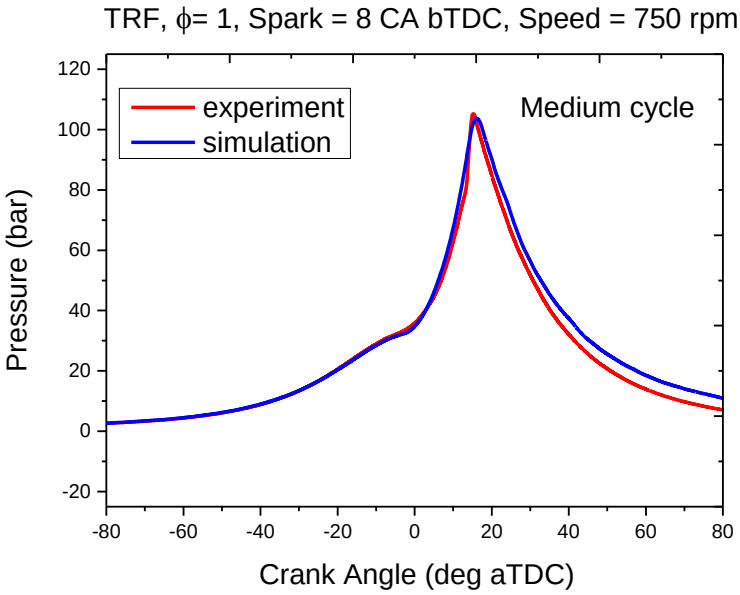

(a)

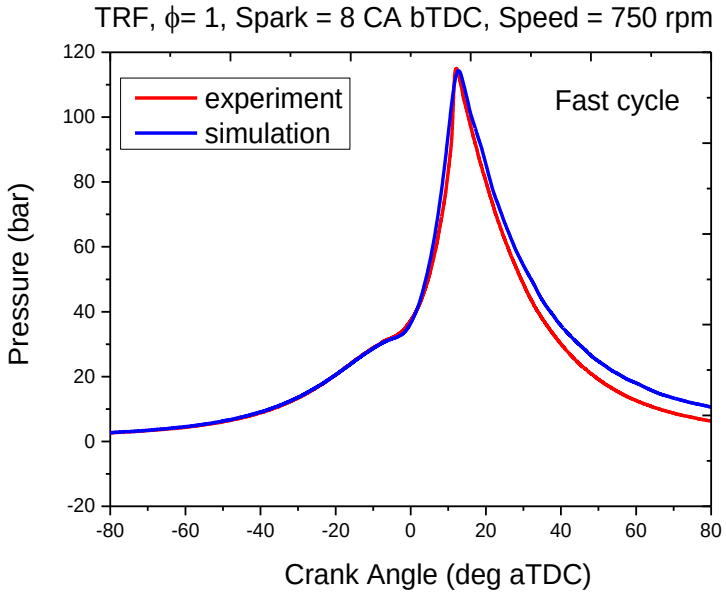

(b)

Figure 6.30: Comparison of experimental and simulated pressure traces for TRF at 8 CA bTDC (a) medium cycle (b) fast cycle.

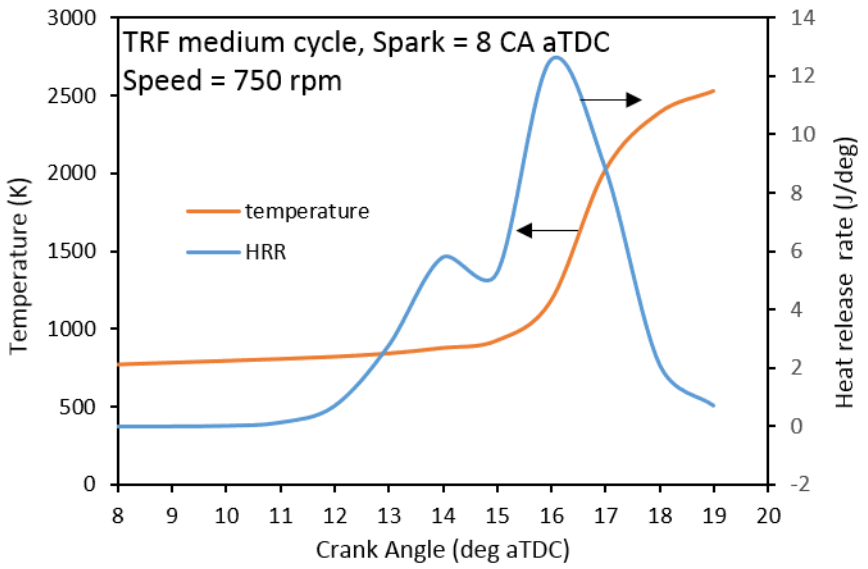

(a)

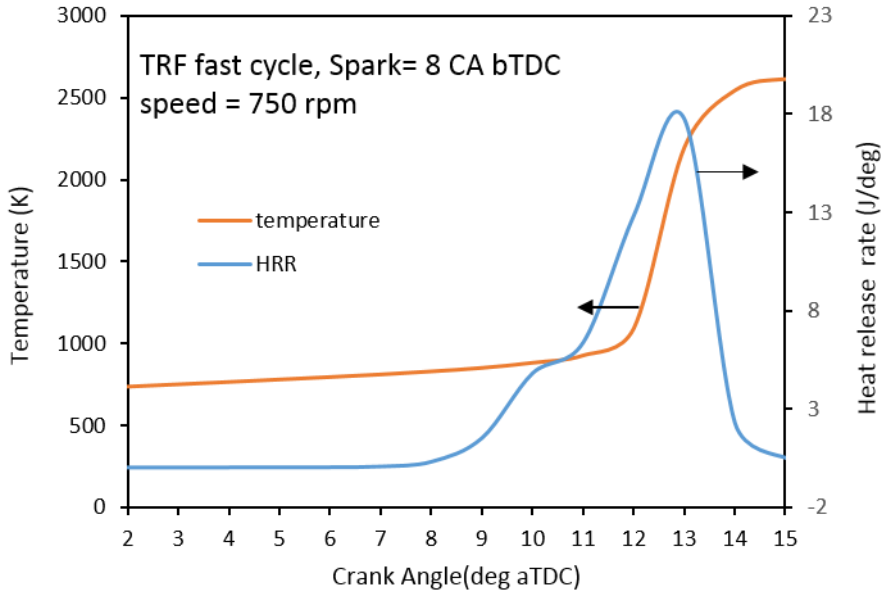

(b)

Figure 6.31: Rate of heat release and temperature histories in the unburned zone simulated for TRF using the Sarathy mechanism at 8 CA aTDC (a) medium cycle (b) fast cycle.

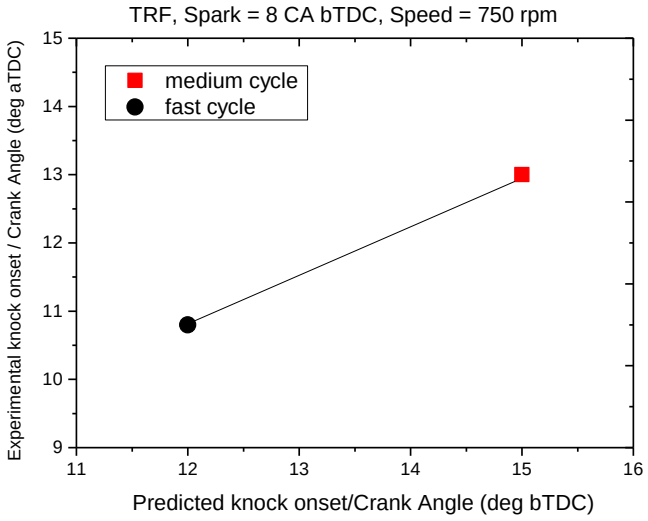

(a)

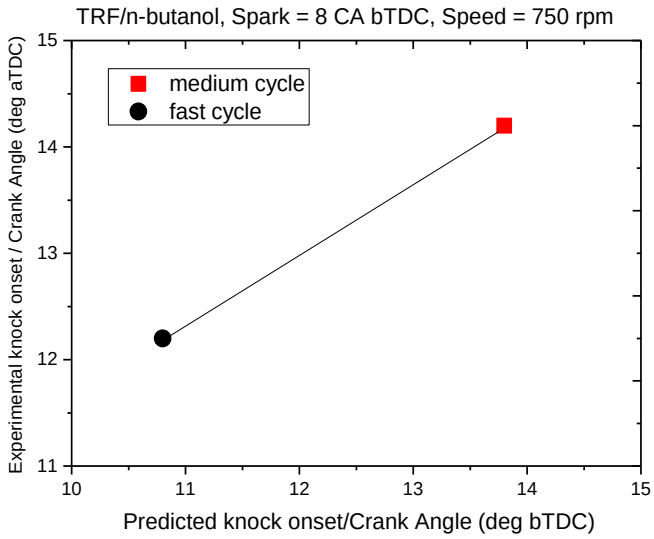

(b)

Figure 6.32: Comparison of predicted and experimental knock onsets of both fast and medium cycles at spark timing of 8 CA bTDC (a) TRF (b) TRFB20.

The knock onsets predicted for both the medium and fast cycles of the TRF/*n*-butanol blend at the spark timing of 8 CA bTDC are compared with the measured knock onsets of both set of cycles in Figure 6.32. In Figure 6.32b we see that the knock onsets predicted by the mechanism for both the medium and fast cycles of TRF/*n*-butanol blend are also higher compared to the experimental data. In the case of the TRF/*n*-butanol blend the agreement between the predicted and measured knock onsets is slightly better

for the medium cycle compared to that for the fast cycle. Comparing the results for both TRF and TRF/*n*-butanol blend we observe similar to the modelling results for the mean in-cylinder conditions, that the predicted knock onsets for TRF are higher compared to those of the blend.

Overall, while the mechanism does not accurately reproduce the influence of *n*-butanol blending on gasoline as seen in the measured data at the retarded spark timing of 6 CA bTDC, by comparing the result obtained within the RCM [65] and the current engine work, we however observe that the performance of the mechanism is quite consistent across both set ups. Therefore, it is important to state that for a chemical kinetic mechanism to correctly predict the autoignition characteristics of any fuel under practical engine conditions, it is crucial that the mechanism be able to accurately reproduce the ignition delay times at the temperature and pressure conditions seen in the RCM and leading up to the conditions prevalent in the engine. This point was also emphasised in the work of Faraz [30] where the ignition delay times predicted by the Golovitchev mechanism were consistently lower for iso-octane and TRF in both the engine and constant volume simulations within the NTC region.

6.3.4 Impact of update on TRF/*n*-butanol blended mechanism on predicted knock onsets

In the local and global sensitivity analysis carried out within the RCM (sections 5.3.2 and 5.3.3), the reaction of toluene + OH = phenol + CH_3 in the mechanism was identified as the most dominant pathway as opposed to the hydrogen abstraction channel by OH (toluene + OH = $C_6H_5CH_3$ + H_2O) which was expected to show the highest sensitivity to ignition delay prediction. Further probing showed that the toluene + OH channel leading to the formation of phenol + CH_3 was omitted in a recent update of all the toluene + OH reaction pathways in the LLNL scheme. It was also demonstrated in section 5.5.3 that updating the current parameterisation of the reaction toluene + OH = phenol + CH_3 in the mechanism with the data from a recent study by Seta [233] led to significant improvement in the predicted ignition delay times within the RCM. Therefore, autoignition simulations have also been performed within the engine framework using the updated mechanism in order to test the impact of the update on the predicted knock onsets of TRF and TRF/*n*-butanol across the spark timings of interest.

The results of the knock onsets predicted in the modelling work using the updated mechanism are presented in Figures 6.33 and 6.34 for TRF and TRF/*n*-butanol respectively alongside the experimental data and the knock onsets predicted by the original mechanism across the spark timing of 6 - 8 CA bTDC.

Figure 6.33 shows that the knock onsets predicted by the updated blend mechanism for TRF are significantly shorter than those predicted by the original mechanism and therefore led to significant improvement in the agreement between the measured and predicted data across the spark timing investigated. A similar trend was exhibited by the updated mechanism within the RCM modelling work where the ignition delays predicted by the updated mechanism were also in better agreement with the experimental data across the temperatures investigated. While the knock onsets predicted by the updated mechanism for the TRF/*n*-butanol blend (Figure 6.34) are also lower than those predicted by the original scheme across the spark timing tested, the agreement with the measured data is only significantly improved at the more advanced spark timing.

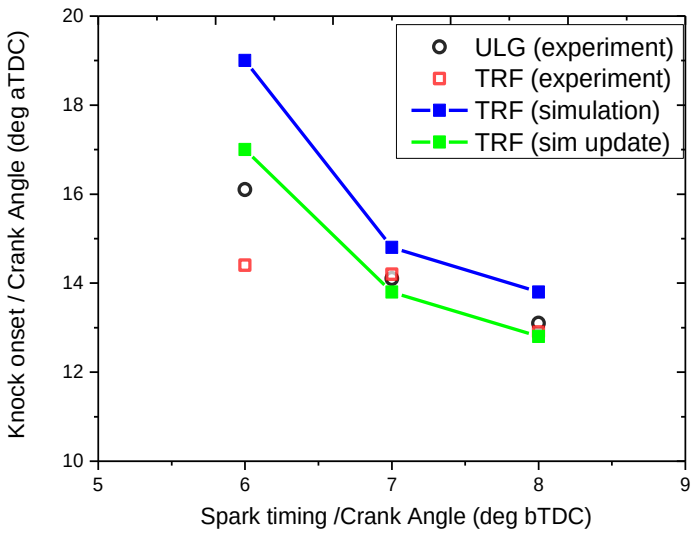

Figure 6.33: Predicted knock onsets of TRF using the updated mechanism in comparison with the knock onsets predicted by the original scheme and the experimental knock onsets for gasoline and TRF.

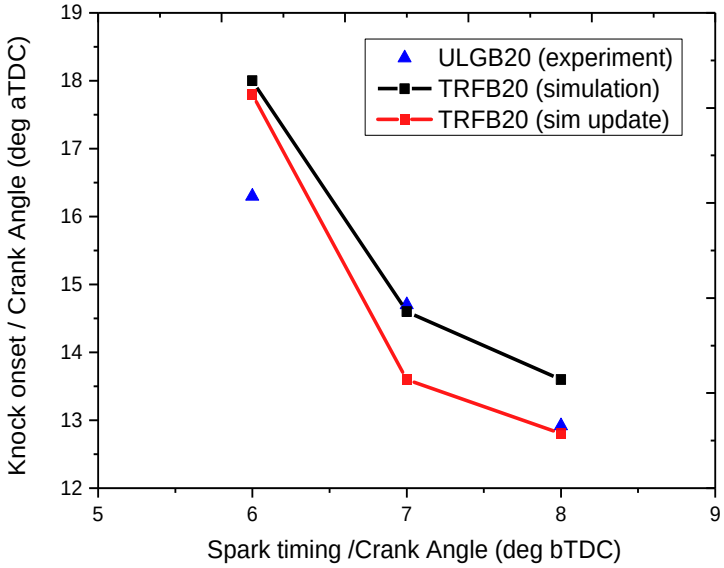

Figure 6.34: Predicted knock onsets of TRF/*n*-butanol blend using the updated mechanism in comparison with the knock onsets predicted by the original scheme and the experimental knock onsets for TRF/*n*-butanol blend.

6.4 Summary

In this work, the impact of *n*-butanol blending on the combustion, autoignition and knock properties of gasoline has been investigated under boosted spark ignition engine conditions using both experimental and modelling approaches for stoichiometric fuel/air mixtures at initial temperature and pressure conditions of 320 K and 1.6 bar respectively for a range of spark timings (2 CA- 8 CA bTDC). A formulated toluene reference fuel (TRF) surrogate for gasoline comprising of toluene, *n*-heptane and iso-octane has been tested experimentally in the Leeds University Ported Optical Engine (LUPOE) alongside a reference gasoline and their blends (a blend mixture of 20 % *n*-butanol and 80 % gasoline/TRF by volume). Although the gasoline/*n*-butanol blend displayed the highest burning rate and consequently the highest peak pressures compared to gasoline, TRF and the TRF/*n*-butanol blend, it knocked the latest and therefore provides an opportunity for enhancing the knock resistance of gasoline as well as the improvement of the engine efficiency via the use of higher compression ratios. The anti-knock

enhancing quality of *n*-butanol on gasoline was however observed to disappear at the more advanced spark timing of 8 CA bTDC. While *n*-butanol has shown some promise based on the current study, its application as an octane enhancer for gasoline under real engine conditions may be limited. This study would therefore benefit from further experiments and numerical simulations incorporating a wider range of blending ratios. As expected, the TRF fuel showed an earlier knocking boundary of 4 CA bTDC compared to 6 CA bTDC for the rest of the fuels and this was attributed to the absence of an oxygenate (i.e. ethanol or *n*-butanol) in the fuel which is present in the rest of the fuels. Knock onset in the end gas computed from the measured cylinder pressure data across the range of knocking spark advance 6 CA - 8 CA bTDC showed lower knock onsets for TRF compared to gasoline and the blended fuels. Overall, the TRF mixture gave a reasonable representation of the reference gasoline in terms of the produced knock onsets but only at the more advanced spark timing of 8 CA bTDC while the TRF/*n*-butanol blend gave a fairly poor agreement with the gasoline/*n*-butanol blend in contrast to what was observed in the RCM, indicating the need for further studies on the blended fuel.

Engine simulations of the combustion progress and autoignition tendency of the end gas, performed using the reduced *n*-butanol/TRF blended reaction mechanism of Sarathy and the SI model of the LOGEengine code showed that the predicted knock onsets for TRF and the TRF/*n*-butanol blend are higher compared to the measured knock onsets. The results are however in agreement with the results of ignition delay times obtained previously in the RCM [65] using the same mechanism. It was also seen in the modelling study that the low-intermediate temperature combustion chemistry within the S.I. engine end gas represented by the presence of a cool flame and NTC phase, plays a very important role in influencing the main or hot autoignition and consequently the overall knock onset due to its sensitisation effect (increasing of temperature and pressure) on the end gas and reduction of the time required for hot ignition to occur. Therefore accurate representation of the low temperature chemistry is crucial for accurate description of the chemical processes and knock occurring within the end gas of an S.I engine. Overall the work provided a link between the ignition delay times predicted in the RCM and the knock onsets predicted within the engine. The work showed that for a mechanism to accurately predict the autoignition characteristics of any

fuel under practical engine conditions, it is important that the mechanism accurately reproduces the ignition delay times at the temperature and pressure conditions occurring in the RCM and leading up to the conditions prevalent in the engine.

Chapter 7

Conclusions and future work

7.1 Summary of thesis main contributions to knowledge

In this work, the chemical kinetic modelling of various alternative and conventional fuels such as DME, *n*-butanol, gasoline, TRF, gasoline/*n*-butanol and a TRF/*n*-butanol blend, developed in the context of simulating practical combustion engines, have been investigated in both fundamental (e.g. RCM and JSR) and practical engine setups using the experimental and modelling approaches described in chapter 3 of this thesis. The main contributions to knowledge arising from this work are highlighted below.

- The work examined for the first time the capability of a toluene reference fuel (TRF) developed in this work, in acting as a suitable surrogate for complex gasoline, not only in isolation, but also upon blending with *n*-butanol. The work therefore demonstrated that chemical mechanisms can be developed that can explore the influence of butanol blending with gasoline. This has not really been investigated extensively in the literature and yet is a significant characteristics of a surrogate fuel which is meant for use in a broader sense e.g. for the development of engines that can operate optimally with different fuel blends.

- The work advances the chemical kinetic understanding of the combustion properties of a gasoline/*n*-butanol blend in comparison with conventional gasoline which it seek to partly replace with the main focus on autoignition and knock in the end gas of an SI engine.
- The work highlights and elucidates on the most important input parameters influencing the predictive uncertainties in the current chemical kinetic models of alternative fuels (e.g. DME, *n*-butanol, and gasoline/*n*-butanol) and gasoline combustion in practical engines with the goal of assisting the process for better quantification of current models.
- The work provides useful data sets for the ignition delay times of gasoline and gasoline/*n*-butanol blend for model validation and improvement including non-reactive volume histories within the RCM.

- Overall, this work provides both relevant science-based results and practical engineering insights to enhance the chemical kinetic modelling simulations of the combustion of alternative fuels such as DME, *n*-butanol and *n*-butanol/gasoline blends in practical engine systems.

7.2 Summary of the research findings

A summary of the different aspects of this study were presented at the end of chapters 4, 5 and 6. Here, some of the findings and conclusions are outlined and reiterated in the order that the chapters appear for the convenience of the reader.

7.2.1 Evaluation of the chemical kinetic modelling of DME and *n*-butanol combustion in fundamental set ups.

In chapter 4 of this thesis, the findings of the computer analysis of various chemical kinetic models of DME and *n*-butanol existing in open literature, performed in the context of ignition delay time prediction were presented.

The study showed that for the three most recent chemical kinetic schemes of DME and a recent *n*-butanol mechanism of Sarathy investigated, there is reasonable agreement between the predicted ignition delay times and the experimental data across a large part of the temperature range. However significant discrepancies of up to a factor of 5 for DME and over 5 for *n*-butanol, also exist for the rich case both at the high and low temperature region.

The results of local sensitivity analysis showed that across the three chemical kinetic models of DME studied, the overall ignition delays are most sensitive to the isomerisation of methoxymethyl-peroxy radical, producing a hydro-peroxy-methoxymethyl radical ($CH_3OCH_2O_2$, = $CH_2OCH_2O_2H$) while for the *n*-butanol mechanism of Sarathy, the predicted ignition delay times were most sensitive to the branching fraction of the main fuel H abstraction reactions via OH across the temperatures studied. The high temperature decomposition reaction of H_2O_2 (H_2O_2 (+M) = OH +OH) was found to dominate the predicted concentration profiles of the three chosen species (*n*-C_4H_9OH, CH_2O and CO) at 830 K, with H abstraction reactions from the α and γ sites of *n*-C_4H_9OH alongside reactions involving HO_2, (*n*-C_4H_9OH +

HO_2 = C_4H_8OH-1 + H_2O_2, HO_2 + HO_2 = H_2O_2 + O_2) also playing key roles in the prediction of *n*-C_4H_9OH and CO in a JSR.

The result of uncertainty analysis using global methods showed that the ranges of the output uncertainties predicted by the three DME mechanisms are large but driven by few reactions. The uncertainties in the predicted ignition delays of DME were shown across the three schemes (using variance-based methods) and across the entire temperature range to be driven mainly by the isomerisation of methoxymethyl-peroxy radical $CH_3OCH_2O_2$, contributing over 60 % to the predicted uncertainties and with a few other reactions such as $CH_2OCH_2O_2H$ + O_2 = $O_2CH_2OCH_2O_2H$, $O_2CH_2OCH_2O_2H$ = HO_2CH_2OCHO + OH and HO_2CH_2OCHO = OCH_2OCHO + OH also contributing to a lesser degree.

Sensitivity plots indicated difficulties in tuning individual rate parameters in the DME mechanism to target data because no single reaction dominated the uncertainty under any condition. Isolated updates made on the DME scheme based on the recent data of Eskola [215] worsened the models performance in terms of agreement with measured data. It was concluded that inherent correlations might be currently existing in the model due to tuning of rate parameters to fit particular output data sets and the update based on the of Eskola is unable to capture these correlations, hence the significant discrepancy. However further modifications to the chain-branching step $CH_2OCH_2O_2H$ + O_2 = $O_2CH_2OCH_2O_2H$ in the DME scheme led to improvement in the models predictions in both the RCM and flow reactor. The study demonstrated that there is urgent need for detailed studies of the *T*/*P* dependence of this 2nd O_2 addition step to reduce the overall uncertainties within predictions of low temperature DME oxidation.

For the *n*-butanol system, the study demonstrated that the predicted uncertainties in ignition delay times were dominated by the Fuel + OH abstraction reactions. The study also revealed that the low temperature ignition delay measurements provide a strong constraint on the branching ratio for abstraction from the α and γ sites but not on the total rate constant and this balance must be adequately captured in the *n*-butanol mechanism in order to bring predicted targets in better agreement with experimental data.

Updates made on the Fuel + OH abstraction reactions in the *n*-butanol mechanism based on the recent data of McGillen [198] led to a decrease in the predicted ignition delay times across all conditions studied and therefore significant improvement between the predicted and measured data under lean conditions at higher temperatures and 15 bar as well under stoichiometric conditions, particularly at P = 30 bar.

7.2.2 Experimental and chemical kinetic modelling study of the effect of *n*-butanol blending on the ignition delay times of gasoline in the RCM.

Chapter 5 of this work was dedicated to the analysis of the ignition delay time data obtained from simulations employing a newly developed combined LLNL TRF mechanism and the *n*-butanol mechanism of Sarathy investigated in chapter 4 of this thesis in comparison with data obtained from the Leeds RCM. TRF was chosen to represent complex gasoline in this work, therefore an appropriate TRF with composition matching the RON and H/C ratio of complex gasoline was developed and used in both the modelling and experimental work.

The results from the measured ignition delay times of TRF in the Leeds RCM showed that although higher discrepancies exist between TRF and gasoline in the lower temperature region of the RCM, the TRF provides a reasonable representation of gasoline across the conditions studied and was further employed in the study of the effect of *n*-butanol blending on gasoline.

Measurement of ignition delay times of gasoline/*n*-butanol and TRF/*n*-butanol in the RCM were also found to lie between those of *n*-butanol and gasoline across the conditions studied indicating that *n*-butanol could possibly act as an octane booster under blending conditions, particularly at low temperature.

The work demonstrated that while the general temperature dependence of the ignition delay times of TRF is well captured by the blended mechanism, the NTC and low temperature reactivity is under predicted. The work also showed that the blended TRF/*n*-butanol mechanism predicts the ignition delay times of TRF/*n*-butanol better than it does those of *n*-butanol as the ignition delay times of *n*-butanol are significantly over predicted at the lower temperature.

The results obtained in the local sensitivity analysis of the TRF/*n*-butanol scheme showed that different set of reactions are important for the accurate prediction of the ignition delay times of the different fuels investigated. For the TRF mixture, the abstraction reactions of iso-octane, *n*-heptane or toluene via OH were found to be more important with the H-abstraction reactions from the α, β and γ sites of iso-octane with sensitivities of 0.739, 0.631 and 1.000 respectively, dominating the predicted ignition delay times. The main toluene + OH pathway highlighted by the sensitivity analysis (i.e. the reversed form leading to the formation of CH_3 and phenol) with sensitivity index of 0.918 is equally as important as the H abstraction reaction from the γ site of iso-octane.

Global uncertainty/sensitivity analysis of the mechanism based on predicted ignition delays of stoichiometric TRF mixtures, showed the toluene + OH route = phenol + CH_3 to be among the most dominant pathways in terms of the predicted output uncertainties but an update on the mechanism based on recent data from the study of Seta led to the toluene + OH hydrogen abstraction reaction becoming the most dominant reaction as expected.

The work showed that the hydrogen abstraction reactions by OH from *n*-butanol are the most important reactions in predicting the effect of *n*-butanol blending on gasoline particularly at the low temperature but these rates are still currently not well known and hence the large discrepancies currently existing in the models prediction in the low temperature region.

7.2.3 Experimental and chemical kinetic modelling study of the effect of *n*-butanol blending on the autoignition and knock properties of gasoline in the engine.

The last part of this research presented in chapter 6 provided the opportunity to assess the chemical kinetic performance of the combined TRF/*n*-butanol scheme (investigated previously in chapter 5) under practical engine conditions and to also link its performance in both the RCM and engine. Here the capacity of the TRF/*n*-butanol mechanism in predicting the impact of *n*-butanol blending on gasoline combustion has been investigated under the framework of autoignition and knock modelling while the experimental measurement of knock onsets and knock intensities carried out in the Leeds engine under boosted conditions was used for the validation of the modelling

work as well as for advancing the understanding of the influence of *n*-butanol on the knocking behaviour of gasoline.

In the study, the formulated surrogate (TRF) displayed an earlier knocking regime compared to the rest of the fuels indicating that TRF may not be a perfect surrogate for gasoline when used in the context of simulating combustion in practical engines. Although the gasoline/*n*-butanol blend knocked the latest, its anti-knock enhancing quality on gasoline was however observed to disappear at the more extreme (*P*-*T*) conditions of the engine. The study therefore showed that while *n*-butanol holds some promise in terms of its knock resistance performance compared to gasoline, its application as an octane enhancer for gasoline under real engine conditions may be limited.

The work showed in agreement with the results of the autoignition delay times obtained in the RCM that the autoignition (knock) onsets of TRF and the TRF/*n*-butanol blend predicted under real engine conditions using the combined TRF/*n*-butanol mechanism are higher compared to the knock onsets measured in the Leeds engine.

In conclusion, the work showed that for a chemical kinetic mechanism to correctly predict the autoignition and knock behaviour of any fuel under practical engine conditions, it is important that the mechanism also reproduce the autoignition delay times at the temperature and pressure conditions occurring in the RCM, i.e. *P*-*T* conditions approaching those that occur in the end gas of an SI engine.

7.3 Direction for future work

- In the analysis of the DME combustion mechanism using both local and global sensitivity analysis, it was shown that the isomerisation reaction of methoxymethyl-peroxy radical, $CH_3OCH_2O_2$ is the most important reaction influencing the predictive uncertainties across the temperature range investigated. There is currently no experimental measurements for this rate and uncertainty in the current rate parameterisation for this reaction in the mechanism is expected to be very large. Therefore fundamental chemical kinetic studies focusing on the isomerisation rate is recommended in order to improve the overall performance of the DME scheme.

- New data indicates pressure dependency of the key chain-branching reaction $CH_2OCH_2O_2H + O_2 = O_2CH_2OCH_2O_2H$. Therefore further studies on the temperature and pressure dependency of the chain branching pathway, $CH_2OCH_2O_2H + O_2 = O_2CH_2OCH_2O_2H$ is strongly recommended in order to reduce uncertainties within DME mechanism for low temperature conditions.
- For the *n*-butanol reaction mechanism, H abstraction by HO_2 (*n*-$C_4H_9OH + HO_2 = C_4H_8OH\text{-}1 + H_2O_2$) was shown to dominate the predicted *n*-butanol and formaldehyde uncertainties in contrast to H abstraction reaction by OH which dominated the prediction uncertainties (in ignition delays) in the case of the RCM. Current uncertainty in the rate of the $C_4H_9OH + HO_2$ system is quite high. Therefore there is need for a detailed and more accurate studies of this reaction rate across a wide range of temperatures and pressures in order to bring predicted targets in better agreement with experimental data.
- In this work, it was demonstrated that although TRF captures the general trend in the temperature dependence of gasoline autoignition, it however does not provide a perfect representation of gasoline under real engine conditions as the measured knock boundary for TRF and knock on sets are significantly lower compared to those of gasoline. It would be interesting to see whether the use of a four component surrogate could fill this gap. Further work exploring the use of a 4-component surrogate involving TRF/1-pentene [96] or TRF/2-pentene [103] is therefore recommended.
- Although a slightly positive result was recorded in this study in terms of the impact *n*-butanol of blending on gasoline at the low temperature region, it is difficult to conclude on the overall effect of blending as only one blend has been considered in this study. Future studies exploring the blending effect of *n*-butanol across a range of blending ratios will therefore be beneficial.
- This study is currently the only one available in open literature exploring the impact of *n*-butanol blending on gasoline under stoichiometric conditions in the lower temperature condition of the RCM. More studies on *n*-butanol blending on gasoline, involving both lean to rich mixtures and higher pressures of up to 40 bar (i.e. conditions closer to those in practical engines) are therefore recommended for further validation of the current TRF/n-butanol mechanism.

- Iso-butanol has been shown to significantly lengthen the ignition delays of TRF under shock tube conditions [228], thus acting as an excellent octane booster at conditions relevant to the engine. Future chemical kinetic modelling studies exploring the potential of iso-butanol in enhancing the octane quality of gasoline in both the RCM and engine in comparison to *n*-butanol are therefore highly recommended.

Appendix A

A.1: Reactions selected from local sensitivity analysis of DME mechanisms and assigned input uncertainty factors

Reaction	G_i	Screened for flow reactor	Screened for RCM	Source of uncertainty information
$H + O_2 (+ M) = HO_2 (+ M)$ (k_∞)	3.16	*	x	[184]
$H + O_2 (+ M) = HO_2 (+ M)$ (k_0)	1.58	*	x	[184]
$H + O_2 = O + OH$	1.41		x	[184]
$OH^* + O_2 = OH + O_2$	10.00		x	Estimated
$OH + OH = O + H_2O$	1.41		x	[184]
$HO_2 + H = OH + OH$	1.41	*	x	[184]
$HO_2 + HO_2 = H_2O_2 + O_2$	1.41	*	x	[184]
$HO_2 + OH = H_2O + O_2$	3.16		x	[184]
$H_2O_2 + H = H_2O + OH$	2.00	*	x	[187]
$H_2O_2 + OH = H_2O + HO_2$	1.58	*	x	[187]
$H_2O_2 (+ M) = OH + OH (+M)$ (k_0,k_∞)	3.16		x	[184]
$HCO + O_2 = O_2CHO$	10.0	*	x	Estimated
$HCO + O_2 = CO + O$	2.24	*	x	[184]
$CO + O_2 = CO_2 + HO_2$	2.00		x	[187]
$CH_2O + OH = HCO + H_2O$	2.24	*	x	[184]
$CH_2O + H = HCO + H_2$	1.58	*		[184]
$CH_2O + HO_2 = HCO + H_2O_2$	2.00	*	x	[184]
$CH_2O + OH = HOCH_2O$	10.0	*		Estimated
$OCHO + HO_2 = HOCHO + O_2$	10.0	*		Estimated
$CH_3 + HO_2 = OH + CH_3O$	10.0		x	[184]
$CH_3 + O = CH_2O + H$	1.58		x	[184]
$CH_3 + HO_2 = CH_4 + O_2$	10.0		x	Estimated
$CH_3 + CH_3 (+ M) = C_2H_6 (+ M)$(k_0,k_∞)	2.00		x	[184]
$CH_4 + H = CH_3 + H_2$	2.82		x	[184]
$HOCHO + OH = H_2O + CO_2 + H$	1.58	*	x	[244]
$HOCHO + H = H_2 + CO + OH$	10.0	*	x	Estimated
$HOCHO + HO_2 = H_2O_2 + CO + OH$	10.0		x	Estimated
$HOCH_2O = HCOOH + H$	10.0	*		Estimated
$HOCH_2O = HOCHO + H$	10.0		x	Estimated
$HCOOH + HO_2 = H_2O_2 + CO + OH$	10.0	*	x	Estimated
$HCOOH + OH = H_2O + CO_2 + H$	10.0		x	Estimated
$CH_3OCH_3 + OH = H_2O + CH_3OCH_2$	2.24	*	x	[184]
$CH_3OCH_3 + H = H_2 + CH_3OCH_2$	3.16	*	x	[184]
$CH_3OH + OH = CH_3O + H_2O$				[245]
$CH_3OCH_2 = CH_2O + CH_3$	2.00		x	Estimated
$CH_3OCH_3 + HO_2 = CH_3OCH_2 + H_2O_2$	10.0	*	x	Estimated
$CH_3OCH_3 + O_2 = CH_3OCH_2 + HO_2$	5.00		x	[184]
$CH_3OCH_3 + CH_3OCH_2O_2 = CH_3OCH_2 + CH_3OCH_2O_2H$	10.0	*	x	Estimated
$CH_3OCH_2 + HO_2 = CH_3OCH_2O + OH$	10.0	*		Estimated
$CH_3OCH_2O_2 + CH_2O = CH_3OCH_2O_2H + HCO$	10.0	*	x	Estimated
$CH_3OCH_2O_2 + CH_3OCH_2O_2 = O_2 + 2CH_3OCH_2O$	7.94	*	x	Estimated
$CH_3OCH_2O_2 + CH_3OCH_2O_2 = O_2 + CH_3OCHO + CH_3OCH_2OH$	10.0	*	x	Estimated
$CH_3OCH_2O_2 = CH_2OCH_2O_2H$	10.0	*	x	Estimated

$CH_2OCH_2O_2H = OH + 2CH_2O$	5.00	*	x	Estimated
$CH_2OCH_2O_2H + O_2 = O_2CH_2OCH_2O_2H$	10.0	*	x	Estimated
$O_2CH_2OCH_2O_2H = HO_2CH_2OCHO + OH$	10.0		x	Estimated
$HO_2CH_2OCHO = OCH_2OCHO + OH$	10.0	*	x	Estimated
$OCH_2OCHO = CH_2O + OCHO$	10.0	*	x	Estimated
$OCH_2OCHO = HOCH_2OCO$	10.0	*	x	Estimated
$CH_3 + OCHO = CH_3OCHO$	10.0	*	x	Estimated
$CH_3OCHO + OH = CH_3OCO + H_2O$	5.00	*	x	Estimated
$CH_3OCHO + OH = CH_2OCHO + H_2O$	5.00	*	x	Estimated
$HOCH_2O + CO = HOCH_2OCO$	10.0	*	x	Estimated
$CH_2OH + CO_2 = HOCH_2OCO$	10.0	*	x	Estimated

A.2: Reactions selected from local sensitivity analysis of Sarathy *n*-butanol mechanism and assigned input uncertainty factors

Reaction	G_i	Screened for JSR	Screened for RCM	Source of uncertainty information
$H + O_2 (+ M) = HO_2 (+ M)$ (k_∞)	3.16	*	x	[184]
$H + O_2 (+ M) = HO_2 (+ M)$ (k_0)	1.58	*	x	[184]
$HO_2 + OH = H_2O + O_2$	3.16	*	x	[184]
$HO_2 + HO_2 = H_2O_2 + O_2$	1.41	*	x	[184]
$H_2O_2 (+ M) = OH + OH (+M)$ (k_0,k_∞)	3.16	*	x	[184]
$H_2O_2 + OH = H_2O + HO_2$	1.58	*		[187]
$HCO + O_2 = O_2CHO$	2.0	*		Estimated
$HCO + O_2 = CO + HO_2$	2.24	*		[184]
$CH_2O + OH = HCO + H_2O$	2.24	*	x	[184]
$CH_2O + O_2CHO = HCO + HO_2CHO$	2.0	*		Estimated
$CH_2O + HO_2 = HCO + H_2O_2$	2.00	*		[184]
$CH_2O + OH = HOCH_2O$	2.0	*		Estimated
$CH_2O + H = HCO + H_2$	3.16	*		[184]
$CO + OH = CO_2 + H$	1.26	*		[184]
$CH_3 + HO_2 = CH_4 + O_2$	2.0	*		Estimated
$CH_3 + HO_2 = OH + CH_3O$	2.0	*		[184]
$HOCHO + OH = H_2O + CO_2 + H$	1.58	*		[246]
$CH_3O_2 + HO_2 = CH_3O_2H + O_2$	2.0	*	x	Estimated
$CH_3CHO + OH = CH_3CO + H_2O$	1.14	*		[184]
$CH3CHO + HO2 = CH3CO + H_2O_2$	2.51	*	x	[184]
$CH_3CHO + OH = CH_3 + HOCHO$	2.0	*		Estimated
$CH_3CHO + OH = CH_2CHO + H_2O$	1.52	*		[184]
$CH_3CHO + H = CH_3CO + H_2$	2.0	*		Estimated
$CH_3O_2H = CH_3O + OH$	3.16		x	[184]
$C_2H_3 + O_2 = CH_2CHO + O$	2.0	*		Estimated
$C_2H_3CHO + HO_2 = C_2H_3CO + H_2O_2$	2.0	*		Estimated
$C_2H_3OH + C_2H_5 = C_4H8OH-1$	2.0	*		Estimated
$C_2H_3OH + OH = CH_2CHO + H_2O$	2.0	*		Estimated
$C_2H_3 + O_2 = CH_2O + HCO$	2.0	*		Estimated

$C_2H_3OH + OH = CH_3CHO$	2.0	*		Estimated
$C_2H_3OH + HOCHO = CH_3CHO + HOCHO$	2.0	*		Estimated
$C_2H_4 + OH = C_2H_3 + H_2O$	2.0	*		Estimated
$sC_2H_4OH + OH = C_2H3OH + H$	2.0	*		Estimated
$C_2H_5 + HO_2 = C_2H_5O + OH$	2.0	*		Estimated
$C_3H_6 + CH_2OH = C_4H_8OH\text{-}3$	2.0	*	x	Estimated
$nC_3H_7O_2 = C_3H_6 + HO_2$	2.0		x	Estimated
$nC_3H_7O_2 = C_3H_6OOH1\text{-}2$	2.0		x	Estimated
$nC_3H_7O_2 = C_3H_6OOH1\text{-}3$	2.0		x	Estimated
$nC3H7CHO + HO_2 = nC_3H_7CO + H_2O_2$	2.0	*	x	Estimated
$nC_3H_7CHO + HOCHO = C_4H_7OH1\text{-}1 + HOCHO$	2.0	*		Estimated
$C_4H_7OH1\text{-}1 + OH = C_4H_6OH1\text{-}13 + H_2O$	2.0	*		Estimated
$C_4H_7OH1\text{-}1+ HOCHO = nC_3H_7CHO\ \ HOCHO$	2.0	*		Estimated
$C_4H_7OH\text{-}3OOH\text{-}1 + O_2 = nC4KET13 + HO_2$	2.0	*	x	Estimated
$C_4H_7OH\text{-}3OOH\text{-}1 + O_2 = C_4H_7OH\text{-}3OOH\text{-}1O_2$	2.0		x	Estimated
$C_4H_7OH\text{-}1OOH\text{-}3 + O_2 = C_4H_7OH\text{-}1OOH\text{-}3O_2$	2.0	*		Estimated
$C_4H_7OH\text{-}1OOH\text{-}3O_2 = C_4OHKET1\text{-}3 + OH$	2.0	*	x	Estimated
$C_4H_7OH\text{-}4OOH\text{-}1 + O_2 = C_4H_7OH\text{-}4OOH\text{-}1O_2$	2.0		x	Estimated
$C_4H_7OH\text{-}4OOH\text{-}1 + O_2 = C_4H_7OH\text{-}O1\text{-}4 + OH$	2.0		x	Estimated
$C_4H_7OH1\text{-}4 = C_2H_3 + pC_2H_4OH$	2.0	*		Estimated
$C_4H_8OH\text{-}1 + O_2 = nC_3H_7CHO + HO_2$	2.0	*	x	Estimated
$C_4H_8OH\text{-}1 + O_2 = C4H_8OH\text{-}1O_2$	2.0	*	x	Estimated
$C_4H_8OH\text{-}1O_2 = C4H_7OH1\text{-}1 + HO_2$	2.0	*		Estimated
$C_4H_8OH\text{-}1O_2 = C4H_7OH\text{-}1OOH\text{-}3$	2.0		x	Estimated
$C_4H_8OH\text{-}4O_2 = C4H_7OH\text{-}4OOH\text{-}1$	2.0		x	Estimated
$C_4H_8OH\text{-}2O_2 = C4H_7OH\text{-}2OOH\text{-}1$	2.0		x	Estimated
$C_4H_8OH\text{-}2O_2 = C4H_7OH\text{-}2OOH\text{-}4$	2.0		x	Estimated
$C_4H_8OH\text{-}3O_2 = C4H_7OH\text{-}3OOH\text{-}1$	2.0		x	Estimated
$C_4H_8OH\text{-}4O_2 = C4H_7OH\text{-}4OOH\text{-}2$	2.0		x	Estimated
$C_4H_8OH\text{-}1O_2 = C4H_7OH1\text{-}1 + HO_2$	2.0		x	Estimated
$C_4H_8OH\text{-}2O_2 = C4H_7OH1\text{-}1 + HO_2$	2.0		x	Estimated
$C_4H_8OH\text{-}2O_2 = C4H_7OH2\text{-}1 + HO_2$	2.0		x	Estimated
$C_4H_8OH\text{-}3O_2 = C4H_7OH2\text{-}1 + HO_2$	2.0		x	Estimated
$C_4H_8OH\text{-}3O_2 = C4H_7OH1\text{-}4+ HO_2$	2.0		x	Estimated
$C_4H_8OH\text{-}4O_2 = C4H_7OH1\text{-}4 + HO_2$	2.0		x	Estimated
$C_4H_9OH +OH = C4H_8OH\text{-}1 + H_2O$	2.0	*	x	Estimated
$C_4H_9OH +OH = C4H_8OH\text{-}2 + H_2O$	2.0		x	Estimated
$C_4H_9OH +OH = C4H_8OH\text{-}3 + H_2O$	2.0	*	x	Estimated
$C_4H_9OH +OH = C4H_8OH\text{-}4 + H_2O$	2.0	*	x	Estimated
$C_4H_9OH + HO_2 = C4H_8OH\text{-}1 + H_2O_2$	2.0	*	x	Estimated
$C_4H_9OH + HO_2 = C4H_8OH\text{-}2 + H_2O_2$	2.0		x	Estimated
$C_4H_9OH + HO_2 = C4H_8OH\text{-}3 + H_2O_2$	2.0		x	Estimated
$C_4H_9OH + HO_2 = C4H_8OH\text{-}4 + H_2O_2$	2.0		x	Estimated
$C_4H_9OH + H = C4H_8OH\text{-}1 + H_2$	2.0	*		Estimated
$C_4H_9OH + H = C4H_8OH\text{-}3 + H_2$	2.0	*		Estimated

A.3: Reactions selected from local sensitivity analysis of TRF/*n*-butanol blended mechanism and assigned input uncertainty factors

Reaction	G_i	K max	K min	Source of uncertainty information
$HO_2 + HO_2 = H_2O_2 + O_2$	1.41			[184]
H_2O_2 (+ M) = OH + OH (+M) (k_0,k_∞)	3.16			[184]
$H_2O_2 + OH = H_2O + HO_2$	1.58			[187]
$CH_2O + OH = HCO + H_2O$	2.24			[184]
$CH_3O_2 + HO_2 = CH_3O_2H + O_2$	5.0			Estimated
$nC_3H_7O_2 = C_3H_6OOH1\text{-}3$	10.0			Estimated
$nC_4KET13 = CH_3CHO + CH_2CHO + OH$	10.0			Estimated
$tC_4H_9O_2 = iC_4H_8 + HO_2$	10.0			Estimated
$iC_8H_{18} + OH = aC_8H_{17} + H_2O$	7.94			Estimated
$iC_8H_{18} + OH = bC_8H_{17} + H_2O$	3.98			Estimated
$iC_8H_{18} + OH = cC_8H_{17} + H_2O$	7.94			Estimated
$aC_8H_{17} + O_2 = aC_8H_{17}O_2$	10.0			Estimated
$dC_8H_{17}O_2 = dC_8H_{16}OOH\text{-}b$	10.0			Estimated
$dC_8H_{17}O_2 = dC_8H_{16}OOH\text{-}c$	10.0			Estimated
$nC_7H_{16} + OH = C_7H_{15}\text{-}1 + + H_2O$	10.0			Estimated
$nC_7H_{16} + OH = C_7H_{15}\text{-}2 + + H_2O$	10.0			Estimated
$nC_7H_{16} + OH = C_7H_{15}\text{-}3 + + H_2O$	10.0			Estimated
$C_7H_{15}O_2\text{-}2 = C_7H_{14}OOH2\text{-}4$	10.0			Estimated
$C_6H_5OH + CH_3 = C_6H_5CH_3 + OH$	10.0			Estimated
$C_6H_5CH_3 + HO_2 = = C_6H_5CH_2j + H_2O_2$	3.16			Estimated
$C_6H_5CH_2j + HO_2 = C_6H_5CH_2Oj + OH$	7.94			Estimated
$C_4H_9OH + OH = C4H_8OH\text{-}1 + H_2O$	10.0			Estimated
$C_4H_9OH + OH = C4H_8OH\text{-}3 + H_2O$	10.0			Estimated
$C_4H_9OH + OH = C4H_8OH\text{-}4 + H_2O$	10.0			Estimated
$C_4H_9OH + HO_2 = C4H_8OH\text{-}1 + H_2O_2$	10.0			Estimated
$C_4H_8OH\text{-}1 + O_2 = C_3H_7CHO + HO_2$	10.0			Estimated
$C_4H_8OH\text{-}1 + O_2 = C4H_8OH\text{-}1O_2$	10.0			Estimated
$C_4H_8OH\text{-}1O_2 = C4H_7OH\text{-}1OOH\text{-}3$	10.0			Estimated
$C_4H_8OH\text{-}3O_2 = C4H_7OH\text{-}3OOH\text{-}1$	10.0			Estimated
$C_4H_8OH\text{-}1O_2 = C4H_7OH1\text{-}1 + HO_2$	10.0			Estimated
$C4H_7OH\text{-}3OOH\text{-}1 + O_2 = nC_4KET13 + HO_2$	10.0			Estimated
$C4H_7OH\text{-}3OOH\text{-}1 + O_2 = C4H_7OH\text{-}3OOH\text{-}1O_2$	10.0			Estimated

References

1. Bp. *BP energy outlook 2017* [online]. 2017. [Accessed 21st June, 2017].

2. Battin-Leclerc, F., E. Blurock, R. Bounaceur, R. Fournet, P.-A. Glaude, O. Herbinet, B. Sirjean and V. Warth. Towards cleaner combustion engines through groundbreaking detailed chemical kinetic models. *Chemical Society Reviews*, 2011, **40**(9), pp.4762-4782.

3. Vancoillie, J. and S. Verhelst. Modeling the combustion of light alcohols in SI engines: a preliminary study. *In: Proceedings of the FISITA 2010 World Automotive Congress*, 2010, pp.1-12.

4. Etsap. *Ethanol Internal Combustion Engines*. [Accessed 23 July 2012]. 2010.

5. Farkade, H. and A. Pathre. Experimental investigation of methanol, ethanol and butanol blends with gasoline on SI engine. *International Journal of Emerging Technology and Advanced Engineering,(ISSN 2250-2459)*, 2012, **2**(4).

6. Srinivasan, A.C. and C.G. Saravanan. Study of Combustion Characteristics of an SI Engine Fuelled with Ethanol and Oxygenated Fuel Additives. *Journal of Sustainable Energy & Environment*, 2013, **1**(2), pp.85-91.

7. Sarkar, A., A. Datta and B.K. Mandal. Performance characteristics of spark ignition engine using ethanol as fuel at different operating conditions. *International Journal of Emerging Technology and Advanced Engineering*, 2013, **3**, pp.96-100.

8. Gopal, M.G. and D.S. Rajendra. Experimental Study on SI Engine At Different Ignition Timing Using CNG And Gasoline-20% n Butanol Blend. 2013, **3**(3), pp.249-255.

9. Wallner, T., S.A. Miers and S. Mcconnell. *A comparison of ethanol and butanol as oxygenates using a direct-injection, spark-ignition (DISI) engine.* 2009.

10. Szulczyk, K.R. Which is a better transportation fuel–butanol or ethanol? *International Journal of Energy and Environment*, 2010, **1**(3), pp.501-512.

11. Wigg, B. *A Study on Emission of Butanol using a Spark Ignition Engine and their Reduction Using Electrostatically Assisted Injection.* PhD thesis, University of Ilinois, Urbana, 2011.

12. Dernotte, J., C. Mounaim-Rousselle, F. Halter and P. Seers. Evaluation of butanol–gasoline blends in a port fuel-injection, spark-ignition engine. *Oil & Gas Science and Technology–Revue de l'Institut Français du Pétrole*, 2009, **65**(2), pp.345-351.

13. Skevis, G. Liquid Biofuels: Biodiesel and Bioalcohols. *In:* F.W. Maximilian Lackner, And Aviinash K. Agarwal, ed. *Handbook of Combustion*. Weinheim: WILEY-VCH 2010, p.366.

14. Rajagopal, R.a.P.P.B. Sustainable Biodiesel Feedstock: Jatropha: A Strategic Option. [online], 2008, [Accessed 23 July 2012].

15. Stiklen, M. *Is Large Scale Production of Biofuel Possible?* [online]. 2010. [Accessed 23 July 2012].

16. Sarathy, S.M. *Chemical Kinetic Modeling of Biofuel Combustion*. thesis, University of Toronto, 2010.

17. Gevo. *MPR News: Isobutanol Production to resume at GEVO Plant* [online]. 2013. [Accessed 12th, May 2013].

18. Ebtp. *Biofuels Research, Demonstration & Deployment* [online]. [Accessed 16 February 2017].

19. Butamax. *Biobutanol Fact Sheet* [online]. 2013. [Accessed 12th May 2013].

20. Dagaut, P., S.M. Sarathy and M.J. Thomson. A chemical kinetic study of n-butanol oxidation at elevated pressure in a jet stirred reactor. *Proceedings of the Combustion Institute*, 2009, **32**(1), pp.229-237.

21. Icis. *Biobutanol development makes a head way* [online]. 2009. [Accessed 16 February 2017].

22. Kohse-Höinghaus, K., P. Oßwald, T.A. Cool, T. Kasper, N. Hansen, F. Qi, C.K. Westbrook and P.R. Westmoreland. Biofuel Combustion Chemistry: From Ethanol to Biodiesel. *Angewandte Chemie International Edition*, 2010, **49**(21), pp.3572-3597.

23. Arcoumanis, C., C. Bae, R. Crookes and E. Kinoshita. The potential of di-methyl ether (DME) as an alternative fuel for compression-ignition engines: a review. *Fuel*, 2008, **87**(7), pp.1014-1030.

24. Patil, K.R. and S.S. Thipse. THE POTENTIAL OF DME-DIESEL BLENDS AS AN ALTERNATIVE FUEL FOR CI ENGINES. 2012.

25. Baulch, D.L. Kinetic Databases. *In:* M.J. Pilling, ed. *Comprehensive Chemical Kinetics: Low Temperature Combustion and Auto-ignition*. Elservier, 1997.

26. Stone, R. *Introduction to internal combustion engines.* Macmilian Press Ltd, 1999.

27. Komninos, N.P. and C.D. Rakopoulos. Modeling HCCI combustion of biofuels: A review. *Renewable and Sustainable Energy Reviews*, 2012, **16**(3), pp.1588-1610.

28. Mattavi, J.N. *Combustion modeling in reciprocating engines.* Plenum Publishing Corporation, 1980.

29. Tomlin, A.S. The role of sensitivity and uncertainty analysis in combustion modelling. *Proceedings of the Combustion Institute*, 2012.

30. Khan, A.F. *Chemical Kinetics Modelling of Combustion Processes in SI Engines*. PhD thesis, The University of Leeds, 2014.

31. Heywood, J.B. Fundamentals of internal combustion engines. *NY: McGraw Hill*, 1988, p.619.

32. Ganesan, V. *Internal Combustion Engines.* McGraw-Hill Publishing Company Limited 1996.

33. Pulkrabek, W.W. *Engineering Fundamentals of the Internal Combustion Engines.* Second ed. Upper Saddle River, New Jersey: Pearson Prentice-Hall, 2004.

34. Liu, K., A.A. Burluka and C.G.W. Sheppard. Turbulent flame and mass burning rate in a spark ignition engine. *Fuel*, 2013, **107**, pp.202-208.

35. Kasseris, E.P. *Knock Limits in Spark Ignited Direct Injected Engines Using Gasolines/Ethanol Blends*. PhD thesis, Massachusetts Institute of Technology, 2011.

36. Liu, Z. *Chemical Kinetics Modelling Study on Fuel Autoignition in Internal Combustion Engines*. PhD thesis, Loughborough University, 2010.

37. Gu, J. *Chemical Kinetics Modelling Study of Naturally Aspirated and Boosted SI Engine Flame Propagation and Knock*. PhD thesis, Loughborough University, 2014.

38. Mohamed, C. *Autoigntion of Hydrocarbons in Relation to Knock*. PhD thesis, University of Leeds, 1997.

39. Konig, G. and C. Sheppard. *End gas autoignition and knock in a spark ignition engine*. 0148-7191. SAE Technical Paper, 1990.

40. Ling, Z. *Flame Propagation and Autoignition in a High Pressure Optical Engine*. PhD thesis, University of Leeds, 2014.

41. Dahnz, C., K.-M. Han, U. Spicher, M. Magar, R. Schiessl and U. Maas. Investigations on Pre-Ignition in Highly Supercharged SI Engines. 2010.

42. Firey, J.C. A detonation wave theory of gasoline engine knock. *Symposium (International) on Combustion*, 1957, **6**(1), pp.878-886.

43. Bradley, D. and G.T. Kalghatgi. Influence of autoignition delay time characteristics of different fuels on pressure waves and knock in reciprocating engines. *Combustion and Flame*, 2009, **156**(12), pp.2307-2318.

44. Kasmani, H. *Flame Propagation in Spark Ignition Engine Combustion Process using Computational Fluid Dynamics (CFD)*. B.Eng thesis, Universiti Malaysia Pahang, 2010.

45. Soylu, S. *Autoignition Modeling of Natural Gas for Engine Modeling Programs: An Experimental and Modeling Study*. PhD thesis, Iowa State University, Ames, Iowa, 2001.

46. Curtis, S., M. Owen, T. Hess and S. Egan. Effect of Ethanol Blends on a Spark Ignition, 4-Stroke, Internal Combustion Engine. 2008.

47. Douaud, A.M. and P. Eyzat. Four-Octane-Number Method for Predicting the Anti-Knock Behavior of Fuels and Engines. *In*. SAE International, 1978.

48. Conway, G.T. *Cyclic Variability of Flame Propagation and Autoignition in Supercharged and Naturally Aspirated SI Engines.* PhD thesis, University of Leeds, 2013.

49. Roberts, L. *Fuel and Residual Effects in Spark Ignition and Homogeneous Charge Compression Ignition Engines.* PhD thesis, University of Leeds, 2010.

50. Smallbone, A. *Fuel and Residual Effects on Knock Onset in Spark Ignition Engines.* PhD thesis, University of Leeds, 2004.

51. Livengood, J.C. and P.C. Wu. Correlation of autoignition phenomena in internal combustion engines and rapid compression machines. *Symposium (International) on Combustion*, 1955, **5**(1), pp.347-356.

52. Walker, R.W., Morley, C. Basic Chemistry of Combustion. *In:* M.J. Pilling, ed. *Comprehensive Chemical Kinetics: Low-temperature Combustion and Autoignition*. Elsevier, 1997.

53. Steurs, F.H.M.S. *Cycle-resolved Analysis and Modeling of Knock in a Homogeneous Charge Spark Ignition Engine Fueled by Ethanol and Iso-octane*. Dr. sc thesis, Swiss Federal Institute of Technology (ETH) in Zurich, Switzerland, 2014.

54. Halstead, M.P., L.J. Kirsch and C.P. Quinn. The autoignition of hydrocarbon fuels at high temperatures and pressures—Fitting of a mathematical model. *Combustion and Flame*, 1977, **30**, pp.45-60.

55. Cox, R.A. and J.A. Cole. Chemical aspects of the autoignition of hydrocarbon□air mixtures. *Combustion and Flame*, 1985, **60**(2), pp.109-123.

56. Hu, H. and J. Keck. *Autoignition of adiabatically compressed combustible gas mixtures*. 0148-7191. SAE technical paper, 1987.

57. Benson, S.W. The kinetics and thermochemistry of chemical oxidation with application to combustion and flames. *Progress in Energy and Combustion Science*, 1981, **7**(2), pp.125-134.

58. Chun, K.M., J.B. Heywood and J.C. Keck. Prediction of knock occurrence in a spark-ignition engine. *Symposium (International) on Combustion*, 1989, **22**(1), pp.455-463.

59. Cowart, J.S., J.C. Keck, J.B. Heywood, C.K. Westbrook and W.J. Pitz. Engine knock predictions using a fully-detailed and a reduced chemical kinetic mechanism. *Symposium (International) on Combustion*, 1991, **23**(1), pp.1055-1062.

60. Nishiwaki, K., Y. Yoshihara and K. Saijyo. *Numerical analysis of the location of knock initiation in SI engines*. 0148-7191. SAE Technical Paper, 2000.

61. Curran, H.J., W.J. Pitz, C.K. Westbrook, G.V. Callahan and F.L. Dryer. Oxidation of automotive primary reference fuels at elevated pressures. *Symposium (International) on Combustion*, 1998, **27**(1), pp.379-387.

62. Andrae, J.C.G. and R.A. Head. HCCI experiments with gasoline surrogate fuels modeled by a semidetailed chemical kinetic model. *Combustion and Flame*, 2009, **156**(4), pp.842-851.

63. Huang, C., V. Golovitchev and A. Lipatnikov. Chemical Model of Gasoline-Ethanol Blends for Internal Combustion Engine Applications. *In*. SAE International, 2010.

64. Ra, Y. and R.D. Reitz. A combustion model for IC engine combustion simulations with multi-component fuels. *Combustion and Flame*, 2011, **158**(1), pp.69-90.

65. Agbro, E., A.S. Tomlin, M. Lawes, S. Park and S.M. Sarathy. The influence of n-butanol blending on the ignition delay times of gasoline and its surrogate at high pressures. *Fuel*, 2017, **187**, pp.211-219.

66. Gardiner, W.C. *Combustion Chemistry.* New York Inc: Springer-Verlag, 1984.

67. Upadhyay, S.K. *Chemical kinetics and reaction dynamics.* New York: Springer, 2006.

68. Heghes, C.I. *C_1-C_4 Hydrocarbon Oxidation Mechanism*. Doctor of Natural Sciences thesis, University of Heidelberg, 2006.

69. Reaction Design. *CHEMKIN-PRO.* San Diego, 2011.

70. Rotexo Gmbh & Co Kg. *COSILAB.* Germany: www.rotexo.com, 2003.

71. Goodwin, D.M., N; Moffat, H; Speth, R. *CANTERA: an object-oriented software toolit for chemical kinetics, thermodynamics, and transport processes.* 2.0.2 ed. https://code.google.com/p/cantera, 2013.

72. Fernandes, R. Combustion Chemistry. *In:* M.W. Lackner, F; Agarwal, A. K, ed. *Handbook of Combustion*. Weinheim: Wiley-VCH Verlag GmbH and Co, 2010.

73. Turns, S.R. *An Introduction to Combustion: Concepts and Applications.* McGraw-Hill, 1996.

74. Cornish-Bowden, A. *Fundamentals of Enzymes Kinetics.* Wiley-VCH Verlag GmbH & CO. KGaA, 2012.

75. Brown, T.L., H.E. Lemay and B.E. Boursten. *Chemistry: The cental science.* Englewood Cliffs, N. J. ; London: Prentice-Hall, 1981.

76. Troe, J. Theory of thermal unimolecular reactions at low pressures. II. Strong collision rate constants. Applications. *The Journal of Chemical Physics*, 1977, **66**, p.4758.

77. Troe, J. Theory of thermal unimolecular reactions at low pressures. I. Solutions of the master equation. *The Journal of Chemical Physics*, 1977, **66**, p.4745.

78. Troe, J. Fall-off Curves of Unimolecular Reactions. *Berichte der Bunsengesellschaft für physikalische Chemie*, 1974, **78**(5), pp.478-488.

79. Troe, J. Theory of Thermal Unimolecular Reactions in the Fall-off Range. I. Strong Collision Rate Constants. *Berichte der Bunsengesellschaft für physikalische Chemie*, 1983, **87**(2), pp.161-169.

80. Gilbert, R., K. Luther and J. Troe. Theory of Thermal Unimolecular Reactions in the Fall-off Range. II. Weak Collision Rate Constants. *Berichte der Bunsengesellschaft für physikalische Chemie*, 1983, **87**(2), pp.169-177.

81. Kukkadapu, G., K. Kumar, C.-J. Sung, M. Mehl and W.J. Pitz. Experimental and surrogate modeling study of gasoline ignition in a rapid compression machine. *Combustion and Flame*, 2012, **159**(10), pp.3066-3078.

82. Pekalski, A.A., J.F. Zevenbergen, H.J. Pasman, S.M. Lemkowitz, A.E. Dahoe and B. Scarlett. The relation of cool flames and auto-ignition phenomena to process safety at elevated pressure and temperature. *Journal of Hazardous Materials*, 2002, **93**(1), pp.93-105.

83. Blurock, E. and F. Battin-Leclerc. Development of Detailed Kinetic Models: The Particular Case of Fuels Obtained from Biomass. *In:* F. Battin-Leclerc, J.M. Simmie and E. Blurock, eds. *Cleaner Combustion: Developing Detailed Chemical Kinetic Models*. London: Springer-Verlag, 2013.

84. Pilling, M.J. From elementary reactions to evaluated chemical mechanisms for combustion models. *Proceedings of the Combustion Institute*, 2009, **32**(1), pp.27-44.

85. Mazi, H.A. *Coupling of Chemical Kinetics with Computational Fluid Dynamics in a Three-Dimensional Engine Model*. Msc, Mechanical Engineering thesis, University of Illinois, 2009.

86. Glassman, I.Y., Richard *Combustion.* Elservier, 2008.

87. Niemeyer, K.E. *Skeletal Mechanism for Surrogates*. Msc, Aerospace Engineering thesis, Case Western Reserve University, 2010.

88. Mehl, M., W.J. Pitz, C.K. Westbrook and H.J. Curran. Kinetic modeling of gasoline surrogate components and mixtures under engine conditions. *Proceedings of the Combustion Institute*, 2011, **33**(1), pp.193-200.

89. Pitz, W.J. and C.J. Mueller. Recent progress in the development of diesel surrogate fuels. *Progress in Energy and Combustion Science*, 2011, **37**(3), pp.330-350.

90. Battin-Leclerc, F. *Detailed chemical kinetic models for the low-temperature combustion of hydrocarbons with application to gasoline and diesel fuel surrogates.* Progress in Energy and Combustion Science. 2008.

91. of on Chemical kinetics modelling of combustion processes in SI engines.

92. Kalghatgi, G. Developments in internal combustion engines and implications for combustion science and future transport fuels. *Proceedings of the Combustion Institute*, 2015, **35**(1), pp.101-115.

93. Gauthier, B.M., D.F. Davidson and R.K. Hanson. Shock tube determination of ignition delay times in full-blend and surrogate fuel mixtures. *Combustion and Flame*, 2004, **139**(4), pp.300-311.

94. Chaos, M., H. Zhao, A. Kazakov, P. Gokulakrishnan, M. Angioletti and F.L. Dryer. A PRF+Toluene Surrogate Fuel Model for Simulating Gasoline Kinetics. 2007.

95. Pitz, W.J., N.P. Cernansky, F.L. Dryer, F.N. Egolfopoulos, J.T. Farrell, D.G. Friend and H. Pitsch. Development of an Experimental Database and Chemical Kinetic Models for Surrogate Gasoline Fuels. *In*. SAE International, 2007.

96. Lenhert, D.B., D.L. Miller, N.P. Cernansky and K.G. Owens. The oxidation of a gasoline surrogate in the negative temperature coefficient region. *Combustion and Flame*, 2009, **156**(3), pp.549-564.

97. Kukkadapu, G., K. Kumar, C.-J. Sung, M. Mehl and W.J. Pitz. Autoignition of gasoline surrogates at low temperature combustion conditions. *Combustion and Flame*, 2015, **162**(5), pp.2272-2285.

98. Fikri, M., J. Herzler, R. Starke, C. Schulz, P. Roth and G.T. Kalghatgi. Autoignition of gasoline surrogates mixtures at intermediate temperatures and high pressures. *Combustion and Flame*, 2008, **152**(1–2), pp.276-281.

99. Sarathy, S.M., G. Kukkadapu, M. Mehl, T. Javed, A. Ahmed, N. Naser, A. Tekawade, G. Kosiba, M. Alabbad, E. Singh, S. Park, M.A. Rashidi, S.H. Chung, W.L. Roberts, M.A. Oehlschlaeger, C.-J. Sung and A. Farooq. Compositional effects on the ignition of FACE gasolines. *Combustion and Flame*, 2016, **169**, pp.171-193.

100. Ahmed, A., G. Goteng, V.S. Shankar, K. Al-Qurashi, W.L. Roberts and S.M. Sarathy. A computational methodology for formulating gasoline surrogate fuels

with accurate physical and chemical kinetic properties. *Fuel*, 2015, **143**, pp.290-300.

101. Morgan, N., A. Smallbone, A. Bhave, M. Kraft, R. Cracknell and G. Kalghatgi. Mapping surrogate gasoline compositions into RON/MON space. *Combustion and Flame*, 2010, **157**(6), pp.1122-1131.

102. Pera, C. and V. Knop. Methodology to define gasoline surrogates dedicated to auto-ignition in engines. *Fuel*, 2012, **96**, pp.59-69.

103. Mehl, M., J.-Y. Chen, W.J. Pitz, S. Sarathy and C.K. Westbrook. An approach for formulating surrogates for gasoline with application toward a reduced surrogate mechanism for CFD engine modeling. *Energy & Fuels*, 2011, **25**(11), pp.5215-5223.

104. Kukkadapu, G., K. Kumar, C.-J. Sung, M. Mehl and W.J. Pitz. Autoignition of gasoline and its surrogates in a rapid compression machine. *Proceedings of the Combustion Institute*, 2013, **34**(1), pp.345-352.

105. Knop, V., M. Loos, C. Pera and N. Jeuland. A linear-by-mole blending rule for octane numbers of n-heptane/iso-octane/toluene mixtures. *Fuel*, 2014, **115**, pp.666-673.

106. Tanaka, S., F. Ayala and J.C. Keck. A reduced chemical kinetic model for HCCI combustion of primary reference fuels in a rapid compression machine. *Combustion and Flame*, 2003, **133**(4), pp.467-481.

107. Glaude, P.A., V. Conraud, R. Fournet, F. Battin-Leclerc, G.M. Côme, G. Scacchi, P. Dagaut and M. Cathonnet. Modeling the Oxidation of Mixtures of Primary Reference Automobile Fuels. *Energy & Fuels*, 2002, **16**(5), pp.1186-1195.

108. Westbrook, C.K., J. Warnatz and W.J. Pitz. A detailed chemical kinetic reaction mechanism for the oxidation of iso-octane and n-heptane over an extended temperature range and its application to analysis of engine knock. *Symposium (International) on Combustion*, 1988, **22**(1), pp.893-901.

109. Andrae, J.C.G., P. Björnbom, R.F. Cracknell and G.T. Kalghatgi. Autoignition of toluene reference fuels at high pressures modeled with detailed chemical kinetics. *Combustion and Flame*, 2007, **149**(1–2), pp.2-24.

110. Andrae, J.C.G. Development of a detailed kinetic model for gasoline surrogate fuels. *Fuel*, 2008, **87**(10–11), pp.2013-2022.

111. Naik, C.V., W.J. Pitz, C.K. Westbrook, M. Sjöberg, J.E. Dec, J. Orme, H.J. Curran and J.M. Simmie. Detailed Chemical Kinetic Modeling of Surrogate Fuels for Gasoline and Application to an HCCI Engine. *In*. SAE International, 2005.

112. Dagaut, P., J.-C. Boettner and M. Cathonnet. Chemical kinetic study of dimethylether oxidation in a jet stirred reactor from 1 to 10 ATM: Experiments

and kinetic modeling. *In: Symposium (International) on Combustion*: Elsevier, 1996, pp.627-632.

113. Pfahl, U., K. Fieweger and G. Adomeit. Self-ignition of diesel-relevant hydrocarbon-air mixtures under engine conditions. *Symposium (International) on Combustion*, 1996, **26**(1), pp.781-789.

114. Curran, H., W. Pitz, C. Westbrook, P. Dagaut, J. Boettner and M. Cathonnet. A wide range modeling study of dimethyl ether oxidation. *International Journal of Chemical Kinetics*, 1998, **30**(3), pp.229-241.

115. Dagaut, P., C. Daly, J.M. Simmie and M. Cathonnet. The oxidation and ignition of dimethylether from low to high temperature (500–1600 K): Experiments and kinetic modeling. *Symposium (International) on Combustion*, 1998, **27**(1), pp.361-369.

116. Fischer, S., F. Dryer and H. Curran. The reaction kinetics of dimethyl ether. I: High-temperature pyrolysis and oxidation in flow reactors. *International Journal of Chemical Kinetics*, 2000, **32**(12), pp.713-740.

117. Curran, H., S. Fischer and F. Dryer. The reaction kinetics of dimethyl ether. II: Low-temperature oxidation in flow reactors. *International Journal of Chemical Kinetics*, 2000, **32**(12), pp.741-759.

118. Kaiser, E.W., T.J. Wallington, M.D. Hurley, J. Platz, H.J. Curran, W.J. Pitz and C.K. Westbrook. Experimental and Modeling Study of Premixed Atmospheric-Pressure Dimethyl Ether−Air Flames. *The Journal of Physical Chemistry A*, 2000, **104**(35), pp.8194-8206.

119. Zhao, Z., A. Kazakov and F.L. Dryer. Measurements of dimethyl ether/air mixture burning velocities by using particle image velocimetry. *Combustion and Flame*, 2004, **139**(1–2), pp.52-60.

120. Daly, C.A., J.M. Simmie, J. Würmel, N. Djebaïli and C. Paillard. Burning velocities of dimethyl ether and air. *Combustion and Flame*, 2001, **125**(4), pp.1329-1340.

121. Wang, H., L. Zhou, D. Jiang and Z. Huang. Study on the performance and emissions of a compression ignition engine fuelled with dimethyl ether. *Proceedings of the Institution of Mechanical Engineers, Part D: Journal of Automobile Engineering*, 2000, **214**(1), pp.101-106.

122. Cool, T.A., J. Wang, N. Hansen, P.R. Westmoreland, F.L. Dryer, Z. Zhao, A. Kazakov, T. Kasper and K. Kohse-Höinghaus. Photoionization mass spectrometry and modeling studies of the chemistry of fuel-rich dimethyl ether flames. *Proceedings of the Combustion Institute*, 2007, **31**(1), pp.285-293.

123. Zheng, X., T. Lu, C. Law, C. Westbrook and H. Curran. Experimental and computational study of nonpremixed ignition of dimethyl ether in counterflow. *Proceedings of the Combustion Institute*, 2005, **30**(1), pp.1101-1109.

124. Zhao, Z., M. Chaos, A. Kazakov and F.L. Dryer. Thermal decomposition reaction and a comprehensive kinetic model of dimethyl ether. *International Journal of Chemical Kinetics*, 2008, **40**(1), pp.1-18.

125. Metcalfe, W.K., S.M. Burke, S.S. Ahmed and H.J. Curran. A Hierarchical and Comparative Kinetic Modeling Study of C1 − C2 Hydrocarbon and Oxygenated Fuels. *International Journal of Chemical Kinetics*, 2013, **45**(10), pp.638-675.

126. Liu, D., J. Santner, C. Togbé, D. Felsmann, J. Koppmann, A. Lackner, X. Yang, X. Shen, Y. Ju and K. Kohse-Höinghaus. Flame structure and kinetic studies of carbon dioxide-diluted dimethyl ether flames at reduced and elevated pressures. *Combustion and Flame*, 2013, **160**(12), pp.2654-2668.

127. Curran, H.J., P. Gaffuri, W.J. Pitz and C.K. Westbrook. A Comprehensive Modeling Study of n-Heptane Oxidation. *Combustion and Flame*, 1998, **114**(1–2), pp.149-177.

128. Guo, H., W. Sun, F.M. Haas, T. Farouk, F.L. Dryer and Y. Ju. Measurements of H 2 O 2 in low temperature dimethyl ether oxidation. *Proceedings of the Combustion Institute*, 2013, **34**(1), pp.573-581.

129. Yasunaga, K., F. Gillespie, J. Simmie, H. Curran, Y. Kuraguchi, H. Hoshikawa, M. Yamane and Y. Hidaka. A multiple shock tube and chemical kinetic modeling study of diethyl ether pyrolysis and oxidation. *The Journal of Physical Chemistry A*, 2010, **114**(34), pp.9098-9109.

130. Cook, R.D., D.F. Davidson and R.K. Hanson. Shock tube measurements of ignition delay times and OH time-histories in dimethyl ether oxidation. *Proceedings of the Combustion Institute*, 2009, **32**(1), pp.189-196.

131. Hu, E., X. Jiang, Z. Huang, J. Zhang, Z. Zhang and X. Man. Experimental and Kinetic Studies on Ignition Delay Times of Dimethyl Ether/n-Butane/O2/Ar Mixtures. *Energy & Fuels*, 2012, **27**(1), pp.530-536.

132. Donato, N., C. Aul, E. Petersen, C. Zinner, H. Curran and G. Bourque. Ignition and Oxidation of 50/50 Butane Isomer Blends. *Journal of Engineering for Gas Turbines and Power*, 2010, **132**(5), pp.051502-051502-9.

133. Jiang, X., Y. Zhang, X. Man, L. Pan and Z. Huang. Shock Tube Measurements and Kinetic Study on Ignition Delay Times of Lean DME/n-Butane Blends at Elevated Pressures. *Energy & Fuels*, 2013, **27**(10), pp.6238-6246.

134. Pan, L., E. Hu, Z. Tian, F. Yang and Z. Huang. Experimental and kinetic study on ignition delay times of dimethyl ether at high temperatures. *Energy & Fuels*, 2015, **29**(5), pp.3495-3506.

135. Pan, L., E. Hu, J. Zhang, Z. Zhang and Z. Huang. Experimental and kinetic study on ignition delay times of DME/H2/O2/Ar mixtures. *Combustion and Flame*, 2014, **161**(3), pp.735-747.

136. Mittal, G., M. Chaos, C.-J. Sung and F.L. Dryer. Dimethyl ether autoignition in a rapid compression machine: Experiments and chemical kinetic modeling. *Fuel Processing Technology*, 2008, **89**(12), pp.1244-1254.

137. Barnard, J.A. The pyrolysis of n-butanol. *Transactions of the Faraday Society*, 1957, **53**(0), pp.1423-1430.

138. Smith, S.R., A.S. Gordon and M.H. Hunt. : Studies of Diffusion Flames. III. The Diffusion Flames of the Butanols. *The Journal of Physical Chemistry*, 1957, **61**(5), pp.553-558.

139. Burgoyne, J. and A. Roberts. The Spread of Flame Across a Liquid Surface. II. Steady-State Conditions. *Proceedings of the Royal Society of London. Series A. Mathematical and Physical Sciences*, 1968, **308**(1492), pp.55-68.

140. Moss, J.T., A.M. Berkowitz, M.A. Oehlschlaeger, J. Biet, V. Warth, P.-A. Glaude and F. Battin-Leclerc. An experimental and kinetic modeling study of the oxidation of the four isomers of butanol. *The Journal of Physical Chemistry A*, 2008, **112**(43), pp.10843-10855.

141. Sarathy, S., M. Thomson, C. Togbé, P. Dagaut, F. Halter and C. Mounaim-Rousselle. An experimental and kinetic modeling study of< i> n</i>-butanol combustion. *Combustion and Flame*, 2009, **156**(4), pp.852-864.

142. Mcenally, C.S. and L.D. Pfefferle. Fuel decomposition and hydrocarbon growth processes for oxygenated hydrocarbons: butyl alcohols. *Proceedings of the Combustion Institute*, 2005, **30**(1), pp.1363-1370.

143. Yang, B., P. Oßwald, Y. Li, J. Wang, L. Wei, Z. Tian, F. Qi and K. Kohse-Höinghaus. Identification of combustion intermediates in isomeric fuel-rich premixed butanol–oxygen flames at low pressure. *Combustion and Flame*, 2007, **148**(4), pp.198-209.

144. Grana, R., A. Frassoldati, T. Faravelli, U. Niemann, E. Ranzi, R. Seiser, R. Cattolica and K. Seshadri. An experimental and kinetic modeling study of combustion of isomers of butanol. *Combustion and Flame*, 2010, **157**(11), pp.2137-2154.

145. Black, G., H.J. Curran, S. Pichon, J.M. Simmie and V. Zhukov. Bio-butanol: Combustion properties and detailed chemical kinetic model. *Combustion and Flame*, 2010, **157**(2), pp.363-373.

146. Harper, M.R., K.M. Van Geem, S.P. Pyl, G.B. Marin and W.H. Green. Comprehensive reaction mechanism for n-butanol pyrolysis and combustion. *Combustion and Flame*, 2011, **158**(1), pp.16-41.

147. Song, J. *Building Robust Chemical Reaction Mechanisms: Next Generation of Automatic Model Construction Software*. PhD thesis, Massachusetts Institute of Technology, Cambridge, 2004.

148. Sarathy, S.M., S. Vranckx, K. Yasunaga, M. Mehl, P. Oßwald, W.K. Metcalfe, C.K. Westbrook, W.J. Pitz, K. Kohse-Höinghaus and R.X. Fernandes. A comprehensive chemical kinetic combustion model for the four butanol isomers. *Combustion and Flame*, 2012, **159**(6), pp.2028-2055.

149. Tomlin, A.S. *Methods for model evaluation and improvement*. Unpublished, 2013.

150. Tomlin, A.S. and T. Turanyi. Investigation and Improvement of Mechanism using Sensitivity Analysis and Optimization. *In:* F. Battin-Leclerc, J.M. Simmie and E. Blurock, eds. *Cleaner Combustion: Developing Detailed Chemical Kinetic Models* London: Springer-Verlag, 2013.

151. Javed, M.T.I.N.I.M.A. Combustion Kinetic Modeling *In:* M.W. Lackner, F; Agarwal, A. K, ed. *Handbook of Combustion*. WILEY-VCH, 2010.

152. Mittal, G. and C.-J. Sung. A rapid compression machine for chemical kinetics studies at elevated pressures and temperatures. *Combustion Science and Technology*, 2007, **179**(3), pp.497-530.

153. Lu, T. and C.K. Law. Toward accommodating realistic fuel chemistry in large-scale computations. *Progress in Energy and Combustion Science*, 2009, **35**(2), pp.192-215.

154. Kéromnès, A. Rapid Compression Machines. *In:* F. Battin-Leclerc, J.M. Simmie and E. Blurock, eds. *Cleaner Combustion: Developing Detailed Chemical Kinetic Models*. London: Springer-Verlag, 2013.

155. Bhaskaran, K.A. and P. Roth. The Shock tube as Wave Reactor for Kinetic Studies and Materials System. *Progress in Energy and Combustion Science*, 2012, **28**, pp.151-192.

156. Schreiber, M., A. Sadat Sakak, A. Lingens and J. Griffiths. A reduced thermokinetic model for the autoignition of fuels with variable octane ratings. *In: Symposium (International) on Combustion*: Elsevier, 1994, pp.933-940.

157. Mittal, G., C.J. Sung and R.A. Yetter. Autoignition of H2/CO at elevated pressures in a rapid compression machine. *International Journal of Chemical Kinetics*, 2006, **38**(8), pp.516-529.

158. Kramer, M.A., H. Rabitz, J.M. Calo and R.J. Kee. Sensitivity analysis in chemical kinetics: Recent developments and computational comparisons. *International Journal of Chemical Kinetics*, 1984, **16**(5), pp.559-578.

159. Salteli, A., M. Ratto, S. Tarantola and F. Campolongo. Sensitivity Analysis for Chemical Models. *American Chemical Society*, 2012.

160. Turanyi, T. Applications of sensitivity analysis to combustion chemistry. *Reliability Engineering & System Safety*, 1997, **57**(1), pp.41-48.

161. Rabitz, H., M. Kramer and D. Dacol. Sensitivity analysis in chemical kinetics. *Annual review of physical chemistry*, 1983, **34**(1), pp.419-461.

162. Dunker, A.M. The decoupled direct method for calculating sensitivity coefficients in chemical kinetics. *The Journal of Chemical Physics*, 1984, **81**(5), pp.2385-2393.

163. Ziehn, T. and A. Tomlin. GUI–HDMR–A software tool for global sensitivity analysis of complex models. *Environmental Modelling & Software*, 2009, **24**(7), pp.775-785.

164. Dlabka, J., A.S. Tomlin, V. Nevrly, M. Vasinek, L. Pecinka and Z. Zelinger. Global Sensitivity analysis of detailed chemical kinetic schemes for DME oxidation in premixed flames. *In: European Combustion Meeting*, Lund University, Sweden. 2013.

165. Tomlin, A.S. The use of global uncertainty methods for the evaluation of combustion mechanisms. *Reliability Engineering & System Safety*, 2006, **91**(10), pp.1219-1231.

166. Tomlin, A.S., E. Agbro, V. Nevrlý, J. Dlabka and M. Vašinek. Evaluation of Combustion Mechanisms Using Global Uncertainty and Sensitivity Analyses: A Case Study for Low-Temperature Dimethyl Ether Oxidation. *International Journal of Chemical Kinetics*, 2014, **46**(11), pp.662-682.

167. Tomlin, A.S. The role of sensitivity and uncertainty analysis in combustion modelling. *Proceedings of the Combustion Institute*, 2013, **34**(1), pp.159-176.

168. Heywood, J.B. Combustion Modeling in Reciprocating Engines. *In:* J.N. Mattavi, Amann, Charles A., ed. *Symposium on Combustion Modeling in Reciprocating Engines*. London: Plenium Press, 1980.

169. Stiesch, G. *Modeling Engine Spray and Combustion Process.* Springer, 2003.

170. Su, H. *Stochastic Reactor Models for Simulating direct injection Homogenous Charge Compression Ignition Engine*. PhD thesis, University of Cambridge, 2010.

171. Ganti, G. *Knock Modelling in Spark-ignition Engines and a Study of the Effect of Combustion Instability on Knock*. PhD thesis, Loughborough University of Technology, 1987.

172. Kalghatgi, G.T. Fuel Anti-Knock Quality - Part I. Engine Studies. *In*. SAE International, 2001.

173. Leppard, W.R. The Chemical Origin of Fuel Octane Sensitivity. *In*. SAE International, 1990.

174. Singh, A., J.F. Forbes, P.J. Vermeer and S.S. Woo. Model-based real-time optimization of automotive gasoline blending operations. *Journal of Process Control*, 2000, **10**(1), pp.43-58.

175. Ghosh, P., K.J. Hickey and S.B. Jaffe. Development of a detailed gasoline composition-based octane model. *Industrial & Engineering Chemistry Research*, 2006, **45**(1), pp.337-345.

176. Anderson, J., U. Kramer, S. Mueller and T. Wallington. Octane numbers of ethanol− and methanol− gasoline blends estimated from molar concentrations. *Energy & Fuels*, 2010, **24**(12), pp.6576-6585.

177. Wallner, T., S.A. Miers and S. Mcconnell. A comparison of ethanol and butanol as oxygenates using a direct-injection, spark-ignition (DISI) engine. *J. Eng. Gas Turbines Power*, 2009, **131**(ANL/ES/CP-61317).

178. Yaws, C.L. *Handbook of Thermodynamic Properties for Hydrocarbons and Chemicals*. Available from: http://app.knovel.com/hotlink/toc/id:kpYHTPHC09/yaws-handbook-thermodynamic/yaws-handbook-thermodynamic. 2009.

179. Liu, Z. and R. Chen. A zero-dimensional combustion model with reduced kinetics for SI engine knock simulation. *Combustion Science and Technology*, 2009, **181**(6), pp.828-852.

180. Sung, C.J. *Experimental Database; available at http://combdiaglab.engr.uconn.edu/database*. [Accessed May 2014]. 2014.

181. Burke, M.P., M. Chaos, Y. Ju, F.L. Dryer and S.J. Klippenstein. Comprehensive H2/O2 kinetic model for high-pressure combustion. *International Journal of Chemical Kinetics*, 2012, **44**(7), pp.444-474.

182. Goos, E., A. Burcat and B. Ruscic. Extended Third Millennium Thermodynamic Database for Combustion and Air-Pollution Use. Available at http://garfield.chem.elte.hu/Burcat/BURCAT.THR,. 2013.

183. Hébrard, É., A.S. Tomlin, R. Bounaceur and F. Battin-Leclerc. Determining predictive uncertainties and global sensitivities for large parameter systems: A case study for n-butane oxidation. *Proceedings of the Combustion Institute*, 2015, **35**(1), pp.607-616.

184. Baulch, D.L., C.T. Bowman, C.J. Cobos, R.A. Cox, T.H. Just, J.A. Kerr, M.J. Pilling, D. Stocker, J. Troe, W. Tsang, R.W. Walker and J. Warnatz. Evaluated kinetic data for combustion modeling: supplement II. *Journal of Physical and Chemical Reference Data*, 2005, **34**, pp.757-1397.

185. Baulch, D.L., C.J. Cobos, R.A. Cox, J.H. Frank, G. Hayman, T.H. Just, J.A. Kerr, T. Murrels, Pilling, J. M. J.; Troe, B.F. Walker and J. Warnatz. Summary table of evaluated kinetic data for combustion modeling: Supplement 1. *Combustion and Flame*, 1994, pp.59-79.

186. Baulch, D.L., C.J. Cobos, R.A. Cox, C. Esser, P. Frank, T. Just, J.A. Kerr, M.J. Pilling, J. Troe, R.W. Walker and J. Warnatz. Evaluated Kinetic Data for

Combustion Modelling. *Journal of Physical and Chemical Reference Data*, 1992, **21**(3), pp.411-734.

187. Tsang, W. Chemical Kinetic Data Base for Propellant Combustion. II. Reactions Involving CN, NCO, and HNCO. *Journal of Physical and Chemical Reference Data*, 1992, **21**(4), pp.753-791.

188. Tsang, W. and R.F. Hampson. Chemical Kinetic Data Base for Combustion Chemistry. Part I. Methane and Related Compounds. *Journal of Physical and Chemical Reference Data*, 1986, **15**(3), pp.1087-1279.

189. Goldsmith, C.F., A.S. Tomlin and S.J. Klippenstein. Uncertainty propagation in the derivation of phenomenological rate coefficients from theory: A case study of n-propyl radical oxidation. *Proceedings of the Combustion Institute*, 2013, **34**(1), pp.177-185.

190. Sobol, I.M. and S.S. Kucherenko. On global sensitivity analysis of quasi-Monte Carlo algorithms. *Monte Carlo Methods and Applications mcma*, 2005, **11**(1), p.83.

191. Ziehn, T., K. Hughes, J. Griffiths, R. Porter and A. Tomlin. A global sensitivity study of cyclohexane oxidation under low temperature fuel-rich conditions using HDMR methods. *Combustion Theory and Modelling*, 2009, **13**(4), pp.589-605.

192. Sobol, I.M. On the distribution of points in a cube and the approximate evaluation of integrals. *USSR Computational Mathematics and Mathematical Physics*, 1967, **7**(4), pp.86-112.

193. Tomlin, A.S. and T. Ziehn. The Use of Global Sensitivity Methods for the Analysis, Evaluation and Improvement of Complex Modelling Systems. *In:* A.N. Gorban and D. Roose, eds. *Coping with Complexity: Model Reduction and Data Analysis*

Berlin: Springer, 2011, pp.9-36.

194. Weber, B.W., K. Kumar, Y. Zhang and C.-J. Sung. Autoignition of n-butanol at elevated pressure and low-to-intermediate temperature. *Combustion and Flame*, 2011, **158**(5), pp.809-819.

195. Materego, M. *Auto-ignition Characterisation of Synthetic Fuels via Rapid Compression Machine*. PhD thesis, The University of Leeds, 2015.

196. Weber, B.W. *GitHub account (https://github.com/bryanwweber /CanSen).* [Accessed July 2014].

197. Agbro, E., M. Mategoro, A.S. Tomlin and M. Lawes. Low Temperature Ignition Properties of n-Butanol: Key Uncertainties and Constraints. *In: in: 7th European Combustion Meeting*, Budapest. 2015.

198. Mcgillen, M.R., M. Baasandorj and J.B. Burkholder. Gas-Phase Rate Coefficients for the OH + n-, i-, s-, and t-Butanol Reactions Measured Between

220 and 380 K: Non-Arrhenius Behavior and Site-Specific Reactivity. *The Journal of Physical Chemistry A*, 2013, **117**(22), pp.4636-4656.

199. Sarathy, S.M., P. Oßwald, N. Hansen and K. Kohse-Höinghaus. Alcohol combustion chemistry. *Progress in Energy and Combustion Science*, 2014, **44**, pp.40-102.

200. Reaction Design. *CHEMKIN-PRO*. Patent number:

201. Weber, B.W. and C.-J. Sung. Comparative Autoignition Trends in Butanol Isomers at Elevated Pressure. *Energy & Fuels*, 2013, **27**(3), pp.1688-1698.

202. Sarathy, S.M., S. Park, B.W. Weber, W. Wang, P.S. Veloo, A.C. Davis, C. Togbe, C.K. Westbrook, O. Park and G. Dayma. A comprehensive experimental and modeling study of iso-pentanol combustion. *Combustion and Flame*, 2013, **160**(12), pp.2712-2728.

203. Somers, K.P., J.M. Simmie, F. Gillespie, U. Burke, J. Connolly, W.K. Metcalfe, F. Battin-Leclerc, P. Dirrenberger, O. Herbinet and P.-A. Glaude. A high temperature and atmospheric pressure experimental and detailed chemical kinetic modelling study of 2-methyl furan oxidation. *Proceedings of the Combustion Institute*, 2013, **34**(1), pp.225-232.

204. Loge Ab -Lund Combustion Engineering Company. *LOGESOFT and LOGEengine.* Sweden, 2016.

205. Woschni, G. *A universally applicable equation for the instantaneous heat transfer coefficient in the internal combustion engine*. 0148-7191. SAE Technical paper, 1967.

206. Peters, N. *Turbulent combustion.* Cambridge Univeristy Press, 2000.

207. Pasternak, M., F. Mauss, F. Xavier, M. Rieß, M. Sens and A. Benz. 0D/3D Simulations of Combustion in Gasoline Engines Operated with Multiple Spark Plug Technology. *In*. SAE International, 2015.

208. Pasternak, M., F. Mauss, M. Sens, M. Riess, A. Benz and K.G. Stapf. Gasoline engine simulations using zero-dimensional spark ignition stochastic reactor model and three-dimensional computational fluid dynamics engine model. *International Journal of Engine Research*, 2015, **17**(1), pp.76-85.

209. Hussein, A.M.T. *New and Renewable Energy: Renewable Fuels in Internal Combustion Engines.* PhD thesis, Univeristy of Leeds, 2012.

210. Bjerkborn, S.P., C; Fröjd, K; Mauss, F. Predictive Flame Propagation Model for Stochastic Reactor Model Based Engine Simulations. *In: International Colloquium on the Dynamics of Explosions and Reactive Systems (ICDERS)*, California, USA., 2011.

211. Bjerkborn, S. *Development and Validation of a Turbulent Flame Propagation Model*. Msc thesis, Lund University 2011.

212. Zhou, D.D.Y., M.J. Davis and R.T. Skodje. Multitarget Global Sensitivity Analysis of n-Butanol Combustion. *The Journal of Physical Chemistry A*, 2013, **117**(17), pp.3569-3584.

213. Ziehn, T. and A.S. Tomlin. A global sensitivity study of sulfur chemistry in a premixed methane flame model using HDMR. *International Journal of Chemical Kinetics*, 2008, **40**(11), pp.742-753.

214. Gao, J. and Y. Nakamura. Low-temperature ignition of dimethyl ether: transition from cool flame to hot flame promoted by decomposition of HPMF (HO 2 CH 2 OCHO). *Combustion and Flame*, 2016, **165**, pp.68-82.

215. Eskola, A., S. Carr, R. Shannon, B. Wang, M. Blitz, M. Pilling, P. Seakins and S. Robertson. Analysis of the Kinetics and Yields of OH Radical Production from the CH3OCH2+ O2 Reaction in the Temperature Range 195–650 K: An Experimental and Computational study. *The Journal of Physical Chemistry A*, 2014, **118**(34), pp.6773-6788.

216. Gao, J. and Y. Nakamura. Two-stage ignition of DME/air mixture at low-temperature (< 500 K) under atmospheric pressure. *Fuel*, 2013, **106**, pp.241-248.

217. Mittal, G., C. Sung, M. Fairweather, A. Tomlin, J. Griffiths and K. Hughes. Significance of the HO 2+ CO reaction during the combustion of CO+ H 2 mixtures at high pressures. *Proceedings of the Combustion Institute*, 2007, **31**(1), pp.419-427.

218. Turányi, T., T. Nagy, I.G. Zsély, M. Cserháti, T. Varga, B. Szabó, I. Sedyó, P. Kiss, A. Zempléni and H. Curran. Determination of rate parameters based on both direct and indirect measurements. *International Journal of Chemical Kinetics*, 2012, **44**(5), pp.284-302.

219. Andersen, A. and E.A. Carter. First-principles-derived kinetics of the reactions involved in low-temperature dimethyl ether oxidation. *Molecular Physics*, 2008, **106**(2-4), pp.367-396.

220. Zádor, J., H. Huang, O. Welz, J. Zetterberg, D. Osborn and C. Taatjes. Directly measuring reaction kinetics of ˙ QOOH--a crucial but elusive intermediate in hydrocarbon autoignition. *Physical chemistry chemical physics: PCCP*, 2013, **15**(26), pp.10753-10760.

221. Goldsmith, C.F., W.H. Green and S.J. Klippenstein. Role of O2+ QOOH in low-temperature ignition of propane. 1. Temperature and pressure dependent rate coefficients. *The Journal of Physical Chemistry A*, 2012, **116**(13), pp.3325-3346.

222. Heufer, K., R. Fernandes, H. Olivier, J. Beeckmann, O. Röhl and N. Peters. Shock tube investigations of ignition delays of n-butanol at elevated pressures between 770 and 1250K. *Proceedings of the Combustion Institute*, 2011, **33**(1), pp.359-366.

223. Da Silva, G., J.W. Bozzelli, L. Liang and J.T. Farrell. Ethanol oxidation: Kinetics of the α-hydroxyethyl radical+ O2 reaction. *The Journal of Physical Chemistry A*, 2009, **113**(31), pp.8923-8933.

224. Zhou, C.-W., J.M. Simmie and H.J. Curran. Rate constants for hydrogen-abstraction by from n-butanol. *Combustion and Flame*, 2011, **158**(4), pp.726-731.

225. Zador, J. and J.A. Miller. *Hydrogen Abstracyion from ni--Propanol and n-Butanol: A Systematic Theorecal Approach*. Sandia National Laboratories (SNL-CA), Livermore, CA (United States), 2011.

226. Agarwal, A.K. Biofuels (alcohols and biodiesel) applications as fuels for internal combustion engines. *Progress in Energy and Combustion Science*, 2007, **33**(3), pp.233-271.

227. Szwaja, S. and J.D. Naber. Combustion of n-butanol in a spark-ignition IC engine. *Fuel*, 2010, **89**(7), pp.1573-1582.

228. Alramadan, A.S., J. Badra, T. Javed, M. Al-Abbad, N. Bokhumseen, P. Gaillard, H. Babiker, A. Farooq and S.M. Sarathy. Mixed butanols addition to gasoline surrogates: Shock tube ignition delay time measurements and chemical kinetic modeling. *Combustion and Flame*, 2015, **162**(10), pp.3971-3979.

229. Badra, J.A., N. Bokhumseen, N. Mulla, S.M. Sarathy, A. Farooq, G. Kalghatgi and P. Gaillard. A methodology to relate octane numbers of binary and ternary n-heptane, iso-octane and toluene mixtures with simulated ignition delay times. *Fuel*, 2015, **160**, pp.458-469.

230. Goldsborough, S.S. A chemical kinetically based ignition delay correlation for iso-octane covering a wide range of conditions including the NTC region. *Combustion and Flame*, 2009, **156**(6), pp.1248-1262.

231. Mittal, G. and C.-J. Sung. Autoignition of toluene and benzene at elevated pressures in a rapid compression machine. *Combustion and Flame*, 2007, **150**(4), pp.355-368.

232. Yuan, W., Y. Li, P. Dagaut, J. Yang and F. Qi. Investigation on the pyrolysis and oxidation of toluene over a wide range conditions. II. A comprehensive kinetic modeling study. *Combustion and Flame*, 2015, **162**(1), pp.22-40.

233. Seta, T., M. Nakajima and A. Miyoshi. High-temperature reactions of OH radicals with benzene and toluene. *The Journal of Physical Chemistry A*, 2006, **110**(15), pp.5081-5090.

234. Nagy, T., É. Valkó, I. Sedyó, I.G. Zsély, M.J. Pilling and T. Turányi. Uncertainty of the rate parameters of several important elementary reactions of the H2 and syngas combustion systems. *Combustion and Flame*, 2015, **162**(5), pp.2059-2076.

235. Frassoldati, A., A. Cuoci, T. Faravelli and E. Ranzi. Kinetic modeling of the oxidation of ethanol and gasoline surrogate mixtures. *Combustion Science and Technology*, 2010, **182**(4-6), pp.653-667.

236. Saisirirat, P., C. Togbé, S. Chanchaona, F. Foucher, C. Mounaim-Rousselle and P. Dagaut. Auto-ignition and combustion characteristics in HCCI and JSR using 1-butanol/n-heptane and ethanol/n-heptane blends. *Proceedings of the Combustion Institute*, 2011, **33**(2), pp.3007-3014.

237. Pang, G.A., R.K. Hanson, D.M. Golden and C.T. Bowman. Rate Constant Measurements for the Overall Reaction of OH + 1-Butanol → Products from 900 to 1200 K. *The Journal of Physical Chemistry A*, 2012, **116**(10), pp.2475-2483.

238. Aghdam, E.A. *Improvement and Validation of a Thermodynamic S. I. Engine Simulation Code.* PhD thesis, University of Leeds, 2003.

239. Ling, Z., A. Burluka and U. Azimov. Knock Properties of Oxygenated Blends in Strongly Charged and Variable Compression Ratio Engines. 2014.

240. Al-Mughanam, T. *Fundamental Characterisation of the Flame Propagation of Synthetic Fuels.* PhD thesis, The University of Leeds, 2013.

241. Moxey, B.G. *A Study Of Flame Development with Iso-octane Alcohol Engine Blended Fuels in an Optical Spark Ignition Engine*. PhD thesis, Brunel University London, 2014.

242. Westbrook, C.K. and W.J. Pitz. Detailed Kinetic Modeling of Autoignition Chemistry. *In*. SAE International, 1987.

243. Yang, C., H. Zhao and T. Megaritis. In-Cylinder Studies of CAI Combustion with Negative Valve Overlap and Simultaneous Chemiluminescence Analysis. *In*. SAE International, 2009.

244. Atkinson, R., D.L. Baulch, R.A. Cox, R.F. Hampson, J.A. Kerr and J. Troe. Evaluated Kinetic and Photochemical Data for Atmospheric Chemistry: Supplement III. IUPAC Subcommittee on Gas Kinetic Data Evaluation for Atmospheric Chemistry. *Journal of Physical and Chemical Reference Data*, 1989, **18**(2), pp.881-1097.

245. Warnatz, J. Rate Coefficients in the C/H/O System. *In:* W.C. Gardiner, ed. *Combustion Chemistry*. Springer-Verlag, NY, 1984.

246. Atkinson, R., D. Baulch, R. Cox, R. Hampson Jr, J. Kerr and J. Troe. Evaluated kinetic and photochemical data for atmospheric chemistry: supplement III. IUPAC subcommittee on gas kinetic data evaluation for atmospheric chemistry. *Journal of Physical and Chemical Reference Data*, 1989, **18**(2), pp.881-1097.